

ENGINEERING THE (VASCULARIZED) PROXIMAL TUBULE, A GUIDE TOWARDS FUNCTIONALITY

ANNE METJE VAN GENDEREN



**Engineering the (vascularized) Proximal Tubule,
a Guide Towards Functionality**

Anne Metje van Genderen
2023



Het keurmerk voor
verantwoord bosbeheer
FSC® C128610

Layout and cover design: Jasmijn de Boer (www.jasmijndeboer.nl)

Printed by: Ipskamp Printing

ISBN: 978-94-6473-053-1

DOI: <https://doi.org/10.33540/1697>

Copyright © 2023 Anne Metje van Genderen

All rights reserved. No part of this thesis may be reproduced or transmitted in any form or by any means, without prior written permission of the author.

Financial support by the Utrecht Institute for Pharmaceutical Sciences for the printing of this thesis is gratefully acknowledged.

The research presented in this thesis was performed at the Division of Pharmacology, Utrecht Institute for Pharmaceutical Sciences, Faculty of Science, Utrecht University and the Division of Engineering in Medicine, Department of Medicine, Brigham and Women's Hospital, Harvard Medical School.

The research project was financially supported by funding from the Dutch Kidney Foundation (17PHD16). Extra financial support to visit Harvard Medical School was provided by the Hofvijverkring Visiting Scientist Program, and the Materials Driven Regeneration Young Talent Grant.

**Engineering the (vascularized) Proximal Tubule,
a Guide Towards Functionality**

**Het Ontwikkelen van een (gevasculariseerd) Nierbuisje,
een Leidraad voor Toepasbaarheid**

(met een samenvatting in het Nederlands)

Proefschrift

ter verkrijging van de graad van doctor aan de
Universiteit Utrecht
op gezag van de
rector magnificus, prof.dr. H.R.B.M. Kummeling,
ingevolge het besluit van het college voor promoties
in het openbaar te verdedigen op

maandag 24 april 2023 des middags te 2.15 uur

door

Anne Metje van Genderen

geboren op 6 juli 1992
te Gorinchem

Promotoren:

Prof. dr. R. Masereeuw

Prof. dr. T. Vermonden

Copromotor:

Dr. J. Jansen

Beoordelingscommissie:

Prof. dr. M.C. Verhaar

Prof. dr. R.J. Kok

Prof. dr. M.A. Tryfonidou

Prof. dr. C.V.C. Bouten

Prof. dr. J.F. Mano

Table of Contents

Chapter 1	Introduction and thesis outline	6
Chapter 2	Renal Tubular- and Vascular Basement Membranes and their Mimicry in Engineering Vascularized Kidney Tubules	18
Chapter 3	Co-axial Printing of Convoluted Proximal Tubule for Kidney Disease Modeling	48
Chapter 4	Complexation-Induced Resolution Enhancement of 3D-printed Hydrogel Constructs	80
Chapter 5	Topographic Guidance in Melt-Electrowritten Tubular Scaffolds Enhances Engineered Kidney Tubule Performance	140
Chapter 6	Organized Melt-Electrowritten Tubular Scaffolds to Build Vascularized Kidney Proximal Tubules	170
Chapter 7	Summary and General Discussion	194
Chapter 8	Nederlandse Samenvatting About the Author List of Publications Dankwoord - Acknowledgements	210

CHAPTER 1

**GENERAL INTRODUCTION
AND THESIS OUTLINE**



1. Chronic kidney disease

Chronic kidney disease (CKD) affects around 13% of the world population, thereby imposing a major effect on global health, directly via global morbidity and mortality, but also indirectly via the increased risk for cardiovascular diseases [1–3]. CKD often results in end-stage kidney disease, for which the preferred treatment is organ transplantation including lifelong immunosuppressive therapy, however, this is hampered by a shortage of donor organs. While waiting for kidney transplantation, patients need to be treated with kidney replacement therapies (KRTs) like dialysis. Current KRTs are only partially capable of replacing kidney function, leading to many different side effects such as anemia [4]. About 1.2 million people are estimated to die directly or indirectly from CKD globally each year, it being in the top twenty of leading causes of death around the world [1].

The kidneys each consist of about one million nephrons (**Figure 1**), the functional units of the kidney that filter approximately 180 liter of blood each day. The nephrons entail 5 main segments, starting with the glomerulus, the proximal tubule (PT), the loop of Henle, the distal tubule, ending in the collecting duct. The main functions of these nephrons are maintaining body homeostasis via waste removal from the blood, regulation of electrolyte concentrations and blood pressure, reabsorption of essential molecules (e.g. glucose), production of hormones, and maintenance of acid-base balance and extracellular fluid volume. The glomerulus is responsible for filtration of the blood, whereafter the tubules are responsible for excretion. KRTs replicate predominantly the glomerular function but are not able to replace the tubular functions. Therefore, novel therapies involving cell-based strategies that can further replace kidney function need to be developed to complement dialysis.

When we focus a bit more on the PT and its specific functions, we can distinguish a large variety of functional transporters located in/at the basolateral and apical side of the proximal tubular epithelial cells (PTEC). These specific transport proteins contribute to the removal of endogenous waste including protein-bound uremic toxins (PBUTs) into the pro-urine, a function that is not replaced by current KRTs. Furthermore, the peritubular capillaries located in close proximity of the PT (**Figure 1**) enable continuous crosstalk and transport between the blood and the tubular compartment [5].

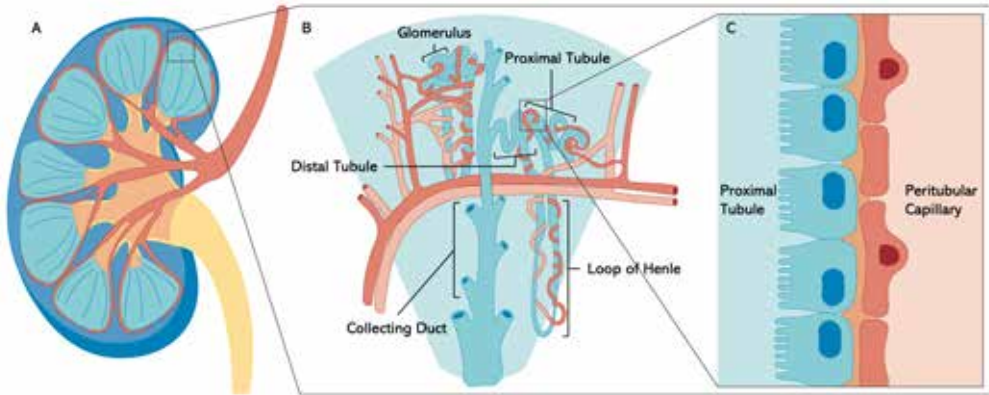


Figure 1. Schematic overview of the kidney. The kidney (A), the nephrons with surrounding vasculature (B), and the proximal tubule cells in close proximity of the peritubular capillaries (C).

2. Kidney tissue engineering

Tissue engineering is an interdisciplinary field that combines the principles of both engineering and biology to develop functional tissue that restores, maintains or improves tissue function.

In search for better KRTs, kidney tissue engineering has received great interest as it can serve multiple purposes including the development of implantable kidney tubules and bioartificial kidney devices. Especially the combination of state-of-the-art biomaterials and kidney cells could result in systems that can facilitate uremic toxin removal from blood into the dialysate. During the past decades various research groups have investigated diverse ways of engineering kidney PTs. Whilst some groups have focused on developments towards a bioartificial kidney, other groups have made first steps towards a transplantable (part of a) kidney [6–17]. Likewise, the progress of numerous microfluidic, on-chip, models for the kidney PT have been reported, mostly developed for studying drug-drug interactions, disease modeling, and drug safety testing, including work towards animal replacements [18–23].

3. Bioartificial kidney

Steps towards a bioartificial kidney were made by culturing conditionally immortalized PTEC (ciPTEC) on hollow fiber membranes (HFM) [11,12,14]. Biofunctionalization of HFM using a coating based on 3,4-dihydroxy-L-phenylalanine (L-DOPA) and collagen IV allowed for cell adhesion [24,25]. Furthermore, up-scalability, as well as safety of using conditionally immortalized proximal tubule epithelial cells (ciPTEC) in KRTs have been studied [13,26,27].

Although HFM provide a promising entity in the engineering of a bioartificial kidney, they might not be suitable for transplantation. CiPTEC are conditionally immortalized and, although immunogenicity testing gave relatively good results, the use of immortalized cells in a bioartificial kidney will most likely not be accepted by approving agencies like the FDA [26,27]. Hence, allogeneous cells, like the use of patient derived induced pluripotent stem cells (iPSC) would be favorable. Additionally, PES membranes, like HFM, although good materials as filtration units, also have some disadvantages as interaction with blood can initiate thrombosis [28]. Hence, looking into (bio)materials and cells that could potentially be implanted is of major importance.

4. Biofabrication

Biofabrication combines engineering, biology, and material science, and is defined as ‘the automated generation of biologically functional products with structural organization from living cells, bioactive molecules, biomaterials, cell aggregates such as micro-tissues, or hybrid cell-material constructs, through bioprinting or bioassembly and subsequent tissue maturation processes [29]. The field of Biofabrication encompasses two main pillars, namely bioprinting and bioassembly [29,30]. Bioprinting allows precise deposition of biomaterial inks or bioinks and enables printing of complex (parts of) tissues in a layer-by-layer approach. In the past decades, numerous bioprinting techniques have been developed, of which some have been utilized for kidney biofabrication [31-34]. Homan et al., (2016) and Lin et al., (2019) used a sacrificial bioprinting technique to create a vascularized convoluted proximal tubule within a gelatin-based hydrogel to improve current 3-dimensional (3D) in vitro models for drug screening and disease modelling [6,7]. Likewise, co-axial 3D cell printing has been studied for printing microfluidic hollow tubes containing PTEC and human umbilical vein endothelial cells (HUVEC), to create tubular tissue grafts [35]. In the last decade, melt-electrowriting (MEW) has gained increased interest [36-38]. MEW is a solvent-free technique that involves extrusion of a molten polymer fiber onto a computer-controlled collector. By precise fiber deposition on a rotating cylinder, organized 3D tubular constructs can be obtained. These organized 3D tubular constructs with defined geometries can be used as scaffolds for cells to grow on, mimicking the collagen fibrous network of the extracellular matrix (ECM) while only giving the cells limited support and, hopefully, guiding the cells to deposit their own ECM. Overall, it has become very clear that the role of the ECM, in which cells are embedded, on cell functionality is important. Therefore, biomaterials mimicking the ECM have been developed using different strategies, including the use of hydrogels, membranes, decellularized scaffolds, or combinations of them.

5. Biocompatibility of materials

When working towards a transplantable construct, it is important that the materials used are biocompatible and suitable for transplantation. Various researchers have investigated different materials that could be used, including polycaprolactone (PCL) which is commonly used for techniques as solution electrospinning or MEW [9,39,40]. Plant-based materials such as decellularized spinach or chive have also been investigated, although these materials hold various limitations such as tissue disintegration and deficient diffusion capacity [8,41]. On the other hand, natural polymers such as gelatin or silk fibroin hold great promise and can be used as scaffold material, or as a component for hydrogels or scaffolds [42,43]. Furthermore, hydrogels are often used biomaterials in tissue engineering as they can function as artificial ECM or scaffolds for cells [44]. Hydrogel matrices usually consist of natural or synthetic polymers, or a combination of both, that are stably connected via covalent or non-covalent crosslinks to form a highly hydrated 3D-polymer network [45]. Finally, in the search for other biomaterials, several groups have worked on (porcine) kidney decellularization, to use the decellularized ECM (dECM) as scaffold or biomaterial for cells to grow on [46–48]. dECM can provide mechanical support and a biochemical microenvironment which is known to facilitate cell growth and differentiation. Additionally, it was recently shown that kidney dECM enhanced vascularization and maturation of kidney organoids after transplantation of kidney organoids with dECM compared to kidney organoids alone [49]. Nonetheless, decellularization has its own difficulties including the recellularization process, as complete repopulation of the dECM scaffolds has not been successful yet [50].

Working towards potentially implantable kidney tubules, the following criteria to which the scaffolds must adhere can be summarized:

- Bio- and hemocompatible, non-immunogenic, and sustainable
- Small-sized to meet kidney physiology, and highly porous to reach a large surface area
- Freely accessible from basolateral and luminal sides for rapid solute exchange and removal
- Flexible and yet strong to withstand intracorporeal forces such as pressure, tear, and wear
- Ideally: initially, providing biophysical instructions to promote cell growth, differentiation, and BM production and finally the materials should be resorbable.

6. Thesis Aim and Outline

The aim of this thesis was to develop 3D bioengineered kidney tubules that can ultimately mediate the clearance of PBUTs. This requires a step-by-step approach of optimizing ECM

mimicking scaffolds and selecting functional cells that can closely mimic the complex environment of the proximal tubule.

In **Chapter 2**, we provide an extensive overview of the kidney tubular- and vascular BM, specialized ECM, and their mimicry in engineering vascularized kidney tubules. This review delivers a blueprint for PT engineering and serves as a base for this thesis as it highlights the most important features of the tubular and vascular BM, by specifying their role, characteristics, and biophysical properties.

In **Chapter 3**, an innovative coaxial printing system is presented suitable to print coiled hollow microfibers using a gelatin-alginate based biomaterial ink to closely mimic the convoluted microenvironment of the PT. While currently used models often provide limited structure, here we aimed to create biomimetic convoluted microfibers. To study the applicability of this model, both a healthy (ciPTEC) and a diseased (knockout for cystinosis: ciPTEC *CTNS*^{-/-}) cell line were used and assessed for monolayer formation, polarization, viability, and finally cell functionality.

Resolution remains one of the limiting factors for 3D (bio)printing in the micron range size (50 μm) of the proximal tubule [51]. To tackle this issue, we propose a novel method in **chapter 4**, where shrinking of hydrogels leads to dimensions that better replicate the physiological proximal kidney tubules. Anionic hydrogels, such as hyaluronic acid methacrylate (HAMA), gelatin methacryloyl (GelMA), and alginate, were selected as ink for 3D printing. We hypothesized that complexation of these negatively charged polymer networks with polycations would yield water expulsion and shrinking. In this chapter, we investigated whether this method could shrink the hydrogels towards physiologically relevant diameters.

In **chapter 3** and **chapter 4**, we focused on using hydrogels as scaffolds or ECM-mimics for the cells to grow on/in. However, hydrogel thickness can hamper oxygen supply, especially in non-perfused constructs, but also transport of nutrients and other compounds can be hampered, which is of vital importance to the kidney tubules [52]. Hence, we have explored other scaffold materials to overcome these issues. MEW, a fiber-based technology, can be used to obtain highly porous scaffolds with well-defined geometries. In **chapter 5**, we hypothesized that using MEW we can create tubular scaffolds where cells, here HUVEC and ciPTEC, form the only barrier between the inner and outer compartment. To examine the effects of scaffolds pore topographical guidance on cell performance, different pore geometries were investigated and evaluated for cell monolayer formation and tightness, ECM deposition, and cell functionality.

In **chapter 6**, we explored further the rhombus shaped tubular scaffolds and focused on developing a vascularized PT. By studying a range of pore sizes, winding angles, and cell sources, we optimized the PCL scaffolds for endothelial cells. Conditionally immortalized glomerular endothelial cells (ciGEnC), which more closely mimic the nature of the peritubular capillaries, were tested for their ability to form monolayers within the tubular scaffolds without extra support from *e.g.* a hydrogel, allowing for the formation of a vascular tubular scaffold. Finally, a direct co-culture model of ciPTEC and ciGEnC was studied using MEW tubular scaffolds.

Conclusively, **chapter 7** provides a general discussion of the findings in this thesis, as well as future perspectives in the kidney tissue engineering field, including pilot experiments using iPSC derived kidney organoids as a source for proximal tubule cells.

References

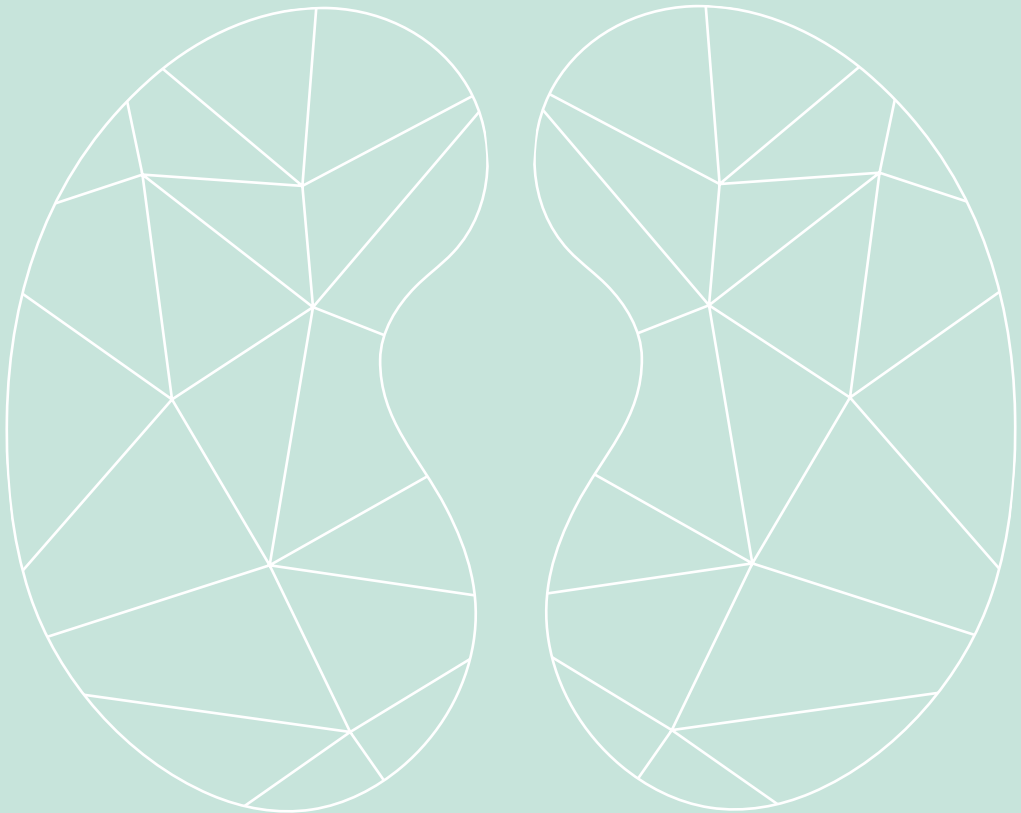
1. Carney, E. F. The impact of chronic kidney disease on global health. *Nat Rev Nephrol* **16**, 251–251 (2020).
2. Lv, J.-C. & Zhang, L.-X. Prevalence and Disease Burden of Chronic Kidney Disease. in 3–15 (2019).
3. Bikbov, B. *et al.* Global, regional, and national burden of chronic kidney disease, 1990–2017: a systematic analysis for the Global Burden of Disease Study 2017. *The Lancet* **395**, 709–733 (2020).
4. Mikhail, A. *et al.* Renal association clinical practice guideline on Anaemia of Chronic Kidney Disease. *BMC Nephrol* **18**, 345 (2017).
5. Zhuo, J. L. & Li, X. C. Proximal Nephron. in *Compr Physiol* 1079–1123 (Wiley, 2013).
6. Lin, N. Y. C. *et al.* Renal reabsorption in 3D vascularized proximal tubule models. *Proc Natl Acad Sci U S A* **116**, 5399–5404 (2019).
7. Homan, K. A. *et al.* Bioprinting of 3D Convoluted Renal Proximal Tubules on Perfusable Chips. *Sci Rep* **6**, 1–13 (2016).
8. Jansen, K. *et al.* Spinach and Chive for Kidney Tubule Engineering: the Limitations of Decellularized Plant Scaffolds and Vasculature. *AAPS J* **23**, 1–7 (2021).
9. Jansen, K. *et al.* Fabrication of Kidney Proximal Tubule Grafts Using Biofunctionalized Electrospun Polymer Scaffolds. *Macromol Biosci* **19**, 1800412 (2019).
10. van Genderen, A. M. *et al.* Topographic Guidance in Melt-Electrowritten Tubular Scaffolds Enhances Engineered Kidney Tubule Performance. *Front Bioeng Biotechnol* **8**, 1542 (2021).
11. Jansen, J. *et al.* Human proximal tubule epithelial cells cultured on hollow fibers: living membranes that actively transport organic cations. *Sci Rep* **5**, 16702 (2015).
12. Schophuizen, C. M. S. *et al.* Development of a living membrane comprising a functional human renal proximal tubule cell monolayer on polyethersulfone polymeric membrane. *Acta Biomater* **14**, 22–32 (2015).
13. Chevtchik, N. V. *et al.* Upscaling of a living membrane for bioartificial kidney device. *Eur J Pharmacol* **790**, 28–35 (2016).
14. Jansen, J. *et al.* Bioengineered kidney tubules efficiently excrete uremic toxins. *Sci Rep* **6**, 1–12 (2016).
15. Aebischer, P., Ip, T. K., Panol, G. & Galletti, P. M. The bioartificial kidney: progress towards an ultrafiltration device with renal epithelial cells processing. *Life Support Syst* **5**, 159–168 (1987).
16. Saito, A. Research into the Development of a Wearable Bioartificial Kidney with a Continuous Hemofilter and a Bioartificial Tubule Device Using Tubular Epithelial Cells. *Artif Organs* **28**, 58–63 (2004).
17. Humes, H. D., MacKay, S. M., Funke, A. J. & Buffington, D. A. The bioartificial renal tubule assist device to enhance CRRT in acute renal failure. *AJKD* **30**, S28–S31 (1997).
18. Weber, E. J. *et al.* Development of a microphysiological model of human kidney proximal tubule function. *Kidney Int* **90**, 627–637 (2016).
19. Jang, K.-J. *et al.* Human kidney proximal tubule-on-a-chip for drug transport and nephrotoxicity assessment. *Integr Biol* **5**, 1119–1129 (2013).
20. Sakolish, C. M., Philip, B. & Mahler, G. J. A human proximal tubule-on-a-chip to study renal disease and toxicity. *Biomicrofluidics* **13**, 014107 (2019).
21. Vedula, E. M., Alonso, J. L., Arnaout, M. A. & Charest, J. L. A microfluidic renal proximal tubule with active reabsorptive function. *PLoS One* **12**, e0184330 (2017).
22. Maass, C. *et al.* Translational Assessment of Drug-Induced Proximal Tubule Injury Using a Kidney Microphysiological System. *CPT Pharmacometrics Syst Pharmacol* **8**, 316–325 (2019).
23. Ashammakhi, N., Wesseling-Perry, K., Hasan, A., Elkhmmas, E. & Zhang, Y. S. Kidney-on-a-chip: untapped opportunities. *Kidney Int* **94**, 1073–1086 (2018).

24. Ni, M. *et al.* Characterization of membrane materials and membrane coatings for bioreactor units of bioartificial kidneys. *Biomaterials* **32**, 1465–1476 (2011).
25. Oo, Z. Y. *et al.* The performance of primary human renal cells in hollow fiber bioreactors for bioartificial kidneys. *Biomaterials* **32**, 8806–8815 (2011).
26. Mihajlovic, M. *et al.* Safety evaluation of conditionally immortalized cells for renal replacement therapy. *Oncotarget* **10**, 5332–5348 (2019).
27. Mihajlovic, M. *et al.* Are cell-based therapies for kidney diseases safe? A systematic review of preclinical evidence. *Pharmacol Ther* **197**, 191–211 (2019).
28. Irfan, M. and Idris, A. Overview of PES biocompatible/hemodialysis membranes: PES–blood interactions and modification techniques *Mater Sci Eng: C* **56** 574–92 (2015).
29. Groll, J. *et al.* Biofabrication: reappraising the definition of an evolving field. *Biofabrication* **8**, 013001 (2016).
30. Moroni, L. *et al.* Biofabrication: A Guide to Technology and Terminology. *Trends Biotechnol* **36**, 384–402 (2018).
31. Fransen, M. F. J. *et al.* Bioprinting of kidney *in vitro* models: cells, biomaterials, and manufacturing techniques. *Essays Biochem* **65**, 587–602 (2021).
32. Chung, J. J., Im, H., Kim, S. H., Park, J. W. & Jung, Y. Toward Biomimetic Scaffolds for Tissue Engineering: 3D Printing Techniques in Regenerative Medicine. *Front Bioeng Biotechnol* **8**, (2020).
33. Zhang, Y. S. *et al.* 3D extrusion bioprinting. *Nature Reviews Methods Primers* **1**, 75 (2021).
34. van Kampen, K. A. *et al.* Biofabrication: From Additive Manufacturing to Bioprinting. in *Reference Module in Biomedical Sciences* (Elsevier, 2019).
35. Singh, N. K. *et al.* Three-dimensional cell-printing of advanced renal tubular tissue analogue. *Biomaterials* **232**, (2020).
36. Dalton, P. D., Joergensen, N. T., Groll, J. & Moeller, M. Patterned melt electrospun substrates for tissue engineering. *Biomater* **3**, 034109 (2008).
37. Brown, T. D., Dalton, P. D. & Hutmacher, D. W. Direct Writing By Way of Melt Electrospinning. *Adv Mater* **23**, 5651–5657 (2011).
38. Brown, T. D. *et al.* Design and Fabrication of Tubular Scaffolds via Direct Writing in a Melt Electrospinning Mode. *Biointerphases* **7**, 13 (2012).
39. Vermue, Ij. M. *et al.* Renal Biology Driven Macro- and Microscale Design Strategies for Creating an Artificial Proximal Tubule Using Fiber-Based Technologies. *ACS Biomater Sci Eng* **7**, 4679–4693 (2021).
40. van Genderen, A. M., Jansen, J., Cheng, C., Vermonden, T. & Masereeuw, R. Renal Tubular- and Vascular Basement Membranes and their Mimicry in Engineering Vascularized Kidney Tubules. *Adv Healthc Mater* vol. 7 1800529 (2018).
41. Gershlak, J. R. *et al.* Crossing kingdoms: Using decellularized plants as perfusable tissue engineering scaffolds. *Biomaterials* **125**, 13–22 (2017).
42. Szymkowiak, S., Sandler, N. & Kaplan, D. L. Aligned Silk Sponge Fabrication and Perfusion Culture for Scalable Proximal Tubule Tissue Engineering. *ACS Appl Mater Interfaces* **13**, 10768–10777 (2021).
43. Gupta, A. K. *et al.* Scaffolding kidney organoids on silk. *J Tissue Eng Regen Med* **13**, 812–822 (2019).
44. Jansen, K., Schuurmans, C. C. L., Jansen, J., Masereeuw, R. & Vermonden, T. Hydrogel-Based Cell Therapies for Kidney Regeneration: Current Trends in Biofabrication and In Vivo Repair. *Curr Pharm Des* **23**, 3845–3857 (2017).
45. Buwalda, S. J. *et al.* Hydrogels in a historical perspective: From simple networks to smart materials. *JCR* **190**, 254–273 (2014).
46. Ali, M. *et al.* A Photo-Crosslinkable Kidney ECM-Derived Bioink Accelerates Renal Tissue Formation. *Adv Healthc Mater* **8**, 1800992 (2019).

47. Caralt, M. *et al.* Optimization and Critical Evaluation of Decellularization Strategies to Develop Renal Extracellular Matrix Scaffolds as Biological Templates for Organ Engineering and Transplantation. *Am J Transplant* **15**, 64–75 (2015).
48. Cintron Pregosin, N., Bronstein, R. & Mallipattu, S. K. Recent Advances in Kidney Bioengineering. *Front Pediatr* **9**, 743301 (2021).
49. Kim, J. W. *et al.* Kidney Decellularized Extracellular Matrix Enhanced the Vascularization and Maturation of Human Kidney Organoids. *Adv Sci* 2103526 (2022).
50. de Haan, M. J. A., Witjas, F. M. R., Engelse, M. A. & Rabelink, T. J. Have we hit a wall with whole kidney decellularization and recellularization: A review. *Curr Opin Biomed Eng* **20**, 100335 (2021).
51. Lote, C. J. *Principles of Renal Physiology*. (Springer New York, 2012).
52. Agarwal, T. *et al.* Oxygen releasing materials: Towards addressing the hypoxia-related issues in tissue engineering. *Mater Sci Eng C* vol. 122 111896 (2021).

CHAPTER 2

**RENAL TUBULAR- AND
VASCULAR BASEMENT
MEMBRANES AND THEIR
MIMICRY IN ENGINEERING
VASCULARIZED KIDNEY
TUBULES**



Abstract

The high prevalence of chronic kidney disease leads to an increased need for renal replacement therapies. While there are simply not enough donor organs available for transplantation, there is a need to seek other therapeutic avenues as current dialysis modalities are insufficient. The field of regenerative medicine and whole organ engineering is emerging, and researchers are looking for innovative ways to create (part of) a functional new organ. To biofabricate a kidney or its functional units, it is necessary to understand and learn from physiology to be able to mimic the specific tissue properties. Herein is provided an overview of the knowledge on tubular and vascular basement membranes' biochemical components and biophysical properties, and the major differences between the two basement membranes are highlighted. Furthermore, an overview of current trends in membrane technology for developing renal replacement therapies and to stimulate kidney regeneration is provided.

1. Introduction

Worldwide more than 10% of the population is affected by chronic kidney disease (CKD) [1]. This can progress until end-stage renal disease (ESRD) for which the preferred treatment is organ transplantation. Yearly, worldwide over eighty thousand kidney transplants are being performed [2]. The high prevalence of ESRD leads to long waiting lists for donor organs. On average, a kidney patient has to wait 3-4 years before transplantation. In the meantime, kidney patients have to deal with renal replacement therapies (RRTs) such as dialysis, which are only partly capable of replacing kidney function and associated with severe side effects such as cardiovascular complications [3, 4]. These side effects are, amongst others, a consequence of the insufficient clearance of uremic toxins, which are metabolic waste products that are in part coupled to plasma proteins such as albumin. Due to their physicochemical properties (large size), these protein-bound uremic toxins cannot be cleared via dialysis and lead to progression of CKD and cardiovascular diseases. As current dialysis therapies have not made significant improvements in the past decades, alternative innovative therapies are warranted. The emergent field of tissue engineering focusses on development of (parts of) bio-artificial organs e.g. by three-dimensional (3D) bioprinting, which may yield a future solution for the shortage of kidney transplants. Although it might still take many years before a fully functional kidney can be fabricated, because of its complexity, important steps towards small functional parts of the organ are currently being made. To enable the creation of biologically active (parts of) organs, fundamental understanding of the organ and its physiological properties is essential.

The kidney plays a key role in maintaining body homeostasis by removing wastes from the blood, regulating blood pressure and electrolyte concentrations, by the production of hormones, and maintaining acid-base balance and extracellular fluid volume. These characteristics are fulfilled by many different cell types within the functional units of the kidney, termed nephrons. Nephrons are composed of five major segments, starting from the glomerulus (or Bowman's capsule), to the proximal kidney tubule, the loop of Henle, the distal kidney tubule, ending in the collecting duct. The removal of protein-bound uremic toxins depends on the activity of transport proteins present in renal tubular cells. This function cannot be replaced by current RRTs. Ongoing research, including from our group, aims to engineer the proximal kidney tubule, which would open a new era of implantable constructs that can replace renal function *in vivo*. The luminal surface of the tubular epithelial cells is covered with microvilli that highly increase their surface area, thereby facilitating the reabsorptive function. The proximal tubule contributes to body homeostasis via the reabsorption of 60-70 percent of water and salts, and almost all of the nutrients in the

ultra-filtrate [5]. Additionally, the proximal tubule is responsible for active solute secretion, from blood into the pro-urine, facilitated by transport proteins. Underneath the epithelial cells, a basement membrane (BM) is located, which provides structural support, but it is also involved in controlling growth factor signaling thereby supporting the tissue's function [6]. BMs are highly specialized extracellular matrices (ECM) and act as scaffolds for the cells, as well as barriers. BMs are dynamic as they are continuously synthesized and degraded by cells, in a well-balanced process, and the composition of BMs can change over the course of renal development and disease.

To create a functional kidney tubule, proximal tubule cells have to be implemented in an (engineered) scaffold that serves as the BM for these cells. In the next chapters, we provide insight into the physiological conditions of the proximal tubular BM (TBM) and vascular BM (VBM), as well as their interplay, to create an overview on the important properties that should be included in a suitable scaffold.

2. The Role of the BM in Kidney Tubules

BMs are specialized sheet-like ECM structures that serve many functions including providing of mechanical stability and involvement in the regulation of essential cellular characteristics and growth factor signaling. BMs offer a structure on which both epithelial and endothelial cells can reside. The interaction between cells and BMs is of high importance for the development of tissues, their homeostasis, and also for the response to injury [7]. The macromolecular composition as well as the stiffness of the BM can affect the interactions between cells and the BM [6, 8, 9]. Defects of BM components have been associated with kidney diseases and/or adverse renal outcome [7, 10-12]. Kidney tubule epithelial cells are attached to the TBM, which is an adhesive substrate that anchors the basal plasma membranes of cells attached [13].

2.1 Biochemical and biophysical characteristics of the TBM

The BM consists of the lamina densa, an electron-dense zone, and the lamina rara or lucida, an electron-lucent zone [14, 15]. **Figure 1** and **Table 1** show the main components of the BM which include collagen type IV, laminins, glycoproteins including nidogens and heparan sulfate proteoglycans (HSPGs) perlecan and agrin, and fibronectin [6, 7, 13, 16-18]. Although these basic components are present in many tissues throughout the body, the exact composition of the ECM including the BM is very specific for every organ. Proteomic analysis revealed that the kidney ECM contains approximately 220 proteins that are kidney-specific

[19]. The molecular heterogeneity of the renal BM is often linked to its segmental nature, and its components vary profoundly between the nephron segments [16]. In this review article, we primarily focus on the proximal TBM.

Renal tubular epithelial cells are prone to lose their characteristics when cultured under standard *in vitro* conditions [20]. One of the reasons might be that while the ECM and BM promote many cell functions, including proliferation and differentiation via their mechanical and physical properties and stimuli, an ECM- or BM-like structure is often absent *in vitro*. Therefore, the establishment of suitable BMs that can be used *in vitro* is of great importance to optimize the culture conditions for these cells and to improve physiological relevance [21].

2.1.1 Biochemical components

The molecular composition of the BM changes over time, especially during embryogenesis the molecular composition deviates from that of mature BM [22]. To form the tubules, mesenchymal cells have to convert to epithelial tubules, and the ECM changes into a BM. The components of the BM are mostly produced by the epithelial and endothelial cells that reside at the BM.

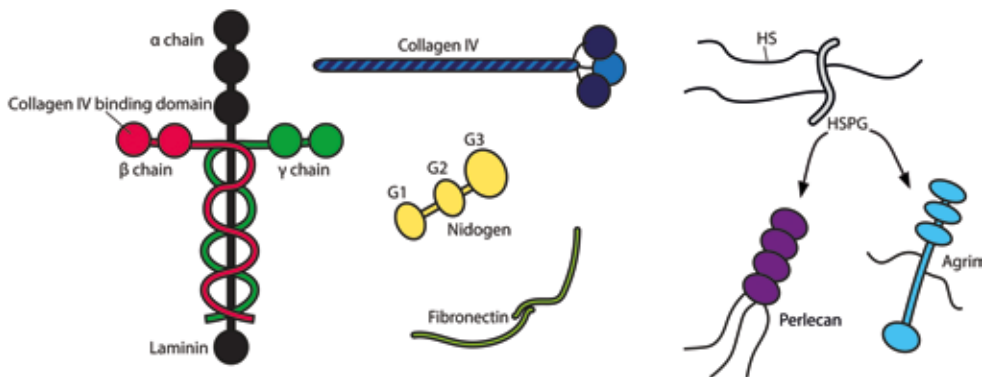


Figure 1. Schematic overview of the main components of the TBM and VBM. Collagen type IV, laminin, nidogen, HSPGs perlecan and agrin, and fibronectin.

Table 1. Overview of the main components of the TBM and VBM.

Component	TBM	VBM	Functions	References
Collagen IV	$\alpha 1(\text{IV})/\alpha 2(\text{IV})$ network	$\alpha 1(\text{IV})/\alpha 2(\text{IV})$ network		[16, 145]
Laminin	Laminin-1 ($\alpha 1\beta 1\gamma 1$) Laminin-2 ($\alpha 2\beta 1\gamma 1$) Laminin-10 ($\alpha 5\beta 1\gamma 1$)	Laminin-2 ($\alpha 2\beta 1\gamma 1$) - Larger vessels Laminin-8 ($\alpha 4\beta 1\gamma 1$) Laminin-10 ($\alpha 5\beta 1\gamma 1$)		[16, 82, 146-150]
Nidogen	Nidogen 1 Nidogen 2	Nidogen 1 Nidogen 2	Binds tightly laminin $\gamma 1$ chain and collagen IV	[42, 44]
Perlecan	Expressed	Expressed	Binds to nidogen, and collagen IV, involved in angiogenesis	[31, 151]

Collagen type IV: Collagen type IV is the most abundant component within TBMs comprising 50 percent or more of the total protein content [13, 23]. Its molecular weight is approximately 500 kDa. Typical for collagens is their triple helical structure that forms fibers that are cross-linked in a specific pattern within the BM, by which they form a flexible meshwork (**Figure 2**) [9]. This meshwork contains pores with diameters that are slightly smaller than albumin molecules, and thereby function as size barrier. Collagen IV consists of three α chains that together form the triple helix. Within the collagen IV family there are three different protomers, which vary in distinct α chains that trimerize. The three protomers are $(\alpha 1)_2\alpha 2$, $\alpha 3\alpha 4\alpha 5$, and $(\alpha 5)_2\alpha 6$. Within the ECM, the protomers self-polymerize to create a flexible network, which is crucial for the stability of the BM [24].

Collagen IV is cross-linked via sulfilimine bonds (S = N) between methionine sulfur and the nitrogen of hydroxylysine [25]. The links are formed by the matrix enzyme peroxidase. Bhav et al. recently showed that in a mouse model with reduced collagen IV sulfilimine cross-links, a reduction in renal TBM stiffness was observed [8]. *Laminins*: Laminins are heterotrimers that consist of one α chain, one β chain and one γ chain (**Figure 1**). Since there are various α , β , and γ chains, a total of 16 laminin isoforms have been identified. Laminins have a high-molecular weight and play a major role in BM assembly [26]. The self-assembly of laminin takes place at the cell surface, where it is anchored to the cell through interactions

with receptors. Opposed to the BM of other organs, laminin-1 accumulates in the renal BM at all stages of development, from embryonic to mature renal tissue [16, 27]. Madri et al. studied the localization of laminin in the murine renal BM, where laminin was located in the mesangial areas of the glomerulus as well as in typical BM-like patterns on both the glomerular BM (GBM) and TBM [28]. Furthermore, laminin was mainly located at the same sites as the collagens [28]. Laminin is located on the endothelial side of the BM, where it is suggested to be synthesized by endothelial cells that subsequently use it for adhesion to the underlying BM, or it might play a role as a glycoprotein that contains acidic residues and sialic acid. Laminin-1 ($\alpha 1\beta 1\gamma 1$), laminin-2 ($\alpha 2\beta 1\gamma 1$), and laminin-10 ($\alpha 5\beta 1\gamma 1$) are found in the TBM [16]. The vital role of laminin has been confirmed by studies in laminin $\alpha 4$ -null mutant mice, that developed severe chronic kidney disease because of their mutation [29]. Furthermore, laminin ($\alpha 1$) deficient mice showed severe kidney impairment, supporting the important role of laminin [30].

Integrins, transmembrane receptors, bind to laminin and collagen and facilitate binding of cells to the BM. Integrins are heterodimers composed of an α and β subunit connected by covalent bonds. The $\alpha 1\beta 1$ and $\alpha 2\beta 1$ integrins interact with collagen polymers, whereas $\alpha 3\beta 1$ and $\alpha 6\beta 1$ integrins specifically bind laminins. $\alpha 6\beta 1$ is specific for laminin-511 [6].

Glycoproteins:

HSPGs: HSPGs are a group of glycoproteins that all contain one or more covalently attached heparan sulfate chain via which they can bind many ligands. They are located at the cell surface and in the ECM, including the BM. HSPGs can be divided into three groups, (1) membrane HSPGs, (2) secreted ECM HSPGs, and (3) secretory vesicle proteoglycans. The HSPGs that are present in the BM are perlecan, agrin and collagen XVIII [31]. HSPGs located in the BM are also referred to as a binding reservoir for growth factors that can assist in creating a stable gradient with growth factors, such as vascular endothelial growth factors (VEGFs) for endothelial cells and fibroblast growth factors (FGFs) for epithelial cells. Additionally, HSPGs provide resistance to compression due to their highly hydrated nature [9, 32]. Furthermore, HSPGs are filling the space between the meshwork formed of laminin and type IV collagen, and have a major role in creating the charge-selective barrier of the kidney tubule because of their negatively charged heparan sulfate side chains [33]. Besides the HSPGs that are present in the BM, there are also HSPGs that are located at the cell surface that can bind to integrins to facilitate cell attachment to the BM, as well as offering cell-cell interactions [31]. Van den Heuvel et al. were able to isolate HSPGs from human TBM, and found that HSPG accounted for approximately 1 percent of dry weight of TBM [34].

The major HSPG is agrin (**Figure 1**), which is present in several isoforms and in many BMs. In the kidney tubule a truncated isoform of agrin that lacks (part of) the C-terminus is predominately present [35, 36]. Agrin is involved in the development of neuromuscular junction, which takes place during embryogenesis [36]. Additionally, it may also play a role in renal filtration and interactions between cells and BM [37].

Perlecan was the first HSPG to be isolated and characterized from the BM [38-40]. The 467 kD core of perlecan is connected to five functional domains of which three are heparin sulfate chains. Perlecan can bind and interact with growth factors and thereby controls cell-signaling [6].

Deletion of either agrin, perlecan or both in the GBM did not result in a loss of the BM structure, which indicates that HSPGs, in contrast to laminin and collagen IV, do not play a pivotal role in the structural arrangement of the BM [41].

Nidogens: Nidogens (nidogen-1 (NID1) and nidogen-2 (NID2)), formerly known as entactins, are sulfated monomeric glycoproteins which are located in BMs. Nidogens (150-200 kDa) consist of three globular domains (G1, G2, and G3) and are thought to play an important role in the assembly of the BM during development. NID1 and NID2 have a high affinity for both laminin-111 and collagen type IV and act as the linking molecule between the collagen type IV meshwork and the laminin network [42-44].

Even though nidogens play an important role in the BM, it seems that they are not crucial for the localization of several BM components (laminin-111, collagen type IV, and perlecan). Mice knockout for either the NID1 or NID2 gene did not show any alterations in the distribution of laminin-111, perlecan, and collagen type IV. Also, mice deficient in both NID1 and NID2 genes, showed similar distributions for laminin-111, perlecan, and collagen type IV. In these double-knockout mice, however, the BM was sometimes thickened [45].

Hyaluronic acid: Hyaluronic acid (HA), also called hyaluronan, is a non-sulfated glycosaminoglycan that is abundant in the ECM. HA is important during the embryonic development of the kidney, as it modulates branching morphogenesis [46]. Additionally, HA plays an important role in processes such as angiogenesis and tissue organization [47]. HA is also a promising polymer for the design of materials for tissue engineering applications as it is non-immunogenic and widely available [48]. In the mature kidney, HA is only present in the interstitium of the renal papilla, but not in the TBM.

Fibronectins: Although its role and presence in the BM has been questioned by several researchers, fibronectin is often stated to be abundant in plasma [49]. While recent literature on the exact role and presence of fibronectin is missing, it is sometimes used as coating agent for tissue culture materials [50]. Fibronectin is a glycoprotein with a large molecular weight (440 kDa) consisting of two nearly identical disulfide bound polypeptides. Many researchers state that fibronectin is located in the mesangium, while other researchers have reached the conclusion that fibronectin must be located in the BM [17, 51-55].

Madri et al. found in an ultrastructural localization of the murine renal BM that fibronectin is mainly located in the mesangial matrix [28]. They were not able to find BM localization for fibronectin. Nevertheless, 20 years later, fibronectin was found in the TBM using high-resolution ultrastructural microscopy [56].

One of the suggested roles for fibronectin is that it mediates the cell adhesion of mesenchymal cells to collagenous, as well as non-collagenous substrates [56-58]. Additionally, it has been associated with tissue repair after inflammation, functioning as a protein scaffold [59].

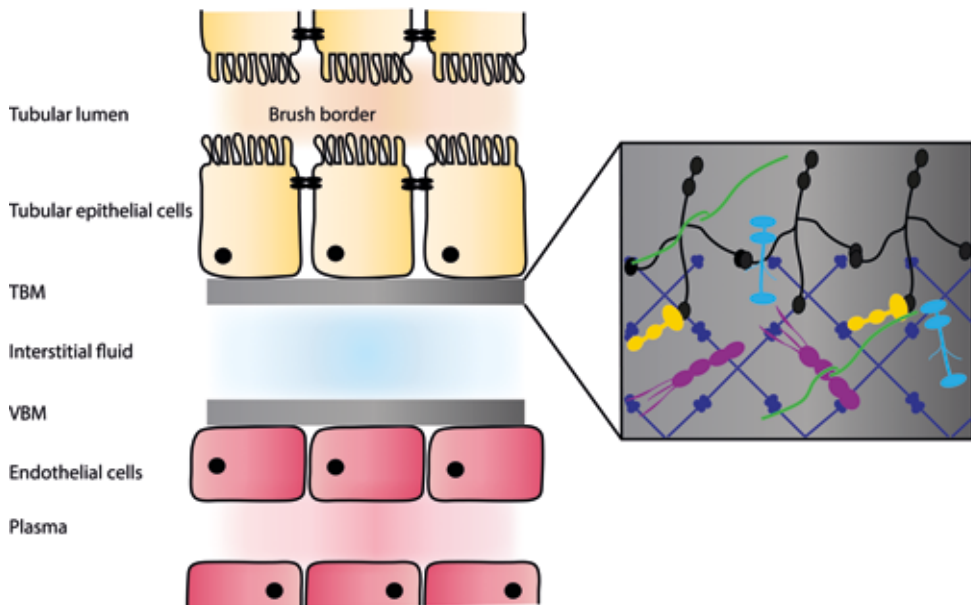


Figure 2. Schematic overview of location of the BM in the renal proximal tubule (TBM) and vasculature (VBM). Enlarged is a schematic drawing of the organized network of the main TBM and VBM components.

2.1.2 Biophysical properties

Chemical cues within the BM control cell behavior, but there are also physical cues, such as BM thickness and tissue stiffness, that can influence cell behavior and functioning of the BM itself in many ways. Limited studies have characterized the properties of the epithelial and endothelial BMs, and some results are conflicting (**Table 2**).

Ogawa et al. looked into the TBM using electron microscopy, which revealed that the TBM consists of a fine meshwork structure consisting of fibrils created by collagen IV and laminin [56]. These fibrils form small pores with variable sizes, ranging from 3.3 ± 0.5 nm (short-pore diameter) to 3.9 ± 0.6 nm (long-pore diameter). In the distal tubule, these pores are bigger, while the GBM consists of smaller pores. Whereas the fibril meshwork works as a size selective barrier, the HSPGs create a charge-selective barrier because of their negatively charged heparin sulfate chains [56].

TBM thickness: The thickness of all BMs throughout the human body range from 100 nm to over 10 μ m, and their morphology and composition change with age [60]. The TBM is not a solid membrane, but it is composed of fibrils sized 3 to 8 nm [61-63]. In rats, the thickness of the TBM ranges from 80–100 nm depending on the position within the tubule, their proximal TBM is the thickest. The BM of the loop of Henle and the distal segment in rats are thinner (< 80 nm) [13]. In humans, the TBM width ranges from ~360–670 nm (**Table 2**) [64, 65].

TBM stiffness: Tissue stiffness is mostly determined by the composition of the ECM. The degree of tissue stiffness will greatly influence proliferation and differentiation of cells. Many tissues are relatively soft, ranging in elastic modulus from 100 Pa to 100 kPa [66]. The Young's modulus (YM), also called elastic modulus, is used to describe the tensile or compression elasticity of any object reflecting its ability to return to its original shape after a force is applied. When looking for the YM of TBMs within the literature, values ranging from 3-10 MPa have been reported [67, 68]. However, these values differ greatly from the YM that has been reported for the whole kidney [13, 69, 70]. In **Table 2**, an overview is given on the YM found in various segments of the kidneys of diverse species. Variations can be explained by the different origin of the tissues used and techniques used for measuring. Recently, Beamish, et al. investigated the effect of ECM stiffness on the ability of renal proximal tubular cells to form an epithelial-like structure [71]. They observed that an increase in substrate stiffness resulted in better renal proximal tubule epithelial cells (RPTEC) spreading as well as their proliferation. Additionally, when culturing RPTEC for a longer time the stiffness of the hydrogel promoted the formation of epithelial monolayers that were more complete with

tight junctions, cell polarity, and an organized BM. However, Chen, et al. showed that mouse PTECs preserve tubular-like structures grown on soft (~60 Pa) matrigel, whereas the cells did not differentiate on hardening (~1200 Pa) Matrigel [72]. Also, in various disease models an increase in TBM stiffness is seen with progression of disease [69, 73].

Table 2. Overview of the literature on biophysical properties of TBM, VBM, and renal ECM measured in various species.

		Mechanical properties					
Species, tissue	Young's modulus (YM) Shear modulus (SM)	BM thickness	BM pore size / fiber size	Method	References		
Kidney							
Human, TBM		558 ± 116 nm		Percutaneous biopsy, light and electron microscopy	[64]		
Human TBM		399.7 ± 33.72 nm		Biopsy, light and electron microscopy	[65]		
Human, Kidney	Axial phase image SM: 4.12 ± 0.24 kPa Coronal oblique image SM: 4.32 ± 0.59 kPa Sinus: 6.78 kPa ± 0.10 kPa Medulla: 5.46 ± 0.48 kPa Cortex: 4.35 ± 0.32 kPa			Magnetic resonance elastography (MRE)	[70]		
Ex vivo : Mouse, TBM	Low-strain (10%) YM: 284 ± 90 kPa High-strain (30-40%) YM: 3230 ± 356 kPa			Mouse kidneys fixed and analyzed using transmission electron microscopy (TEM)	[8]		
Ex vivo Rabbit, TBM	YM: Proximal straight tubule BM: 10 ± 1 MPa YM: Proximal convoluted tubule BM: 8 ± 2 MPa	0.26 µm in intact perfused rabbit proximal and collecting tubules		Rabbit kidneys were analyzed using an inverted microscope	[67]		

In vivo: Rabbit, kidney cortex, medulla and sinus	YM: kidney Cortex: 16.34 ± 1.01 kPa Medulla: 13.71 ± 1.16 kPa Sinus: 12.61 ± 0.84 kPa	Shear wave elastography (SWE)	[69]		
In vivo: rat, kidney	SM: renal cortex: 3.87 ± 0.83 kPa	MRE	[73]		
Ex vivo: rat, TBM		Rat kidneys were fixed and analyzed using TEM	[56]		
In vivo: Swine, kidney	SM: Cortex: 6.0 ± 0.7 kPa Medulla: 6.5 ± 0.6 kPa	MRE	[74]		
Human, Descemet's BM	Descemet's BM: 50 ± 17.8 kPa	AFM	[75]		
Rabbit, Corneal endothelium	Endothelium: 4.1 ± 1.7 kPa Descemet's BM: 11.7 ± 7.4 kPa	AFM	[76]		
Ex vivo: Rhesus Macaque, VBM		DA: 506 ± 14 nm LCC: 319 ± 14 nm LSV: 112 ± 8.2 nm IVC: 286 ± 8.2 nm	DA: 59 ± 4.5 nm/ 31 ± 1 nm LCC: 63 ± 6 nm/ 30 ± 2 nm LSV: 38 ± 2 nm/ 27 ± 1 nm IVC: 49 ± 2 nm/ 24 ± 0.6 nm	TEM, scanning electron microscopy (SEM)	[77]
Descending aorta (DA) Left common carotid (LCC) Left saphenous vein (LSV) Inferior vena cava (IVC)					

3. The Role of the BM in Vascularization and its Major Components

The vascular BM (VBM) is located between the endothelial cell lining and the pericytes that make up the outer wall of the blood vessel. Pericytes are contractile, mural cells embedded in the VBM [78, 79]. The VBM separates various tissue compartments, and stabilizes the vascular tubule. Additionally, it provides cues to the endothelial cells through its chemical components. The VBM is a complex meshwork that consists of pores and fibers [77]. While the VBM functions as a substratum for the endothelial cells, it is also a selective barrier and regulates the survival of the cells. Changes in the thickness of the VBM affect the physical features and thereby the cell behavior. Therefore, it is important to know the exact dimensions of the physiological BM, to be able to mimic such a structure for tissue engineering strategies.

Similar to the TBM, the three-dimensional networks of laminin and collagen IV within the VBM are formed independently and connected via HPSCs (perlecan) and nidogens [80]. Nidogens bind both collagen type IV and laminin and thereby bridge the two networks [42]. The various components of the VBM can bind many growth factors and cytokines and thereby function as a storage depot of growth factors for the cells. Growth factors and cytokines such as VEGF-A can be released from the VBM to stimulate differentiation and proliferation of cells [81]. VEGF stimulates both vasculogenesis and angiogenesis, primarily via interactions with receptors located in the endothelial cells (VEGFR1 and -R2).

3.1 Collagen type IV

Collagen IV is the major component of the VBM and crucial for membrane stability, as well as the structural integrity of small vessels [24]. Similar to the TBM the collagen IV isoform present in the VBM is $\alpha 1(\text{IV})/\alpha 2(\text{IV})$. Via its eight cysteine residues, collagen IV can make intra- and intermolecular disulfide bonds, which aids the stabilization of the collagen IV network.

3.2 Laminins

The major isoforms present in the vessel wall are laminin $\alpha 4$ and $\alpha 5$ which bind with laminin $\beta 1$ and $\gamma 1$ to form laminins 411 and 511. In many tissues laminins shift in specificity over time, as laminin-332 is expressed by endothelial cells during early development and angiogenesis. In mature vasculature it shifts from laminin-332 to laminin-511 [6, 82]. Without laminin $\alpha 4$ microvessel maturation is impaired in mice, indicating that laminin $\alpha 4$ plays a central role in the microvessel development [83]. Endothelial cells are anchored via endothelial $\beta 1$ and $\beta 3$ integrins to the laminins in the VBM [80, 84-87].

3.3 Glycoproteins

3.3.1 HSPGs

Perlecan and agrin are the main HSPGs present in the VBM, however certain HSPGs can also be located at the cell surface. Perlecan can bind to growth factors from the FGF family, and is a regulator of neovascularization as binding to FGF leads to enhanced angiogenesis [88, 89]. In zebrafish, it was found that perlecan is involved in developmental angiogenesis by interfering with VEGF-VEGFR2 signaling events [90]. The main roles of HSPGs include adhesion of cells to the BM, and promoting cell proliferation and differentiation [91-93].

3.3.2 Nidogens

Both NID1 and NID2 are present in the VBM and seem to be complementary in function, NID2 is enriched in endothelial BMs [94, 95]. Nidogens conserve the structural integrity of the VBM via connecting BM components laminin and collagen type IV via domain-specific interactions [42]. While nidogens are involved in connecting the laminin and collagen IV networks, nidogens are not crucial for the formation of the BM. Mice mutant for either nidogen-1 or nidogen-2 developed normal endothelial and epithelial BMs and no abnormalities were observed in the vasculature, but they did show neurologic deficits [95-97]. One of the reasons might be that in mice with a deficiency for one of the nidogens, the other nidogen compensates for its loss in function [98]. Nevertheless, deletion of both the nidogen-1 and nidogen-2 gene in mice resulted in perinatal lethality due to incomplete lung development, as well as cardiac defects [99]. Besides their role in connecting laminin and collagen type IV, nidogens can also interact with the integrin receptors on cells to mediate cell adhesion to the BM.

3.4 Other components

In addition to the major components, the VBM contains some minor, vessel specific, components including BM40 (osteonectin), fibulins-1 and -2, collagen VIII, XV, and XVIII, and thrombospondins-1 and -2 [100]. Collagen XV and XVIII are both expressed in capillary BMs, but in the fenestrated endothelium of the glomerulus only type XVIII is found to be present [101]. Whether this also holds true for the TBM is unknown, although it seems that in many specialized vessels only type XVIII is present including in liver sinusoid, splenic sinusoid, and alveolar capillaries. The differential distribution of collagen XV and XVIII might be an initiator of the different functions of the various capillaries.

3.5 Biophysical properties VBM

While several approaches have been made towards engineering of vascular tissue, the biophysical properties of the vasculature are not always incorporated in the design of

the biofabricated vessels. Since the topography and compliance of the vessel can largely influence its nature, a better understanding of the biophysical properties of the VBM might improve the tissue engineered vessels [102, 103].

3.5.1 VBM thickness

Thickness of the VBM ranges from the nano- to submicron scale but varies significantly between vascular tissues, which indicates that membrane thickness can influence biophysical properties such as compliance and topography [77]. The data available on VBM topography is limited to the corneal VBM and rhesus macaque vessels VBM (**Table 2**). The data shown on the VBM indicates of ~100–500 nm in rhesus macaque [77]. However, it is not clear whether the dimensions for the renal tubular VBM are in the same range. Whole organ engineering involves the use of various bioprinting techniques which are, depending on the method used, often limited by their printing resolution. Hence, much higher printing resolutions might be needed to obtain a physiologically-relevant model. Yet, most literature on VBM thickness originates from animal studies, which is not directly translatable to humans as VBM thickness will be related to the size of the animal and the blood pressure it needs to endure.

3.5.2 VBM stiffness

Data available on the stiffness of the VBM is limited to Descemet's BM, which is the membrane underlying the endothelial cells in the cornea (**Table 2**). In two independent studies the Young's modulus of Descemet's BM was measured using atomic force microscopy (AFM), whereby values were found ranging from 11.7 ± 7.4 kPa in rabbits to 50 ± 17.8 kPa in humans [75, 76]. Like the thickness of the membrane, also the stiffness will greatly depend on the size of the animal, as well as the blood pressure it needs to endure. More accurate data is needed to have a clear overview of the elasticity and strength of the BMs, to be able to mimic those properties in any synthetic or biologic BM.

3.6 Connection between VBM and TBM

In the nephron, there is a constant exchange of molecules between the renal epithelial cells and the endothelial cells, as waste products and endogenous and exogenous solutes are filtered from the blood into the tubular lumen and form the ultra-filtrate. One can imagine that it is of vital importance that peritubular capillaries and the renal proximal tubules with their BMs are in close proximity to allow efficient and effective exchange. For the GBM, it has been shown that it firmly connects to the VBM and even can fuse to form one single BM between the capillaries and the podocytes [104, 105]. The exact distance or fusion of/ between the proximal TBM and VBM remains unknown.

4. Current and novel applications of membrane technology in kidney research

The most recent strategies for tissue engineering of (parts of the) kidneys include 3D-bioprinting and molding hydrogels, as well as decellularization of organs for generation of suitable (native) scaffolds. For this, researchers have used BM components to improve the quality of engineered ECM of the scaffolds [48].

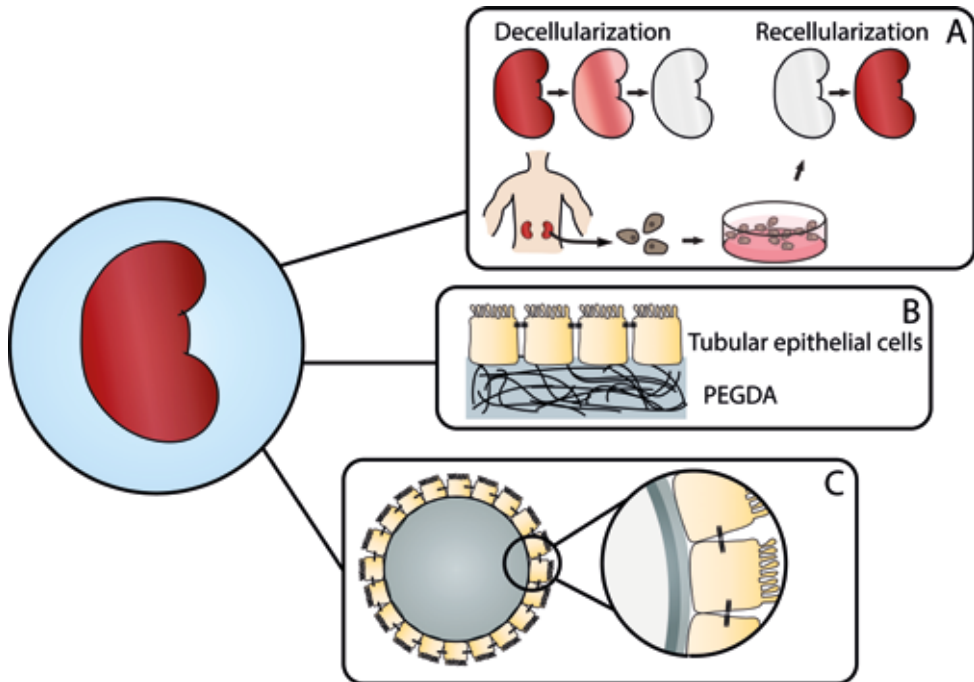


Figure 3. Schematic overview of applications of membrane technology in kidney research. (A) De- and recellularization of native kidney scaffolds (B) Hydrogels for tissue engineering applications (C) Hollow fiber membranes as scaffolds for kidney cells.

4.1 Decellularization and recellularization of kidney scaffolds

Decellularization is a method whereby all cellular components are removed from the organ matrix by perfusing the vasculature of the organ with a range of detergents such as Triton X-100 and SDS, enzymes or cell lysing solutions [106-109]. What is left after decellularization is the ECM of the organ which is still specific in terms of morphology and certain biological cues. These organ scaffolds can be recellularized to create a new organized tissue (**Figure 3A**). Several research groups have successfully shown the decellularization of rat kidneys [106,

110-113]. Ross et al. were the first to report the complete recellularization of a rat kidney scaffold [110]. Bonandrini et al. showed that the expression of the ECM proteins such as collagen IV, laminin and fibronectin in a decellularized rat kidney were similar to that of a native kidney, confirming the ECM remains intact [111]. Caralt et al. compared the different protocols for decellularization and found that the best results are obtained with Triton X-100 and SDS, where the cells are effectively removed, but the ECM scaffold and the ECM growth factors remain preserved [112]. Next to rats, also the kidneys of rhesus monkeys, pigs and humans have been used for decellularization [114-117]. Human kidneys are of course the best source of renal ECM, as differences in ECM composition and architecture of the scaffolds between species have been reported (**Table 2**). To this end, human kidneys discarded from transplantation have been used [118-121].

With decellularization, all native cells are removed as well as immunogenic proteins present in the scaffold. One of the major advantages of this strategy is that the ECM with its 3D structure and composition remains intact, while in other biofabrication techniques it is a challenge to mimic the ECM with all its tissue-specific structural and chemical components [107]. The most challenging part, however, is the recellularization of the scaffold because of the complexity of the kidney which consists of over 20 cell types. Therefore, complete repopulation of the scaffold and its functional restoration have as of yet not been successful. There are many more difficulties in the recellularization process, and often incorporation of certain growth factors or bioactive molecules are needed to enhance the function of the created tissue [122, 123]. But also technical challenges are a reason for the unsuccessful recellularization of kidney scaffolds. De- and recellularized scaffolds that are implanted *in vivo* often lead to cell clotting within the scaffolds, forming a major risk for thrombosis [115]. Whether this is inherent to the use of synthetic ECM components needs to be thoroughly investigated. In addition, it seems that although most of the structure and composition of the scaffolds remain intact after decellularization, depending on the method of decellularization, the compliance, Young's Modulus and stress-strain curves can decrease or increase, as reviewed by Boccafoschi et al [124-127].

Decellularization strategies are not limited to kidney research, a similar approach has been used for vascular tissues whereby intact human greater saphenous vein specimens were decellularized and used for vascular tissue engineering [128-131]. In canines, decellularized veins were used as vascular grafts *in vivo*, which exhibited satisfactory strength and supported cell repopulation after 8 weeks of arterial flow [128]. Zhao et al. created tissue-engineered blood vessels (TEBV) using decellularized ovine carotid arteries [130]. After decellularization

the scaffolds were seeded with autologous cells and interposed into the carotid arteries in an ovine host model. The TEBV were mechanically stable for 5 months *in vivo*, and showed presence of endothelium, smooth muscle, collagen and elastin.

4.2 Hollow fiber membranes

To improve current renal replacement treatment strategies such as hemo- and peritoneal dialysis, the development of a bioartificial kidney device (BAK) has sparked considerable interest during the past decades. Whereas in current RRTs synthetic membranes are used to filter the blood from toxins, in a BAK device these membranes are covered with renal cell monolayers that increase the efficacy of the membranes (**Figure 3C**).

Researchers from our group developed living membranes by culturing conditionally immortalized proximal tubule epithelial cells (ciPTEC) on biofunctionalized MicroPES (polyethersulfone) hollow fiber membranes (HFM) [132]. The ciPTEC were able to form a functional monolayer on the HFM with zonula occludens-1 (ZO-1) protein expression, and organic cation transporter 2 (OCT2) activity. The HFM were coated with combinations of laminin, gelatin, matrigel, collagen IV, and L-3,4-dihydroxydiphenylalanine (L-DOPA) coatings, prior to seeding of ciPTEC [133]. The coating procedures were established first by other groups in search for BAK materials and coatings for bioreactor units [134-136]. Finally, most promising results were obtained with a combination of collagen IV and L-DOPA [132, 135]. More recent, Jansen et al. also showed that living membranes obtained with the double-coating strategy were able to mediate the active transport of protein-bound uremic metabolites [137]. These results are a promising step forward and demonstrate that also other materials mimicking the ECM can serve as a base for kidney cells to grow and function. Also, the researchers have shown that using a BM component such as collagen type IV to coat the matrix can improve cell adhesion and proliferation. The next step is to further upscale this device so that it can eventually be used in the clinic [138].

4.3 Hydrogels as extracellular matrix

The use of hydrogels as biomaterials in tissue engineering has significantly increased over the past decades. Hydrogel matrices consist of (a combination of) biological and synthetic polymers which are stably connected via physical (non-covalent) or chemical (covalent) crosslinks [139]. Because of their biocompatibility and easy modifications in biochemical and mechanical properties, these three-dimensional polymer networks are often used as artificial ECM or scaffolds for cells (**Figure 3B**). As their name implies, hydrogels can retain water, called the swollen state of a hydrogel. Certain hydrogels can be used in combination

with 3D-printing techniques to create free standing tubes, or other shapes. Often techniques such as molding are used as well, to create channels within a hydrogel. The mechanical properties of hydrogels can easily be tuned by changing e.g. the crosslinking density or the polymer concentration. One benefit of hydrogels is that they can easily be combined with microfluidics, whereby the hydrogel functions as the ECM within the microfluidic chip and flow can easily be controlled [140]. In physiology, the VBM has to endure a lot of shear stress because of the circulating blood volume, for which stiff synthetic hydrogels can be used to support the physiological shear stress levels. However, when a gel is too stiff, cell growth as well as migration of growth factors and nutrients can be limited.

A poly(ethylene glycol) (PEG) based hydrogel has been used to study the effect of the mechanical properties of the substrate on the proliferation of renal cells [71]. Increased hydrogel stiffness promoted monolayer formation of renal epithelial cells when cultured for up to 2 weeks, suggesting that ECM stiffness can regulate monolayer formation.

Kolesky et al. created thick (> 1cm) vascularized tissues whereby parenchyma, stroma and endothelium were integrated into a single thick tissue. Using several cell types in a customized hydrogel ECM, the vascularized tissues were viable for over 6 weeks. Their matrix is based on a combination of gelatin, fibrinogen, transglutaminase, calcium chloride and thrombin, which allows for cell adherence and monolayer formation [141].

The same group has developed bioprinting approaches for renal proximal tubules using a similar gelatin-based matrix [142]. For this, they used a sacrificial bioprinting method using Pluronic-127 to create a perfusable channel in the gel-matrix, subsequently seeded with proximal tubule epithelial cells. Within this set-up, the cells formed a tight monolayer with a functional barrier which was assessed using FITC-labeled inulin perfusion, the cells were cultured for over 2 months. Furthermore, in this set-up the tubule cells exhibited superior albumin uptake function compared to a 2D control.

Remarkably, the components that are used in the hydrogels mentioned here (e.g. PEG, gelatin, fibrinogen and thrombin) are not the main components of the native BM. While hydrogel components partly mimic physical characteristics of the BM by exerting similar structures or mechanical properties, they lack chemical components that can trigger cell proliferation and differentiation. Hence, there is a potential for improving hydrogel composition for mimicking the BM. The group of Su et al. have used hydrogels derived from tissue- and organ- specific decellularized ECM for culturing of glomerular endothelial cells

[143]. While the glomerular endothelial cells showed high viability and proliferation, their gene expression for relevant genes was decreased compared to cells encapsulated within hydrogels that were composed of collagen I. Further research is needed to investigate the benefit of ECM-derived hydrogels, or maybe a combination of ECM-derived hydrogels and hydrogels such as PEG for tissue engineering.

4.4 Biofunctionalized polymers

Mollet et al. established BM mimics made from ureidopyrimidinone (UPy)-functionalized polymer and bioactive peptides by electrospinning [21]. Cells were seeded on the BM mimics in a bioreactor. They were able to show that human kidney-2 (HK-2) epithelial cells were able to form a polarized monolayer on the BM mimics, and show modulation of gene expression and important membrane transporter proteins. Biofunctionalized polymers are used to mimic the BM via (melt) electrospinning, whereby thin fibers are spun to create a meshwork which finally functions as the scaffold [144]. While the polymers itself might lack some of the biochemical properties of the BM, they can largely mimic the biophysical properties by optimizing the size of the fibers to create a meshwork like the ones formed by collagen IV and laminin. Scaffolds designed using melt electrospinning writing have shown to support cell attachment, proliferation, ECM formation and infiltration. By coating biofunctionalized polymers with collagen IV or laminin, the polymers could mimic the BM to an even higher extent.

5. Conclusions

The BM plays an important role in organogenesis, as it stimulates cell growth, cell attachment and proliferation, it enhances angiogenesis, and serves as a growth factor depot for the cells attached to the BM. Although the major components of the BM have been discovered, knowledge on the exact physical properties remain unclear. This opens up opportunities for researchers to further investigate the properties of the BM, and to be able to mimic their role in bioengineered kidneys or related structures.

Many approaches have been made to mimic the BM using various strategies, such as scaffolds obtained from native kidney decellularization, hydrogels, hollow fiber membranes, or biofunctionalized polymers. The major advantage of decellularization is that the ECM, including the BM, remains intact. Creating BM from scratch requires critical steps to take, as it is a very complex matrix. Nevertheless, it is still very difficult to recellularize complex structures such as the kidney, which consist of many different segments and cell types.

Other, more simple approaches have been shown to be quite effective and promising, as it appeared possible to mimic the meshwork of the BM using hollow fiber membranes and biofunctionalized polymers, whereby a porous membrane serves as the BM. Additional coatings such as collagen IV can improve cell attachment and proliferation. Using more elaborate compositions of coatings might improve cell behavior as well, as a collagen IV coating only partly resembles the major components of the BM. Three-dimensional bioprinting of kidney tubules still seems to be a challenging task, many researchers therefore use molding techniques to create channels within a hydrogel matrix instead.

While we still have a long way to go before we can create a fully functional kidney, the first steps have already been taken by many researchers in the field. When combining hydrogels that can be fine-tuned and enriched with some of the major components of the BM such as collagen IV, laminin, and fibronectin, with biofunctionalized polymers physically mimicking the collagen IV/laminin meshwork, we may be able to create a BM that allows for better cell proliferation and differentiation. A better understanding of the exact composition of the BM and its role in tissue performance, will advance the process of engineering functional vascularized kidney tubules, as it will guide us to fabricate scaffolds that are suitable for the growth of functional renal proximal tubule- and endothelial cells.

Acknowledgements

A.M.v.G. was supported by the Nierstichting Ph.D. grant 17PhD16. J.J., C.C., T.V., and R.M. were supported by the partners of Regenerative Medicine Crossing Borders (RegMedXB), powered by Health Holland, Top Sector Life Sciences & Health.

References

- 1 Hill, N. R. *et al.* Global Prevalence of Chronic Kidney Disease - A Systematic Review and Meta-Analysis. *PLoS One* **11**, e0158765 (2016).
- 2 Carmona, M. *et al.* Global Organ Transplant Activities in 2015. Data from the Global Observatory on Donation and Transplantation (GODT). *Transplantation* **101**, S29-S29 (2017).
- 3 Harmankaya, O. *et al.* Comparison of risk factors for cardiovascular disease in hemodialysis and peritoneal dialysis patients. *Clinics (Sao Paulo)* **70**, 601-605 (2015).
- 4 Helal, I. *et al.* Cardiovascular risk factors in hemodialysis and peritoneal dialysis patients. *Saudi J Kidney Dis Transpl* **21**, 59-62 (2010).
- 5 Zhuo, J. L. & Li, X. C. Proximal nephron. *Compr Physiol* **3**, 1079-1123 (2013).
- 6 Yurchenco, P. D. Basement membranes: cell scaffoldings and signaling platforms. *Cold Spring Harb Perspect Biol* **3** (2011).
- 7 Borza, C. M., Chen, X., Zent, R. & Pozzi, A. Cell Receptor-Basement Membrane Interactions in Health and Disease: A Kidney-Centric View. *Curr Top Membr* **76**, 231-253 (2015).
- 8 Bhave, G., Colon, S. & Ferrell, N. The sulfilimine cross-link of collagen IV contributes to kidney tubular basement membrane stiffness. *Am J Physiol Renal Physiol* **313**, F596-F602 (2017).
- 9 Miller, R. T. Mechanical properties of basement membrane in health and disease. *Matrix Biol* **57-58**, 366-373 (2017).
- 10 Wang, H. *et al.* Tubular basement membrane immune complex deposition is associated with activity and progression of lupus nephritis: a large multicenter Chinese study. *Lupus*, 961203317732407 (2017).
- 11 Lusco, M. A., Fogo, A. B., Najafian, B. & Alpers, C. E. AJKD Atlas of Renal Pathology: Anti-Tubular Basement Membrane Antibody Disease. *Am J Kidney Dis* **70**, e3-e4 (2017).
- 12 Jones, F. E. *et al.* ER stress and basement membrane defects combine to cause glomerular and tubular renal disease resulting from Col4a1 mutations in mice. *Dis Model Mech* **9**, 165-176 (2016).
- 13 Abrahamson, D. R. & Leardkamolkarn, V. Development of kidney tubular basement membranes. *Kidney Int* **39**, 382-393 (1991).
- 14 Halfter, W. *et al.* The bi-functional organization of human basement membranes. *PLoS One* **8**, e67660 (2013).
- 15 Halfter, W. *et al.* New concepts in basement membrane biology. *FEBS J* **282**, 4466-4479 (2015).
- 16 Miner, J. H. Renal basement membrane components. *Kidney Int* **56**, 2016-2024 (1999).
- 17 Laurie, G. W., Leblond, C. P., Inoue, S., Martin, G. R. & Chung, A. Fine structure of the glomerular basement membrane and immunolocalization of five basement membrane components to the lamina densa (basal lamina) and its extensions in both glomeruli and tubules of the rat kidney. *Am J Anat* **169**, 463-481 (1984).
- 18 Glentis, A., Gurchenkov, V. & Matic Vignjevic, D. Assembly, heterogeneity, and breaching of the basement membranes. *Cell Adh Migr* **8**, 236-245 (2014).
- 19 Nakayama, K. H., Lee, C. C., Batchelder, C. A. & Tarantal, A. F. Tissue specificity of decellularized rhesus monkey kidney and lung scaffolds. *PLoS One* **8**, e64134 (2013).
- 20 Gozalpour, E. & Fenner, K. S. Current State Of In Vitro Cell-Based Renal Models. *Curr Drug Metab* (2018).
- 21 Mollet, B. B., Bogaerts, I. L. J., van Almen, G. C. & Dankers, P. Y. W. A bioartificial environment for kidney epithelial cells based on a supramolecular polymer basement membrane mimic and an organotypical culture system. *J Tissue Eng Regen Med* **11**, 1820-1834 (2017).
- 22 Ekblom, P. Formation of basement membranes in the embryonic kidney: an immunohistological study. *J Cell Biol* **91**, 1-10 (1981).
- 23 Martin, G. R., Timpl, R. & Kuhn, K. Basement membrane proteins: molecular structure and function. *Adv Protein Chem* **39**, 1-50 (1988).

- 24 Poschl, E. *et al.* Collagen IV is essential for basement membrane stability but dispensable for initiation of its assembly during early development. *Development* **131**, 1619-1628 (2004).
- 25 Vanacore, R. *et al.* A sulfilimine bond identified in collagen IV. *Science* **325**, 1230-1234 (2009).
- 26 Hohenester, E. & Yurchenco, P. D. Laminins in basement membrane assembly. *Cell Adh Migr* **7**, 56-63 (2013).
- 27 Sorokin, L. M., Pausch, F., Durbeek, M. & Ekblom, P. Differential expression of five laminin alpha (1-5) chains in developing and adult mouse kidney. *Dev Dyn* **210**, 446-462 (1997).
- 28 Madri, J. A., Roll, F. J., Furthmayr, H. & Foidart, J. M. Ultrastructural localization of fibronectin and laminin in the basement membranes of the murine kidney. *J Cell Biol* **86**, 682-687 (1980).
- 29 Abrass, C. K., Hansen, K. M. & Patton, B. L. Laminin alpha4-null mutant mice develop chronic kidney disease with persistent overexpression of platelet-derived growth factor. *Am J Pathol* **176**, 839-849 (2010).
- 30 Ning, L. *et al.* Laminin alpha1 regulates age-related mesangial cell proliferation and mesangial matrix accumulation through the TGF-beta pathway. *Am J Pathol* **184**, 1683-1694 (2014).
- 31 Sarrazin, S., Lamanna, W. C. & Esko, J. D. Heparan sulfate proteoglycans. *Cold Spring Harb Perspect Biol* **3** (2011).
- 32 Hynes, R. O. The extracellular matrix: not just pretty fibrils. *Science* **326**, 1216-1219 (2009).
- 33 Groggel, G. C., Stevenson, J., Hovingh, P., Linker, A. & Border, W. A. Changes in heparan sulfate correlate with increased glomerular permeability. *Kidney Int* **33**, 517-523 (1988).
- 34 van den Heuvel, L. P. *et al.* Heparan sulfate proteoglycan from human tubular basement membrane. Comparison with this component from the glomerular basement membrane. *Biochim Biophys Acta* **1025**, 67-76 (1990).
- 35 Raats, C. J. *et al.* Differential expression of agrin in renal basement membranes as revealed by domain-specific antibodies. *J Biol Chem* **273**, 17832-17838 (1998).
- 36 Bezakova, G. & Ruegg, M. A. New insights into the roles of agrin. *Nat Rev Mol Cell Biol* **4**, 295-308 (2003).
- 37 Groffen, A. J. *et al.* Agrin is a major heparan sulfate proteoglycan in the human glomerular basement membrane. *J Histochem Cytochem* **46**, 19-27 (1998).
- 38 Noonan, D. M. *et al.* The complete sequence of perlecan, a basement membrane heparan sulfate proteoglycan, reveals extensive similarity with laminin A chain, low density lipoprotein-receptor, and the neural cell adhesion molecule. *J Biol Chem* **266**, 22939-22947 (1991).
- 39 Kallunki, P. & Tryggvason, K. Human basement membrane heparan sulfate proteoglycan core protein: a 467-kD protein containing multiple domains resembling elements of the low density lipoprotein receptor, laminin, neural cell adhesion molecules, and epidermal growth factor. *J Cell Biol* **116**, 559-571 (1992).
- 40 Murdoch, A. D., Dodge, G. R., Cohen, I., Tuan, R. S. & Iozzo, R. V. Primary structure of the human heparan sulfate proteoglycan from basement membrane (HSPG2/perlecan). A chimeric molecule with multiple domains homologous to the low density lipoprotein receptor, laminin, neural cell adhesion molecules, and epidermal growth factor. *J Biol Chem* **267**, 8544-8557 (1992).
- 41 Goldberg, S., Harvey, S. J., Cunningham, J., Tryggvason, K. & Miner, J. H. Glomerular filtration is normal in the absence of both agrin and perlecan-heparan sulfate from the glomerular basement membrane. *Nephrol Dial Transplant* **24**, 2044-2051 (2009).
- 42 Fox, J. W. *et al.* Recombinant nidogen consists of three globular domains and mediates binding of laminin to collagen type IV. *EMBO J* **10**, 3137-3146 (1991).
- 43 Mayer, U. *et al.* A single EGF-like motif of laminin is responsible for high affinity nidogen binding. *EMBO J* **12**, 1879-1885 (1993).
- 44 Aumailley, M., Wiedemann, H., Mann, K. & Timpl, R. Binding of nidogen and the laminin-nidogen complex to basement membrane collagen type IV. *Eur J Biochem* **184**, 241-248 (1989).
- 45 Gersdorff, N., Otto, S., Roediger, M., Kruegel, J. & Miosge, N. The absence of one or both nidogens does not alter basement membrane composition in adult murine kidney. *Histol Histopathol* **22**, 1077-1084 (2007).

- 46 Rosines, E., Schmidt, H. J. & Nigam, S. K. The effect of hyaluronic acid size and concentration on branching morphogenesis and tubule differentiation in developing kidney culture systems: potential applications to engineering of renal tissues. *Biomaterials* **28**, 4806-4817 (2007).
- 47 Ito, T., Williams, J. D., Al-Assaf, S., Phillips, G. O. & Phillips, A. O. Hyaluronan and proximal tubular cell migration. *Kidney Int* **65**, 823-833 (2004).
- 48 Allison, D. D. & Grande-Allen, K. J. Review. Hyaluronan: a powerful tissue engineering tool. *Tissue Eng* **12**, 2131-2140 (2006).
- 49 Martinez-Hernandez, A., Marsh, C. A., Clark, C. C., Macarak, E. J. & Brownell, A. G. Fibronectin: its relationship to basement membranes. II. Ultrastructural studies in rat kidney. *Coll Relat Res* **1**, 405-418 (1981).
- 50 Leclerc, E. *et al.* Selective control of liver and kidney cells migration during organotypic cocultures inside fibronectin-coated rectangular silicone microchannels. *Biomaterials* **28**, 1820-1829 (2007).
- 51 Linder, E., Miettinen, A. & Tornroth, T. Fibronectin as a marker for the glomerular mesangium in immunohistology of kidney biopsies. *Lab Invest* **42**, 70-75 (1980).
- 52 Linder, E., Stenman, S., Lehto, V. P. & Vaheri, A. Distribution of fibronectin in human tissues and relationship to other connective tissue components. *Ann N Y Acad Sci* **312**, 151-159 (1978).
- 53 Roll, F. J., Madri, J. A., Albert, J. & Furthmayr, H. Codistribution of collagen types IV and AB₂ in basement membranes and mesangium of the kidney. an immunoferritin study of ultrathin frozen sections. *J Cell Biol* **85**, 597-616 (1980).
- 54 Oberley, T. D., Mosher, D. F. & Mills, M. D. Localization of fibronectin within the renal glomerulus and its production by cultured glomerular cells. *Am J Pathol* **96**, 651-662 (1979).
- 55 Pettersson, E. E. & Colvin, R. B. Cold-insoluble globulin (fibronectin, LETS protein) in normal and diseased human glomeruli: papain-sensitive attachment to normal glomeruli and deposition in crescents. *Clin Immunol Immunopathol* **11**, 425-436 (1978).
- 56 Ogawa, S. *et al.* High-resolution ultrastructural comparison of renal glomerular and tubular basement membranes. *Am J Nephrol* **19**, 686-693 (1999).
- 57 Pearlstein, E. Plasma membrane glycoprotein which mediates adhesion of fibroblasts to collagen. *Nature* **262**, 497-500 (1976).
- 58 Klebe, R. J. Isolation of a collagen-dependent cell attachment factor. *Nature* **250**, 248-251 (1974).
- 59 Oberley, T. D. & Murphy-Ullrich, J. in *Fibronectin* (ed D. F. Mosher) 309 - 326 (Academic Press, Inc., 1989).
- 60 Candiello, J., Cole, G. J. & Halfter, W. Age-dependent changes in the structure, composition and biophysical properties of a human basement membrane. *Matrix Biol* **29**, 402-410 (2010).
- 61 Leblond, C. P. & Inoue, S. Structure, composition, and assembly of basement membrane. *Am J Anat* **185**, 367-390 (1989).
- 62 Inoue, S., Leblond, C. P. & Laurie, G. W. Ultrastructure of Reichert's membrane, a multilayered basement membrane in the parietal wall of the rat yolk sac. *J Cell Biol* **97**, 1524-1537 (1983).
- 63 Ruoslahti, E. Structure and biology of proteoglycans. *Annu Rev Cell Biol* **4**, 229-255 (1988).
- 64 Brito, P. L. *et al.* Proximal tubular basement membrane width in insulin-dependent diabetes mellitus. *Kidney Int* **53**, 754-761 (1998).
- 65 Tyagi, I., Agrawal, U., Amitabh, V., Jain, A. K. & Saxena, S. Thickness of glomerular and tubular basement membranes in preclinical and clinical stages of diabetic nephropathy. *Indian J Nephrol* **18**, 64-69 (2008).
- 66 Levental, I., Georges, P. C. & Janmey, P. A. Soft biological materials and their impact on cell function. *Soft Matter* **3**, 299-306 (2007).
- 67 Welling, L. W. & Grantham, J. J. Physical properties of isolated perfused renal tubules and tubular basement membranes. *J Clin Invest* **51**, 1063-1075 (1972).

- 68 Candiello, J. *et al.* Biomechanical properties of native basement membranes. *FEBS J* **274**, 2897-2908 (2007).
- 69 Liu, X. *et al.* Effect of renal perfusion and structural heterogeneity on shear wave elastography of the kidney: an in vivo and ex vivo study. *BMC Nephrol* **18**, 265 (2017).
- 70 Bensamoun, S. F., Robert, L., Leclerc, G. E., Debernard, L. & Charleux, F. Stiffness imaging of the kidney and adjacent abdominal tissues measured simultaneously using magnetic resonance elastography. *Clin Imaging* **35**, 284-287 (2011).
- 71 Beamish, J. A., Chen, E. & Putnam, A. J. Engineered extracellular matrices with controlled mechanics modulate renal proximal tubular cell epithelialization. *PLoS One* **12**, e0181085 (2017).
- 72 Chen, W. C., Lin, H. H. & Tang, M. J. Regulation of proximal tubular cell differentiation and proliferation in primary culture by matrix stiffness and ECM components. *Am J Physiol Renal Physiol* **307**, F695-707 (2014).
- 73 Shah, N. S. *et al.* Evaluation of renal parenchymal disease in a rat model with magnetic resonance elastography. *Magn Reson Med* **52**, 56-64 (2004).
- 74 Warner, L., Yin, M., Ehman, R. L. & Lerman, L. O. in *International Society for Magnetic Resonance in Medicine*.
- 75 Last, J. A., Liliensiek, S. J., Nealey, P. F. & Murphy, C. J. Determining the mechanical properties of human corneal basement membranes with atomic force microscopy. *J Struct Biol* **167**, 19-24 (2009).
- 76 Thomasy, S. M. *et al.* Elastic modulus and collagen organization of the rabbit cornea: epithelium to endothelium. *Acta Biomater* **10**, 785-791 (2014).
- 77 Liliensiek, S. J., Nealey, P. F. & Murphy, C. J. Characterization of endothelial basement membrane nanotopography in rhesus macaque as a guide for vessel tissue engineering. *Tissue Eng Part A* **15**, 2643-2651 (2009).
- 78 Attwell, D., Mishra, A., Hall, C. N., O'Farrell, F. M. & Dalkara, T. What is a pericyte? *Cereb Blood Flow Metab* **36**, 451-455 (2016).
- 79 van Dijk, C. G. *et al.* The complex mural cell: pericyte function in health and disease. *Int J Cardiol* **190**, 75-89 (2015).
- 80 Hallmann, R. *et al.* Expression and function of laminins in the embryonic and mature vasculature. *Physiol Rev* **85**, 979-1000 (2005).
- 81 Taipale, J. & Keski-Oja, J. Growth factors in the extracellular matrix. *FASEB J* **11**, 51-59 (1997).
- 82 Yousif, L. F., Di Russo, J. & Sorokin, L. Laminin isoforms in endothelial and perivascular basement membranes. *Cell Adh Migr* **7**, 101-110 (2013).
- 83 Thyboll, J. *et al.* Deletion of the laminin alpha4 chain leads to impaired microvessel maturation. *Mol Cell Biol* **22**, 1194-1202 (2002).
- 84 Koster, J., Borradori, L. & Sonnenberg, A. Hemidesmosomes: molecular organization and their importance for cell adhesion and disease. *Handb Exp Pharmacol*, 243-280 (2004).
- 85 Fujiwara, H., Gu, J. & Sekiguchi, K. Rac regulates integrin-mediated endothelial cell adhesion and migration on laminin-8. *Exp Cell Res* **292**, 67-77 (2004).
- 86 Fujiwara, H., Kikkawa, Y., Sanzen, N. & Sekiguchi, K. Purification and characterization of human laminin-8. Laminin-8 stimulates cell adhesion and migration through alpha3beta1 and alpha6beta1 integrins. *J Biol Chem* **276**, 17550-17558 (2001).
- 87 Doi, M. *et al.* Recombinant human laminin-10 (alpha5beta1gamma1). Production, purification, and migration-promoting activity on vascular endothelial cells. *J Biol Chem* **277**, 12741-12748 (2002).
- 88 Gubbiotti, M. A., Neill, T. & Iozzo, R. V. A current view of perlecan in physiology and pathology: A mosaic of functions. *Matrix Biol* **57-58**, 285-298 (2017).
- 89 Aviezer, D. *et al.* Perlecan, basal lamina proteoglycan, promotes basic fibroblast growth factor-receptor binding, mitogenesis, and angiogenesis. *Cell* **79**, 1005-1013 (1994).
- 90 Zoeller, J. J., Whitelock, J. M. & Iozzo, R. V. Perlecan regulates developmental angiogenesis by modulating the VEGF-VEGFR2 axis. *Matrix Biology* **28**, 284-291 (2009).

- 91 Rops, A. L. *et al.* Heparan sulfate proteoglycans in glomerular inflammation. *Kidney Int* **65**, 768-785 (2004).
- 92 Iozzo, R. V. Matrix proteoglycans: from molecular design to cellular function. *Annu Rev Biochem* **67**, 609-652 (1998).
- 93 Bernfield, M. *et al.* Functions of cell surface heparan sulfate proteoglycans. *Annu Rev Biochem* **68**, 729-777 (1999).
- 94 Salmivirta, K. *et al.* Binding of mouse nidogen-2 to basement membrane components and cells and its expression in embryonic and adult tissues suggest complementary functions of the two nidogens. *Exp Cell Res* **279**, 188-201 (2002).
- 95 Schymeinsky, J. *et al.* Gene structure and functional analysis of the mouse nidogen-2 gene: nidogen-2 is not essential for basement membrane formation in mice. *Mol Cell Biol* **22**, 6820-6830 (2002).
- 96 Murshed, M. *et al.* The absence of nidogen 1 does not affect murine basement membrane formation. *Mol Cell Biol* **20**, 7007-7012 (2000).
- 97 Dong, L. *et al.* Neurologic defects and selective disruption of basement membranes in mice lacking entactin-1/nidogen-1. *Lab Invest* **82**, 1617-1630 (2002).
- 98 Miosge, N., Sasaki, T. & Timpl, R. Evidence of nidogen-2 compensation for nidogen-1 deficiency in transgenic mice. *Matrix Biol* **21**, 611-621 (2002).
- 99 Bader, B. L. *et al.* Compound genetic ablation of nidogen 1 and 2 causes basement membrane defects and perinatal lethality in mice. *Mol Cell Biol* **25**, 6846-6856 (2005).
- 100 Timpl, R. Structure and biological activity of basement membrane proteins. *Eur J Biochem* **180**, 487-502 (1989).
- 101 Tomono, Y. *et al.* Epitope-defined monoclonal antibodies against multiplexin collagens demonstrate that type XV and XVIII collagens are expressed in specialized basement membranes. *Cell Struct Funct* **27**, 9-20 (2002).
- 102 L'Heureux, N. *et al.* Human tissue-engineered blood vessels for adult arterial revascularization. *Nat Med* **12**, 361-365 (2006).
- 103 Kasaj, A. *et al.* In vitro evaluation of various bioabsorbable and nonresorbable barrier membranes for guided tissue regeneration. *Head Face Med* **4**, 22 (2008).
- 104 Clay, M. R. & Sherwood, D. R. Basement Membranes in the Worm: A Dynamic Scaffolding that Instructs Cellular Behaviors and Shapes Tissues. *Curr Top Membr* **76**, 337-371 (2015).
- 105 Abrahamson, D. R. Origin of the glomerular basement membrane visualized after in vivo labeling of laminin in newborn rat kidneys. *J Cell Biol* **100**, 1988-2000 (1985).
- 106 Peloso, A. *et al.* In-Lab Manufacturing of Decellularized Rat Renal Scaffold for Kidney Bioengineering. *Methods Mol Biol* (2017).
- 107 Figliuzzi, M., Bonandrini, B. & Remuzzi, A. Decellularized kidney matrix as functional material for whole organ tissue engineering. *J Appl Biomater Funct Mater* **15**, 0 (2017).
- 108 Wang, Y. *et al.* Method for perfusion decellularization of porcine whole liver and kidney for use as a scaffold for clinical-scale bioengineering engrafts. *Xenotransplantation* **22**, 48-61 (2015).
- 109 Fedecostante, M., Onciu, O. G., Westphal, K. G. C. & Masereeuw, R. Towards a bioengineered kidney: recellularization strategies for decellularized native kidney scaffolds. *Int J Artif Organs* **40**, 150-158 (2017).
- 110 Ross, E. A. *et al.* Embryonic stem cells proliferate and differentiate when seeded into kidney scaffolds. *J Am Soc Nephrol* **20**, 2338-2347 (2009).
- 111 Bonandrini, B. *et al.* Recellularization of well-preserved acellular kidney scaffold using embryonic stem cells. *Tissue Eng Part A* **20**, 1486-1498 (2014).
- 112 Caralt, M. *et al.* Optimization and critical evaluation of decellularization strategies to develop renal extracellular matrix scaffolds as biological templates for organ engineering and transplantation. *Am J Transplant* **15**, 64-75 (2015).

- 113 He, M., Callanan, A., Lagaras, K., Steele, J. A. M. & Stevens, M. M. Optimization of SDS exposure on preservation of ECM characteristics in whole organ decellularization of rat kidneys. *J Biomed Mater Res B Appl Biomater* **105**, 1352-1360 (2017).
- 114 Nakayama, K. H., Batchelder, C. A., Lee, C. I. & Tarantal, A. F. Decellularized rhesus monkey kidney as a three-dimensional scaffold for renal tissue engineering. *Tissue Eng Part A* **16**, 2207-2216 (2010).
- 115 Orlando, G. *et al.* Production and implantation of renal extracellular matrix scaffolds from porcine kidneys as a platform for renal bioengineering investigations. *Ann Surg* **256**, 363-370 (2012).
- 116 Sullivan, D. C. *et al.* Decellularization methods of porcine kidneys for whole organ engineering using a high-throughput system. *Biomaterials* **33**, 7756-7764 (2012).
- 117 Poornejad, N. *et al.* Efficient decellularization of whole porcine kidneys improves reseeded cell behavior. *Biomed Mater* **11**, 025003 (2016).
- 118 Katari, R. *et al.* Renal bioengineering with scaffolds generated from human kidneys. *Nephron Exp Nephrol* **126**, 119 (2014).
- 119 Gifford, S., Zambon, J. P. & Orlando, G. Recycling organs - growing tailor-made replacement kidneys. *Regen Med* **10**, 913-915 (2015).
- 120 Orlando, G. *et al.* Discarded human kidneys as a source of ECM scaffold for kidney regeneration technologies. *Biomaterials* **34**, 5915-5925 (2013).
- 121 Peloso, A. *et al.* Renal Extracellular Matrix Scaffolds From Discarded Kidneys Maintain Glomerular Morphometry and Vascular Resilience and Retains Critical Growth Factors. *Transplantation* **99**, 1807-1816 (2015).
- 122 Zhou, J. *et al.* Tissue engineering of heart valves: PEGylation of decellularized porcine aortic valve as a scaffold for in vitro recellularization. *Biomed Eng Online* **12**, 87 (2013).
- 123 Rana, D., Zreiqat, H., Benkirane-Jessel, N., Ramakrishna, S. & Ramalingam, M. Development of decellularized scaffolds for stem cell-driven tissue engineering. *J Tissue Eng Regen Med* **11**, 942-965 (2017).
- 124 Mancuso, L., Gualerzi, A., Boschetti, F., Loy, F. & Cao, G. Decellularized ovine arteries as small-diameter vascular grafts. *Biomed Mater* **9**, 045011 (2014).
- 125 Lu, W. D., Zhang, M., Wu, Z. S. & Hu, T. H. Decellularized and photooxidatively crosslinked bovine jugular veins as potential tissue engineering scaffolds. *Interact Cardiovasc Thorac Surg* **8**, 301-305 (2009).
- 126 Sheridan, W. S., Duffy, G. P. & Murphy, B. P. Mechanical characterization of a customized decellularized scaffold for vascular tissue engineering. *J Mech Behav Biomed Mater* **8**, 58-70 (2012).
- 127 Boccafoschi, F. *et al.* Decellularized biological matrices: an interesting approach for cardiovascular tissue repair and regeneration. *J Tissue Eng Regen Med* **11**, 1648-1657 (2017).
- 128 Martin, N. D. *et al.* In vivo behavior of decellularized vein allograft. *J Surg Res* **129**, 17-23 (2005).
- 129 Schaner, P. J. *et al.* Decellularized vein as a potential scaffold for vascular tissue engineering. *J Vasc Surg* **40**, 146-153 (2004).
- 130 Zhao, Y. *et al.* The development of a tissue-engineered artery using decellularized scaffold and autologous ovine mesenchymal stem cells. *Biomaterials* **31**, 296-307 (2010).
- 131 Wang, X., Lin, P., Yao, Q. & Chen, C. Development of small-diameter vascular grafts. *World J Surg* **31**, 682-689 (2007).
- 132 Jansen, J. *et al.* Human proximal tubule epithelial cells cultured on hollow fibers: living membranes that actively transport organic cations. *Sci Rep* **5**, 16702 (2015).
- 133 Schophuizen, C. M. *et al.* Development of a living membrane comprising a functional human renal proximal tubule cell monolayer on polyethersulfone polymeric membrane. *Acta Biomater* **14**, 22-32 (2015).
- 134 Ni, M. *et al.* Characterization of membrane materials and membrane coatings for bioreactor units of bioartificial kidneys. *Biomaterials* **32**, 1465-1476 (2011).

- 135 Oo, Z. Y. *et al.* The performance of primary human renal cells in hollow fiber bioreactors for bioartificial kidneys. *Biomaterials* **32**, 8806-8815 (2011).
- 136 Zhang, H., Tasnim, F., Ying, J. Y. & Zink, D. The impact of extracellular matrix coatings on the performance of human renal cells applied in bioartificial kidneys. *Biomaterials* **30**, 2899-2911 (2009).
- 137 Jansen, J. *et al.* Bioengineered kidney tubules efficiently excrete uremic toxins. *Sci Rep* **6**, 26715 (2016).
- 138 Chevtchik, N. V. *et al.* Upscaling of a living membrane for bioartificial kidney device. *Eur J Pharmacol* **790**, 28-35 (2016).
- 139 Buwalda, S. J. *et al.* Hydrogels in a historical perspective: from simple networks to smart materials. *J Control Release* **190**, 254-273 (2014).
- 140 Huang, C. Y. *et al.* Microfluidic hydrogels for tissue engineering. *Biofabrication* **3**, 012001 (2011).
- 141 Kolesky, D. B., Homan, K. A., Skylar-Scott, M. A. & Lewis, J. A. Three-dimensional bioprinting of thick vascularized tissues. *Proc Natl Acad Sci U S A* **113**, 3179-3184 (2016).
- 142 Homan, K. A. *et al.* Bioprinting of 3D Convoluted Renal Proximal Tubules on Perfusable Chips. *Sci Rep* **6**, 34845 (2016).
- 143 Su, J., Satchell, S. C., Shah, R. N. & Wertheim, J. A. Kidney Decellularized Extracellular Matrix Hydrogels: Rheological Characterization and Human Glomerular Endothelial Cell Response to Encapsulation. *J Biomed Mater Res A* (2018).
- 144 Muerza-Cascante, M. L., Haylock, D., Hutmacher, D. W. & Dalton, P. D. Melt electrospinning and its technologization in tissue engineering. *Tissue Eng Part B Rev* **21**, 187-202 (2015).
- 145 Sado, Y. *et al.* Organization and expression of basement membrane collagen IV genes and their roles in human disorders. *J Biochem* **123**, 767-776 (1998).
- 146 Beck, K., Hunter, I. & Engel, J. Structure and function of laminin: anatomy of a multidomain glycoprotein. *FASEB J* **4**, 148-160 (1990).
- 147 Engvall, E., Earwicker, D., Haaparanta, T., Ruoslahti, E. & Sanes, J. R. Distribution and isolation of four laminin variants; tissue restricted distribution of heterotrimers assembled from five different subunits. *Cell Regul* **1**, 731-740 (1990).
- 148 Miner, J. H. *et al.* The laminin alpha chains: expression, developmental transitions, and chromosomal locations of alpha1-5, identification of heterotrimeric laminins 8-11, and cloning of a novel alpha3 isoform. *J Cell Biol* **137**, 685-701 (1997).
- 149 Sorokin, L. M. *et al.* Developmental regulation of the laminin alpha5 chain suggests a role in epithelial and endothelial cell maturation. *Dev Biol* **189**, 285-300 (1997).
- 150 Miner, J. H. Laminins and their roles in mammals. *Microsc Res Tech* **71**, 349-356 (2008).
- 151 Bix, G. & Iozzo, R. V. Novel interactions of perlecan: unraveling perlecan's role in angiogenesis. *Microsc Res Tech* **71**, 339-348 (2008).

A.M. van Genderen^{1,2,^}, M.G. Valverde^{1,2,^}, P.E. Capendale^{1,2}, M.V. Kersten¹, E. Sendino Garvía,
C.C.L. Schuurmans^{2,3}, M. Ruelas², J.T. Soeiro¹, G. Tang², M.J. Janssen¹, J. Jansen^{4,5}, S. M. Mihăilă¹, T. Vermonden³,
Y.S. Zhang^{2*}, R. Masereeuw^{1*}

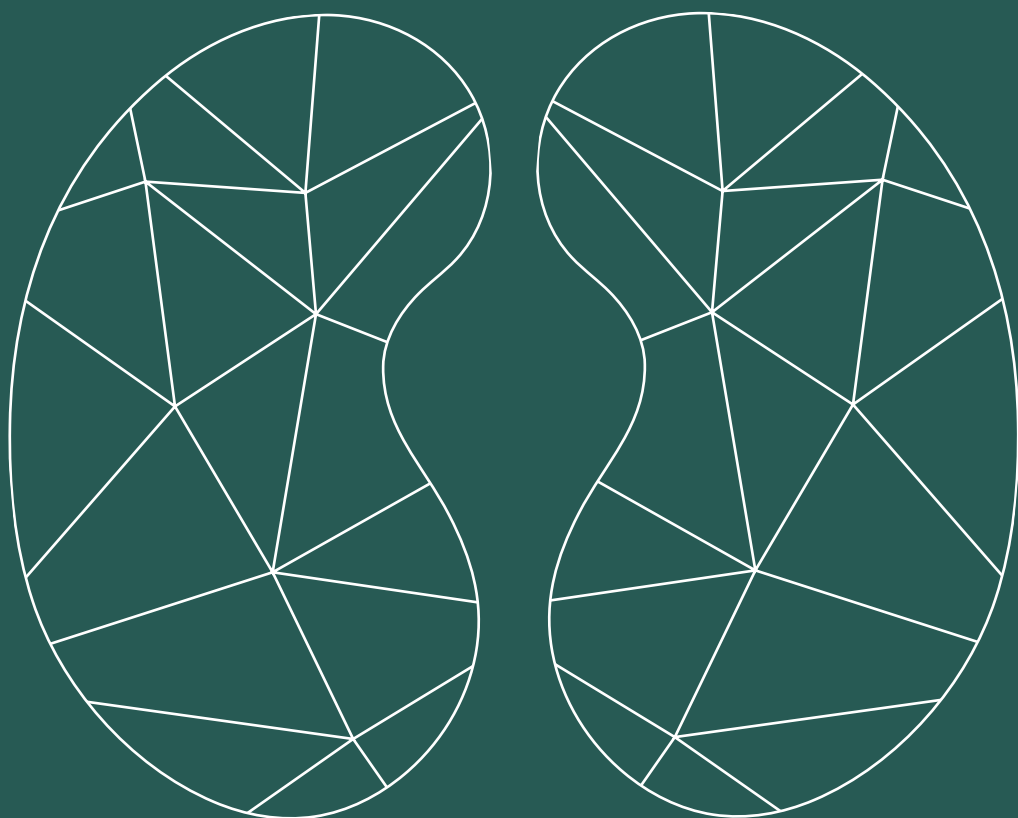
- 1 Division of Pharmacology, Utrecht Institute for Pharmaceutical Sciences, Utrecht University, Universiteitsweg 99, 3584 CG Utrecht, The Netherlands
- 2 Division of Engineering in Medicine, Department of Medicine, Brigham and Women's Hospital, Harvard Medical School, 65 Landsdowne Street, Cambridge, MA 02139, USA
- 3 Division of Pharmaceutics, Utrecht Institute for Pharmaceutical Sciences, Utrecht University, Universiteitsweg 99, 3584 CG Utrecht, The Netherlands
- 4 Department of Pathology and Pediatric Nephrology, Radboud University Medical Center, 6525 GA Nijmegen, The Netherlands
- 5 Institute of Experimental Medicine and Systems Biology, RWTH Aachen University, Aachen, Germany

[^] These authors contributed equally to this work

^{*} Corresponding authors

CHAPTER 3

CO-AXIAL PRINTING OF CONVOLUTED PROXIMAL TUBULE FOR KIDNEY DISEASE MODELING



Abstract

Despite the increasing incidence of kidney-related diseases, we are still far from understanding the underlying mechanisms of these diseases and their progression. This lack of understanding is partly because of a poor replication of the diseases *in vitro*, limited to planar culture. Advancing towards three-dimensional models, hereby we propose coaxial printing to obtain microfibers containing a helical hollow microchannel. These recapitulate the architecture of the proximal tubule (PT), an important nephron segment often affected in kidney disorders. A stable gelatin/alginate-based ink was formulated to allow printability while maintaining structural properties. Fine tuning of the composition, printing temperature and extrusion rate allowed for optimal ink viscosity that led to coiling of the microfiber's inner channel. The printed microfibers exhibited prolonged structural stability (42 days) and cytocompatibility in culture. Healthy conditionally immortalized PT epithelial cells and a knockout cell model for cystinosis (*CTNS*^{-/-}) were seeded to mimic two genotypes of PT. Upon culturing for 14 days, engineered PT showed homogenous cytoskeleton organization as indicated by staining for filamentous actin, barrier-formation and polarization with apical marker α -tubulin and basolateral marker Na⁺/K⁺-ATPase. Cell viability was slightly decreased upon prolonged culturing for 14 days, which was more pronounced in *CTNS*^{-/-} microfibers. Finally, cystinosis cells showed reduced apical transport activity in the microfibers compared to healthy PT epithelial cells when looking at breast cancer resistance protein and multidrug resistance-associated protein 4. Engineered PT incorporated in a custom-designed microfluidic chip allowed to assess leak-tightness of the epithelium, which appeared less tight in cystinosis PT compared to healthy PT, in agreement with its *in vivo* phenotype. While we are still on the verge of patient-oriented medicine, this system holds great promise for further research in establishing advanced *in vitro* disease models.

Keywords: *coaxial 3D printing; biomaterials; proximal tubule; cystinosis; in vitro modeling; kidney*

1. Introduction

With over 10% of the global population suffering from chronic kidney disease (CKD), kidney failure is a silent epidemic [1]. Within the kidney, the proximal tubule (PT) has been identified as a major target of injury and progression of CKD [2,3]. Hence, gaining insights into the PT's pathological mechanisms is essential for the development of effective therapies. While traditional *in vitro* two-dimensional (2D) and *in vivo* animal models have been of great use, it is well-appreciated that these models only limitedly recapitulate human PT pathology. The growth of the kidney tissue engineering (TE) field brings forward pioneering alternatives to circumvent the limitations of traditional models, including absence of microenvironmental triggers and species-specific differences [4,5]. Combining biomaterials and patient-derived cells, models of phenotypic relevance can be created while avoiding the loss of cell signature markers as a result of the planar culture [6].

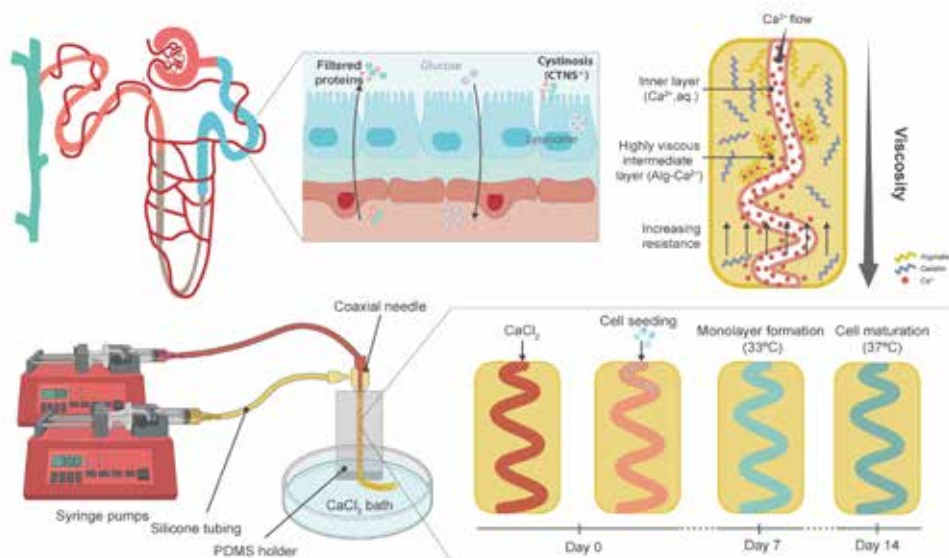


Figure 1. Graphical abstract. A) The proximal tubule (PT, blue) is the second segment of the nephron. In healthy circumstances, proteins are filtered from the bloodstream to the PT lumen (in blue) and amino acids and glucose are reabsorbed. Nephropathic cystinosis is a chronic kidney disease condition in which a mutation of the CTNS gene leads to a loss of function of cystinosin, a lysosomal transporter. Hence, cystine accumulates in the lysosome, causing severe damage to the kidneys with a loss of amino acids and glucose in urine. B) Ca²⁺ ions instantly crosslink with alginate, forming metal ion coordination bonds that increase the viscosity of the gel in the intermediate layer. The change of the viscosity combined with the increasing resistance from printing device walls allows the channel to coil. Adapted from [6]. (C) Schematics on the printing process and microfiber formation, seeding and maturation. After forming the inner channel via CaCl₂ perfusion, PT epithelial cells were seeded. Upon culturing at 33°C, the conditionally immortalized cells grew to form a monolayer. At 37°C, these cells started to differentiate until full maturation within 7 days.

In recent years, gene-editing has provided researchers with the tools for fast and secure generation of mutation-specific diseased cells, advancing towards personalized medicine [8]. CRISPR/Cas9 has been used on human conditionally immortalized PT epithelial cells (ciPTEC) to generate a nephropathic cell line in which the first exons of the *CTNS* gene are deleted (*CTNS*^{-/-}) [9]. Mutations in this gene result in nephropathic cystinosis, a chronic condition in which lysosomal accumulation of cystine leads to loss of PT integrity (**Figure 1A**). Furthermore, it has been demonstrated that a 3D membrane-based model of ciPTEC *CTNS*^{-/-} recapitulated better the nephropathic phenotype at a molecular, structural, and functional PT level compared to 2D cell cultures [10]. This observation highlights the importance of using a biomimetic microenvironment to recapitulate kidney functions.

Kidney TE focuses on replicating the tissue microenvironment to understand and guide cell-cell and cell-extracellular matrix (ECM) interactions. Biocompatible hydrogels have received great attention because of their similarities to the ECM [11]. Moreover, their polymeric nature makes them easily tailorable to the mechanobiological properties of the ECM composition and compatible with 3D (bio)printing techniques to create structures that resemble the PT [6,12-14]. For PT-(bio)printing, the hydrogel biomaterials must meet specific criteria contingent on the printing modality. Extrusion (bio)printing in particular requires precursors that stabilize rapidly from a non-viscous stage [15]. Therefore, gelatin and alginate solutions prevail as favorable candidates since aqueous gelatin solutions respond rapidly to thermal variations and dissolved alginate to divalent ions such as Ca²⁺ [16]. Others have used the swift chemical crosslinking of alginate to create microfibers with coiled channels [7,17]. Relying on a rapid viscosity change of the (bio)ink, a helicoidal lumen is formed within an extruded microfiber (**Figure 1B**). Several 3D (bio)printing alternatives have been proposed, including sacrificial 3D printing to establish a perfusable PT and its adjacent capillary, a layer-by-layer construct focused on the interface between kidney epithelium and vascular endothelium and core-sheath microfluidic printing and self-organization for co-culture of epithelium and endothelium [6,12-14]. Homan's thorough study proved enhanced tubular polarization markers (basolaterally expressed Na⁺/K⁺-ATPase and cilia at the apical membrane) and functionality (characterized by albumin uptake and megalin expression) as a result of a 3D convoluted microenvironment when compared to the 2D analogues [6]. Microfluidics-based core-shell extrusion has been proposed by Addario et al., to assemble PT constructs containing endothelial and epithelial cells [12]. Relying on PTEC migration, a straight hollow filament surrounded by endothelial cells was formed. Overall, the recent literature recognizes the urgent need for a 3D convoluted, and perfusable model of the PT and highlights its potential for pharmacological research. Yet, the architecture of the proposed

models is not fully recapitulating the PT as relevant diameters and convolution seem to be elusive and mutually exclusive. Sacrificial printing allows for tubular diameters down to 150 μm according to the authors, yet quantitative results and assays were carried out for larger lumens (400 μm) [6]. Conventional microfluidic core-sheath extrusion achieves smaller channels (~200 μm in diameter) but lacks convolution. The specific object of this study was to investigate the potential of one-step coaxial printing to achieve both convoluted architecture and a small diameter. Moreover, the beforementioned works were carried out with healthy epithelial cells. As of yet, phenotypically diseased cells have not been included. Thus, the suitability of (bio)printing for diseased PT models remains unassessed [6,13].

Here, we hypothesized that a coaxial printing system can produce convoluted microfibers that mimic PT physiology, suitable for hosting healthy and cystinotic PTEC lines (**Figure 1C**). We assessed the viability of the model during proliferation and differentiation of the cells. Cellular organization within the microfiber, monolayer integrity and polarization were evaluated by means of immunostaining. Finally, as a hallmark of PT function, transporter activity was studied for two important apical efflux pumps: breast cancer resistance protein (BCRP) and multidrug resistance protein 4 (MRP4).

2. Materials and Methods

2.1 Cell culture

ciPTEC (MTA number A16-0147) were obtained from Cell4Pharma (Nijmegen, The Netherlands) and developed as described [18]. Briefly, PT cells obtained from urine from healthy volunteers (in compliance with the guidelines of the Radboud Institutional Review Board) were transfected with a temperature sensitive mutant U19tsA58 of SV40 large T antigen (SV40T) and the essential catalytic subunit of human telomerase (hTERT). Two types of human ciPTEC were used in this study. The healthy control ciPTEC, also referred to in this paper as ciPTEC 14.4, and the cystinotic ciPTEC labeled as ciPTEC *CTNS*^{-/-}. ciPTEC *CTNS*^{-/-} is an isogenic cell line derived from ciPTEC 14.4 and generated using CRISPR-Cas9 [9], which harbors a biallelic mutation in exon 4 of the *CTNS* gene.

ciPTEC were cultured at 33°C and 5% (v/v) CO₂ up to 90% confluency to maintain a cell proliferation state. For maturation, ciPTEC were transferred to 37°C for at least 5 days prior to experimental readout. ciPTEC were cultured in T175 culture flasks (Greiner Bio-One, Alphen aan den Rijn, The Netherlands), using Dulbecco's modified Eagle medium/Nutrient Mixture F-12 (DMEM/F-12) without phenol red (Gibco, Thermo Fisher Scientific, Paisley, UK),

supplemented with 5 µg/ml of insulin, 5 µg/ml of transferrin, 5 µg/ml of selenium, 35 ng/ml of hydrocortisone, 10 ng/ml of epidermal growth factor, 40 pg/ml of tri-iodothyronine (Sigma-Aldrich, Saint Louis, MO, USA), 10% fetal bovine serum (FBS) (v/v, Greiner Bio-One, Alphen aan den Rijn, The Netherlands), and 1% penicillin/streptomycin (v/v, Gibco, Thermo Fisher Scientific, Paisley, UK).

2.2 Biomaterial ink

The formulation of the biomaterial ink was optimized to 1% alginic acid sodium salt from brown algae (w/v, Sigma-Aldrich, Saint Louis, MO, USA) and 8% gelatin (w/v, 300 grams Bloom Type A, Sigma-Aldrich, Saint Louis, MO, USA) in MilliQ water. Crosslinking solution was prepared with 2% calcium chloride (CaCl₂, w/v, Sigma-Aldrich, Saint Louis, MO, USA) in MilliQ water, which was filter sterilized. To visualize the formation of the hollow channels within the microfiber, the crosslinking solution was mixed with filter-sterilized food dye. Crosslinking of the microfibers was achieved by adding 2% microbial transglutaminase (w/v, mTG, MooGlue, Modernist Pantry, Eliot, ME, USA) to the cell culture medium for a minimum of 4 hrs. All components used were handled in a flow hood and filter sterilized to prevent contamination.

2.3 Wet weight measurements

Biomaterial ink blocks (n=12) consisting of 1% (w/v) alginate and 8% (w/v) gelatin were assessed for long-term stability using a degradation assay. The biomaterial ink was crosslinked by a 2% (w/v) mTG solution for 4 hrs in 37°C. Instant crosslinking of the alginate in the constructs was further obtained using 2% (w/v) CaCl₂ solution. The samples (5 mm in length, 5 mm in width, and 1 mm in height) were cultured in DMEM/F-12 + 0.02% (w/v) disodium pyrophosphate (Sigma-Aldrich, Saint Louis, MO, USA) at 37°C and 5% (v/v) CO₂ with medium refreshed every 2 to 3 days. Over a period of 4 weeks, the wet weights of the samples were measured at predefined time points and compared to the initial wet weights of the corresponding samples (t=0).

2.4 Hydrogel permeability

Permeability of the used biomaterial ink was measured by the diffusion rate of inulin-fluorescein isothiocyanate (inulin-FITC, Sigma-Aldrich, Saint Louis, MO, USA) over a layer of the hydrogel using a Transwell® system (0.4 µm pore, Corning, NY, USA). The Transwell® inserts were washed with warm Hank's balanced salt solution (HBSS, Gibco, Thermo Fisher Scientific, Paisley, UK) buffer before being coated with pre-heated ink containing 1% (w/v) alginate and 8% (w/v) gelatin and deposited in different volumes to obtain a range of

diameters (100, 200, 400 and 800 μm). The ink was crosslinked with 2% (w/v) CaCl_2 for 1 h at room temperature whereafter it was removed and incubated with a 2% mTG (w/v) solution overnight at 37°C. The basolateral compartment was exposed to 25 $\mu\text{g}/\text{ml}$ of inulin-FITC in phosphate-buffered saline (PBS, Lonza, Basel, Switzerland) for 1 h at 37°C and 5% (v/v) CO_2 . To measure the values of migrated inulin-FITC over the biomaterial ink layer, fluorescence of the apical compartment (100 μl per sample) was detected by a plate reader at excitation wavelength of 475 nm and emission wavelength of 530 nm. A calibration curve was included to relate the excitation and emission values to the associated concentration values. The measured values of migrated inulin-FITC over an empty Transwell® were used as the maximum value (100% leakage).

2.5 Printing device

The printing set-up consisted of *i*) two syringe pumps, *ii*) a tailored printing device, *iii*) silicone tubing and *iv*) a CaCl_2 bath. The printing device consisted of a polydimethylsiloxane (PDMS, SYLGARD™ 184 Silicone Elastomer, Dow, Midland, MI, USA) block that held a coaxial multi-layered nozzle while printing, allowing the extrusion of the hollow microfiber directly into the CaCl_2 bath (12-mm Petri Dish Corning, NY, USA) (**Supplementary Figure 1**). The coaxial nozzle consisted of one 30G needle that created the hollow channel and two 18G needles, one to align the core and sheath and the second one to feed the biomaterial ink. The set-up was easy to use and clean, not easily clogged, reusable and autoclavable. Before use, the printing device, connectors, and tubing were autoclaved. The syringe pumps were cleaned with ethanol and air-dried in the flow hood.

2.6 Fabrication of and cell culture in microfibers

For the fabrication of microfibers, syringes were connected to pumps using 50 and 300 $\mu\text{l}/\text{min}$ as settings for the core and sheath flows, respectively. The microfluidic device was connected to syringes containing the crosslinking solution (2% (w/v) CaCl_2) and prewarmed ink ($\sim 50^\circ\text{C}$). Once the hollow microfiber was formed, ciPTEC were seeded immediately after at a concentration of 1×10^7 cells/ml and a flow rate of 50 $\mu\text{l}/\text{min}$ up until the entire construct contained cells. From a practical standpoint, when the transparent cell suspension is perfused, it replaces the dyed calcium chloride inside the lumen of the microfiber, which can be easily discern upon bare-eye inspection of the fiber. Next, the seeded tubes were sliced into <5-cm pieces and transferred to the wells of 6-well plates by carefully handling them with tweezers. The samples were further crosslinked overnight at 33°C and 5% (v/v) CO_2 by adding 2% (w/v) mTG solution in the culture medium. The seeded tubes were incubated for 7 days at 33°C and 5% (v/v) CO_2 and then transferred to 37°C and 5% (v/v) CO_2 for, at least, 5 additional days.

2.7 Parameter influence on microfiber morphology

Flow rate and formulation of the ink are known factors that influence the morphology of the microchannel. To test the effects of experimental parameters on microfiber formation, the biomaterial ink composition was altered in the range of 0.5-1.25% (w/v) for the alginate concentration and 4-10% (w/v) for the gelatin concentration. These experiments were performed under a range of core flow (30-80 $\mu\text{l}/\text{min}$) while the sheath flow was kept constant (300 $\mu\text{l}/\text{min}$) to evaluate the influence of the core flow on the morphology of the microchannels in the microfibers.

The consistency of the results for this optimized protocol for microfiber fabrication was analyzed by measuring the inner and outer diameters of the produced microfibers ($n=3$). The samples of each experiment were imaged at >15 different spots of the microfiber and 5 measurements per image were quantified using ImageJ (National Institutes of Health, Bethesda, MD, USA).

2.8 Diameter assay

To analyze the swelling and shrinking behavior of the microfibers over time, microfibers (1% (w/v) alginate and 8% (w/v) gelatin) were cultured over a period of 4 weeks in an incubator at 37°C and 5% (v/v) CO_2 in DMEM-F12 and 0.02% (w/v) disodium pyrophosphate with medium refreshed every 2 to 3 days. Multiple images (≥ 15) of the microfiber were taken at each time point and each image was measured at 5 places to ensure a representative measurement for each timepoint. Images were taken using a Nikon Eclipse Ti microscope (Nikon, Tokyo, Japan). The inner and outer diameters of the microfibers were measured over a period of 4 weeks, using ImageJ, and compared to the initial inner and outer diameters ($t=0$).

2.9 Cell viability

To assess the viability of cells in the microfibers, calcein-acetoxymethyl-ester (calcein-AM, Invitrogen, Thermo Fisher Scientific, Carlsbad, CA, USA) and ethidium homodimer-1 (EthD-1, Invitrogen, Thermo Fisher Scientific, Carlsbad, CA, USA) staining was carried out on days 1, 3, 7 and 14 after printing. Cell culture media was removed from the samples and samples were rinsed twice with HBSS after which they were submerged in calcein-AM (2 μM in HBSS) and EthD-1 (4 μM in HBSS). Calcein-AM is hydrolyzed in living cells by esterase resulting in the fluorescent calcein that visualizes living cells. EthD-1 can visualize dead cells by staining the DNA as cell death causes cell membrane permeability allowing the dye to enter the cells. The samples were incubated at 37°C, 5% (v/v) CO_2 in the dark for 30 min followed by two quick rinses with HBSS. The visualization of the viable and dead cells was obtained using

a confocal Leica TCS SP8 X microscope (Leica, Wetzlar, Germany) with fluorescent light at emission wavelengths of 490 nm and 535 nm for calcein-AM and EthD-1, respectively. Images were analyzed using ImageJ software Cell Counter plugin; cell viability is expressed as the percentage of number of live cells to total number of cells.

2.10 Immunocytochemistry

Microfibers with ciPTEC embedded were fixed for 30 min with 4% (v/v) paraformaldehyde (Pierce™, Thermo Fisher Scientific, Carlsbad, CA, USA) in PBS and permeabilized with 0.3% (v/v) triton X-100 (Sigma-Aldrich, Saint Louis, MO, USA) in PBS for 30 min at room temperature. Subsequently, the cells were exposed to the blocking buffer consisting of 2% (v/v) FBS, 0.5% (w/v) bovine serum albumin (BSA, Sigma-Aldrich, Saint Louis, MO, USA) and 0.1% (v/v) Tween-20 (Sigma-Aldrich, Saint Louis, MO, USA) in PBS for 60 min at RT. Antibodies were diluted in the blocking buffer. Primary and secondary antibodies were incubated on a shaker overnight at 4°C. A list of primary and secondary antibodies and their dilutions can be found in **Supplementary Table 1**. Immunofluorescence was examined using confocal microscopy and software Leica Application Suite X. Images were analyzed using ImageJ. Images were converted to 8-bit, Z-projections were made, and the same threshold was applied for every image. Actin filament directionality was quantified using the directionality functionality and Fourier components analyses.

2.11 Membrane transporter activity measurements

For functionality testing of various transporters (MRP4, BCRP), microfibers with ciPTEC encapsulated were cultured up to confluency at 33°C 5% (v/v) CO₂ and allowed to mature at 37°C for 1 week. The samples were incubated for 15 min at 37°C with 1 μM of non-fluorescent calcein-AM in HBSS, in which viable cells enzymatically converted calcein-AM to fluorescent calcein. To validate functionality of MRP4 and BCRP (excretion of calcein), incubation was done in presence or absence of MK571 (5 μM; Sigma-Aldrich, Saint Louis, MO, USA) and KO143 (5 μM, Sigma-Aldrich, Saint Louis, MO, USA) inhibitors of MRP4 and BCRP. The NucRed™ Live 647 ReadyProbes™ Reagent (Invitrogen, Thermo Fisher Scientific, Carlsbad, CA, USA) was added as a nuclear marker to be able to normalize for the number of cells. Samples that were incubated in presence of the inhibitors were pre-incubated with the inhibitors alone for 15 min. After incubation with calcein-AM (with or without inhibitors) the samples were washed with ice-cold HBSS, and images were taken using confocal microscopy. Images were analyzed using ImageJ. Images were converted to SUM Z-stacks and 'Area', 'Mean gray value' and 'Integrated density' were measured for microfiber regions of interest (ROI). Background fluorescence was corrected for microfiber ROI area and subtracted (protocol adapted

from 70). The resulting mean fluorescence intensity was then divided over the number of cells, counted manually with the ImageJ Cell Counter plugin.

2.12 Real time (RT)-qPCR of mRNA expressions

Gene expression analysis was performed by RT-qPCR on ciPTEC after growing in the microfiber at 33°C until confluency and 7 days at 37°C. To obtain enough mRNA for a reliable gene expression measurement, up to 30 cm of cell layer confluent microfiber from the same printing batch was pooled. The samples were stored for at least 30 min at -80°C and mechanically homogenized with vortex before mRNA was isolated using a RNeasy mini kit (Qiagen, Hilden, Germany) following the manufacturer's protocol. cDNA was prepared using 100 ng of sample RNA templates using the iScript¹ cDNA Synthesis Kit (Bio-Rad Laboratories Inc., Hercules, CA, USA). For BCRP (*ABCG2*) and MRP4 (*ABCC4*) RT-qPCR was performed using Taqman Universal PCR Master Mix and Taqman Gene Expression assay (Applied Biosystems, Thermo Fisher Scientific, Carlsbad, CA, USA) for *ABCG2* (Hs01053790_m1), *ABCC4* (Hs00988721_m1) and reference gene *RPS13* (Hs01011487_g1). Relative gene expression levels were calculated as fold changes using the $2^{-\Delta\Delta Ct}$ method. All reactions were carried out with equivalent dilutions of each cDNA sample.

2.13 Perfusable chip system and inulin-FITC leakage assay

A custom-made chip was designed with Autodesk Fusion 360 software to connect the microfibers to a perfusion system after their maturation. The chip consisted of an open square with lateral channels in which 18G syringe elbow needles are inserted (**Supplementary Figure 2**). The design was prepared for digital light processing (DLP) 3D printing and printed with an EnvisionTEC Perfactory 3 Mini Multi Lens 3D printer (PIC 100 resin). The chips were post-processed *via* sonication (5 min, 2 times, 100% ethanol) and flashed (3000 times, EnvisionTEC, Dearborn, MI, USA). Microfibers were manipulated through the lateral chip channels and endings were inserted in the hollow lumen of the 18G syringe needle. The syringe needles were pushed inside the chip lateral channels, forming a tight seal. A perfusable setup was created by connecting a syringe pump to tubing (PFA, 0.020" ID, IDEX Health & Science, Sigma-Aldrich, Saint Louis, MO, USA) *via* a luer lock, and connecting the tubing to the syringe needles *via* elastic tubing (1.6 mm of ID, Tygon, VWR, Amsterdam, The Netherlands). The water tightness of the system was tested assessing liquid leakage in the attaching points by perfusing food dyed MilliQ at 25 μ l/min for 15 min.

To quantify the tightness of the cell monolayer, inulin-FITC solution (0.1 mg/ml in HBSS, Sigma-Aldrich, Saint Louis, MO, USA) was perfused through the microfiber lumen at 25 μ l/min for 15 min using a syringe pump (Terumo, Tokyo, Japan). Empty and ciPTEC-containing

microfibers were filmed with a fluorescence microscope with a green filter Nikon Ts2-FL microscope (Nikon, Tokyo, Japan). Images were taken at the moment of perfusion, after 5 min, and after 15 min perfusion. For quantification, images were also taken 10 seconds before and after previously mentioned timepoints. In ImageJ 'Integrated density' was measured for each whole image and a background intensity ($>T_0$) was subtracted.

2.14 Statistical analyses

Unless specified otherwise, three microfibers per condition were used in three independent experiments. ImageJ (National Institutes of Health, Bethesda, MD, USA) was used for image analysis and quantification. Statistical analysis was performed in GraphPad PRISM 8 (GraphPad Software Inc., La Jolla, CA, USA), using unpaired t-tests and two-way ANOVA with Tukey's or Sidák's post-hoc test for multiple comparison analysis, where appropriate. Differences were considered significant with a p-value of $p < 0.05$. * indicates $p < 0.05$, ** $p < 0.01$, *** $p < 0.001$ and **** $p < 0.0001$. Results are shown as the mean \pm standard error of the mean (SEM) of at least three replicates.

3. Results

3.1 The printing system reveals robust printing of perfusable coiled microfibers

A co-axial microfluidic device has been previously presented for the fabrication of microfibers with geometrically complex channels within a range of 20-300 μm [7]. The generation of the coiling microchannels during printing can be ascribed to the instant formation of calcium-alginate (Ca-Alg) bonds that cause the hydrogel to acquire a higher viscosity while printing. By regulating the rates of these fluids ($5 < Q_{\text{sheath}}/Q_{\text{core}} < 10$), the increase in viscosity around the core fluid will cause it to start spiraling (**Figure 1**). The generation and characteristics of this helical channel within the microfiber can be managed by the control of the flow rate ratio of the fluids [7]. However, since unmodified alginate lacks cell-favorable bioactive elements and cells are unable to interact with the alginate matrix due to its hydrophilic nature, gelatin was included to improve cytocompatibility.

Biomaterial ink stabilization is proposed in two phases: a rapid ionic crosslinking process for alginate with Ca^{2+} and a prolonged enzymatic crosslinking of gelatin with mTG [20]. For the potential use of the microfibers in long-term culture, physical stability is of major importance. This stability was assessed in terms of changes in wet weight. Wet weight measured over the period of a month increased for the biomaterial ink blocks with 21% ($\pm 5\%$, $p = 0.0001$, unpaired t-test) in comparison to the initial weight at $t = 0$ (W_0) in a gradual

way (**Figure 2A**). Additionally, the composition of the microfibers must allow the diffusion of nutrients, oxygen, and protein-bound toxins. To mimic reabsorption of solutes in the PT, a permeability assay was performed. **Figure 2B** shows an inversely proportional correlation between diffusion of inulin-FITC and thickness of the biomaterial ink in a time span of 60 min. The relative diffusion rates compared to the 100% control (empty Transwell®) were measured for hydrogel layers with a thickness of 100 μm ($82.9\% \pm 2.65\%$), 200 μm ($61.5\% \pm 1.3\%$), 400 μm ($39.3\% \pm 4.5\%$) and 800 μm ($27.1\% \pm 1.3\%$).

Simultaneously, the printing system was established. **Figures 2C** and **D** show the robust and sterilizable printing system for the fabrication of coiled and perfusable microfibers. All elements were compatible with decontamination strategies, either by air drying with ethanol 70% in the flow hood, UV light exposure for 20 min (syringe pumps, coaxial nozzles) or in a regular autoclave cycle (tubing, PDMS holder). Moreover, our system allows continuous printing, and was only limited by the size of the syringes containing the ink and the crosslinker solution.

Different core and sheath flows (Q_{core} , Q_{sheath}), in combination with several alginate and gelatin proportions in the biomaterial ink were tested to assess their influence on the structure of the microfibers. A coiling nature was observed throughout the images and no trend was observed in the morphology of the microfibers due to the increase of gelatin or alginate concentration (**Supplementary Figure 3**). Accordingly, intermediate values of gelatin (8% w/v) and alginate (1% w/v) were chosen for the microfiber compositions. Additionally, the study of core and sheath flows showed no trend regarding the coiling of the inner microchannel (**Figure 2E, Supplementary Figure 4**). However, there was a significant increase in the outer diameter of the microfibers corresponding to higher sheath feeding rates (**Figure 2F**). The compromise between permeability and coiling set the core and sheath flows at 50 $\mu\text{l}/\text{min}$ and 300 $\mu\text{l}/\text{min}$, respectively, allowing the robust printing of perfusable microchannels with inner diameters of approximately 250 μm (**Figure 2F**).

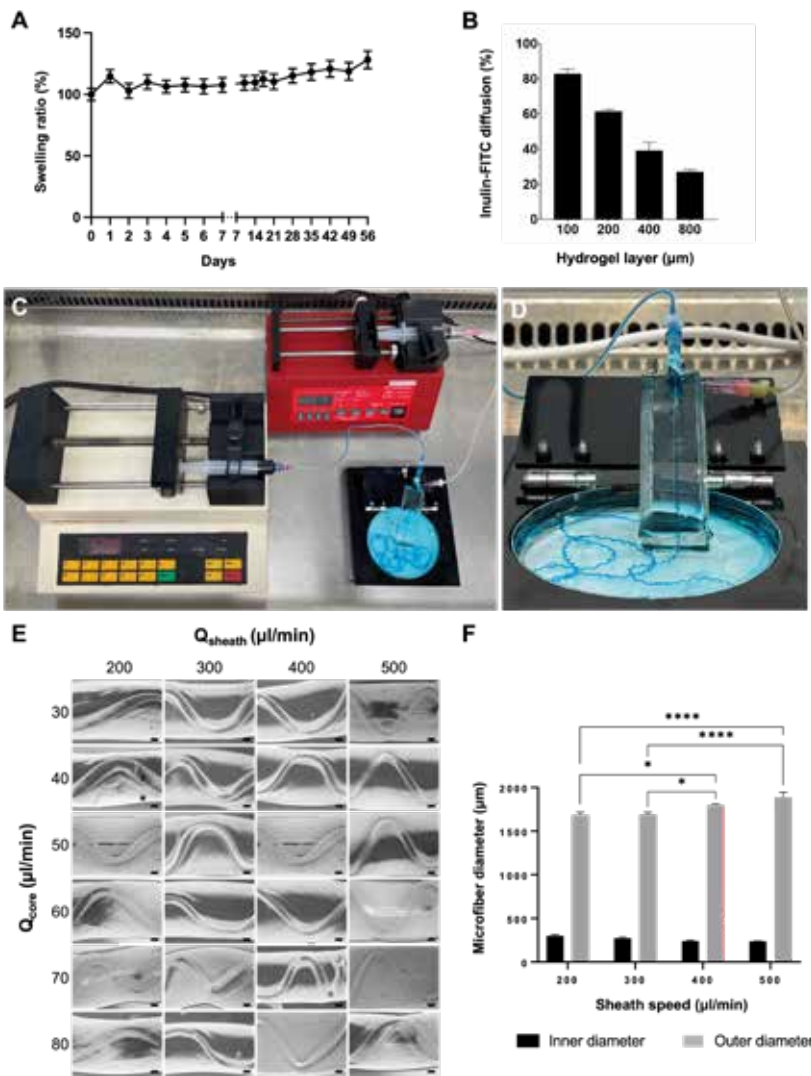


Figure 2. Biomaterial ink properties, printing system and printed microfibers. A) Wet weight changes over a period of 42 days is presented as swelling ratio (%) compared to its initial wet weight (100%) on day 0. Overall minor gradual increase in weight was observed (data are presented as mean ± SEM of 12 experiments). B) Quantification of diffusion of inulin-FITC over a hydrogel layer during 60 min compared to control (diffusion over empty Transwell® insert) showed an inversely proportional relation (mean ± SEM of 2 experiments). C) Sterile printing setup inside the flow hood. Two syringe pumps extrude the sheath biomaterial ink (300 μl/min) and the CaCl₂ core (50 μl/min). D) Close up of the printing device consisting of the coaxial needles, silicon holder and petri dish. E) Different sheath (Q_{sheath}) and core (Q_{core}) rates were tested for the biomaterial ink formulation, but no trend was observed. F) Quantification of inner and outer microfiber diameters showed a gradual increase of the outer diameter proportional to the sheath speed. No differences were found for the width of the inner channels (two-way ANOVA with Tukey's post-hoc test. Data are presented as mean ± SEM of 18 experiments). * p-value<0.05, **** p-value<0.0001. Scale bars: 200 μm.

3.2 Engineered microfibers are stable over an extended test period of 42 days

Integrity of the bioengineered microfibers was examined at different time points: after printing (**Figure 3A**), after seeding (**Figure 3B**), and after culture for 14 days without and with ciPTEC (**Figures 3C and D**, respectively). The fibers remained firm, and were able to withstand manual handling from the printing setup to a common culture plate. Neither the seeding process nor the culture of cells for 14 days (including refreshing of the culture medium) affected the dimensions of the inner channels (**Figure 3E**). Moreover, the bioengineered microfibers showed physical stability with an open lumen in long-term culture (42 days). Microfibers and the channels embedded within showed a minor reduction in diameter over a period of 1 month in the inner diameter ($5\% \pm 1\%$, $p < 0.0001$), but not in the outer diameter ($1\% \pm 1\%$, $p = 0.4432$), compared to the initial day (100%, $t = 0$) (**Figure 3F**). Both inner and outer diameters showed no sudden changes during a period of 42 days.

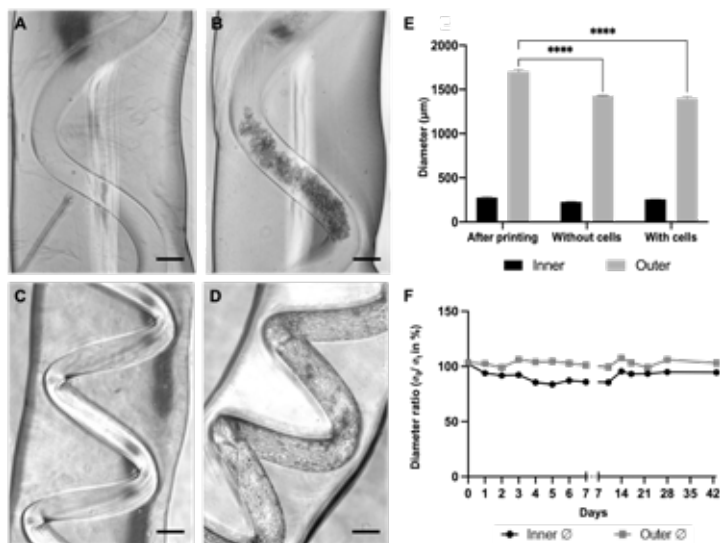


Figure 3. Microfiber stability over time and biocompatibility with PT cells. A-D) Bright-field microscopy showing the hollow channel immediately after printing (A), after seeding (B), cultured for 14 days without cells (C), and cultured for 14 days with ciPTEC forming a monolayer (D). Due to the coiling and because of gravity and vestigial flows after the printing, the cells tended to accumulate in the lower regions of the microfiber (B). However, as they proliferate, they eventually covered the lumen to form a tight monolayer. E) Microfiber inner diameter did not change by the presence of cells, whereas the outer diameter slightly decreased during the culture period (two-way ANOVA with Sídák's multiple comparison test). Data are presented as mean \pm SEM of 3 microfibers after printing, 6 microfibers without cells, and 8 microfibers with cells). The bioengineered PT microfibers were stable over an extended test period of 42 days, with a minor and fluctuating reduction of the inner diameter (unpaired t-test). Data are presented as mean \pm SEM of 3 microfibers, each measured ≤ 75 times) (F). **** p-value < 0.0001 . Scale bars: 200 μm .

3.3 Convoluted cystinosis tubules are less viable upon prolonged culturing

The ciPTEC 14.4 line used for this work has shown to stably express the PT phenotype over a very high number of passages and when grown as kidney tubules on a fiber [10,21,22]. Further, the cystinotic cell line (ciPTEC *CTNS*^{-/-}) showed lysosomal cystine accumulation, increased autophagy and vesicle trafficking deterioration, the impairment of several metabolic pathways, and disruption of the epithelial monolayer tightness as compared to control kidney tubules [10]. These features are representative of the nephropathic phenotype. We here evaluated the cytocompatibility of the convoluted microfibers by performing live/dead staining for both cell lines (**Figure 4A**). The results show that cell viability was high within the first week of culture, with significant differences between the cell types for days 1 ($p=0.0020$), 3 ($p=0.0224$), and 14 ($p=0.0284$) (**Figure 4B**). Upon prolonged culturing a decline in viability was observed, which was more pronounced in ciPTEC *CTNS*^{-/-}.

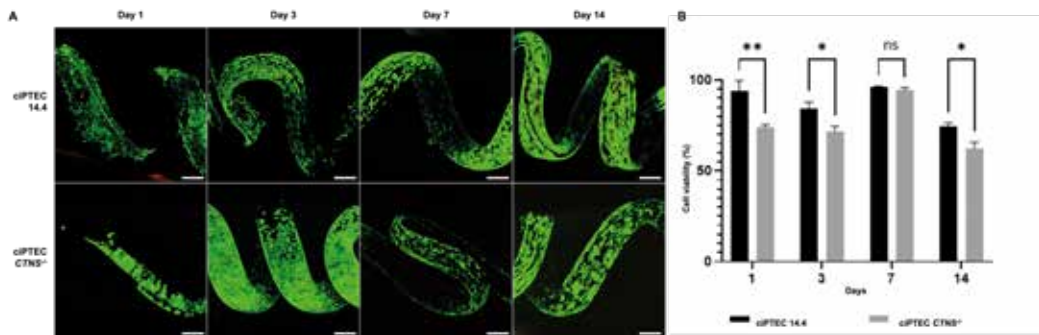


Figure 4. Microfiber biocompatibility with proximal tubule cells. A) Live/Dead staining (Calcein-AM/EthD-2) of ciPTEC 14.4 and ciPTEC *CTNS*^{-/-}. B) Cell viability (%) over time (number of days) obtained from A. (Two-way ANOVA with Sidák's multiple comparison test. Data are presented as mean \pm SEM of 2 experiments for day 7, and 3 experiments for all other days). * p -value <0.05 , ** p -value <0.01 . Scale bars: 200 μ m.

3.4 Both ciPTEC 14.4 and *CTNS*^{-/-} form organized and polarized monolayers in the microfibers

Next, the organization of the cell monolayer was evaluated by immunofluorescence staining and quantification of the intracellular F-actin filaments. Both ciPTEC lines were able to attach and grow for 14 days with phalloidin covering the lumens of the microfibers entirely (**Figure 5A, C, Supplementary Figure 5**). The cytoskeleton appeared aligned circumferentially to the channel for both cell lines, with comparable cell directionality for ciPTEC 14.4 and ciPTEC *CTNS*^{-/-} (**Figure 5B, D**). Furthermore, the cell polarization was assessed by the basolateral expressions of Na⁺/K⁺-ATPase and apical α -tubulin. Both ciPTEC lines exhibited positive

immunostainings for the polarization markers, confirming the establishment of confluent epithelial monolayer and a response to basal-apical guidance (**Figure 5E, F**).

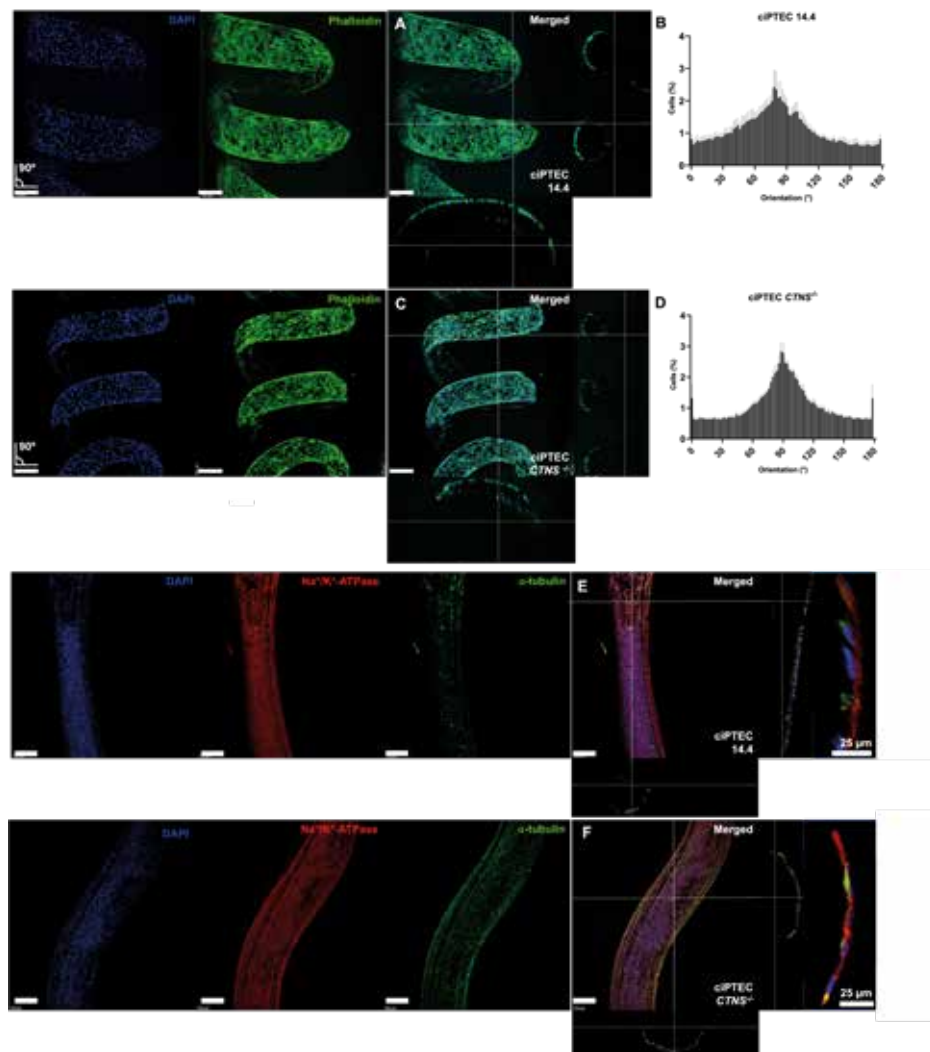


Figure 5. Cell organization and polarization in the PT microfibers. A) Microfibers were stained using phalloidin to show the organization of F-actin filaments in ciPTEC 14.4 (A) and CTNS^{-/-} (C). Both models present an undisrupted cell monolayer covering the open lumen (see orthogonal sections). In blue: 4',6-diamidino-2-phenylindole (DAPI) (nuclei staining), in green: phalloidin (binds to actin filaments). (B, D) Directionality analysis performed for at least 4 replicates. (E, F) After maturation of 7 days the control (E) and cystinotic ciPTEC (F) form an organized 3D structure including primary cilia (α -tubulin staining). In blue: DAPI (nuclei staining), in red: Na⁺/K⁺-ATPase, in green: α -tubulin staining. Scale bars: 200 μ m, unless indicated differently.

3.5 Healthy and cystinotic ciPTEC form tight monolayers in coaxially printed microfibers

Tight sealing of our engineered chip was confirmed by perfusing colored MilliQ water through a microfiber not containing cells (**Supplementary Movie 1**). It has been previously demonstrated that cystinosis cells grown on hollow fiber membranes form a less tight monolayer in comparison to a healthy control [10]. Here, we evaluated cell monolayer tightness by means of an inulin-FITC leakage assay. For this, microfibers with ciPTEC 14.4, ciPTEC *CTNS*^{-/-}, and without cells were inserted in our custom designed chip and perfused with inulin-FITC at a rate of 25 $\mu\text{l}/\text{min}$ for 15 min and visualized with an inverted microscope. In the empty (cell-free) microfiber, inulin-FITC diffused from the channel into the ink formulation from the start of perfusion (**Figure 6A**), whereas in the microfibers with ciPTEC 14.4 the dye was retained in the channel (**Figures 6B, D**), confirming a tight barrier formation. In the ciPTEC *CTNS*^{-/-} channel the dye diffused significantly further into the ink than either the empty ($p < 0.0001$) or ciPTEC 14.4 ($p < 0.0001$) microfiber, confirming ciPTEC *CTNS*^{-/-} are incapable of forming a leakage-tight barrier (**Figure 6C, D**).

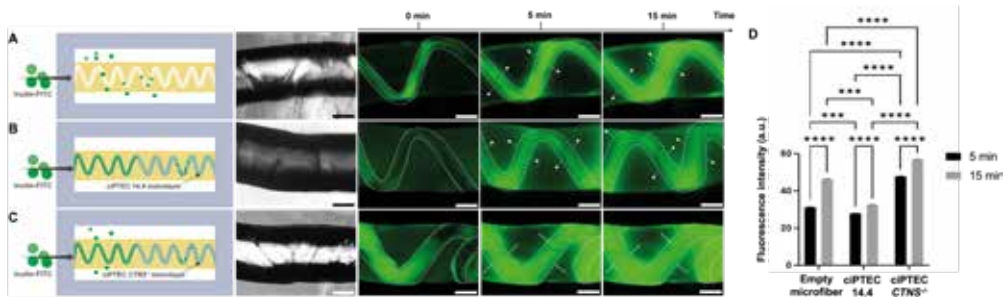


Figure 6. Renal barrier function in the microfiber chip tested by means of inulin-FITC. A-C) Microfibers without cells (A), with ciPTEC 14.4 (B) and with ciPTEC *CTNS*^{-/-} (C). Immunofluorescent images were captured after 0, 5 and 15 min of inulin-FITC perfusion. Dotted line in each image indicates the area measured for $t=0$. D) Fluorescence intensity at $t=5$ and 15 min. A significant difference was found between the two timepoints for each condition, as well as between the different microfibers (two-way ANOVA with Sidák's post-hoc test. Data are presented as mean \pm SEM of 3 measurements). *** p -value < 0.0005 , **** p -value < 0.0001 . Scale bars: 500 μm .

3.6 Engineered cystinosis tubules show reduced apical transport activities

Cystinosis is characterized by generalized dysfunction of the apical proximal tubular influx transporters (so-called renal Fanconi syndrome), developed during infancy, and gradually progressing towards end-stage kidney disease in the first decade of life in the majority of patients that are not treated with the cystine-depleting drug cysteamine [23,24]. In the

present study, we investigated whether the proximal tubular efflux transporters BCRP and MRP4 are affected in cystinosis. For this, we used calcein-AM that diffuses into live cells and is hydrolyzed into the fluorescent calcein, which can be actively secreted by the efflux pumps (**Figure 7A**) [25]. **Figure 7B** shows representative images of the ciPTEC present in the channel of a microfiber exposed to calcein-AM with or without inhibitors for BCRP and MRP4 (MK571 and KO143). Upon addition of the inhibitors, an increase in intracellular fluorescence was observed (**Figure 7B**, right panels) demonstrative of the activities of both membrane transporters. Evaluation of the transporter gene expressions revealed no differences in *ABCG2* between the two cell lines but a reduced expression of *ABCC4* (**Figure 7C**). Semi-quantification of the fluorescent images resulted in a 2.5-fold increase in signal after efflux pump inhibition in ciPTEC 14.4 whereas in ciPTEC *CTNS*^{-/-} this increase was only 1.3-fold, suggesting reduced transporter activities in these cystinotic cells (**Figure 7D**).

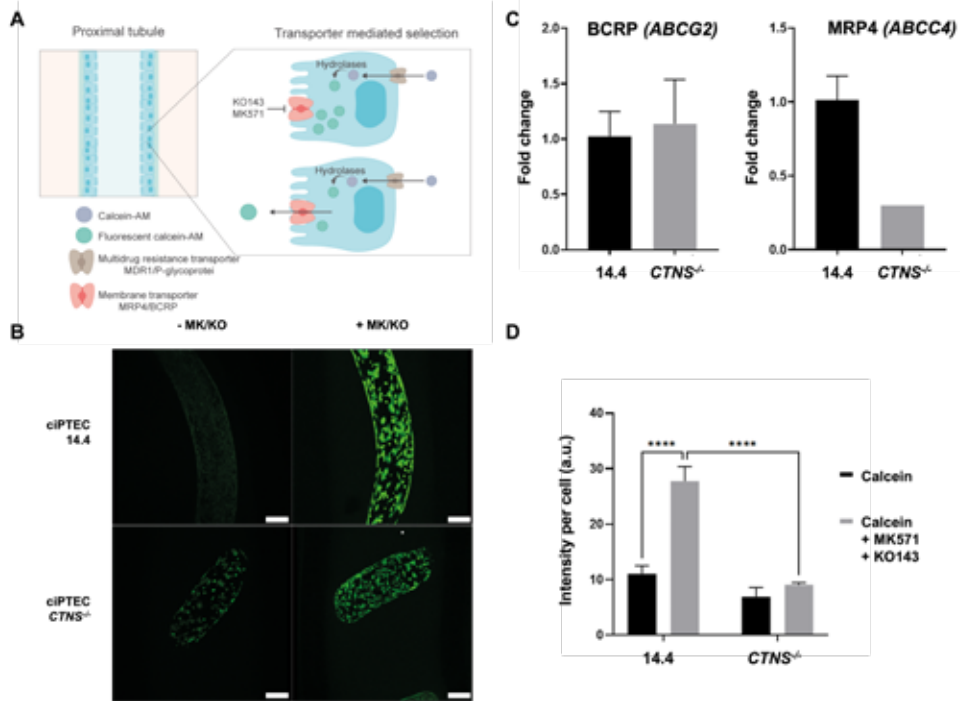


Figure 7. Engineered cystinotic tubules show reduced apical transport activities. A) The non-fluorescent calcein-AM enters the ciPTEC cytoplasm via diffusion and is expelled via the Multidrug resistance transporter MDR/P-glycoprotein. Upon inhibition of the apical membrane transporter MRP4/BCRP the accumulating calcein-AM is converted to the fluorescent calcein through intracellular hydrolases. The inhibitors MK571 and KO143 (MK/KO) prevented the intracellular fluorescent calcein from being transported extracellularly, which otherwise would be mediated by the membrane transporters BCRP and MRP4. B) Representative images of PT exposed to calcein-AM with and without inhibitors to visualize the membrane transporter activities. C) Relative ABCG2 and ABCC4 mRNA expressions of ciPTEC 14.4 and CTNS^{-/-} cultured in microfibers. D) Semi-quantification of the intracellular fluorescence intensities with MK571/KO143 inhibitors revealed in ciPTEC 14.4 a significant increase in intracellular fluorescent calcein compared to cells in the absence of inhibitors. This increase was not seen in ciPTEC CTNS^{-/-} (two-way ANOVA with Tukey's post-hoc test. Data presented as mean \pm SEM of at least n=4 experiments). **** p-value < 0.0001. Scale bars: 200 μ m.

4. Discussion

The PT is a tube-like microfluidic structure in which curvature of the substrate plays a critical role in influencing PT cell polarization [26]. Accordingly, developing PT models should revolve around mimicking the same working principle. Previous reports support 3D (bio) printing as a suitable technique for generating tube-like structures, often accompanied by endothelial cells that account for a rudimentary microvasculature [6,27]. Yet, these proposed models mainly resembled the straight region of the PT, simpler to fabricate with the currently available biofabrication methods. We hypothesized that co-axial printing is a suitable technique for generating microfibers to model the convoluted PT microenvironment, combining biomaterials and cells into a 3D design representing architectural complexity of the native tissue. Accordingly, we developed an innovative printing system for helical microfiber fabrication which closely mimics the convoluted PT microenvironment and allows for cell proliferation and maturation. By using a biomaterial ink consisting of alginate and gelatin, crosslinked by CaCl_2 and mTG, the microfibers are stable over a long period of time. We demonstrated that they can be used to study healthy and diseased PT by looking at cell viability and transepithelial transport, as both ciPTEC 14.4 and *CNTS*^{-/-} formed tight and polarized monolayers in the microfibers.

Previous approaches for helical coaxial printing used a glass capillary to create the microfibers or manual insertion of a needle within the channel to perfuse the channels with a cell suspension [7,17]. However, these methods appeared laborious, material consuming and limited the microfiber to contain one microchannel only and one cell type. This approach was not a suitable seeding option for our system as the diameter of the microchannel within the microfibers was too small and convoluted in shape to manually insert the needle without perforating the fiber. Others have proposed the use of syringes and glass capillaries to attach fibers to a perfusion system with vacuum, but the limitations were similar: labor-intensive and not straight-forward [28]. Here, the glass was substituted by a PDMS holder and a coaxial needle, allowing the automatization of the system using syringe pumps both for the channel formation and cell seeding. We achieved a one-step method for microfiber fabrication and cell seeding, by perfusing the cell suspension through the channels directly after the fabrication of the fiber. PDMS is a widely used polymer in the field of microfluidics, due to its favorable mechanical properties, cytocompatibility, moldability, gas permeability, and optical clarity. Nevertheless, PDMS has limited capacities for high-throughput manufacturing and is known for resorption of small hydrophobic molecules [29]. However, the advantages of this PDMS microfluidic printing device further include its fast production time, the ability to reuse and autoclave the material, and ease to handle compared to glass

capillaries. Using this device, we obtained robust fabrication of microfibers with specific parameters optimized for PT engineering.

Besides a robust and sterilizable manufacturing system, the formulation of a cytocompatible and stable biomaterial ink is key for the fabrication of the coiled microfibers. Alginate has been proposed earlier for microfiber fabrication, due to its rapid physical crosslinking when exposed to Ca^{2+} [7,17]. Nevertheless, alginate in its unmodified form fails to support cell adhesion and cell proliferation [30]. Hence, it is often combined with gelatin, a derivative from collagen which is a main component of connective tissues [6,13,31-37]. Gelatin supports cell adhesion as it retains many functional groups identified by cells and it can be stabilized in the long-term *via* enzyme-induced chemical crosslinking. We showed that the biomaterial ink remained stable over 42 days, enabling long-term cultures. Moreover, we characterized and defined the diffusion limit of the hydrogel *via* inulin-FITC measurements. As expected, thickness restricted diffusion. When studying the microfiber diameter, our results indicated a gradual increase of the outer fiber diameter directly proportional to higher sheath rates. Thick hydrogels might jeopardize the passive diffusion of nutrients towards the inner channels, while permeability for nutrients, oxygen and solutes are critical for cell viability and modeling PT. In previous reports on perfusable coiled microfibers, the properties of the helix (amplitude, helix pitch) were tunable and responded to flow rates [7,17]. However, we did not observe a major difference in the coils' features for either feeding rates or ink compositions with regards to relative percentages of alginate and gelatin. While the reason remains unclear, the previously reported coiled microfibers used only alginate, whereas we introduced a second polymer to improve cytocompatibility. Changes in the rheological properties when mixing gelatin and alginate have been identified and might be responsible for the observed phenomenon [38].

The incorporation of cells in a precise manner is essential to generating a monolayer in the channels and this was achieved in a one-step process, where the cells could be incorporated in the system immediately after the channel formation. Cells from both healthy and cystinotic ciPTEC lines were able to adhere and proliferate in the helical microchannels, with high viability over the first week of culture but a slight decrease over time that was more pronounced for the cystinosis model. An explanation for this decrease in viability is that the natural turnover of dead cells (EtHd-1, red fluorescence) that detached from the microfiber accumulated in the lumen, because there was no active perfusion of the microfiber during the culture period. Another explanation might be a lack of oxygen supply that is quite common in thick hydrogels and leads to cell necrosis, which could be prevented by having a perfusable or a vascularized set-up [39].

The correct function of a bioengineered PT relies on the establishment of a tight and cohesive barrier-forming monolayer responsible for vectorial transport [40]. The F-actin staining of the microfibers showed a homogeneous monolayer for both healthy and cystinosis ciPTEC, advocating for coiled microfibers as a 3D model of the PT. A recent study using the same cell lines in a 3D microenvironment showed monolayer dysregulation with differences in the cell orientation in the *CTNS*^{-/-} knockout model compared to healthy cells [10]. Inconsistencies between this and a previous study can be attributed to the 3D models applied, that is, microPES type TF10 hollow fiber capillary membrane *versus* hybrid hydrogel material in this study, but also the distribution of the cells within the structures, *i.e.* convex *versus* concave surfaces, with ciPTEC exhibiting a preference for concave over convex surfaces [26,41,42].

In the coaxially printed constructs, both cell lines were able to mature and polarize with a basolateral localization of Na⁺/K⁺-ATPase and α -tubulin at the apical side of the cells, which is crucial for performing key PT functions like transepithelial transport. In cystinosis, a generalized dysfunction of the PT is observed, which is characterized by the presence of, among others, polyuria, phosphaturia, glycosuria and proteinuria, also termed as renal Fanconi syndrome [23,24]. Our inulin-FITC leakage confirmed this by showing significantly higher leakage in the *CNTS*^{-/-} group compared to the healthy cells in the microfiber, which shows a dysfunction of the monolayer tightness. Remarkably, inulin-FITC leakage in the *CTNS*^{-/-}-seeded microfibers was higher than empty microfibers. A possible explanation could be that due to the accumulation of intra-lysosomal cystine, lysosomal acidification occurs. Indeed, renal acidosis is the most common symptom in cystinosis patients [43], which impacts directly the pH environment. Local pH alterations can induce destabilization and degradation of the microfiber gel, leading to an increased inulin-FITC leakage.

The cystine-induced injury of proximal tubular cells leads to altered ATP metabolism, altered glutathione metabolism, and apoptotic cell death and affects apically expressed transporters. However, it was previously shown that P-glycoprotein (*ABCB1*), an ATP-dependent efflux pump, may not be affected in cystinosis, despite a renal Fanconi-like phenotype in knockout mice [44, 45]. We evaluated two other apically expressed ATP-dependent efflux pumps, namely BCRP (*ABCG2*) and MRP4 (*ABCC4*), and demonstrated their functional presence in the engineered healthy PT microfibers, and impaired function in the cystinosis PT model. The reduced transport activity can likely be attributed to diminished MRP4 function as its gene expression was found to be 3-fold downregulated whereas *ABCG2* expression was not affected in the *CTNS*^{-/-} knockout model. Dysregulation of MRP4 in cystinosis has not been

reported earlier, although a decreased transporter expression was found in other diseases, including endotoxemia and prostate cancer, and polymorphisms in *ABCC4* may lead to hyperuricemia [46-49].

In this paper, we demonstrate how coiled microfiber channels favorably model the healthy and cystinotic PT. The next step would be to create a vascularized PT model by introducing endothelial cells to the system. Early attempts of vascularized PT models open a new venue to further study healthy and diseased PT function, crosstalk between epithelial and endothelial cells and solute transport across lumens [13]. Pilot experiments using our printing set-up show the feasibility of creating two channels within a single microfiber, allowing for both epithelial and endothelial cell compartments (**Supplementary Figure 6**). Because of the high cell-affinity of the hydrogel precursor, supporting tubular cells such as fibroblasts or immune cells can potentially be included in the present model by, for instance, direct seeding on top of the microfiber. Future studies are aimed to propose a more complete PT model, which entails advancing the printing, seeding and perfusion techniques, and ensuring different cell-lines seeded in separate channels. Fluid shear stress is known to be important for enhancement of cell functionality and cell morphology, which in the future could be studied in a perfusable set-up as proposed in **Supplementary Movie 1** [6,50-52]. Additionally, recent progress in differentiation methods for PTEC and endothelial cells from induced pluripotent stem cells (iPSC) enable the creation of personalized models [53-55].

5. Conclusions

Our coaxial printing system allows the robust and straightforward fabrication of coiled perfusable microfibers, which replicate the kidney proximal convoluted tubules. The microfibers offer a complex microenvironment in which the cells exhibit mature markers, such as functional transporters and polarized monolayers. Moreover, this model has proven to support healthy and cystinotic PT cell lines and allows for mechanistically studying tubulopathies. Furthermore, with the future aim to incorporate two separate channels with different cell types, a more sophisticated method that enables independent perfusion is needed. By including patient-derived cells of various diseases, this model could offer a broad platform for personalized medicine in the PT. Finally, with the possibility to perfuse the microfibers, we are paving the way for assessment of metabolite transport and drug testing, making this model one step closer to a structurally relevant PT model.

Funding

This work was supported by funding from The Dutch Kidney Foundation (17PHD16, AMG and 18KVP01, AMG, CS, YSZ), the Hofvijverkring Visiting Scientist Program (YSZ, AMG, CS), the Materials Driven Regeneration Young Talent Grant (AMG, CS), H2020 WIDESPREAD-05-2018-TWINNING Remodel (SMM; RM), the IMAGEN project which is co-funded by the PPP Allowance made available by Health-Holland, Top Sector Life Sciences & Health, to stimulate public-private partnerships (Implementation of Advancements in GENetic Kidney Disease, LSHM20009; ESG, RM), Utrecht Institute for Pharmaceutical Sciences (MGV) and Brigham Research Institute (YSZ).

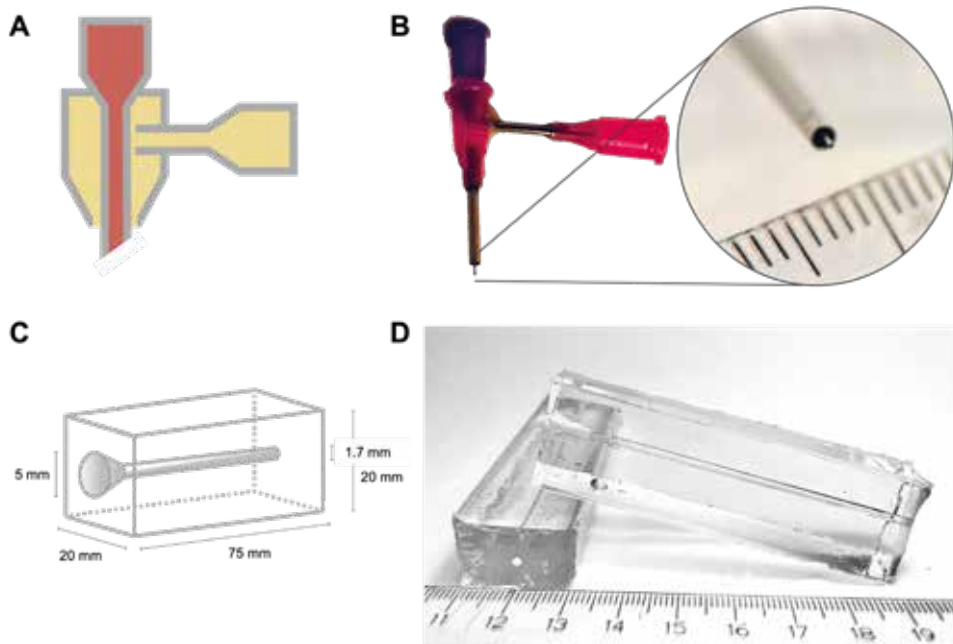
Acknowledgements

The authors would like to gratefully thank Koen Westphal for the training provided for the confocal microscopy.

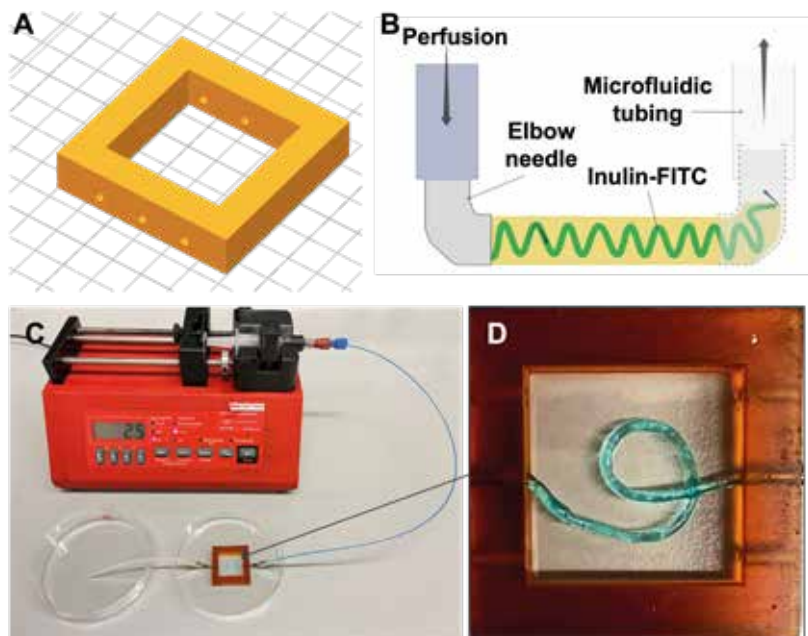
Supplementary Materials

Supplementary Movie 1. Microfiber perfusion in the chip

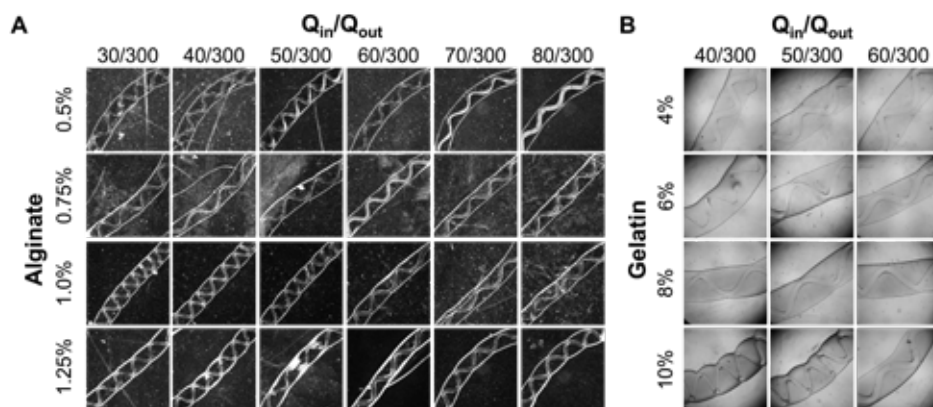
<https://iopscience.iop.org/article/10.1088/1758-5090/ac7895>



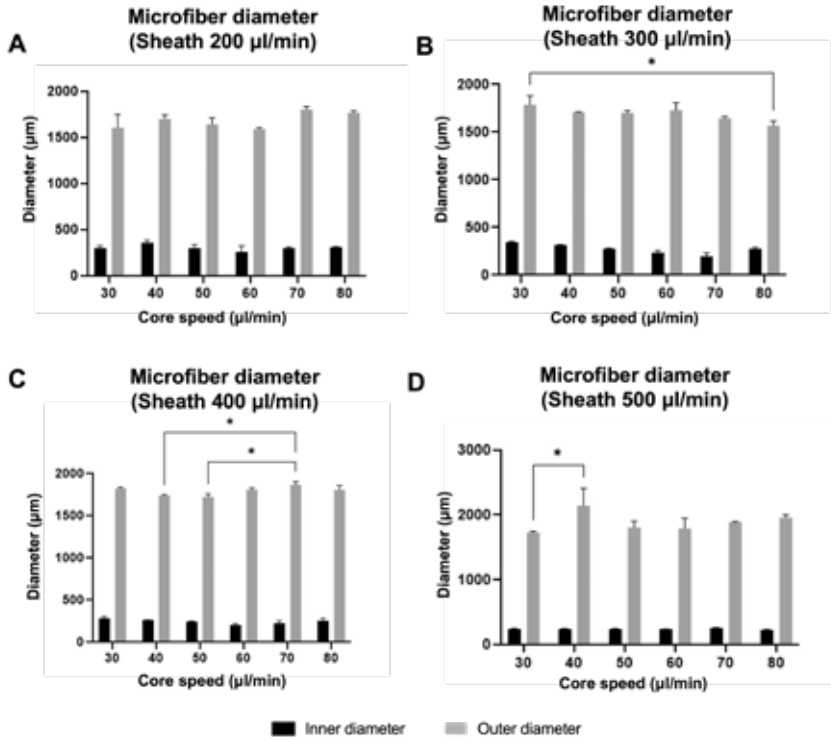
Supplementary Figure 1. Printing device components. A) Schematic of the coaxial needle, consisting of one 30G needle (core) which feeds CaCl_2 creating the hollow channel and two 18G needles; one to align the core and sheath and the second one to feed the biomaterial ink. B) Photograph of the coaxial needle. C) Schematic of the PDMS holder, with actual photograph in D). A PDMS block contains a 1.7-mm channel, wider in the upper part to allow the insertion of the co-axial needle. The optical clarity of the PDMS allows to see the microfiber during the printing process.



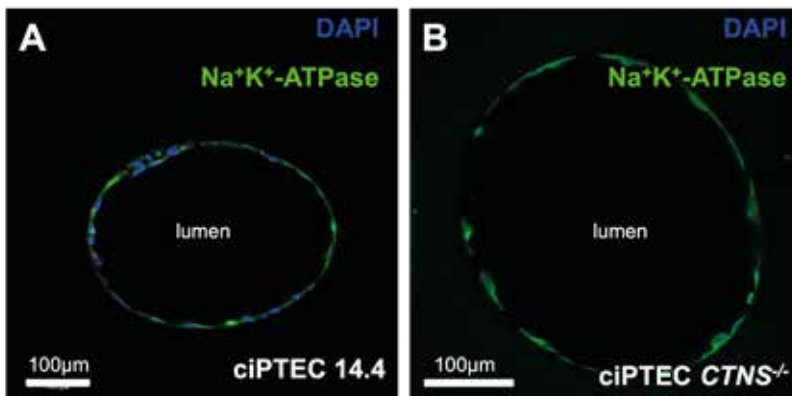
Supplementary Figure 2. Perfusable chip. A) CAD design. The chip consisted of an open square ($30 \times 30 \times 7$ -mm³ outer dimension, $20 \times 20 \times 7$ -mm³ inner dimension) with lateral openings (1.65-mm diameter) in which 18G syringe needles were inserted. B) The microfibers were fitted through the lateral openings and onto the needles creating a sealed environment and FITC-inulin was perfused. C) Complete set-up of the perfusion assay with a close-up of the chip (D).



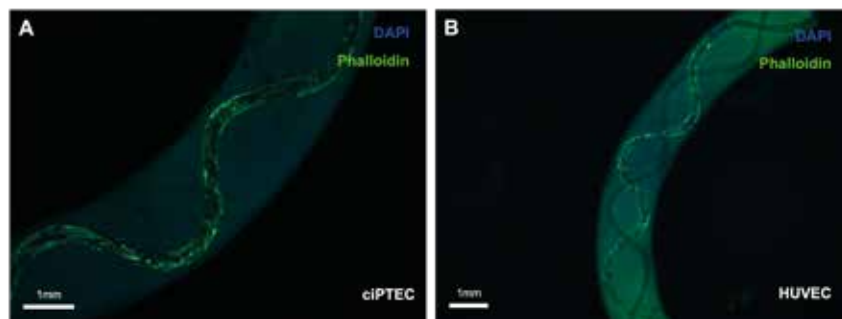
Supplementary Figure 3. Optimization of the biomaterial ink formulation and bioprinting parameters attending to the microfiber morphology. A) Alginate concentration was optimized for gelatin 8% (w/v). B) In parallel, gelatin concentration was optimized for alginate 1% (w/v). In both cases, different core flow rates were tested with a constant sheath flow of 300 μ l/min.



Supplementary Figure 4. Variation of microfiber diameter (μm) for different sheath and core feeding rates ($\mu\text{l}/\text{min}$). A-D) Correspond to increasing sheath flows ranging from 200 $\mu\text{l}/\text{min}$ to 500 $\mu\text{l}/\text{min}$. Only significant differences are shown. * p-value < 0.05.



Supplementary Figure 5. Cross-sections of hollow channel with confluent cell layers within the microfiber. Successful seeding of ciPTEC 14.4 (A) and ciPTEC $CTNS^{-/-}$ (B), stained for $\text{Na}^+\text{K}^+\text{-ATPase}$ (green) and DAPI (blue).



Supplementary Figure 6. Coaxial printing of two channels in a single microfiber. Successful seeding of ciPTEC 21.2 (A) and human umbilical vein endothelial cells (HUVECs) (B) separately.

Supplementary Table 1. Antibodies for immunocytochemistry.

Primary antibody	Secondary antibody
Mouse monoclonal anti- α -tubulin 1:200 T6793, Sigma-Aldrich	AlexaFluor 488 goat-anti-mouse 1:200 Invitrogen
Rabbit anti human Na-K-ATPase 1:250 Gifted kindly by Prof. Jan Koenderink, Radboudumc, The Netherlands	AlexaFluor 594 goat-anti-rabbit 1:200 Invitrogen
Goat monoclonal anti-collagen IV 1:50 1340-01, Southern Biotech	AlexaFluor 568 donkey-anti-goat 1:200 Invitrogen
AlexaFluor 488 phalloidin 1:1000 A22283, Thermo Fisher Scientific	N.a.
DAPI 1:1000 D9542, Sigma-Aldrich	N.a.

References

1. de Nicola, L. & Minutolo, R. Worldwide growing epidemic of CKD: fact or fiction? *Kidney International* vol. 90
2. Chevalier, R. L. The proximal tubule is the primary target of injury and progression of kidney disease: Role of the glomerulotubular junction. *Am J Physiol Renal Physiol* vol. 311
3. Nakhoul, N. & Batuman, V. Role of proximal tubules in the pathogenesis of kidney disease. *Contrib Nephrol* **169**, (2011).
4. Maharjan, S., Bonilla, D. & Zhang, Y. S. Strategies towards kidney tissue biofabrication. *Curr Opin Biomed Eng* **21**, 100362 (2022).
5. Valverde, M. G. *et al.* Biomimetic models of the glomerulus. *Nat Rev Nephrol* (2022).
6. Homan, K. A. *et al.* Bioprinting of 3D Convoluted Renal Proximal Tubules on Perfusable Chips. *Sci Rep* **6**, 1–13 (2016).
7. Xu, P. *et al.* Bioinspired Microfibers with Embedded Perfusable Helical Channels. *Adv Mater* **29**, (2017).
8. WareJoncas, Z. *et al.* Precision gene editing technology and applications in nephrology. *Nat Rev Nephrol* vol. 14 (2018).
9. Jamalpoor, A. *et al.* Cysteamine–bicalutamide combination therapy corrects proximal tubule phenotype in cystinosis. *EMBO Mol Med* **13**, (2021).
10. Sendino Garv, E., Masereeuw, R. & Janssen, M. J. Bioengineered Cystinotic Kidney Tubules Recapitulate a Nephropathic Phenotype. *Cells* **11**, 177 (2022).
11. van Genderen, A. M., Jansen, J., Cheng, C., Vermonden, T. & Masereeuw, R. Renal Tubular- and Vascular Basement Membranes and their Mimicry in Engineering Vascularized Kidney Tubules. *Adv Healthc Mat* vol. 7 1800529 (2018).
12. Addario, G. *et al.* Microfluidic bioprinting towards a renal in vitro model. *Bioprinting* **20**, (2020).
13. Lin, N. Y. C. *et al.* Renal reabsorption in 3D vascularized proximal tubule models. *Proc Natl Acad Sci U S A* **116**, 5399–5404 (2019).
14. King, S. M. *et al.* 3D proximal tubule tissues recapitulate key aspects of renal physiology to enable nephrotoxicity testing. *Front Physiol* **8**, (2017).
15. Moroni, L. *et al.* Biofabrication strategies for 3D in vitro models and regenerative medicine. *Nature Reviews Materials* vol. 3 (2018).
16. Ligon, S. C., Liska, R., Stampfl, J., Gurr, M. & Mlhaupt, R. Polymers for 3D Printing and Customized Additive Manufacturing. *Chemical Reviews* vol. 117 (2017).
17. Jia, L. *et al.* Microfluidic Fabrication of Biomimetic Helical Hydrogel Microfibers for Blood-Vessel-on-a-Chip Applications. *Adv Healthc Mater* **8**, (2019).
18. Wilmer, M. J. *et al.* Novel conditionally immortalized human proximal tubule cell line expressing functional influx and efflux transporters. *Cell Tissue Res* **339**, (2010).
19. Shihan, M. H., Novo, S. G., le Marchand, S. J., Wang, Y. & Duncan, M. K. A simple method for quantitating confocal fluorescent images. *Biochem Biophys Res* **25**, (2021).
20. Zhang, Y. S. & Khademhosseini, A. Advances in engineering hydrogels. *Science (1979)* **356**, (2017).
21. Chevtchik, N. v. *et al.* A bioartificial kidney device with polarized secretion of immune modulators. *J Tissue Eng Regen Med* **12**, 1670–1678 (2018).
22. Jansen, J. *et al.* Human proximal tubule epithelial cells cultured on hollow fibers: living membranes that actively transport organic cations. *Sci Rep* **5**, 16702 (2015).
23. Jamalpoor, A., Othman, A., Levchenko, E. N., Masereeuw, R. & Janssen, M. J. Molecular Mechanisms and Treatment Options of Nephropathic Cystinosis. *Trends Mol Med* **27**, 673–686 (2021).

24. Cherqui, S. & Courtoy, P. J. The renal Fanconi syndrome in cystinosis: pathogenic insights and therapeutic perspectives. *Nat Rev Nephrol* **13**, 115–131 (2017).
25. Caetano-Pinto, P. *et al.* Fluorescence-Based Transport Assays Revisited in a Human Renal Proximal Tubule Cell Line. *Mol Pharm* **13**, (2016).
26. Yu, S. M. *et al.* Substrate curvature affects the shape, orientation, and polarization of renal epithelial cells. *Acta Biomater* **77**, (2018).
27. Singh, N. K. *et al.* Three-dimensional cell-printing of advanced renal tubular tissue analogue. *Biomaterials* **232**, (2020).
28. Onoe, H. *et al.* Metre-long cell-laden microfibres exhibit tissue morphologies and functions. *Nat Mater* **12**, (2013).
29. Campbell, S. B. *et al.* Beyond Polydimethylsiloxane: Alternative Materials for Fabrication of Organ-on-a-Chip Devices and Microphysiological Systems. *ACS Biomater Sci Eng* **7**, 2880–2899 (2021).
30. Lee, K. Y. & Mooney, D. J. Hydrogels for tissue engineering. *Chemical Reviews* vol. 101 (2001).
31. Giuseppe, M. di *et al.* Mechanical behaviour of alginate-gelatin hydrogels for 3D bioprinting. *J Mech Behav Biomed Mater* **79**, (2018).
32. Li, Z. *et al.* Tuning Alginate-Gelatin Bioink Properties by Varying Solvent and Their Impact on Stem Cell Behavior. *Sci Rep* **8**, (2018).
33. Liu, W. *et al.* Coaxial extrusion bioprinting of 3D microfibrinous constructs with cell-favorable gelatin methacryloyl microenvironments. *Biofabrication* **10**, 024102 (2018).
34. Jiang, T. *et al.* Directing the Self-Assembly of Tumour Spheroids by Bioprinting Cellular Heterogeneous Models within Alginate/Gelatin Hydrogels. *Sci Rep* **7**, (2017).
35. Huang, S., Yao, B., Xie, J. & Fu, X. 3D bioprinted extracellular matrix mimics facilitate directed differentiation of epithelial progenitors for sweat gland regeneration. *Acta Biomater* **32**, (2016).
36. Yao, R., Zhang, R., Luan, J. & Lin, F. Alginate and alginate/gelatin microspheres for human adipose-derived stem cell encapsulation and differentiation. *Biofabrication* **4**, (2012).
37. Shengjie, L. *et al.* Direct fabrication of a hybrid cell/hydrogel construct by a double-nozzle assembling technology. *J Bioact Compat Polym* **24**, (2009).
38. Gao, T. *et al.* Optimization of gelatin-alginate composite bioink printability using rheological parameters: A systematic approach. *Biofabrication* **10**, (2018).
39. Agarwal, T. *et al.* Oxygen releasing materials: Towards addressing the hypoxia-related issues in tissue engineering. *Materials Science and Engineering C* vol. 122 111896 (2021).
40. van Genderen, A. M. *et al.* Topographic Guidance in Melt-Electrowritten Tubular Scaffolds Enhances Engineered Kidney Tubule Performance. *Front Bioeng Biotechnol* **8**, 1542 (2021).
41. Gaal, R. C., Miltenburg, R. P. R. S., Kurniawan, N. A., Bouten, C. V. C. & Dankers, P. Y. W. Renal Epithelial Cell Responses to Supramolecular Thermoplastic Elastomeric Concave and Convex Structures. *Adv Mater Interfaces* **8**, 2001490 (2021).
42. Shen, C., Meng, Q. & Zhang, G. Increased curvature of hollow fiber membranes could up-regulate differential functions of renal tubular cell layers. *Biotechnol Bioeng* **110**, 2173–2183 (2013).
43. Bäumner, S. & Weber, L. T. Nephropathic Cystinosis: Symptoms, Treatment, and Perspectives of a Systemic Disease. *Front Pediatr* **6**, (2018).
44. Peeters, K. *et al.* Role of P-glycoprotein expression and function in cystinotic renal proximal tubular cells. *Pharmaceutics* **3**, (2011).
45. Huls, M. *et al.* P-glycoprotein-deficient mice have proximal tubule dysfunction but are protected against ischemic renal injury. *Kidney Int* **72**, 1233–1241 (2007).

46. Russel, F., Koenderink, J. & Masereeuw, R. Multidrug resistance protein 4 (MRP4/ABCC4): a versatile efflux transporter for drugs and signalling molecules. *Trends Pharmacol Sci* **29**, 200–207 (2008).
47. Heemskerk, S. *et al.* Nitric oxide differentially regulates renal ATP-binding cassette transporters during endotoxemia. *Pflugers Arch* **454**, 321–334 (2007).
48. Montani, M. *et al.* Multidrug resistance protein 4 (MRP4) expression in prostate cancer is associated with androgen signaling and decreases with tumor progression. *Virchows Archiv* **462**, 437–443 (2013).
49. Wang, Z. *et al.* The effect of polymorphism of uric acid transporters on uric acid transport. *J Nephrol* **32**, 177–187 (2019).
50. Vriend, J. *et al.* Flow stimulates drug transport in a human kidney proximal tubule-on-a-chip independent of primary cilia. *Biochimica et Biophysica Acta (BBA) - General Subjects* **1864**, 129433 (2020).
51. Weber, E. J. *et al.* Development of a microphysiological model of human kidney proximal tubule function. *Kidney Int* **90**, 627–637 (2016).
52. Jang, K.-J. *et al.* Human kidney proximal tubule-on-a-chip for drug transport and nephrotoxicity assessment. *Integrative Biology* **5**, 1119–1129 (2013).
53. Chandrasekaran, V. *et al.* Generation and characterization of iPSC-derived renal proximal tubule-like cells with extended stability. *Sci Rep* **11**, 11575 (2021).
54. Koning, M., van den Berg, C. W. & Rabelink, T. J. Stem cell-derived kidney organoids: engineering the vasculature. *CMLS* **77**, 2257–2273 (2020).
55. Takasato, M., Er, P.X., Chiu, H. S. & Little, M. H. Generation of kidney organoids from human pluripotent stem cells. *Nat Protoc* **11**, 1681–1692 (2016).

J. Gong^{^1,2,3}, C. C. L. Schuurmans^{^1,4,5}, A. M. van Genderen^{1,5}, X. Cao¹, W. Li¹, F. Cheng¹, J. J. He¹, A. López¹, V. Huerta¹, J. Manríquez¹, R. Li⁵, H. Li¹, C. Delavaux¹, S. Sebastian¹, P. E. Capendale^{1,4,5}, H. Wang^{2,3}, J. Xie⁶, M. Yu^{2,3}, R. Masereeuw⁵, T. Vermonden^{4,*}, and Y. S. Zhang^{1,*}

1 Division of Engineering in Medicine, Department of Medicine, Brigham and Women's Hospital, Harvard Medical School, Cambridge, MA 02139, USA.

2 The Affiliated Stomatology Hospital, Zhejiang University School of Medicine, Hangzhou 310003, P.R. China.

3 Key Laboratory of Oral Biomedical Research of Zhejiang Province, Hangzhou 310003, P.R. China.

4 Department of Pharmaceutics, Utrecht Institute for Pharmaceutical Sciences (UIPS), Science for Life, Utrecht University, 3508 TB Utrecht, The Netherlands.

5 Department of Pharmacology, Utrecht Institute for Pharmaceutical Sciences (UIPS), Science for Life, Utrecht University, 3508 TB Utrecht, The Netherlands.

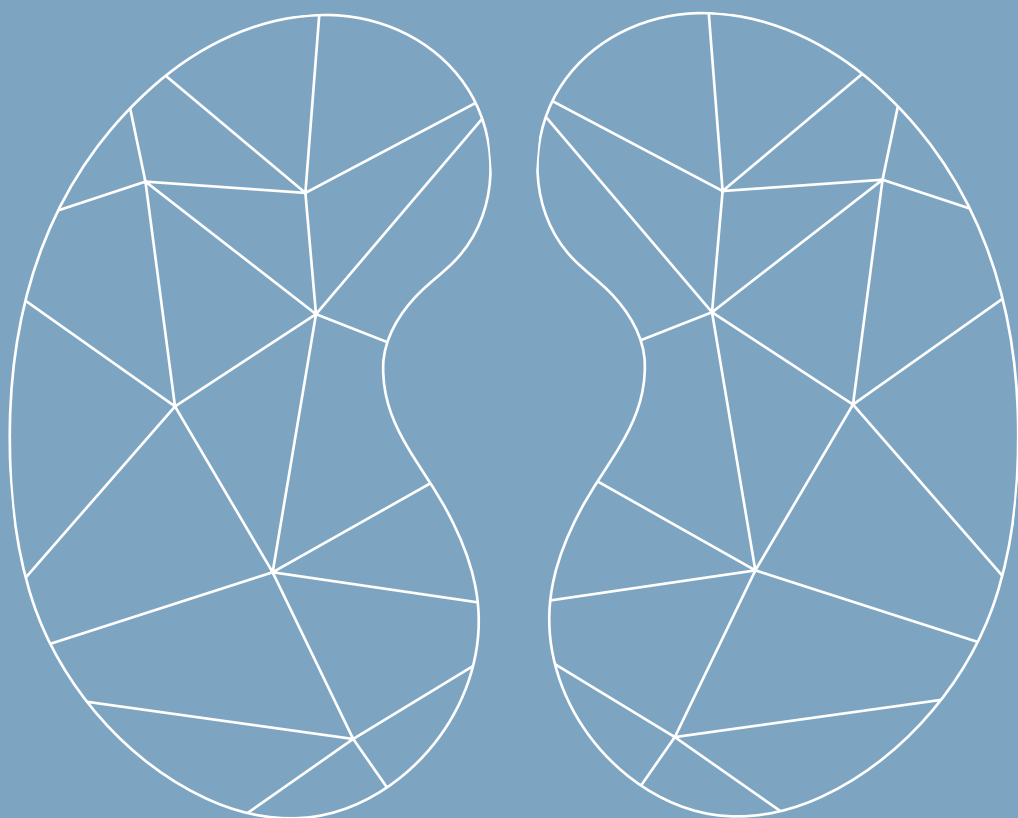
6 Department of Surgery-Transplant and Holland Regenerative Medicine Program, University of Nebraska Medical Center, Omaha, NE 68198, USA.

[^] These authors contributed equally to this work

^{*} Corresponding authors

CHAPTER 4

COMPLEXATION- INDUCED RESOLUTION ENHANCEMENT OF 3D-PRINTED HYDROGEL CONSTRUCTS



Abstract

Three-dimensional (3D) hydrogel printing enables production of volumetric architectures containing desired structures using programmed automation processes. Our study reports a unique method of resolution enhancement purely relying on post-printing treatment of hydrogel constructs. By immersing a 3D-printed patterned hydrogel consisting of a hydrophilic polyionic polymer network in a solution of polyions of the opposite net charge, shrinking can rapidly occur resulting in various degrees of reduced dimensions comparing to the original pattern. This phenomenon, caused by complex coacervation and water expulsion, enables us to reduce linear dimensions of printed constructs while maintaining cytocompatible conditions in a cell type-dependent manner. We anticipate our shrinking printing technology to find widespread applications in promoting the current 3D printing capacities for generating higher-resolution hydrogel-based structures without necessarily having to involve complex hardware upgrades or other printing parameter alterations.

Introduction

Three-dimensional (3D) printing has become a collection of enabling biofabrication technologies to generate volumetric structures featuring high complexity through robotically controlled dispensing or stabilization processes [1,2]. The programmed fabrication further makes the procedures highly reproducible. As such, 3D printing is finding widespread applications in biomedicine including, but not limited to, tissue engineering, microphysiological systems, and biomedical devices [3]. Nevertheless, existing printing strategies all have their minimally producible resolutions, which are factors of multiplexed parameters, such as the printer hardware and ink properties [4]. For example, in extrusion printing using hydrogels as inks, the resolutions are typically sub-millimeter for the dispensed microfibers [4]. The same holds true for microfluidic coaxial printing, where the diameters of the created hollow microfibers usually fall in the range of a couple hundred micrometers or larger [4,5]. Although some other printing strategies, such as those based on light (e.g., two-photon lithography) can achieve varying degrees of higher resolutions [6], their instrumentation is usually complicated limiting the broader adoption for general use.

To this end, efforts have conventionally been focused on improving the printer hardware or ink properties. Examples in extrusion printing include using smaller nozzles or using inks of high viscosity values, both of which inevitably elevate the need for much higher forces during the dispensing processes, inducing significantly increased shear stresses on the encapsulated cells. Even though, the resolution improvements are still limited. Meanwhile, the progress in printer hardware or tuning the ink formulations may not always be straightforward, leaving these methods still impractical for some applications.

More recently, an implosion fabrication method was proposed [7], in which a swollen hydrogel matrix was used to photopattern metals, semiconductors, and biomolecules, followed by acid-driven shrinking to achieve nano-sized structures. While efficient for two-photon lithography, this method is not amenable to most other 3D printing modalities due to the necessity of a preexisting, swollen hydrogel matrix to allow anchoring points for secondary biomolecules or inorganic species subsequently patterned in the volumetric space. Further, such shrinking is unstable and would revert once the stimulus is removed. Finally, the harsh implosion conditions (i.e., low pH) utilized are largely incompatible with living cell-based applications.

Here, we propose a strategy of complexation-induced resolution enhancement in 3D printing that we term as shrinking printing, through post-treatment of the printed structures, for

resolution improvement without requiring changing any of the printer hardware or much of the ink compositions. In particular, we select inks that are anionic, such as those based on commonly used hyaluronic acid methacrylate (HAMA) [8], gelatin methacryloyl (GelMA) [9], and alginate [10]. Following standard printing procedures, we subject the HAMA-, GelMA-, or alginate-based hydrogel constructs to immersion in a polycationic chitosan solution. Through charge complexation and subsequent expulsion of water from the gels, these printed constructs are found to reduce in their linear dimensions in various degrees. We conduct our proof-of-concept studies with several 3D printing techniques, including direct extrusion printing, sacrificial printing, and microfluidic hollow fiber printing, where successful shrinking is observed in all cases. Additionally, we prove the wide applicability of our method by demonstrating shrinking of printed polycationic chitosan-based hydrogel constructs, with polyanionic alginate. We finally demonstrate that selected types of cells embedded in the printed hydrogel matrices remain viable upon successive shrinking in contrast to a single, longer shrinking procedure, further revealing the potential applications of our shrinking printing method in the presence of living cells. We anticipate wide adoption of this technology in future printing of acellular or cellularized structures with further optimizations.

2. Results

2.1 Shrinking behaviors of polyionic hydrogels

The carboxyl groups present in HAMA render the hydrogel negatively charged under physiological conditions. When a HAMA hydrogel is placed in the presence of polycations of high charge densities, such as chitosan, a type of glucosamine featuring reasonable biocompatibility and densely cationic nature due to the abundantly available amino groups [11], charge compensation occurs leading to expulsion of water and eventual size reduction of the HAMA hydrogel (**Figure 1a and Supplementary Figure 1**). Indeed, this phenomenon was previously observed for microgels [12]. We also recently demonstrated, that when a solution of positively charged lysozyme was introduced to microfluidics-fabricated HAMA microspheres, the size of these microspheres was decreased due to a mechanism akin to complex coacervation, facilitating their use in drug delivery [13].

To prove the concept, we first fabricated cylindrical HAMA hydrogels (1.0 w/v%, $D = 6$ mm, $H = 2$ mm, ~ 56.5 μL in volume). When immersed in 2.0 w/v% chitosan (M_w : 50–190 kDa) dissolved in 1.0 v/v% acetic acid aqueous solution for 24 h, the hydrogels shrank $\sim 60\%$ in height and diameter, leading to a reduction to 21% in volume as compared to the original

constructs (**Figure 1b,c**). The changes of concentrations of HAMA hydrogels before and after complete shrinkage in chitosan (M_w : 700–800 kDa) were subsequently evaluated. Our calculations revealed that the concentrations increased from the initial 0.5–2.5 w/v% to 7.9–12.1 w/v% after shrinking (**Supplementary Figure 2**). Scanning electron microscopy (SEM) images of the HAMA structures before and after shrinking in chitosan (M_w : 700–800 kDa) are illustrated in **Supplementary Figure 3**. Although the concentrations of HAMA in the shrunken hydrogels were much higher than those of the initial constructs (**Supplementary Figure 2**), water was still the main constituent maintaining their hydrogel nature for various relevant applications.

Considering that the molecular weight of chitosan might affect the shrinkage extent, we compared chitosan of different molecular weights (low-molecular weight, LM_w : 15 kDa; medium-molecular weight, MM_w : 50–190 kDa; high-molecular weight, HM_w : 700–800 kDa). All chitosan types had a similar degree of deacetylation (85%). As shown in **Figure 1d**, the HAMA hydrogels (1.0 w/v%) at pH = 1.0 shrank to $19.0 \pm 0.2\%$ of their original size, while the ones in 2.0 w/v% LM_w chitosan, MM_w chitosan, and HM_w chitosan in 1.0 v/v% acetic acid aqueous solutions (pH = 4.7) shrank to 28.9 ± 1.1 , 21.6 ± 0.9 , and $11.0 \pm 0.7\%$, respectively. In addition to the molecular weight, the charge density of the shrinking agent might be an important factor affecting the shrinkage degree. Therefore, we compared three types of chitosan with different degrees of deacetylation (72.5%, 77.8%, and 94.6%) but similar molecular weights (50–250 kDa). As shown in **Supplementary Figure 4**, the HAMA hydrogels (1.0 w/v%) in 1.0 v/v% acetic acid aqueous solution (pH = 4.7) shrank to $55.1 \pm 1.5\%$ of their original size, and the ones in 2.0 w/v% chitosan in 1.0 v/v% acetic acid aqueous solutions shrank to 23.5 ± 1.0 , 18.5 ± 0.8 , and $12.6 \pm 0.7\%$ for chitosan with different degrees of deacetylation (72.5%, 77.8%, and 94.6%), respectively. Moreover, the shrinkage ratio with quaternary ammonium salt chitosan (Q. chitosan, M_w : 50–100 kDa, 90% of deacetylation degree, 95% of quaternization degree) was observed to be the highest among all chitosan types, at $9.7 \pm 0.4\%$ (**Figure 1d**).

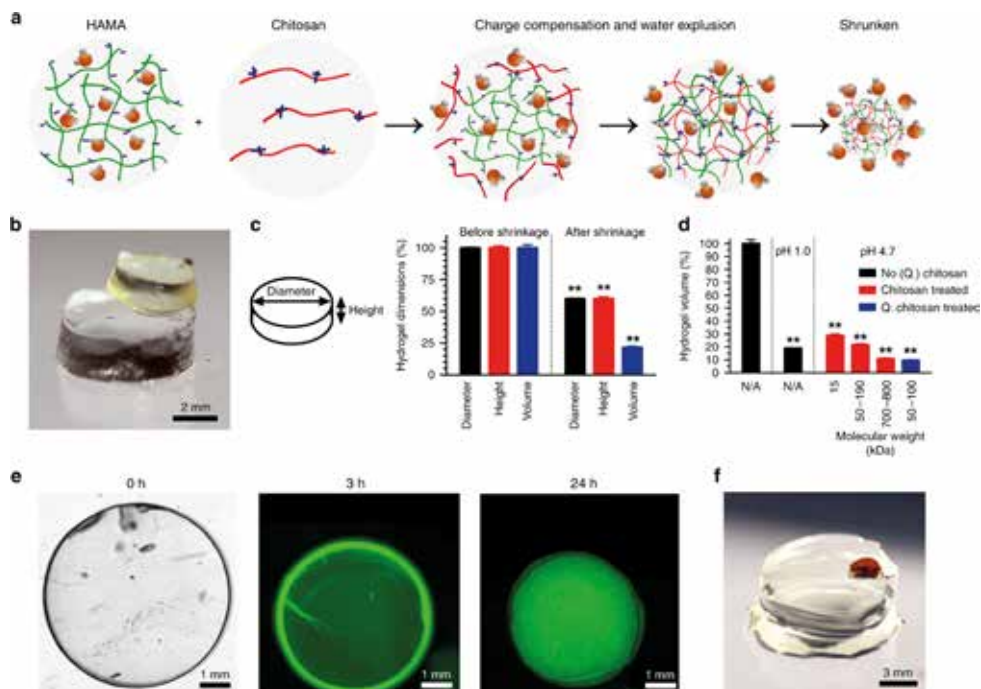


Figure 1. The general mechanism of complexation-induced hydrogel shrinking. **a** Schematics showing the shrinking effect based on charge compensation. **b** Photograph showing size change of fabricated HAMA hydrogel (1.0 w/v%) before (lower) and after (upper) shrinking in 2.0 w/v% M_w chitosan dissolved in 1.0 v/v% acetic acid aqueous solution. **c** Schematic representation of a HAMA hydrogel disc together with the dimensions and corresponding quantitative analyses showing the dimensions and volume changes before and after shrinking in 2.0 w/v% M_w chitosan dissolved in 1.0 v/v% acetic acid aqueous solution. **d** Corresponding quantitative analyses showing the shrinking of HAMA hydrogels in perchloric acid solution (pH = 1.0) or in 1.0 v/v% acetic acid aqueous solutions (pH = 4.7) with 2.0 w/v% of chitosan of different molecular weights and types. **e** Confocal images showing the diffusion of FITC-Q chitosan solution in PBS into a 2.0 w/v% HAMA hydrogel at 3 and 24 h of shrinking. The bright-field image at 0 h serves as the size reference of the initial hydrogel. **f** Photograph showing size change of H_{Mw} chitosan hydrogels (2.0 w/v%), where the lower one was swollen in 1.0 v/v% acetic acid aqueous solution and the upper one was shrunken in 2.0 w/v% alginate in 1.0 v/v% acetic acid aqueous solution. ** $P < 0.01$; one-way ANOVA (c, d, compared with the values of corresponding as-prepared samples); mean \pm s.d. (n = 3).

These results indicated that both the average polymer chain length and the average charge per monomer of the chosen cationic polymer, i.e., chitosan, influenced the extent of the HAMA hydrogels. The strength of electrostatic complexation between two oppositely charged polymers is known to be dependent on the chain length and charge density (i.e., amount of monomers/charges in a single polymer chain) [14,15]. These observations coupled to the fact that shrinking with polycations resulted in lower-volume (i.e., more heavily

dehydrated) hydro- gels than when compared to a similar hydrogel incubated in a buffered pH 1.0 solution bring us to the conclusion that, the hydrogel shrinks due to the formation of a complex coacervate- like structure between the oppositely charged hydrophilic polymer network and the free polymer. Dehydration is commonly seen in both complex coacervation and precipitation in an electrostatic strength-dependent manner [14,15]. The characteristics of all types of chitosan used in this set of experiments and the shrinkage ratios of HAMA hydrogels (1.0 w/v%) are listed in **Supplementary Table 1**. When the deacetylation degree and thus the average positive charge per monomer remained constant (i.e., 85% of deacetylation degree, +1 per 271.8 Da of charge density), the higher molecular weight of chitosan was, the higher degree of shrinking was observed. The average charge density of every chitosan monomer would also be of great importance; the higher the charge density (+1 per 328.8 Da, +1 per 298.7 Da, +1 per 238.3 Da, for different degrees of deacetylation [72.5%, 77.8%, 94.6%] of chitosan, respectively), the higher the shrinkage ratio.

Moreover, we made two types of bulk HAMA hydrogels (2.0 w/v%) of similar aspect ratios to study effects of the initial hydrogel volume on hydrogel shrinking (cylinders, $D = 6$ mm, $H = 2$ mm, ~ 56.5 μL , or $D = 8$ mm, $H = 3.4$ mm, ~ 170.9 μL). As shown in **Supplementary Figure 5a,b**, the thicker structures took longer to shrink, but shrank to a similar degree as the thinner structures did (**Supplementary Fig. 5c**). To investigate the shrinking process, we visualized the polycation diffusion using fluorescein isothiocyanate-labeled Q. chitosan (FITC-Q. chitosan), by incubating 2.0 w/v% HAMA cylinders in a 2.0 w/v% FITC-Q. chitosan solution, and after 3 and 24 h, observations were made with confocal microscopy (**Figure 1e**). The results revealed that FITC-Q. chitosan diffused into the entire structure and complexed with the polyanion (HAMA) already at 3 h, yet with most of the FITC-Q. chitosan still located at the periphery. However, after complete shrinking at 24 h, we observed a homogeneous distribution of FITC-Q. chitosan throughout the cylinder, indicating that the shrinking agent fully penetrated the hydrogel matrix, and that the relatively low weight percentage of HAMA used for forming the hydrogel did not hamper the diffusion of large polymer chains of chitosan into the matrix. Subsequent release of FITC-Q. chitosan from the fully shrunken hydrogels was quantified in phosphate- buffered saline (PBS) and followed for 21 days (**Supplementary Figure 6a,b**). Only in the first few days, release of FITC-Q. chitosan was observed, which can be attributed to the loss of FITC-Q. chitosan loosely bound (non-ionically) to the surfaces of the hydrogels that was washed off rapidly during the incubation. After the first few days, no further release was observed. The hydrogel volumes did not change over time, indicating that the shrunken constructs remained stable without further significant release of chitosan (**Supplementary Figure 6c**).

Since alginate is one of the most commonly used hydrogels in 3D printing, we investigated whether our shrinking process was also compatible with alginate hydrogels (2.0 w/v%). After physical crosslinking in a CaCl_2 solution (0.3 M), the alginate cylinders ($D = 6$ mm, $H = 2$ mm, ~ 56.5 μL) were obtained and washed in de-ionized water, or shrunken in 2.0 w/v% of chitosan of different molecular weights and types, as shown in **Supplementary Figure 7**. The alginate hydrogels in water swelled to $105.9 \pm 2.5\%$, and when incubated in 1.0 v/v% acetic acid aqueous solution, the cylinders shrank to $51.2 \pm 1.4\%$ of their original volume, whereas the ones in LM_w chitosan, MM_w chitosan, and HM_w chitosan solutions shrank to $37.6 \pm 1.2\%$, $28.9 \pm 1.1\%$, and $27.7 \pm 1.0\%$, respectively. Moreover, the shrinkage degree in Q. chitosan was validated at $25.4 \pm 3.9\%$, similar to that shrunken by the HM_w chitosan. These results indicated that alginate, as a negatively charged polymer similar to HAMA, could also shrink in a polycationic solution using our complexation-based technique.

To investigate whether this approach was generally applicable to polycationic inks as well, we prepared chitosan-based cylindrical hydrogels for further study. HM_w chitosan hydrogel (2.0 w/v%) cylinders ($D = 6$ mm, $H = 2$ mm, ~ 56.5 μL) cross-linked with different concentrations of glutaraldehyde were incubated either in 1.0 v/v% acetic acid aqueous solution or 2.0 w/v% alginate in 1.0 v/v% acetic acid aqueous solution. As shown in **Supplementary Figure 8**, the chitosan hydrogels swelled in 1.0 v/v% acetic acid aqueous solution and shrank when incubated in the presence of alginate, validating that this approach is applicable to hydrogels formed by polycationic polymers as well. **Figure 1f** visually shows the swollen chitosan hydrogel (2.0 w/v%) in 1.0 v/v% acetic acid aqueous solution (lower construct) and the shrunken hydrogel (upper construct) in 2.0 w/v% alginate in 1.0 v/v% acetic acid aqueous solution when the molar ratio of glutaraldehyde to chitosan chains was 5:1. With increasing amounts of glutaraldehyde, lower swelling in acetic acid solution and lower shrinking in alginate solution were observed, which can be ascribed to the removal of the positive charges in chitosan by the reaction of the primary amines with glutaraldehyde.

In general, positively charged hydrogels are less frequently utilized and are typically adopted for situations where their charge is key for the application (a feature that would be negated by our complexation-based technique). Moreover, cationic hydrogels in general are more cytotoxic [16] and therefore less commonly used for applications intended to grow cells in before charge neutralization. Therefore, we intended to focus more on the shrinking abilities of negatively charged hydrogels (i.e., HAMA, GelMA, and alginate), with a brief demonstration also on the shrinking of positively charged hydrogels (chitosan).

2.2 Shrinking behaviors of extrusion-printed structures

Here, we sought to demonstrate that the same process might be adapted to the printed hydrogel structures to achieve resolution improvement otherwise only possible through changes in printing parameters (such as nozzle size, pressure, and/or nozzle moving speed). We first evaluated the printability of HAMA inks (0.5–2.5 w/v%) in extrusion printing by depositing hexagonal patterns (**Figure 2a**). Our printability mapping (**Figure 2b, c**) suggested an optimal HAMA ink formulation of 2.0 w/v%, which was chosen for the subsequent experiments using extrusion printing. Young's moduli of the resulting HAMA hydrogels after photocrosslinking were evaluated (**Supplementary Figure 9a**), where the values ranged from 1.7 ± 0.2 to 24.1 ± 3.3 kPa. These values are in accordance with those reported in literature for HAMA hydrogels [17].

We immersed our printed structures in 2.0 w/v% HM_w chitosan dissolved in 1.0 v/v% acetic acid in deionized water (pH = 4.7). It was observed that the hexagonal HAMA hydrogels shrank to smaller sizes as a function of time (**Supplementary Movie 1**). As illustrated in **Figure 2d–f**, the distance (side-to-side) of the hexagons was reduced from 893 ± 377 to 3674 ± 163 μm in 24 h, or 41.1% of the original size (**Figure 2e**). The thickness of the fibers in the hexagons also decreased from 1295 ± 113 to 424 ± 68 μm, or 32.7% of the original size (**Figure 2f**). The Young's modulus of HAMA increased from 15.9 ± 1.8 kPa to 24.3 ± 3.0 kPa in the 2.0 w/v% HAMA group (**Supplementary Figure 9a**). Shrinking of the HAMA hydrogels was also validated by measuring their volume changes, where the 2.0 w/v% HAMA hydrogel shrank to ~20% of the original volume after chitosan complexation for 24 h (**Supplementary Figure 9b**).

We subsequently investigated how different concentrations of HM_w chitosan (0.5, 1.0, 1.5, 2.0, 3.0, or 5.0 w/v%) dissolved in 1.0 v/v% acetic acid affected the shrinking of the printed HAMA (2.0 w/v%) structures. As revealed in **Figure 2g–i** and **Supplementary Figure 10**, at 2 h of shrinkage, the side-to-side distances of the hexagons decreased to a range between 4144 ± 98 μm (3.0 w/v% of HM_w chitosan) and 5664 ± 91 μm (0.5 w/v% of HM_w chitosan), or 47.6–65.1% of the original size. After 24 h of immersion, the side-to-side distance of the hexagons was further reduced to ~3700 μm, while the thickness of the fibers shrank from the initial 1350 μm to 360 μm. Distinct from those at 2 h of shrinking, neither the distance of the hexagons nor the thickness of the fibers indicated significant differences among the concentrations of HM_w chitosan, suggesting that the higher concentration of chitosan led to faster shrinking but the final gel volume could be reached in 24 h or earlier. It should be noted though, that the printed structures in the 5.0 w/v% HM_w chitosan group became irregular likely due to the high viscosity of the chitosan solution at this concentration that prevented

uniform shrinking of the patterns. Since the fidelity of shrinking is important for retaining the printed structures, here we visualized the distortions of the 2-h shrinking and 24-h shrinking images by superimposing the 2-h shrinking images on top of the corresponding 24-h shrinking images [18]. As shown in **Figure 2j**, the distortions (indicated by background grids) were deemed to be within an acceptable range, indicating that only little deformation of the total structure had taken place during the shrinking.

Considering that chitosan was dissolved in 1.0 v/v% acetic acid at a pH value of 4.7, we subsequently evaluated the possibility of utilizing Q₂ chitosan, which easily dissolves in deionized water and aqueous solutions at physiological pH [19], as also used for shrinking non-printed hydrogel constructs above. As a control, we initially dissolved Q₂ chitosan in 1.0 v/v% acetic acid aqueous solution and investigated the shrinking behavior of the printed 2.0 w/v% HAMA structures (**Supplementary Figures 11a, 12**). The results were similar to those obtained with regular HM_w chitosan solutions. The shrinking rate was proportional to the concentration of Q₂ chitosan and reached equilibrium at or before 24 h. Remarkably, the hexagons in 5.0 w/v% Q₂ chitosan were able to retain their shape and shrank to $40.8 \pm 1.8\%$ in side-to-side distance and $24.1 \pm 2.6\%$ in thickness as compared to the original dimensions, since the viscosity of Q₂ chitosan solution was much lower than that of the chitosan solution at this concentration, which facilitated uniform shrinking. When we shifted to the use of Q₂ chitosan in de-ionized water, the rate of shrinking seemed to become slightly slower as compared to using Q₂ chitosan or HM_w chitosan in acetic acid aqueous solution, where the side-to-side distance was reduced to 62.0–99.3% and the thickness to 52.1–99.5% of the original constructs after 2 h of incubation (**Supplementary Figures 13a and 14**). Nevertheless, when the time was extended to 24 h, hydrogel sizes shrank down to 41.2–56.4% for the side-to-side distances and 33.0–45.9% for the thicknesses, both similar to the degrees of shrinking with HM_w chitosan or Q₂ chitosan in 1.0 v/v% acetic acid aqueous solution. Moreover, the distortions of the 2-h shrinking and 24-h shrinking images were also visualized (**Supplementary Figures. 11b and 13b**).

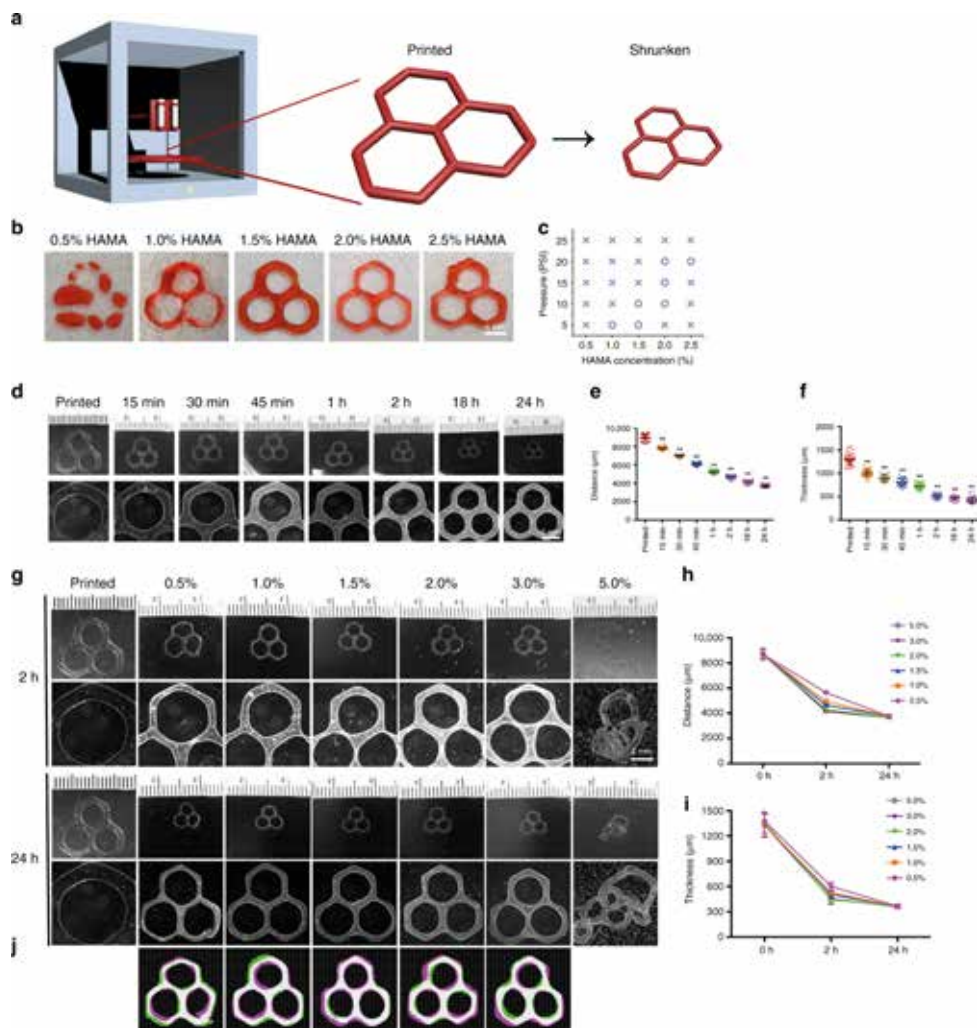


Figure 2. Direct extrusion printing of HAMA constructs and their shrinking behaviors. **a** Schematics showing the concept of shrinking printing, where a printed hydrogel structure is post-treated to reduce its size and achieve higher resolution. **b, c** Printability mapping of HAMA inks at different concentrations and extrusion pressures. **d** Photographs (upper) and micrographs (lower) showing size changes of printed HAMA hexagons (2.0 w/v%) immersed in 2.0 w/v% HM_w chitosan dissolved in 1.0 v/v% acetic acid aqueous solution during the 24h shrinking process. **e, f** Corresponding quantitative analyses of size changes of the printed HAMA hexagons (2.0 w/v%), include **e** side-to-side distance and **f** thickness, during the 24h shrinking process. **g** Photographs (upper) and micrographs (lower) showing size changes of printed HAMA hexagons (2.0 w/v%) at 2 h and 24 h of shrinking in different concentrations of HM_w chitosan (0.5–5.0 w/v%) dissolved in 1.0 v/v% acetic acid aqueous solution, **h, i** Corresponding quantitative analyses of size changes in **h** side-to-side distance and **i** thickness. **j** Vector-field maps comparing the 24-h shrinking images (magenta) to the corresponding 2-h shrinking images (green) by a B-spline-based non-rigid registration algorithm, where the overlaps appear in white and the grids show local distortions. Note that the 2-h shrinking images have been rescaled to match the sizes of the 24-h shrinking images to enable comparisons. $^{**}P < 0.01$; one-way ANOVA (**e, f**, compared with the values of corresponding as-prepared samples); mean \pm s.d. (**e, f**, $n = 40$; **h, i**, $n = 10$).

To illustrate that our method truly works in all three spatial dimensions, we further printed a HAMA (2.0 w/v%) pyramid frame in a gelatin supporting matrix (1.5 w/v%) followed by UV crosslinking (**Supplementary Figure 15a**) [8]. After photocrosslinking of HAMA, the gelatin was heated and stepwise replaced with water. Finally, the 3D-printed pyramidal frame structure was incubated in 1.0 w/v% HM_w chitosan in 1.0 v/v% acetic acid aqueous solution for 24 h to achieve complete shrinking. As shown in **Supplementary Figure 15b, c**, the printed HAMA pyramid shrank uniformly in every direction (length, height, thickness), to about 60% in linear dimensions those of the original constructs.

To eliminate the effect caused by changes in pH, we further incubated the samples in aqueous solutions of HM_w chitosan and Q₂ chitosan (both dissolved at 2.0 w/v% in 1.0 v/v% acetic acid aqueous solution), or an aqueous solution of pH = 1.0 (adjusted using perchloric acid without chitosan). The volume of the HAMA hydrogel in perchloric acid was still significantly larger than those incubated in the chitosan solutions (**Supplementary Figure 16a**), verifying that the mechanism of shrinking with chitosan was not purely related to neutralizing the negative charges on the HAMA molecules. The Young's moduli post-shrinking as expected, showed an opposite trend with their volumes (**Supplementary Figure 16b**). We next evaluated the shrinking behavior of the printed HAMA structures (2.0 w/v%) in acetic acid aqueous solutions of different pH values. During the experiments, we found that the sizes of the printed HAMA hexagons shrank in acetic acid solutions of different pH values, where the lower the pH, the smaller the size, which yet were still larger than those shrunken with 2.0 w/v% HM_w chitosan in 1.0 v/v% acetic acid aqueous solution (**Supplementary Figure 17**). The pH-induced shrinking was reversible, initially causing structures incubated in acid to shrink but recovering to the original printed size when subsequently placed into de-ionized water (**Supplementary Figure 18**). In contrast, the chitosan-driven shrinking was stable during the investigated time frame attributed to the complexation process, consistent with our stability analysis on the bulk HAMA constructs (**Supplementary Figure 6**). Therefore, the neutralization of charges by changes in pH could lead to a certain degree of shrinkage, but charge compensation by polyelectrolyte complexation of the polyanionic polymers and the polycationic hydrogels resulted in irreversible shrinkage in an electrostatic binding strength-dependent manner (also see **Figure 1d**).

Interestingly, we found that the printed HAMA structures could shrink in cell culture medium as well. When subjecting the HAMA hydrogels to Q₂ chitosan dissolved in Dulbecco's modified Eagle medium (DMEM, 2.0 w/v%), the constructs shrank to approximately half of their thickness and about 75% in size-to-size distance (**Supplementary Figure 19**), although

the shrinking rate was slower compared to those in acid or in water. This observation could be attributed to the higher ionic strength of DMEM (~170 mM) as compared to the 0–20 mM found in de-ionized water, where ionic strength of the medium dampens electrostatic interactions between positive and negative moieties. Nevertheless, our results indicated that shrinking of the printed constructs in the presence of cells is possible.

Printed alginate hexagons (2.0 w/v%) were physically cross-linked by 0.3-M CaCl_2 (**Supplementary Figure 20**), after which they were shrunken in 1.0 v/v% acetic acid aqueous solution, or in 2.0 w/v% chitosan of different molecular weights and types in 1.0 v/v% acetic acid aqueous solution. The corresponding quantitative analyses of size changes of the printed alginate hexagons are shown in **Supplementary Figure 21a** for side-to-side distances and in **Supplementary Figure 21b** for thicknesses.

Finally, we printed chitosan hexagons (2.5 w/v%), which were subsequently crosslinked by glutaraldehyde (800 μM). As expected, the printed chitosan hexagons shrank in 2.0 w/v% alginate in 1.0 v/v% acetic acid aqueous solution (**Supplementary Figure 22a**), where the thickness and side-to-side distance changes were further reflected upon in **Supplementary Figure 22b**.

2.3 Shrinking behaviors of sacrificially printed microchannel- embedded constructs

Once we validated the hypothesis that electrostatic complexation could enable efficient size reduction of extrusion-printed HAMA patterns, we explored if the same concept can be applied to other commonly used 3D printing strategies. Again, we aimed to achieve improved resolution without needing to adjust the printing hardware or parameters. Among all approaches, sacrificial printing is a frequently used method to generate hollow, perfusable microchannels within hydrogel constructs. These microchannels would serve as bio-mimetic cannular structures to emulate human tissues, such as the vasculature [20] or the proximal tubules found in kidneys [21]. A Pluronic F127 solution is thermosensitive, meaning that it flows at low temperatures but forms a solid hydrogel at elevated temperatures. As such, it has been frequently used as a fugitive ink, serving as a template during printing that can later be selectively removed from the hydrogel matrices to create hollow microchannels [21,22] (**Figure 3a**). We produced HAMA hydrogel constructs with a channel (2.0 w/v%) using Pluronic-based sacrificial printing (**Figure 3b**). Measuring the diameter of the microchannels after removing the Pluronic fugitive template showed a value of $355 \pm 21 \mu\text{m}$, in accordance with those previously fabricated under similar conditions [21,22]. When the entire constructs

were immersed in 2.0 w/v% HM_w chitosan in 1.0 v/v% acetic acid aqueous solution for 24 h, a gel size reduction was observed with associated decrease in the microchannel diameter to $174 \pm 12 \mu\text{m}$, or $49.0 \pm 3.4\%$ of the original size (**Figure 3b, c**). The distortions between pre-shrinking and post-shrinking patterns were visualized and showed negligible changes in original shape (**Supplementary Figure 23**).

While sacrificial printing using Pluronic as the fugitive ink renders the fabrication of hydrogel-embedded microchannels convenient, the channel sizes are typically limited to a few hundred micrometers or larger. Although with our unique shrinking strategy we could further reduce the channel diameter by a factor of 2, creating microchannels in the sub-100 μm scale with conventional sacrificial printing, relying on fugitive hydrogel inks is still challenging. More recently, melt electrospinning writing (MEW) has attracted increasing attention due to its ability to deposit well-defined meshes with filament sizes ranging from few micrometers down to sub-micron levels [23,24]. MEW-enabled sacrificial printing to generate microvascular networks has also been reported [25]. To further demonstrate the utility of our shrinking method, we manufactured MEW-printed polycaprolactone (PCL) grids (**Supplementary Figure 24**) and embedded them in HAMA hydrogels (2.0 w/v%). After UV-crosslinking, we selectively dissolved the PCL templates, and subjected the microchannel-containing HAMA constructs to shrinking (**Figure 3d**). As revealed in **Figure 3e**, the pristine MEW meshes embedded in the hydrogels were $20 \pm 1 \mu\text{m}$ in diameter with an interfiber distance of $490 \pm 29 \mu\text{m}$. The microchannels created by sacrificing the MEW templates following washing and swelling were $39 \pm 2 \mu\text{m}$ in diameter, and the distance between the adjacent microchannels (length of grid) was $772 \pm 10 \mu\text{m}$ (**Figure 3f**). After immersing in 2.0 w/v% HM_w chitosan in 1.0 v/v% acetic acid aqueous solution for 24 h, the microchannels shrank down to $10 \pm 2 \mu\text{m}$ ($\sim 50.9\%$ of original size, **Figure 3g, h**), which was comparable to the diameter of single capillaries. In addition, the grid length was reduced to $292 \pm 16 \mu\text{m}$ ($\sim 59.5\%$ of the original size, **Figure 3g, i**) with an associated decrease in the overall volume of the HAMA constructs. As such, using our shrinking method, the sacrificial MEW fibers of tens of micrometers could also be used to still generate sub-micron microchannels without needing the ultrafine fibers to start with.

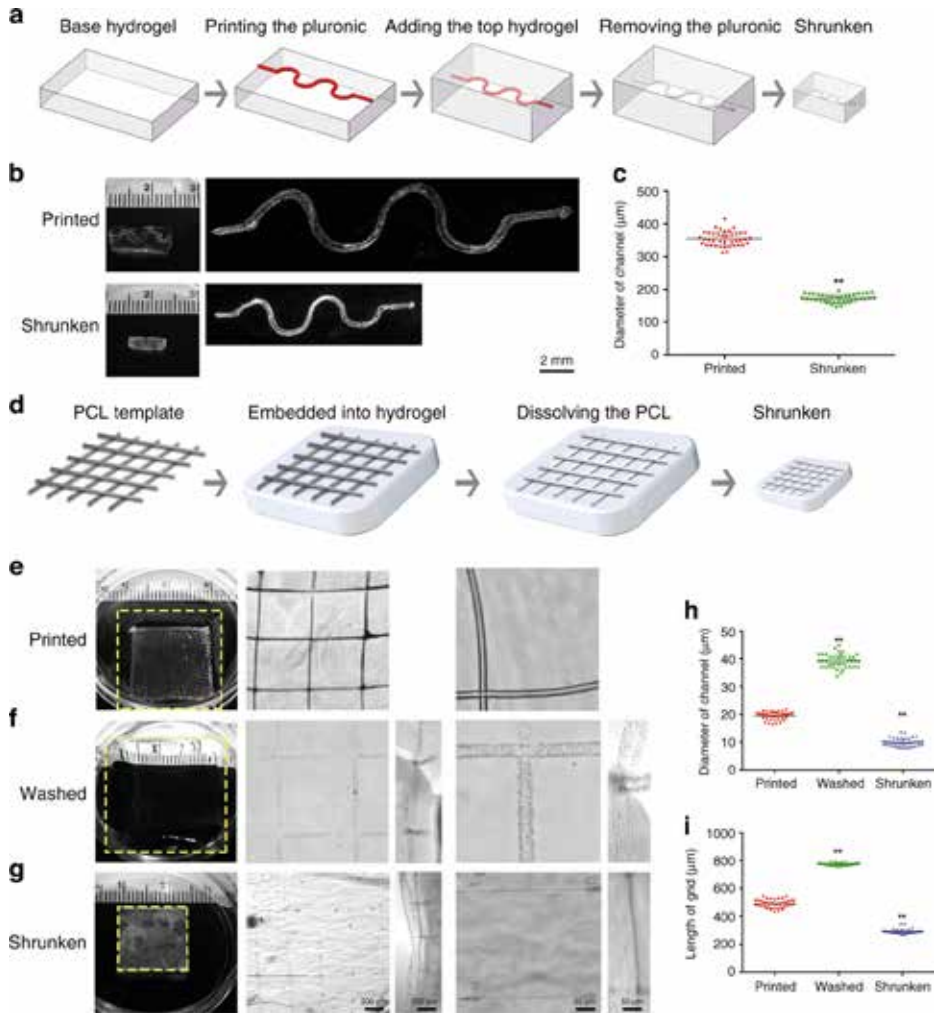


Figure 3. Sacrificial printing of microchannel-embedded HAMA constructs and their shrinking behaviors. **a** Schematic of the sacrificial printing process using an extrusion-printed Pluronic F-127 microfiber as the fugitive ink and subsequent shrinking of the construct. **b** Photographs showing the size change of the HAMA construct (2.0 w/v%) along with the embedded microchannel before (upper) and after (lower) 24 h of shrinkage in 2.0 w/v% HM_w chitosan dissolved in 1.0 v/v% acetic acid aqueous solution. **c** Corresponding quantitative analysis of diameter change of the microchannel before and after shrinking. **d** Schematic of the sacrificial printing process using a MEW-printed PCL grid as the fugitive ink and subsequent shrinking of the construct. **e–g** Photographs (left) and micrographs (right) showing the size change of the HAMA construct (2.0 w/v%) along with the embedded microchannel printed (**e**), washed (**f**) and shrunken (**g**) in 2.0 w/v% HM_w chitosan dissolved in 1.0 v/v% acetic acid aqueous solution (24 h). **h, i**, Corresponding quantitative analyses of changes in **h** diameter of the microchannel and **(i)** length of the grid before and after shrinking. ***P* < 0.01; two-tailed Student's *t*-test (**c**), one-way ANOVA (**h, i**, compared with the corresponding as-printed structures); mean ± sd (n = 40).

2.4 Shrinking behaviors of coaxially printed cannular constructs

Human tissues contain various cannular structures, such as the blood vessels for transporting cells, nutrients, and waste [26], the lymphatic vessels for draining fluids [27], and the tubules present in the kidney for secretion and reabsorption functions [28]. While sacrificial printing allows for emulation of matrix-embedded microchannels, microfluidic printing enabled by the adoption of coaxial, concentric printheads has featured single-step fabrication of standalone cannular structures. Both others [5,29] and we [30,31] have previously reported similar techniques in producing perfusable cannular tissues, where the minimum diameters of the obtained microfibers were limited to no smaller than a couple hundred micrometers due to the physical constraints of the sizes of the multilayered nozzles.

A coaxial printhead was thus designed and optimized to print HAMA-based tubes (**Figure 4a, b**). Different from direct extrusion printing and sacrificial printing, we mixed HAMA (0.5–2.5 w/v%) with alginate (0–2.0 w/v%) of different concentrations for use as the inks, to accommodate the microfluidic printing needs. The inks were delivered from the outer layer of the coaxial printhead, whereas the crosslinking CaCl_2 solution (0.3M) was carried from the interior. The printability of the inks was first examined (**Supplementary Figure 25**). It was observed that, when the concentrations of HAMA ranged from 0.5 to 1.0 w/v% and the alginate was in the range of 0.5–2.0%, the tubes were smoothly printed and uniform in shape (**Figure 4c, d**). The cannular structures became non-uniform when the concentration of HAMA was increased to higher than 1.0 w/v%. The optimal ink composition consisted of 1.0 w/v% HAMA, 0.5 w/v% alginate and 0.5 w/v% photoinitiator, and was used throughout the subsequent experiments.

The inner diameters of the as-printed tubular structures were measured at $670 \pm 10 \mu\text{m}$ (0.5 w/v% HAMA), $648 \pm 10 \mu\text{m}$ (1.0 w/v% HAMA), $583 \pm 16 \mu\text{m}$ (1.5 w/v% HAMA), $478 \pm 28 \mu\text{m}$ (2.0 w/v% HAMA) and $483 \pm 29 \mu\text{m}$ (2.5 w/v% HAMA) (**Figure 4e–g**). The tubes were then subjected to the same shrinking process (2.0 w/v% HM_w chitosan in 1.0 v/v% acetic acid aqueous solution for 24 h) we here established. After shrinking, the inner diameters narrowed down by 3–8 times of their original sizes to $90 \pm 7 \mu\text{m}$, $93 \pm 4 \mu\text{m}$ (**Supplementary Movie 2**), $115 \pm 7 \mu\text{m}$, $108 \pm 19 \mu\text{m}$, and $176 \pm 41 \mu\text{m}$, respectively (**Figure 4e**). Their outer diameters were decreased to 20.7–42.0% of original ones as well (**Figure 4f**), so did the wall thicknesses (38.7–79.1%, **Figure 4g**). We also compared the ratios obtained by the outer diameter divided by the inner diameter (OD/ID) before and after shrinkage, as well as the ratios of the outer diameter divided by the wall thickness (OD/WT), as measurements of fidelity of shrinkage in the printed cannular structures. As shown in **Supplementary Figure**

26a, before shrinkage, the ratios of OD/ID were 1.38 ± 0.02 (0.5 w/v% HAMA), 1.50 ± 0.02 (1.0 w/v% HAMA), 1.71 ± 0.04 (1.5 w/v% HAMA), 2.16 ± 0.13 (2.0 w/v% HAMA), and 2.52 ± 0.03 (2.5 w/v% HAMA) for the respective tubes. After shrinkage, the ratios increased to 2.15 ± 0.22 , 3.78 ± 0.26 , 3.64 ± 0.23 , 3.85 ± 0.60 , and 2.73 ± 0.58 , respectively. As for the OD/WT, there were decreases comparing to the as-printed cannular structures, from 7.25 ± 0.33 , 5.97 ± 0.13 , 4.83 ± 0.15 , 3.74 ± 0.23 , and 3.32 ± 0.03 to 3.81 ± 0.35 , 2.73 ± 0.07 , 2.76 ± 0.06 , 2.73 ± 0.19 , and 3.30 ± 0.47 , respectively (**Supplementary Figure 26b**). These metrics can guide the designs of cannular structures before shrinking according to the needs of the final desired sizes post-shrinking.

A printhead constructed with smaller needles (inner: 30G, outer: 18G) was used to print thinner HAMA/alginate tubes, which possessed an inner diameter, outer diameter, and wall thickness of 301 ± 3 , 438 ± 6 , and 68 ± 3 μm , respectively (**Supplementary Figure 27a, b**). Following shrinking, the sizes were reduced to 37 ± 3 , 148 ± 14 , and 56 ± 7 μm , respectively. This set of values is close to the sizes of small blood vessels (arterioles and venules, 8–100 μm) [26], lymphatic capillaries (30–80 μm) [27], and proximal tubules (50–60 μm) [28,32], making them physiologically relevant. The changes in the volumes and Young's moduli of constructs formed with inks containing different concentrations of HAMA but constant 0.5 w/v% alginate before and after shrinking in 2.0 w/v% HM_w chitosan were measured (**Supplementary Figure 28**), as well as for HM_w chitosan and Q. chitosan (both dissolved at 2.0 w/v % in 1.0 v/v % acetic acid aqueous solution) or in a perchloric acid solution of pH = 1 (**Supplementary Figure 29**), and similar trends were found as reported for the HAMA hydrogels earlier.

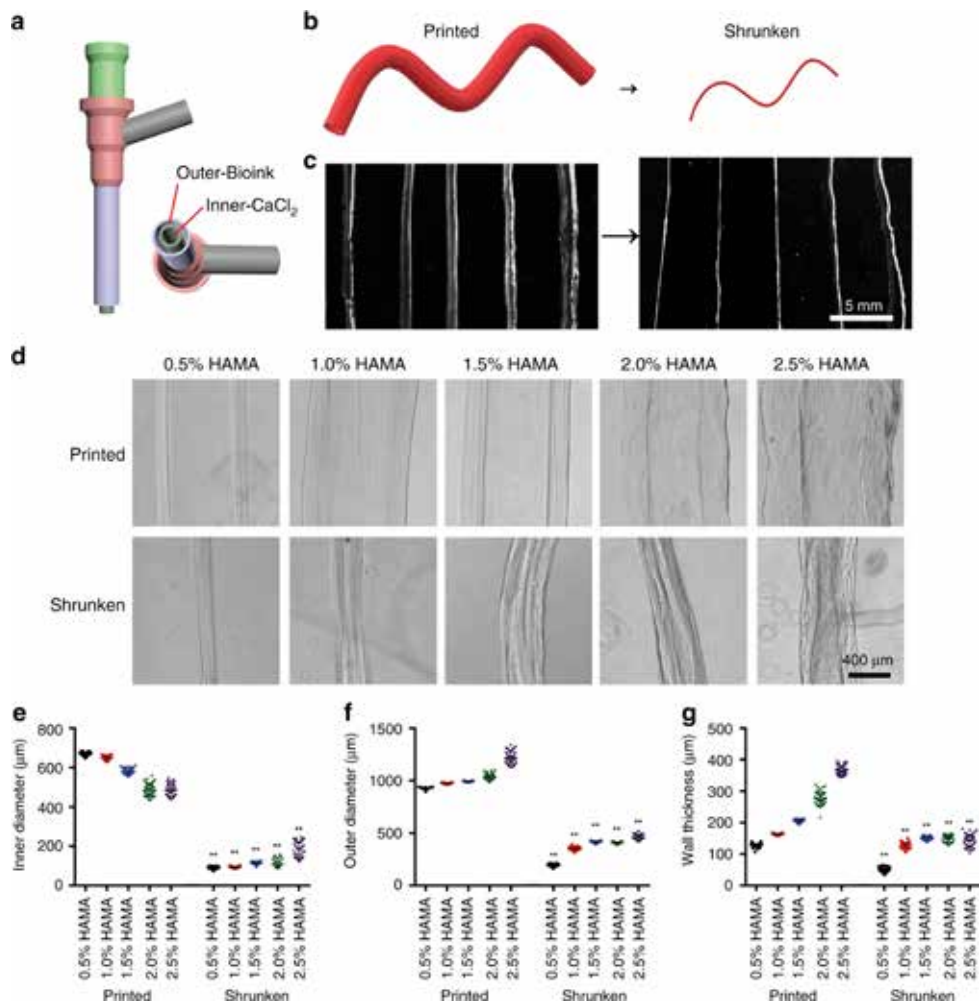


Figure 4. Coaxial printing of cannular HAMA-based constructs and their shrinking behaviors. **a** Schematic illustrations of the core-sheath coaxial nozzle used as the printhead, where the ink is delivered through the sheath flow and the CaCl_2 solution is co-delivered through the core flow. **b** Printing of the cannular construct and its subsequent shrinkage. **c, d** Photographs and micrographs showing the size changes of the tubes, coaxial-printed with inks containing different concentrations of HAMA (0.5–2.5 w/v%), before and after 24 h of shrinkage in 2.0 w/v% HM_w chitosan dissolved in 1.0 v/v% acetic acid aqueous solution. **e, f, g** Corresponding quantitative analyses of diameter (**e**, inner diameter; **f**, outer diameter; **g**, wall thickness) changes before and after shrinkage. $**P < 0.01$; one-way ANOVA (**e, f, g**, compared with the corresponding as-printed structures); mean \pm s.d. ($n = 40$).

2.5 Shrinking bioprinting for applications involving cells

We endeavored on two aspects that are relevant to the future applications of this shrinking printing strategy in cell cultures, i.e., to expand its conceptual feasibility to a more bioactive ink of GelMA, and to prove the concept that the density of embedded cells in a sacrificially bioprinted construct may be increased through the shrinking process without significantly affecting their viability.

We first investigated whether our shrinking concept could be extended to GelMA, which is a gelatin derivative featuring intrinsic cell-binding moieties and is capable of on-demand photocrosslinking [9,33]. GelMA solutions or hydrogels also exhibit a net negative charge under neutral or slightly acidic pH values [34], and we therefore hypothesized that an environment rich of cationic polymers would also shrink bioprinted GelMA constructs. Indeed, GelMA constructs sacrificially bioprinted to contain microchannels of $612 \pm 32 \mu\text{m}$ in diameter through the fugitive Pluronic F127 ink shrank to $55.6 \pm 9.1\%$ of the original size ($341 \pm 56 \mu\text{m}$) when immersed in 2.0 w/v% chitosan in 1.0 v/v% acetic acid aqueous solution (**Supplementary Figure 30a, b**), and the distortions were deemed to be in an acceptable range (**Supplementary Figure 31**).

To demonstrate the versatility of our shrinking technology, we further used a modified embedded sacrificial printing method [7] to generate microchannels within GelMA/HAMA hydrogel constructs using gelatin as the fugitive ink, and subsequently illustrated their ability to be shrunken (using 2.0 w/v% HM_w chitosan dissolved in 1.0 v/v% acetic acid aqueous solution) and perfused (**Supplementary Figure 32, Supplementary Movies 3, 4**). Consistent with other reports, it was shown that endothelial cells could be populated on the surfaces of the microchannels when seeded post-shrinking, indicating the reasonably good biocompatibility of the GelMA/HAMA-chitosan matrix after complexation (**Supplementary Figure 33**). In addition, GelMA constructs made from MEW-PCL templates through washing out the PCL shrank from 19 ± 1 to $12 \pm 2 \mu\text{m}$, or $\sim 62.1\%$ of original size, whereas the length of grid was reduced from $503 \pm 26 \mu\text{m}$ to $333 \pm 16 \mu\text{m}$, or $\sim 66.3\%$ of the original dimension (**Supplementary Fig. 30c–g**).

In microfluidic bioprinting, the inner diameter of the resultant GelMA (5.0 w/v%)/alginate (0.5 w/v%) cannular constructs decreased from $313 \pm 8 \mu\text{m}$ prior to shrinking to $39 \pm 4 \mu\text{m}$ afterwards (**Supplementary Figure 27c, d** and **Supplementary Movie 2**), which was 12.5% of its original size or a factor 8 in reduction. The outer diameter and the wall thickness also became proportionally smaller. The shrinking results were comparable to those with bioprinted HAMA constructs.

We subsequently explored the cytocompatibility of the shrinking method, where the Q. chitosan solution at physiological pH was used as the shrinking agent. A mixture of GelMA (2.5 w/v%) and HAMA (0.5 w/v%) was adopted as the ink to improve the bioactivity of the hydrogel constructs over those made from pure HAMA. We designed two shrinking processes and compared their effects on size reduction and cell viability. The first procedure consisted of a single shrinkage step (**Figure 5a**), i.e., a hydrogel construct encapsulating MCF-7 breast cancer cells, was left in 1.0 w/v% Q. chitosan in culture medium for 4 h, while in the second procedure termed successive shrinkage, we shrank the same type of construct twice in the same shrinking agent each time for 2 h, on the 1st day and the 3rd day (**Figure 5b**). Through live/dead staining, we found that the cell density was significantly elevated after 4 h of shrinkage (single shrinkage; 1080 ± 49 total cells per field of view [FoV], i.e., 1417 by $1417 \mu\text{m}^2$), compared to shrinkage for only 2 h (549 ± 40 total cells per FoV), on the 1st day (**Figure 5b, c**). In contrast, the original cell density was calculated to be in between 350 and 400 total cells per FoV. Nevertheless, a large number of cells were dead in the single-shrinkage process likely due to the prolonged exposure to the shrinking agent. On the 3rd day, the samples in the successive shrinkage group were shrunken again for another 2 h, which brought the cell density up to 883 ± 32 total cells per FoV. It should be noted that, although this density was lower than that of the single-shrinkage method on the 1st day, when we counted only viable cells, the values were in fact similar (748 ± 19 versus 747 ± 29 live cells per FoV), indicating that two successive size reductions each at a lower degree could minimize the harm of the process to the embedded cells and maintain their proliferation potential. Indeed, this trend became more pronounced during longer cultures. The viability of MCF-7 cells on the 5th day in the successive shrinking group (905 ± 49 total cells per FoV, percentage of live cells: $88.1 \pm 4.7\%$, or 797 ± 42 live cells) was much higher than those in the single shrinkage group (406 ± 32 total cells per FoV, percentage of live cells: $73.8 \pm 8.9\%$, or 297 ± 36 live cells). Ki67 was also assessed as a proliferation marker to show proliferation before and after shrinkage in GelMA/HAMA constructs. As revealed in **Figure 5d, e**, the percentage of Ki67+ stained nuclei in the control group at the 1st day was $86.1 \pm 6.5\%$, and for the cells in the successive shrinkage group, the positive rate was $84.9 \pm 2.6\%$, similar to the control group. In contrast, it significantly decreased to $58.5 \pm 8.0\%$ when single shrinkage for 4 h was adopted. After 5 days of culture, the percentage of Ki67+ stained nuclei were 77.5 ± 4.0 , 75.3 ± 8.0 , and $61.4 \pm 7.6\%$ in the control group, successive shrinkage group, and single shrinkage group, respectively. Interestingly, the MCF-7 cells that underwent two successive shrinkages still exhibited a good proliferative potential comparable to the control group and higher than the single shrinkage group at the same time.

The method was extended to several other cell types including the C2C12 mouse skeletal muscle cells, which maintained satisfactory viability post-shrinking. As shown in **Supplementary Figure 34**, the C2C12 cells spread well in the as-printed GelMA/HAMA hydrogel constructs, and after 2 h of shrinkage the density of the cells was doubled although their sizes seemed to have decreased possibly caused by the shrinking process. However, following 3 days of culture, the cells were able to spread again and proliferated throughout the subsequent culture period.

We noted that however, while MCF-7 cells and C2C12 cells performed reasonably well after shrinkage, another cell type that we examined, i.e., human umbilical vein endothelial cells (HUVECs), appeared to be much more sensitive to the shrinking processes. The percentage of Ki67+ stained nuclei was analyzed as a proliferation marker; at the 5th day of culture, only $42.2 \pm 3.0\%$ (successive shrinkage group) and $31.1 \pm 2.1\%$ (single shrinkage group) of HUVECs were Ki67+stained, significantly lower than the control group at the 1st day of culture (**Supplementary Figure 35a, b**). We reason that such observations might be relevant to the differential sensitivities of the different cell types to the shrinking agent, Q. chitosan, for which we measured the metabolic activity of MCF-7 cells (**Supplementary Figure 36a**) and HUVECs (**Supplementary Figure 36b**) exposed to Q. chitosan PBS solutions at different concentrations for 30 min, 2, 4, and 24 h. The concentrations reflecting 50% reduction in cell metabolic activity, depicted as toxic concentration (TC_{50}) values of these two cell types were calculated. Indeed, as revealed by **Supplementary Figure 36**, the TC_{50} values for MCF-7 cells at 30 min, 2, 4, and 24 h of Q. chitosan treatment were 0.505, 1.487, 0.371, and 0.131 mg mL⁻¹, respectively, whereas those for HUVECs were significantly lower at all time points at 0.002, 0.077, 0.002, and 0.009 mg mL⁻¹, respectively. These results suggested that HUVECs are remarkably more sensitive to Q. chitosan than MCF-7 cells, explaining their pronounced reduction in proliferation potential during the shrinking conditions that we used, even in the case of two successive shrinkage. We anticipate that these observations will provide insights towards selection of shrinking agent concentrations for sensitive and resistant cells in the future.

We finally demonstrated the feasibility of shrinking sacrificially printed hydrogels in the presence of cells. GelMA/HAMA constructs containing green fluorescent protein-labeled HUVECs (GFP-HUVECs) were produced with the Pluronic fugitive inks, and subjected to the two different shrinking procedures. As shown in **Supplementary Figure 37a, b**, in the single shrinkage group, the microchannels inside the block were reduced to $64.2 \pm 3.5\%$ of their initial diameters. In the successive-shrinkage group, the microchannels shrank to 74.9

$\pm 5.8\%$ after the first shrinkage, and after another shrinkage on the 3rd day, the diameter of the microchannels was reduced to $58.3 \pm 7.3\%$ of its original size, similar to the case of single shrinkage and within the physiological range of small blood vessels. As expected, the loss of the GFP signals was more pronounced in the single shrinkage group.

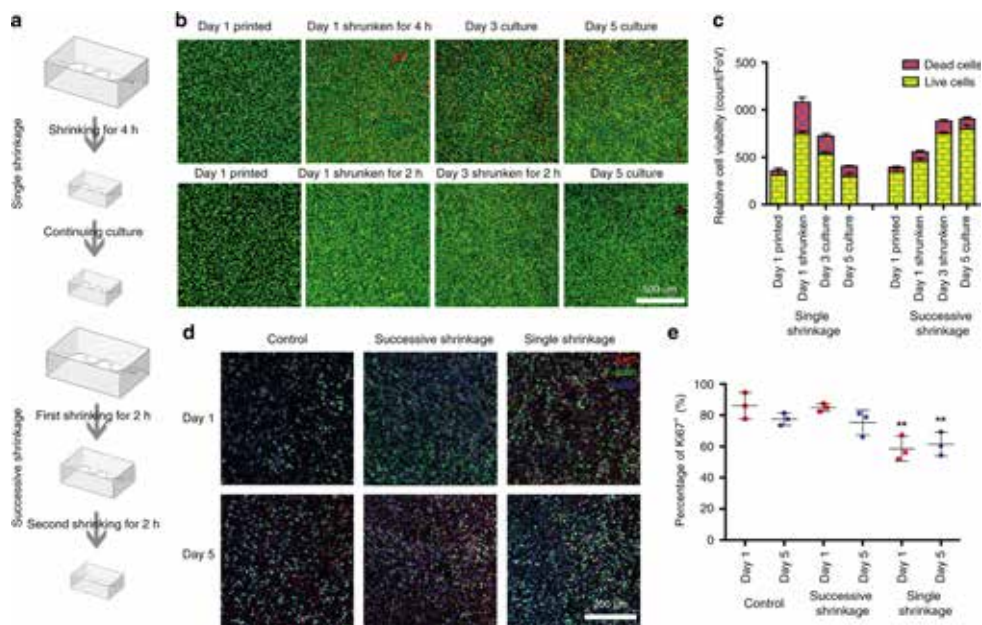


Figure 5. Biocompatibility of the shrinking process and shrinking in the presence of cells. **a** Schematics showing the single shrinkage (upper) and the successive shrinkage (lower). **b** Micrographs showing live (green)/dead (red) staining of MCF-7 cells embedded in GelMA/HAMA constructs following a single shrinking process (upper) and a successive shrinking process (lower). **c** Corresponding quantitative analyses of the numbers of live/dead cells during the two type of shrinking processes. **d** Fluorescence micrographs of MCF-7 cells in GelMA/HAMA constructs without any treatment (control) as well as after successive shrinkage and single shrinkage, stained for Ki67 (red), F-actin (green), and nuclei (blue). **e** Corresponding quantitative analyses of the percentages of Ki67+ stained nuclei in the three groups. $**P < 0.01$; one-way ANOVA (compared with the control group on Day 1), mean \pm s.d. (**b**, **c** $n = 10$; **d**, **e** $n = 1$, deviations obtained from eight distinct layers of a confocal stack for each sample).

3. Discussion

In conclusion, we report here a printing strategy of complexation-induced resolution enhancement, i.e., shrinking printing, through post-treatment of the printed structures without changing the printer hardware or printing parameters. We conducted our proof-of-concept studies with several techniques of printing and succeeded in all cases, including

direct extrusion printing, sacrificial printing, and microfluidic hollow tube printing. Notably, our data showed that these printed constructs could reduce in their sizes by different degrees, comparing to their original dimensions. In addition, results indicated that this method is broadly applicable, i.e., a printed anionic hydrogel structure might be shrunken by a cationic polymer, or vice versa. We finally demonstrated that successive shrinking could preserve, in a cell type-dependent manner, the viability of cells embedded in the printed hydrogel matrices compared to a single, longer shrinking procedure, revealing the potential applications of our shrinking printing method towards tissue biofabrication. We therefore anticipate widespread adoption of our unique technology in future printing of hydrogel constructs for various application areas with further optimizations.

4. Methods

4.1 Synthesis and characterizations of HAMA

Hyaluronic acid was functionalized with methacrylate groups through a transesterification reaction with methacrylic anhydride [8,35]. In a typical synthesis, 3 g of hyaluronic acid sodium salt (M_w : 1530 kDa, Lifecore Biomedical, USA) was dissolved overnight in 400 mL of de-ionized water at 4 °C. The solution was placed on ice and an equal volume of dimethyl formamide (DMF, Sigma-Aldrich, USA) was added whilst stirring vigorously. Methacrylic anhydride (MA, Sigma-Aldrich) was added in a 5:1 molar ratio of MA (5.8 g, 37.5 mmol) to hyaluronic acid disaccharide units over the course of 4 h using a syringe pump (1.375 mL h^{-1}). During these 4 h, the pH was controlled using a Mettler DL21 titrator (Mettler-Toledo, The Netherlands) connected to a pH meter, which dispensed an aqueous 0.5M NaOH (Sigma-Aldrich) solution whenever the pH of the solution dropped below 8.5. After complete addition of the methacrylic anhydride, pH was monitored for an additional hour and maintained above pH 8.5. Subsequently, the reaction mixture was left at 4 °C overnight. The next day, NaCl (Sigma-Aldrich) was dissolved in the reaction mixture to up to 0.5 M and the mixture was precipitated in 10 equal volumes of ethanol at -78 °C (cooled with an acetone dry ice bath). HAMA was collected as dry white pellets, dissolved in de-ionized water and dialyzed against de-ionized water for 2 days to remove impurities (Visking, regenerated cellulose dialysis membrane, molecular weight cut off [MWCO]: 12–14 kDa, VWR, The Netherlands). After dialysis the HAMA solution was freeze-dried to yield a white powder.

4.2 Synthesis and characterizations of FITC-Q. chitosan

Quaternized chitosan was fluorescently labeled using FITC (Sigma-Aldrich). In short, 1 g of Q. chitosan was dissolved overnight in 200 mL of freshly made sodium carbonate buffer (pH =

9.0). Subsequently, a fresh solution of 10 mg of FITC in 10 mL of dry dimethylsulfoxide (DMSO, Sigma-Aldrich) was added dropwise to the Q₂ chitosan solution under vigorous stirring. The reaction was left to proceed for 4 h. Both the dissolution FITC in DMSO solution and the reaction with Q₂ Chitosan were performed in a dark environment to limit potential photodegradation. Upon completion of the reaction, the solution was directly poured into dialysis bags (MWCO: 10–14 kDa) and dialyzed in de-ionized water for 6 days whilst protected from light. Finally, the dialyzed solution was freeze-dried overnight to yield FITC-Q₂ chitosan as an orange powder.

The degree of substitution of FITC onto the Q₂ chitosan was studied using UV-vis spectrometry, where absorbances were measured at 280 (A_{280}) and 488 (A_{488}) nm, respectively. Molar extinction coefficients of 175 and 68 M cm⁻¹ were used for Q₂ Chitosan (ϵ_c) and FITC (ϵ_{FITC}), respectively. Labeling density was determined according to:

$$Q_2 \text{ Chitosan concentration (M)} = \frac{A_{280} - (A_{488} \times CF)}{\epsilon_c}$$

and

$$\text{Moles of FITC per mol } Q_2 \text{ Chitosan} = \frac{A_{488}}{\epsilon_{FITC} \times Q_2 \text{ Chitosan concentration}}$$

It was found that one mole of Q₂ chitosan was conjugated with 29.7 mol of FITC.

4.3 Synthesis and characterizations of GelMA

GelMA was synthesized by reaction of type B bovine skin gelatin (~225 bloom, Sigma-Aldrich) with methacrylate anhydride at 50 °C for 1 h in PBS (pH = 7.4, Gibco, USA) [36]. Methacrylic anhydride was added dropwise in a 0.6:1 weight ratio of anhydride to gelatin. Next, the solution was diluted 1:1 with de-ionized water and dialyzed for 5 days (dialysis membrane as used for the HAMA synthesis), and subsequently freeze-dried to yield a white powder.

4.4 Determination of degree of methacrylation and methacrylate conversion

The degree of methacrylation (DM) for the synthesized HAMA was determined using a previously developed high-performance liquid chromatography (HPLC) method [37]. In short, 15 mg of polymer or dried hydrogel was dissolved overnight at room temperature in 6 mL of aqueous 0.02-M NaOH solution. Next, 1 mL of acetic acid was added and the samples were injected into an Alliance Waters HPLC system equipped with UV-VIS detection monitoring at 210 nm (Dual Lambda Absorbance, USA) and a Sunfire C18 column (column temperature: 50 °C). An isocratic method was used based on eluent consisting of 15:85 acetonitrile: de-ionized water (pH = 2, adjusted with perchloric acid) with a set flow of 1 mL min⁻¹. The

samples were referenced to a calibration curve of known concentrations of methacrylic acid. Concentrations were then calculated to yield the DM, defined as the number of methacrylate groups per 100 disaccharide units. The DM of HAMA was found to be $28.8 \pm 0.4\%$ ($n = 3$).

The DM of GelMA was defined as the number of methacrylate groups per available lysine found in the gelatin and was determined by ^1H NMR in D_2O according to Hoch et al. [38]. The DM of GelMA was found to be approximately 50%.

4.5 Preparation and printability of the HAMA inks

For the inks used in extrusion printing and sacrificial printing, various concentrations (w/v) of HAMA (0.5%, 1.0%, 1.5%, 2.0%, or 2.5%) were dissolved in de-ionized water in room temperature overnight. In addition, 0.5 w/v% photoinitiator (Irgacure 2959; Sigma-Aldrich) was added to initiate photocrosslinking upon UV-irradiation (approximately 10 mW cm^{-2} , 360–480 nm, 40 s). For the blend inks for coaxial printing, different concentrations of HAMA (0–3.0 w/v%) and alginate (0–2.0 w/v%; lot number: BCBP9590V, Sigma-Aldrich) were evaluated, where the final formulations were determined to be 0.5, 1.0, 1.5, 2.0, or 2.5 w/v% HAMA + 0.5 w/v% alginate + 0.5 w/v% photoinitiator. Inks were prepared and stored at 4°C until use.

4.6 Preparation of GelMA inks

For the inks used in sacrificial printing, the GelMA was dissolved in de-ionized water in 37°C for 1 h at a concentration of 5.0 w/v%. In addition, 0.5 w/v% photoinitiator was added to enable crosslinking. In the blend ink used for coaxial printing, the final formulation was 5.0 w/v% GelMA + 0.5 w/v% alginate + 0.5 w/v% photoinitiator. Inks were stored at 4°C until use.

4.7 Preparation of chitosan solutions and shrinking efficiency in different chitosan solutions

Four types of chitosan were used, where three of different molecular weights (LM_w : 15 kDa; MM_w : 50–190 kDa; HM_w : 700–800 kDa) were of similar degree of deacetylation (85%) and from Golden-Shell, China. Q. chitosan (M_w : 50–100 kDa), which was ~90% deacetylated and subsequently 95% quaternized to yield permanent, was from Cool Chemistry, China. They were dissolved at a concentration of 2.0 w/v%, in 1.0 v/v% acetic acid aqueous solution when comparing the effect of chitosan of different molecular weights and types. Another three types of chitosan with different degrees of deacetylation (72.5%, 77.8%, and 94.6%; Hepepe Biomedical, Germany) were used to study the effects of shrinking agent deacetylation. All chitosan types were of similar molecular weights (50–250 kDa), and were all dissolved at

a concentration of 2.0 w/v% in 1.0 v/v% acetic acid aqueous solution for usage. 1.0 w/v% HAMA hydrogels were fabricated and immersed in these shrinking agents for 24 h and the volumes before and after shrinking were measured.

Various concentrations (0.5, 1.0, 1.5, 2.0, 3.0, or 5.0 w/v%) of HM_w chitosan and Q_c chitosan were dissolved in 1.0 v/v% acetic acid aqueous solution, de-ionized water, or DMEM (Gibco) at 37 °C. The solutions were vortexed and stored at 4 °C. Before use, they were pre-heated to 37 °C. The printed hexagons were immersed in HM_w chitosan (0.5, 1.0, 1.5, 2.0, 3.0, or 5.0 w/v%) dissolved in 1.0 v/v% acetic acid aqueous solution, or Q_c chitosan (0.5, 1.0, 1.5, 2.0, 3.0, or 5.0 w/v%), which was dissolved in 1.0 v/v% acetic acid aqueous solution, de-ionized water, or DMEM. The shrinking processes were recorded at 2 and 24 h microscopically and through photography, and measurements were made using imageJ (National Institutes of Health, USA).

4.8 Preparation of hydrogel discs and dimension measurements

The anionic polymer solutions (2.0 w/v% HAMA, 2.0 w/v% alginate) were cast in circular PDMS molds ($D = 4.5$ cm) and subsequently gelled through either exposure to UV irradiation (HAMA) or a $CaCl_2$ solution (alginate), or both. Hydrogels that were gelled with $CaCl_2$ were washed with de-ionized water to remove excess ions. Subsequently, biopsy punches (Integra Miltex, The Netherlands) were used to produce cylindrical hydrogels ($D = 6$ mm, $H = 2$ mm, ~ 56.5 μ L or $D = 8$ mm, $H = 3.4$ mm, ~ 170.9 μ L).

The cationic polymer (HM_w chitosan) solution was prepared in 1.0 v/v% acetic acid in water at concentrations of 2.0 w/v%. The HM_w chitosan solution was then cast into the PDMS molds, and subsequently, 2 mL of glutaraldehyde (with concentrations of 200, 400, 800, or 2400 μ M) in 1.0 v/v% acetic acid solution was gently pipetted on top. The crosslinking reaction was left to proceed for 1 h, biopsy punch was used to produce cylindrical hydrogels ($D = 6$ mm, $H = 2$ mm, ~ 56.5 μ L). The hydrogels were incubated in a perchloric acid solution (pH = 1.0), 1.0 v/v% acetic acid aqueous solution (pH = 4.7), or 1.0 v/v% acetic acid aqueous solution with 2.0 w/v% of the shrinking agent. For all hydrogel shrinking studies, measurements before and after shrinking were performed using Vernier calipers (measurement error ~ 30 μ m).

4.9 Measurements of mechanical properties

To measure the Young's modulus and volume of HAMA hydrogels with/without alginate before and after shrinkage, crosslinked hydrogel disks ($D = 6$ mm, $H = 2$ mm, ~ 56.5 μ L) were prepared as mentioned before, incubated for 24 h in HM_w chitosan, Q_c chitosan (both

dissolved up to 2.0 w/v% in 1.0 v/v% acetic acid aqueous solution), or an aqueous solution of perchloric acid adjusted to pH 1.0. Moreover, the hydrogels containing alginate were briefly incubated in a CaCl_2 solution before shrinking. Compression tests were performed in triplicate on a 2980 DMA (TA Instruments, the Netherlands) with a ramp of 2.0 N min^{-1} up to a maximum of 18.0 N. The elastic modulus was calculated as the slope of the start of the stress-strain curve that was obtained from the compression test. Specifically, we used the linear region between 10 and 30% strain.

4.10 Stability studies of the shrunken hydrogels

The following hydrogel formulations were used to study the stability of the shrinking effect, i.e., 2.0 w/v% HAMA, 1.5 w/v% HAMA + 0.5 w/v% alginate, and 0.5 w/v% HAMA + 2.0 w/v% GelMA. All hydrogels were incubated in 2.0 w/v% FITC-Q₂ chitosan solution in PBS until fully shrunken and then rinsed twice with PBS. The hydrogels were weighed and measured (diameters and heights), and then incubated at 37 °C in individual vials containing 1 mL of PBS per vial. The PBS was completely changed every 2 days. The absorbance (= 488 nm) of the supernatant was determined on Days 1, 3, 7, 11, 15, and 21. In addition, the diameters and heights of the hydrogels were also measured at these time points. After all measurements, the hydrogels were placed back into the vials and fresh PBS was added. By measuring the absorbance of a standard curve of known FITC concentrations at 488 nm and through factoring in the degree of FITC labeling of the Q₂ chitosan, the amounts of FITC-labeled Q₂ chitosan released ($\mu\text{g mL}^{-1}$) from the hydrogels per time point were calculated.

4.11 SEM sample preparation and imaging

Hydrogels consisting of 1.0 w/v% HAMA were fabricated and incubated in 2.0 w/v% HM_w chitosan in 1.0 v/v% acetic acid aqueous solution for 24 h and freeze-dried or freeze-dried immediately post-fabrication. The freeze-dried samples were cut using a razor blade, and subsequently sputter-coated with a nanometer-layer of Pt. The sputter-coated samples were imaged with SEM (PhenomTM, FEI, The Netherlands). An electron beam of 5 kV was used, and the samples were imaged at 1000 times of magnification.

4.12 Extrusion printing

Constructs were first designed by 3D Studio Max (Autodesk, USA) and sliced by Repetier (Hot-World, Germany). An Allevi 2 bioprinter (Allevi, USA) was used to fabricate the constructs. For the extrusion printing of hexagonal patterns, the printhead moving speed was 6 mm s^{-1} , and the inks were crosslinked by exposing to UV light ($\sim 10 \text{ mW cm}^{-2}$, 360–480 nm, 40 s). In this case, we did not use in situ photocrosslinking for our printing processes but

performed post-printing photocrosslinking. The HAMA inks were sufficiently viscous to maintain the shape stability immediately post-printing. The printed and photocrosslinked HAMA hexagons were immersed in the chitosan solutions (0.5, 1.0, 1.5, 2.0, 3.0 or 5.0 w/v% in 1.0 v/v% acetic acid aqueous solution) for 24 h. We used microscopy (Eclipse Ti, Nikon, Japan) and a camera (Canon, Japan) to image the constructs after 2 h and 24 h of incubation. We also measured the printability and the Young's modulus of HAMA constructs made with different HAMA concentrations before and after shrinkage.

The alginate and chitosan hexagons were printed in the same way, where alginate hexagons were crosslinked in 0.3-M CaCl_2 and chitosan hexagons crosslinked with glutaraldehyde (800 μM).

For the pyramid (six 10-mm lines converging in four vertices) hydrogel fabrication, the construct was designed and sliced by the same software as mentioned above. The ink consisted of 2.0 w/v% HAMA, 0.1 w/v% Irgacure 2959, and fluorescent microbeads (purple, 15–35 μm ; CREATEX, USA), where a 1.5 w/v% gelatin type A (Sigma-Aldrich) hydrogel bath (formed by cooling at 4 °C for 40 min) was used as the support matrix to facilitate freeform printing of the pyramid [8]. The structure was printed by an Allevi 2 bioprinter equipped with a 23G needle (BD Biosciences, USA), followed by crosslinking by exposing to UV light ($\sim 10 \text{ mW cm}^{-2}$, 360–480 nm) for 60 s. After photocrosslinking, the gelatin bath was heated and stepwise replaced with water. Finally, the 3D-printed pyramidal structure was incubated in 1.0 w/v% HM_w chitosan in 1.0 v/v% acetic acid aqueous solution for 24 h for complete shrinkage.

4.13 Sacrificial printing

Sacrificial printing based on Pluronic F127 followed previously established protocols [22]. Pluronic F127 (Sigma-Aldrich) solution was used as the fugitive ink in sacrificial printing, which is a hydrogel at room temperature but liquefies at low temperatures. Specifically, 40 w/v% Pluronic F127 aqueous solution was used for printing the fugitive templates. A PDMS mold (length: 1.5 cm, width: 0.5 cm) was first made. The 2.0 w/v% HAMA solution was cast into the PDMS mold at a thickness of 0.2 cm and UV-crosslinked (10 mW cm^{-2} , 360–480 nm, 40 s) to act as the base layer. Then, Pluronic F127 (40.0 w/v%) mixed with fluorescent microbeads (red) was printed onto the HAMA gel surface. Subsequently, another layer of 2.0 w/v% HAMA solution was poured into the mold to cover the Pluronic, immediately followed by another UV crosslinking procedure. The construct was placed in water overnight at 4 °C to liquefy and remove the Pluronic, leaving the open channel. Later, the block with

open channel was immersed in a HM_w chitosan solution (2.0 w/v% in 1.0 v/v% acetic acid aqueous solution) for 24 h. The diameter change of the channel was recorded before and after shrinking. Sacrificial printing of GelMA constructs was done in a similar fashion as for HAMA. It should be noted that, the Pluronic fugitive ink was not completely removed and the residual coating on the channels containing the fluorescent microbeads facilitated visualization.

Sacrificial printing in combination with an embedded freeform printing strategy was also demonstrated, where a blend solution of GelMA (2.5 w/v%) and HAMA (0.5 w/v%) containing 0.1 w/v% photoinitiator was cast into a PDMS mold and placed at 4 °C for 30 min until it became a semi-solid hydrogel bath. Then, 5.0 w/v% gelatin type A was prepared as the bioink at room temperature and printed directly into the GelMA/HAMA bath as a serpentine microfiber, then UV-crosslinked (10 mW cm^{-2} , 360–480 nm, 60 s). The gelatin was subsequently washed out by incubating the block at 37 °C to form the microchannel. To shrink, the blocks with open channels were immersed in the HM_w chitosan solution (2.0 w/v% in 1.0 v/v% acetic acid aqueous solution) for 24 h. HUVECs were subsequently seeded into the microchannels post-shrinking. Perfusion of the channels before and after shrinking was also demonstrated.

Alternatively, PCL meshes were fabricated by the MEW technique and used as sacrificial templates [25] and 2.0 w/v% HAMA was cast around the templates. To leach the PCL template from the HAMA constructs, a multi-stage removal process was optimized. The constructs were immersed sequentially in de-ionized water for 1.5 h, 50 v/v% acetone (Sigma-Aldrich) in water for 1.5 h, in 100 v/v% acetone overnight, 50 v/v% dichloromethane (DCM, Sigma-Aldrich) in acetone for 1.5 h, and 100 v/v% DCM overnight. After dissolution of the PCL, the hydrogel was treated in the reverse order of the steps described until in 100% de-ionized water for rehydration. Later, the block with open channels was immersed into the chitosan solution (2.0 w/v% in 1.0 v/v% acetic acid aqueous solution) for 24 h. The diameters of channels and the lengths of grids were recorded and analyzed.

4.14 Coaxial printing

A coaxial printhead containing two injection channels was fabricated, where the size of the internal needle was 23G and the outer was 16G. These two needles were fixed concentrically with epoxy resin (Devcon, USA). The internal channel was perfused with a 0.3-M CaCl_2 solution (Sigma-Aldrich) and the external channel was used to print blend inks of HAMA (0.5, 1.0, 1.5, 2.0, or 2.5 w/v%) + 0.5 w/v% alginate + 0.5 w/v% photoinitiator. Both layers of

flows were controlled by syringe pumps (NE-1000, New Era Pump Systems Inc, USA) and the extrusion rates were set at $400 \mu\text{L min}^{-1}$ (0.3-M CaCl_2 solution) and $200 \mu\text{L min}^{-1}$ (inks). The CaCl_2 solution was used for immediate physical crosslinking of the alginate component for tube formation during printing, whereas the tubes were subsequently shrunken in the HM_w chitosan solution (2.0 w/v% in 1.0 v/v% acetic acid aqueous solution) for 24 h and UV-crosslinked ($\sim 10 \text{ mW cm}^{-2}$, 360–480 nm, 40 s). The ID, OD, WT, as well as the ratios of OD/ID and OD/WT before and after shrinkage were all measured. Alternatively, a coaxial printhead made of 30 G/18 G needles was also produced to print smaller-sized tubes using the blend ink containing 1.0 w/v% HAMA or 5.0 w/v% GelMA, together with 0.5 w/v% alginate and 0.5 w/v% photoinitiator.

4.15 Visualization of shrinking distortions using non-rigid registration

The distortions of co-registered pre-shrinking/2-h shrinking structures and post-shrinking structures were visualized by deforming the pre-shrinking/2-h shrinking images using a non-rigid registration process to attempt an exact match of the post-shrinking images of the corresponding samples [18]. Using a B-spline based non-registration algorithm (i), which generates a deformation grid between the pre-shrinking/2-h shrinking (green) and post-shrinking (magenta) patterns, we were able to map the deformation between them. Pre-shrinking/2-h shrinking and post-shrinking images were first converted to binary images using the Matlab function `im2bw` (ii), which converts an image to a binary image, based on threshold, by replacing all the pixels in the input image with luminance greater than the level 1 (white) and replacing all other pixels with the value 0 (black). Both images were smoothed for faster registration using a Gaussian blur filter, with a standard deviation of 5 pixels.

- (i) D.-J. Kroon, “B-spline Grid, Image and Point based Registration”; available at: <https://www.mathworks.com/matlabcentral/fileexchange/20057-b-spline-grid-image-and-point-based-registration>
- (ii) Matlab Documentation, “`im2bw`”; available at: <https://www.mathworks.com/help/images/ref/im2bw.html>

4.16 Shrinking bioprinting in the presence of cells

MCF-7 breast cancer cells (American type culture collection [ATCC], USA) were suspended in 2.5 w/v% GelMA + 0.5 w/v% HAMA aqueous solutions at a density of 1.0×10^7 cells/mL, 0.3 w/v% photoinitiator (lithium phenyl-2,4,6-trimethylbenzoylphosphinate, LAP; Allevi) was added for inducing photocrosslinking ($\sim 10 \text{ mW cm}^{-2}$, 360–480 nm, 20 s). Half of the samples were shrunken once for 4 h (single shrinkage, the 1st day) in 1.0 w/v% Q. chitosan

in DMEM supplemented with 10 v/v% fetal bovine serum (FBS, Gibco), or shrunken twice at 2 h each (successive shrinkage, the 1st day and the 3rd day). In the single shrinkage group, live/dead staining was performed before and after shrinking on the 1st day, the 3rd day, and the 5th day. For the successive shrinkage group, the live/dead staining was carried out before shrinkage and subsequently on the 1st day, the 3rd day, and the 5th day. The specimens with cells were rinsed with PBS and incubated with 2 μM of calcein-AM and 4 μM of ethidium homodimer-1 (Invitrogen, USA) for 30 min to examine viability. Moreover, the cells were also stained for Ki67 as a proliferation marker. The samples were fixed in 4% paraformaldehyde (Thermo Fisher, USA) for 15 min, permeabilized with 0.05% Triton X-100, and then blocked with 2% FBS and 2% bovine serum albumin (BSA, Sigma-Aldrich) in PBS. Samples were incubated with recombinant anti-Ki67 antibody conjugated to Alexa Fluor[®] 594 (Abcam, USA) overnight at 4 °C. FITC-phalloidin (Cytoskeleton, USA) was used to stain for F-actin and the nuclei were counter-stained with 4',6-diamidino-2-phenylindole (DAPI, Vector Laboratories, USA). The samples were then rinsed in PBS and visualized using confocal laser scanning microscopy (LSM880, Zeiss, Germany) and measurements were made using image]. The same protocols were used for shrinking HUVECs (ATCC)-encapsulated hydrogel constructs and associated analyses, only the cultures were maintained in endothelial cell growth medium (EGM-2, PromoCell, USA) and the constructs were shrunken in 1.0 w/v% Q chitosan in EGM-2. C2C12 mouse skeletal myoblasts (ATCC) were also encapsulated in the same GelMA/HAMA hydrogel and evaluated against the shrinking process. The samples were fixed in 4% paraformaldehyde for 15 min, permeabilized with 0.05% Triton X-100, and then blocked with 2% FBS and 2% bovine serum albumin in PBS. FITC-phalloidin was used to stain F-actin and the nuclei were counter-stained with DAPI. The samples were visualized by an inverted fluorescence microscope (Eclipse Ti).

For the IC_{50} experiments, MCF-7 cells and HUVECs were cultured in 96-well plates until confluency. The cells were exposed to different concentrations (0.5 $\mu\text{g mL}^{-1}$ –0.5 mg mL^{-1}) of Q chitosan dissolved in culture medium for various lengths of time (30 min–24 h). After exposure, the cells were incubated with the PrestoBlue[™] Cell Viability Reagent (Thermo Fisher) in medium for 30 min and measured for absorbance.

We further tested the shrinkage of sacrificially bioprinted GelMA/HAMA constructs in which GFP-HUVECs (Angio-Proteomie, USA) were encapsulated within the hydrogels where each construct contained a central microchannel formed by removing the Pluronic template embedded with red fluorescent microbeads. The procedure was similar to that without cells, but the Pluronic was washed out in PBS after liquefying at 4 °C for 5 min. Before and after

shrinking in 1.0 w/v% Q. chitosan in EGM-2. The samples were visualized with the inverted fluorescence microscope (Eclipse Ti).

4.17 Statistical analysis

Data are presented as the mean \pm standard deviation (SD). Differences between the values were evaluated using one-way analysis of variance (ANOVA; Tukey's post hoc test) or two-tailed Student's *t*-test. Data are presented as means with 95% confidence interval. $p < 0.05$ was considered statistically significant.

4.18 Data availability

The datasets that support the findings of this study are available from the corresponding authors upon reasonable request. All requests for raw and analyzed data and materials will be promptly reviewed by the Brigham and Women's Hospital and Utrecht University to verify whether the request is subject to any intellectual property or confidentiality obligations. Any data and materials that can be shared will be released via a Material Transfer Agreement.

4.19 Code availability

The codes developed in this study are available from the corresponding authors upon reasonable request. All requests will be promptly reviewed by the Brigham and Women's Hospital and Utrecht University to verify whether the request is subject to any intellectual property or confidentiality obligations. Any codes that can be shared will be released via a Material Transfer Agreement.

Acknowledgements

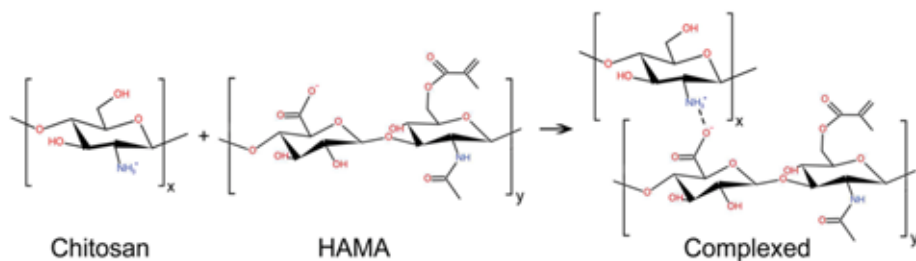
This work was supported by funding from the National Institutes of Health (K99CA201603, R01CA201603, R21EB025270, R21EB026175, R01EB028143), the Brigham Research Institute, the New England Anti-Vivisection Society, the Hofvijverkring Visiting Scientist Program, the Materials Driven Regeneration Young Talent Grant, the Future Medicines Program financed by the Netherlands Organisation for Scientific Research (NWO No. 022.006.003), and the Dutch Kidney Foundation (18KVP01,17PHD16).

Additional information

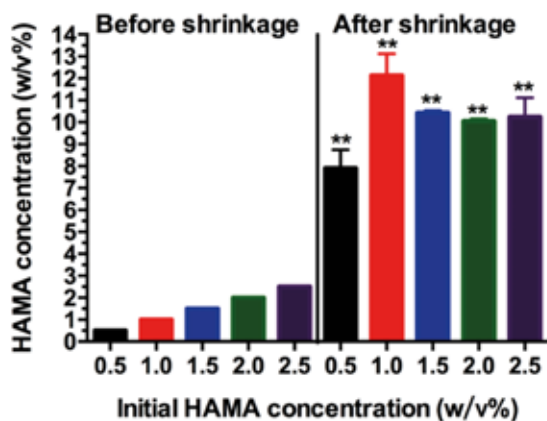
Supplementary information is available for this paper at

<https://doi.org/10.1038/s41467-020-14997-4>

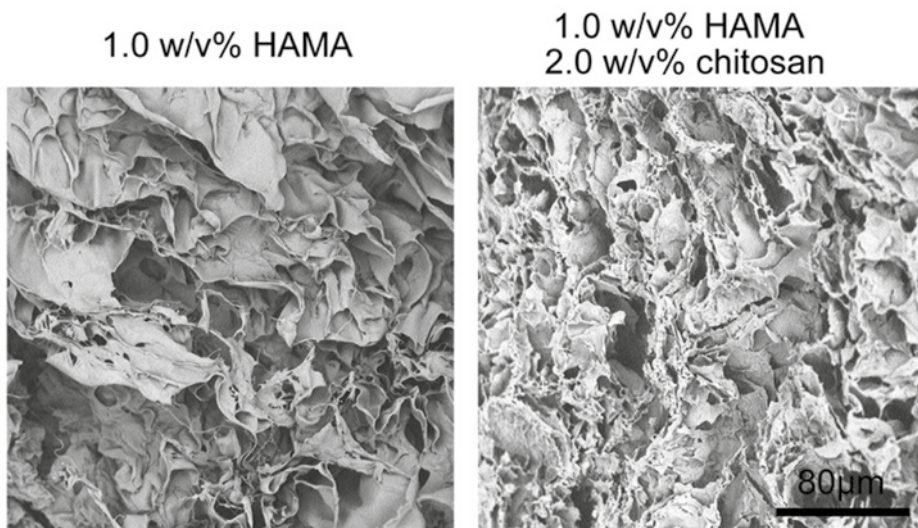
Supplementary Materials



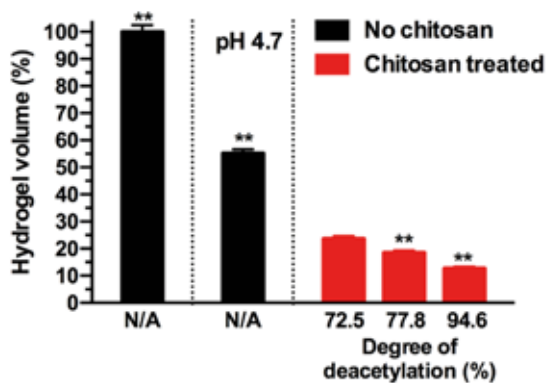
Supplementary Figure 1. Chemical structures of HAMA, chitosan, and their charge complexation interaction. The primary amine groups on chitosan and the carboxyl groups on HAMA undergo a complexation interaction, followed by water expulsion from the hydrogel, which forms the basis of the shrinking behavior of the HAMA hydrogels.



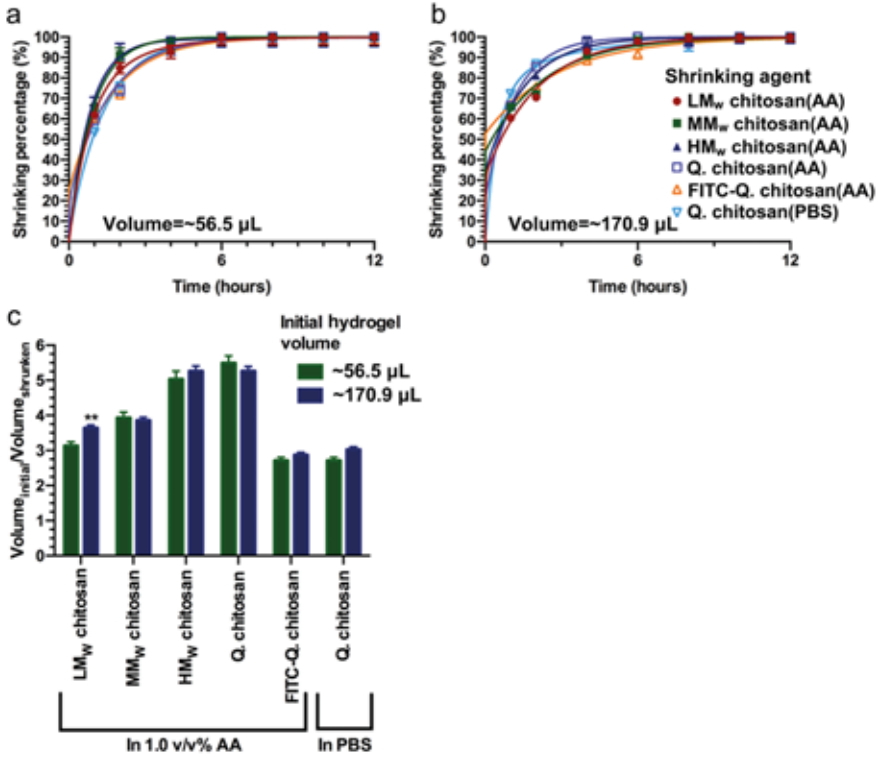
Supplementary Figure 2. Changes in HAMA concentration before and after shrinkage. Estimated changes of concentrations of HAMA in the hydrogels made with different initial HAMA concentrations after shrinkage in 2.0 w/v% HM_{w} chitosan dissolved in 1.0 v/v% acetic acid aqueous solution for 24 h. ** $P < 0.01$; one-way ANOVA (compared with the values of corresponding as-prepared samples); mean \pm SD ($n = 3$).



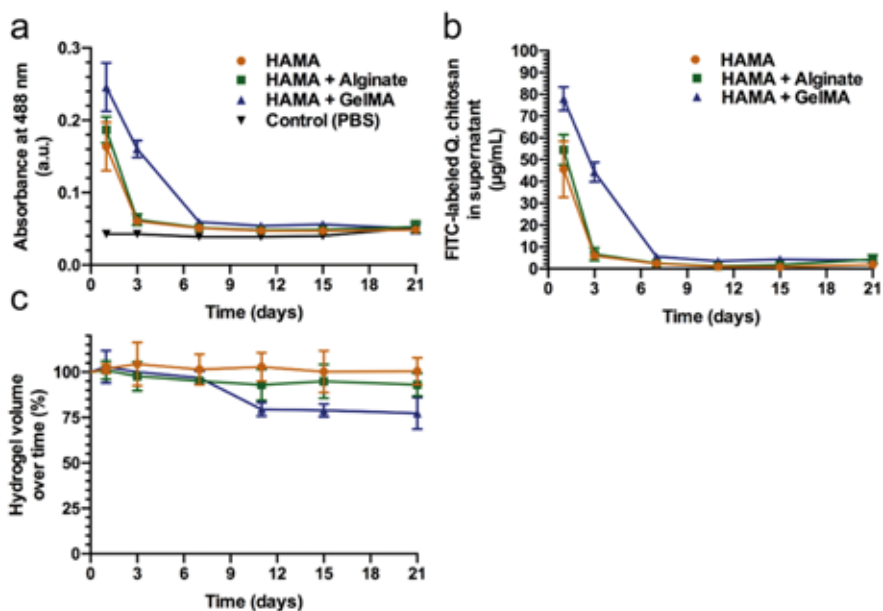
Supplementary Figure 3. SEM images of HAMA hydrogels before and after shrinkage. 1.0 w/v% HAMA hydrogel constructs (left) before shrinkage and (right) shrunk in 2.0 w/v% M_w chitosan for 24 h.



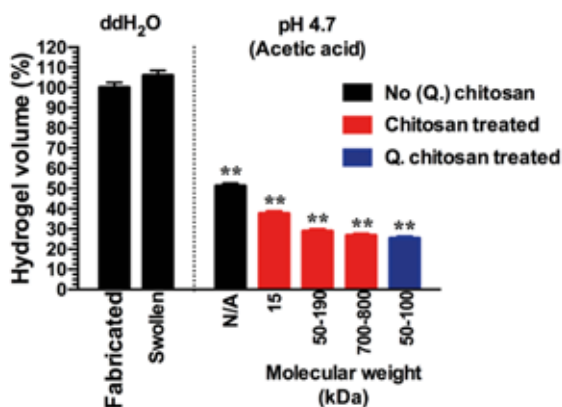
Supplementary Figure 4. Changes in HAMA hydrogel volume. Changes in volumes of 1.0 w/v% HAMA hydrogel discs as-prepared, shrunk in 1.0 v/v% acetic acid aqueous solutions (pH = 4.7) or 2.0 w/v% chitosan of different deacetylations in 1.0 v/v% acetic acid aqueous solutions (pH = 4.7). **P < 0.01; one-way ANOVA (compared with the values of samples in deacetylation = 72.5% group); mean \pm SD% (n = 3).



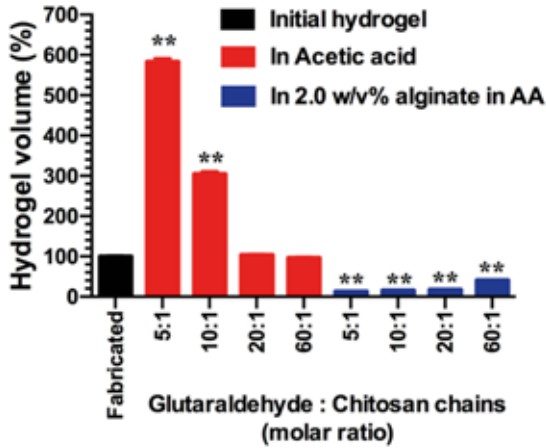
Supplementary Figure 5. Shrinking kinetics of 2.0 w/v% HAMA hydrogels of two different volumes. (a, ~56.5 µL and b, ~170.9 µL), in 2.0 w/v% chitosan of different molecular weights and types in 1.0 v/v% acetic acid aqueous solution (AA) or in PBS. c, Corresponding quantitative analyzes of the shrinkage ratio (initial volume/shrunken volume) in 2.0 w/v% chitosan of different molecular weights and types in 1.0 v/v% acetic acid aqueous solution or in PBS, **P < 0.01; two-tailed Student's t-test (c, compared with the hydrogel of ~56.5µL in initial volume); mean ± s.d. (n = 3).



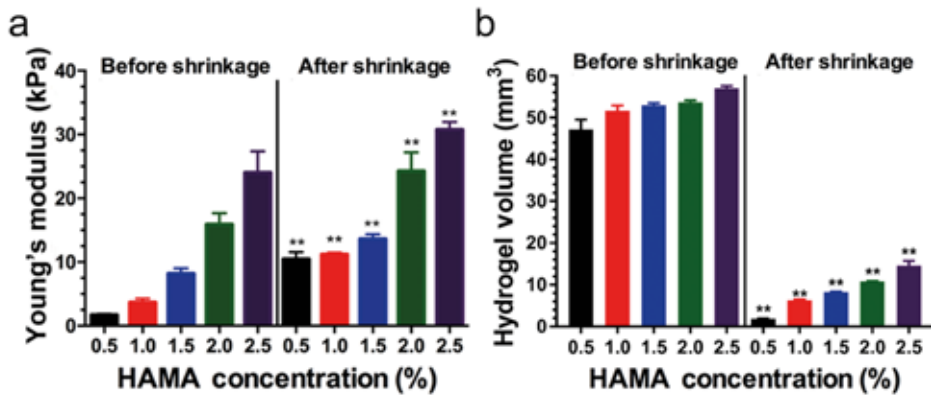
Supplementary Figure 6. Stability of shrunken hydrogels. **a**, Quantitative analyses of absorbance ($\lambda = 488$ nm) of the supernatant from fully shrunken hydrogels in PBS as a function of time, made of 2.0 w/v% HAMA, 1.5 w/v% HAMA + 0.5 w/v% alginate, and 0.5 w/v% HAMA + 2.0 w/v% GelMA, and the control group (PBS). **b**, Quantitative analyses of FITC-labeled Q. chitosan in the supernatant from fully shrunken hydrogels in PBS as a function of time, made of 2.0 w/v% HAMA, 1.5 w/v% HAMA + 0.5 w/v% alginate, and 0.5 w/v% HAMA + 2.0 w/v% GelMA. **c**, Quantitative analyses of volume changes of fully shrunken hydrogels in PBS as a function of time, made of 2.0 w/v% HAMA, 1.5 w/v% HAMA + 0.5 w/v% alginate, and 0.5 w/v% HAMA + 2.0 w/v% GelMA. mean \pm s.d. (n = 5).



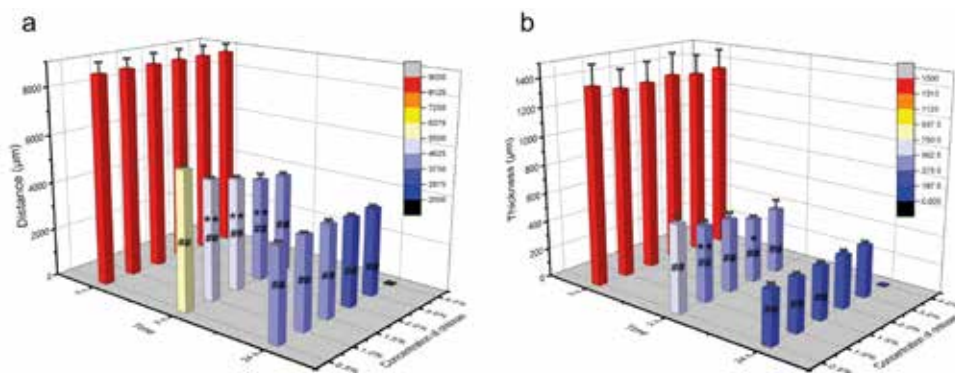
Supplementary Figure 7. Changes in alginate hydrogel volume. Changes in volumes of alginate hydrogel discs as-prepared, swollen in de-ionized water, or shrunken in 2.0 w/v% chitosan of different molecular weights and types in 1.0 v/v% acetic acid aqueous solutions (pH = 4.7). **P < 0.01; one-way ANOVA (compared with the values of corresponding as-prepared samples); mean \pm s.d. (n = 3).



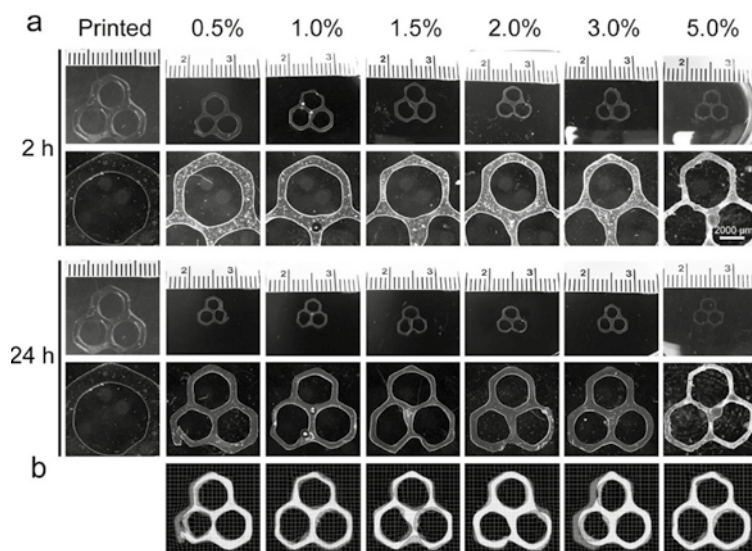
Supplementary Figure 8. Quantitative analyses of 2.0 w/v% HMw chitosan hydrogels. Chitosan hydrogels are swollen and shrunken under different conditions with or without 2.0 w/v% alginate in 1.0 v/v% acetic acid aqueous solution. ** $P < 0.01$; one-way ANOVA (compared with the values of corresponding as-prepared samples); mean \pm s.d. ($n = 3$).



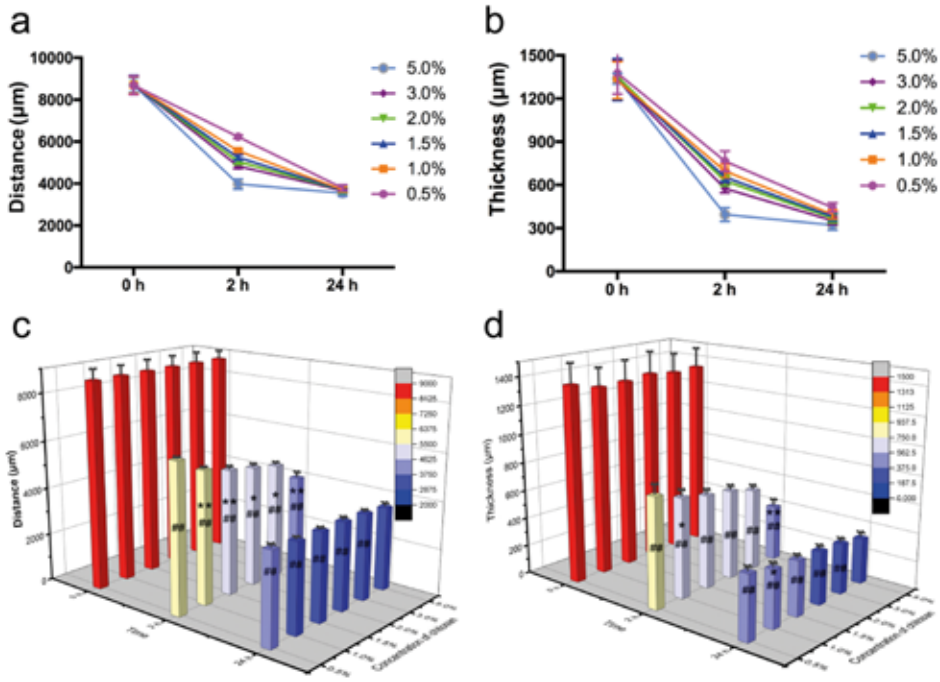
Supplementary Figure 9. Changes in Young's modulus and volume of HAMA hydrogel constructs. **a**, Change in Young's modulus of HAMA hydrogels made with different HAMA concentrations before and after shrinking in 2.0 w/v% HMw chitosan. **b**, Change in volume of HAMA hydrogels made with different HAMA concentrations before and after shrinking in 2.0 w/v% HMw chitosan. ** $P < 0.01$; one-way ANOVA (compared with the values of corresponding as-prepared samples); mean \pm s.d. ($n = 3$ or 4).



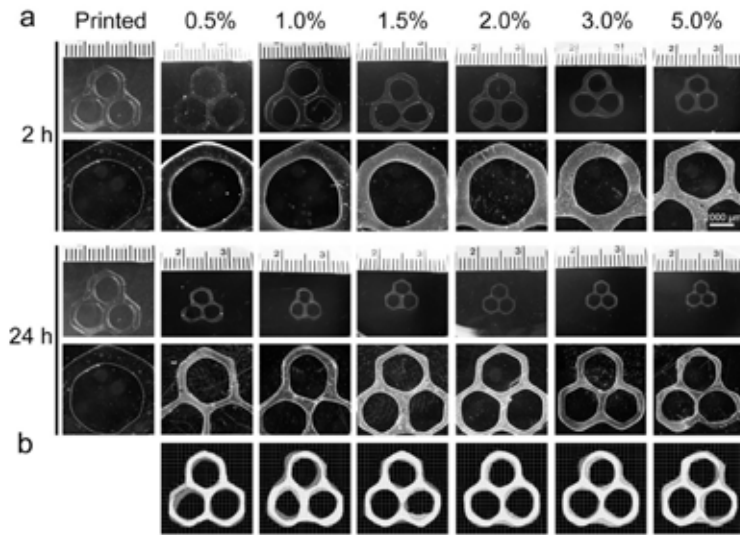
Supplementary Figure 10. Quantitative analysis of distance and thickness of HAMA constructs. Quantitative analyses of (a) side-to-side distance and (b) thickness changes of extrusion-printed HAMA constructs (2.0 w/v%) following shrinking in different concentrations of HMw chitosan dissolved in 1.0 v/v% acetic acid aqueous solution. * $P < 0.05$, ** $P < 0.01$; one-way ANOVA (compared with the group shrunk in chitosan solution of the immediate lower concentration); ## $P < 0.01$; one-way ANOVA (compared with the preceding time point in the same group); mean \pm s.d. ($n = 10$).



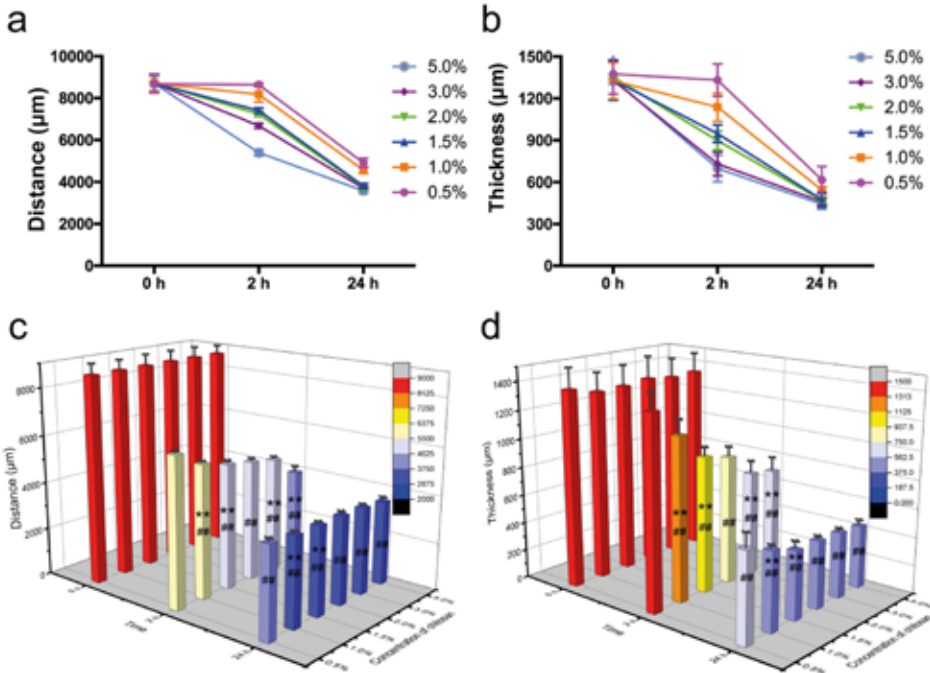
Supplementary Figure 11. Size changes of printed HAMA hexagons. a, Photographs (upper) and micrographs (lower) showing size changes of printed HAMA hexagons (2.0 w/v%) at 2 h and 24 h of shrinking in different concentrations of Q. chitosan (0.5 - 5.0 w/v%) dissolved in 1.0 v/v% acetic acid aqueous solution. b, Vector-field maps comparing the 24 h-shrinking images (magenta) to the corresponding 2 h-shrinking images (green) by a B-spline-based non-rigid registration algorithm, where the overlaps appear in white and the grids show local distortions. Note that the 2 h-shrinking images have been rescaled to match the sizes of the 24 h-shrinking images to enable comparisons.



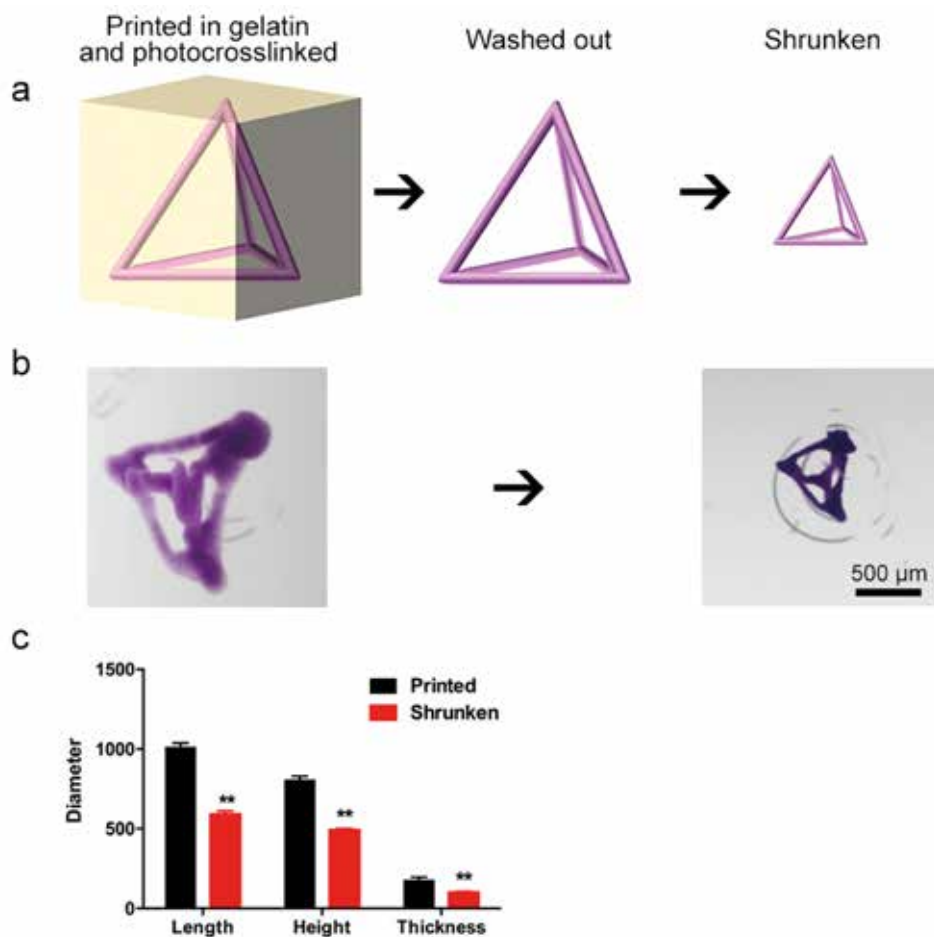
Supplementary Figure 12. Quantitative analysis of distance and thickness of HAMA constructs. Quantitative analyses of (a, c) side-to-side distance and (b, d) thickness changes of extrusion-printed HAMA constructs (2.0 w/v%) following shrinking in different concentrations of Q. chitosan (0.5 - 5.0 w/v%) dissolved in 1.0 v/v% acetic acid aqueous solution. *P < 0.05, **P < 0.01; one-way ANOVA (c, d, compared with the group shrunk in Q. chitosan solution of the immediate lower concentration); ##P < 0.01; one-way ANOVA (c, d, compared with the preceding time point in the same group); mean ± s.d. (n = 10).



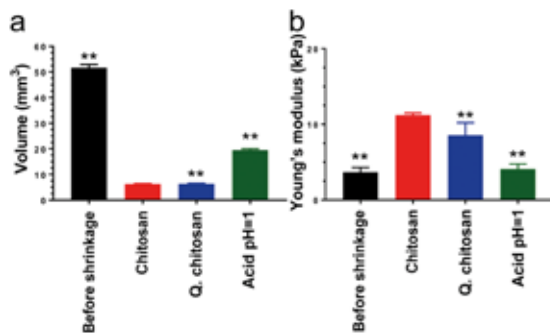
Supplementary Figure 13. Size changes of printed HAMA hexagons. **a**, Photographs (upper) and micrographs (lower) showing size changes of printed HAMA hexagons (2.0 w/v%) at 2 h and 24 h of shrinking in different concentrations of Q. chitosan (0.5 - 5.0 w/v%) dissolved in de-ionized water. **b**, Vector-field maps comparing the 24 h-shrinking images (magenta) to the corresponding 2 h-shrinking images (green) by a B-spline-based non-rigid registration algorithm, where the overlaps appear in white and the grids show local distortions. Note that the 2 h-shrinking images have been rescaled to match the sizes of the 24 h-shrinking images to enable comparisons.



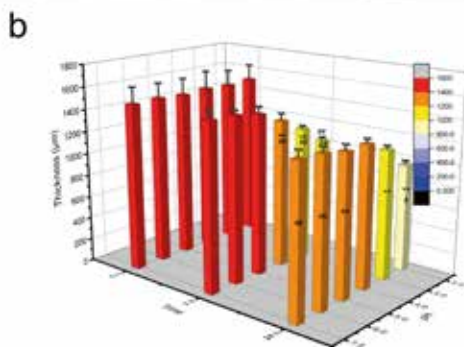
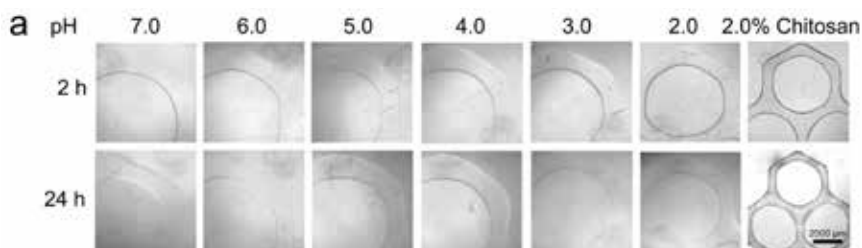
Supplementary Figure 14. Quantitative analysis of distance and thickness of HAMA constructs Quantitative analyses of (a, c) side-to-side distance and (b, d) thickness changes of extrusion-printed HAMA constructs (2.0 w/v%) following shrinking in different concentrations of Q. chitosan (0.5 - 5.0 w/v%) dissolved de-ionized water. **P < 0.01; one-way ANOVA (c, d, compared with the group shrunk in Q. chitosan solution of the immediate lower concentration); ##P < 0.01; one-way ANOVA (c, d, compared with the preceding time point in the same group); mean ± s.d. (n = 10).



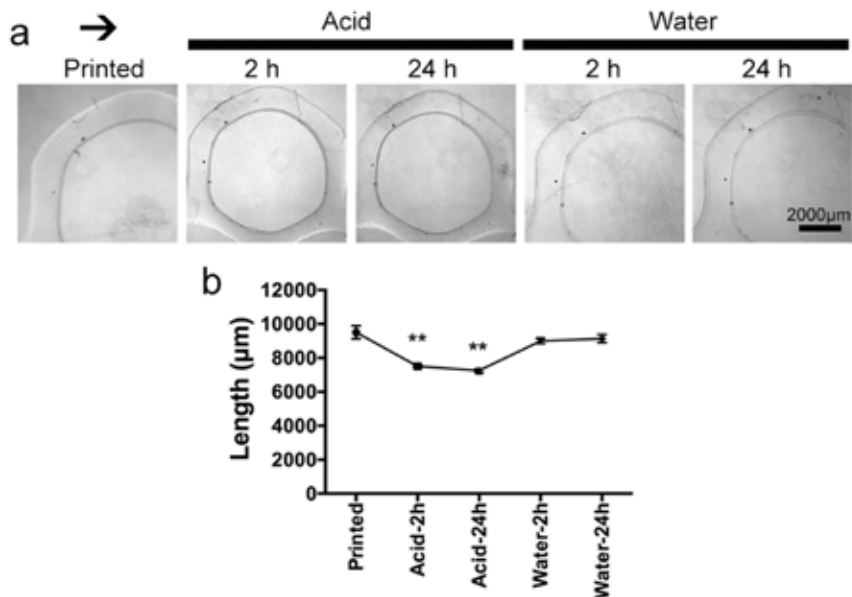
Supplementary Figure 15. Shrinking of 3D structures, schematics, photographs and analyses. **a**, Schematic representation of the printing and photocrosslinking, washing, and shrinking process of a 3D structure. **b**, Photographs showing a printed and photocrosslinked HAMA (2.0 w/v%) pyramid in gelatin (1.5 w/v%), left, fully shrunken pyramid in 1.0 w/v% HM_w chitosan dissolved in 1.0 v/v% acetic acid aqueous solution for 24 h (right). **c**, Quantitative analyses of length, height and thickness changes of extrusion-printed HAMA pyramid following shrinking in 1.0 w/v% HM_w chitosan solution in 1.0 v/v% acetic acid aqueous solution. **P < 0.01; two-tailed Student's t-test (compared with the corresponding as-printed structures); mean ± s.d. (n = 3).



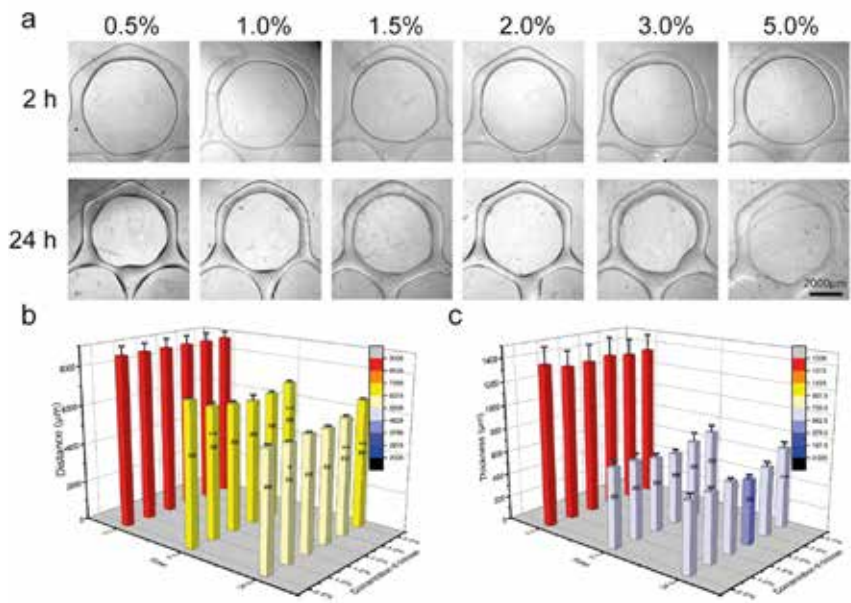
Supplementary Figure 16. Changes in volume and Young's modulus of HAMA hydrogel constructs. **a**, Changes in volume of 2.0 w/v% HAMA hydrogels before and after shrinkage in HM_w chitosan, Q. chitosan (both dissolved at 2.0 w/v % in 1.0 v/v % acetic acid aqueous solution), and an aqueous solution of perchloric acid at pH 1.0. **b**, Change in Young's modulus of 2.0 w/v% HAMA hydrogels before and after shrinkage in HM_w chitosan, Q. chitosan (both dissolved at 2.0 w/v % in 1.0 v/v % acetic acid aqueous solution), and an aqueous solution of perchloric acid at pH 1.0. **P < 0.01; one-way ANOVA (compared with the group shrunken in chitosan); mean ± s.d. (n = 3 or 4).



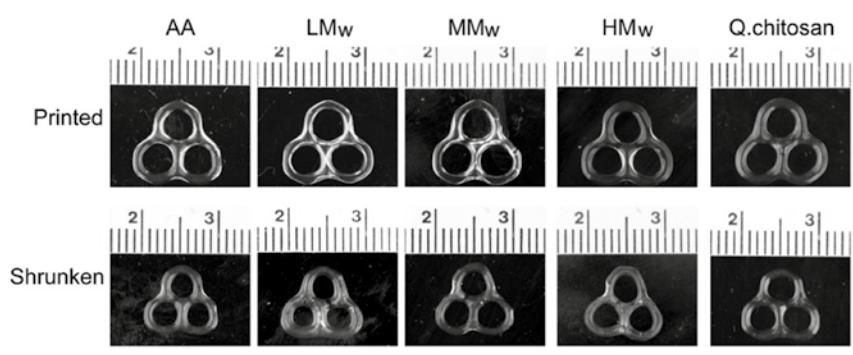
Supplementary Figure 17. Quantitative analyses of sizes changes of printed HAMA hexagons. **a**, Micrographs showing size changes of printed HAMA hexagons (2.0 w/v%) at 2 h and 24 h of incubation in acetic acid aqueous solutions of different pH values (adjusted using acetic acid). The construct shrunken in 2.0 w/v% HM_w chitosan dissolved in 1.0 v/v% acetic acid aqueous solution was used as the control. **b**, Corresponding quantitative analyses. **P < 0.01; one-way ANOVA (compared with the group pH = 7); #P < 0.05, ##P < 0.01; one-way ANOVA (compared with the preceding time point at the same pH); mean ± s.d. (n = 10).



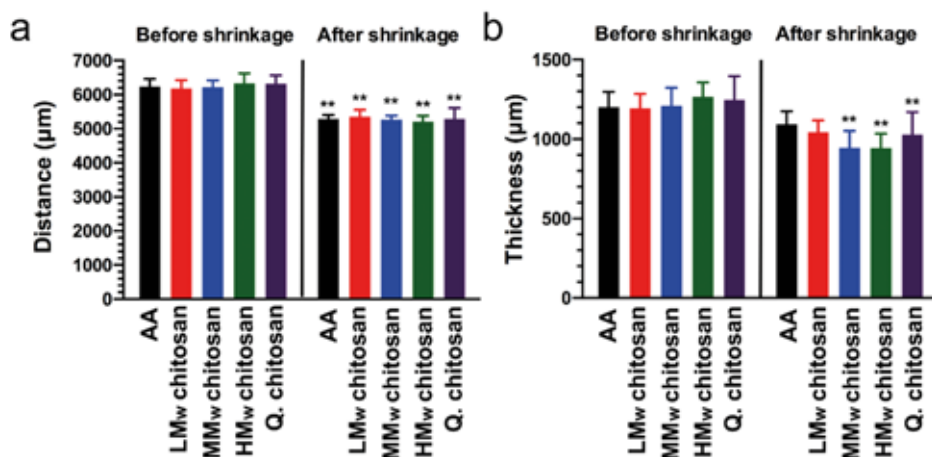
Supplementary Figure 18. Size change in acid and water. **a**, Micrographs showing size change of a printed HAMA construct (2.0 w/v%) at 2 h and 24 h of incubation in acetic acid aqueous solutions at pH = 2, followed by incubation again in water for another 24 h. **b**, Corresponding quantitative analyses of the change in the side-to-side distance. **P < 0.01; one-way ANOVA (compared with the as-printed structures); mean ± s.d. (n = 10).



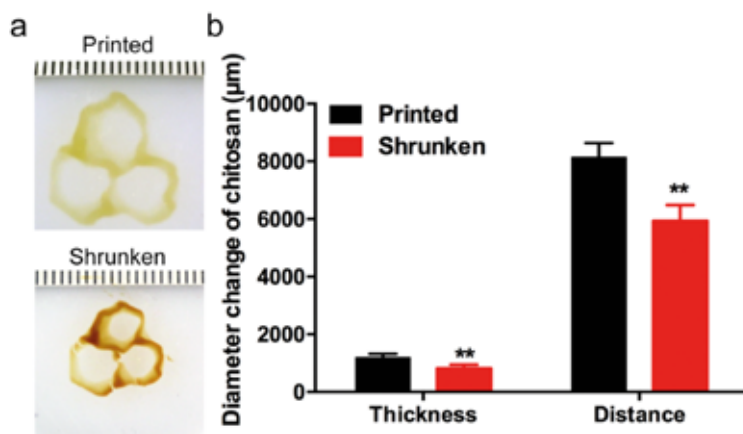
Supplementary Figure 19. Changes in size of HAMA hexagons. **a**, Micrographs showing size changes of printed HAMA hexagons (2.0 w/v%) at 2 h and 24 h of shrinking in different concentrations of Q. chitosan (0.5 - 5.0 w/v%) dissolved in DMEM. **b, c**, Quantitative analyses of **(b)** side-to-side distance and **(c)** thickness changes of extrusion-printed HAMA constructs (2.0 w/v%) following shrinking in different concentrations of chitosan dissolved in DMEM. *P < 0.05, **P < 0.01; one-way ANOVA (**b, c**, compared with the group shrunk in chitosan solution of the immediate lower concentration); #P < 0.05, ##P < 0.01; one-way ANOVA (**b, c**, compared with the preceding time point in the same group of concentration); mean ± s.d. (n = 10).



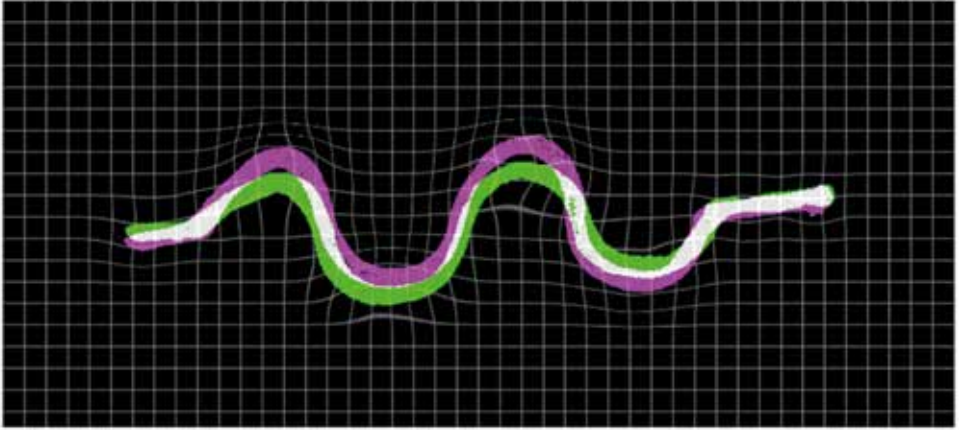
Supplementary Figure 20. Changes in size Alginate hexagons. Micrographs showing size changes of printed and crosslinked 2.0 w/v% alginate hexagons before and after shrinkage in 1.0 v/v% acetic acid aqueous solution, or in 2.0 w/v% chitosan of different molecular weights and types in 1.0 v/v% acetic acid aqueous solutions.



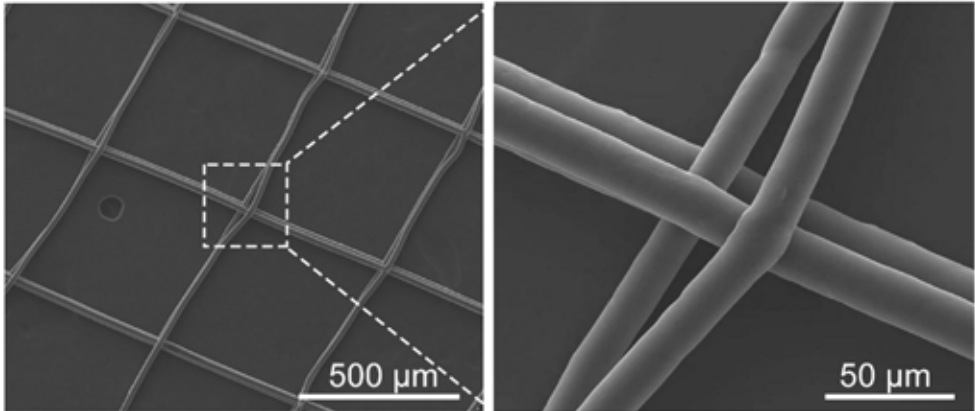
Supplementary Figure 21. Corresponding quantitative analyses of size changes of the printed 2.0 w/v% alginate hexagons, in 1.0 v/v% acetic acid aqueous solution, or in 2.0 w/v% chitosan of different molecular weights and types in 1.0 v/v% acetic acid aqueous solutions. (a) side-to-side distance and (b) thickness. **P < 0.01; one-way ANOVA (compared with the corresponding as-printed structures); mean ± s.d. (n = 6).



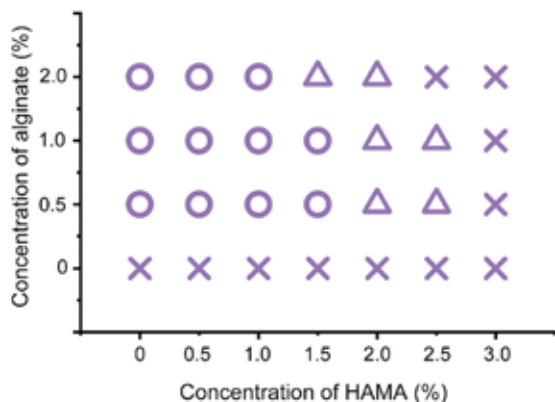
Supplementary Figure 22. Size changes of chitosan hexagons. a, Photographs showing size changes of printed chitosan hexagons (2.5 w/v%, crosslinked by 800-µM glutaraldehyde) before and after shrinkage in 2.0 w/v% alginate solution in 1.0 v/v% acetic acid aqueous solution. b, Quantitative analyses of thickness and side-to-side distance changes of extrusion-printed chitosan constructs following shrinking in 2.0 w/v% alginate solution in 1.0 v/v% acetic acid aqueous solution. **P < 0.01; two-tailed Student's t-test (compared with the corresponding as-printed structures); mean ± s.d. (n = 10).



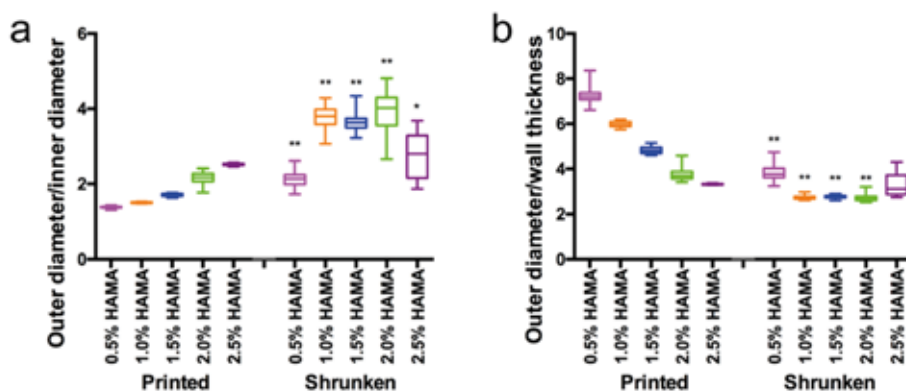
Supplementary Figure 23. Vector-field map of the sacrificially printed microchannel-embedded HAMA hydrogel (relating to Figure 3b). Comparing the post-shrinking image (magenta) to the corresponding pre-shrinking image (green) by a B-spline-based non-rigid registration algorithm, where the overlaps appear in white and the grids show local distortions. Note that the pre-shrinking images have been rescaled to match the sizes of the post-shrinking images to enable comparisons.



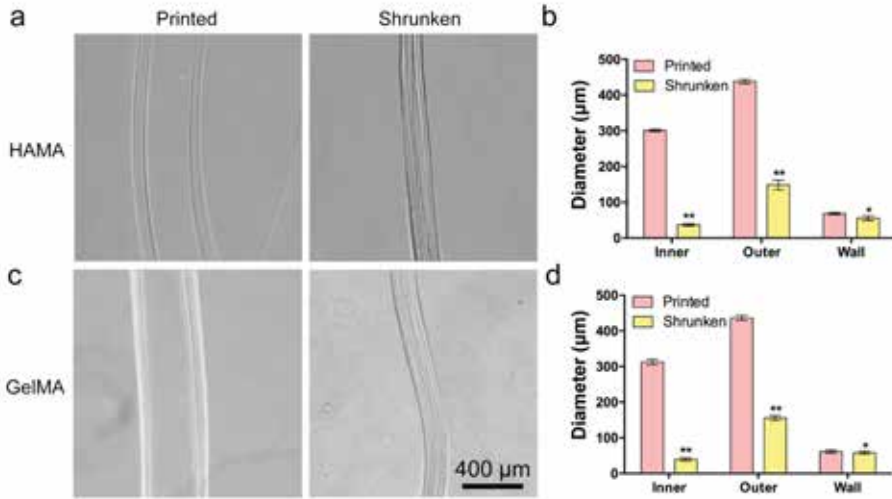
Supplementary Figure 24. SEM images of a PCL mesh printed with MEW.



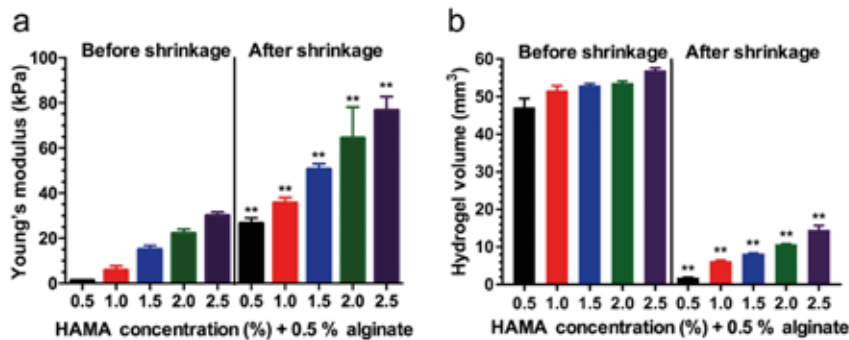
Supplementary Figure 25. Printability mapping of HAMA/alginate ink of different concentrations of the components. o: printable; Δ: partially printable but not uniform; x: non-printable.



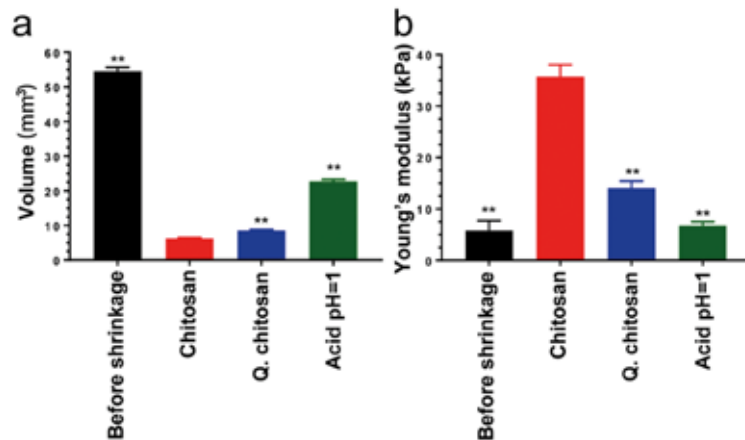
Supplementary Figure 26. Quantitative analyses of shrinkage. Quantitative analyses of the ratios of (a) OD/ID and (b) OD/WT before and after shrinkage, for printed tubular HAMA/alginate structures (relating to Fig. 4). ** $P < 0.01$; one-way ANOVA (a, b, compared with the corresponding as-printed structures); mean \pm s.d. (n = 40).



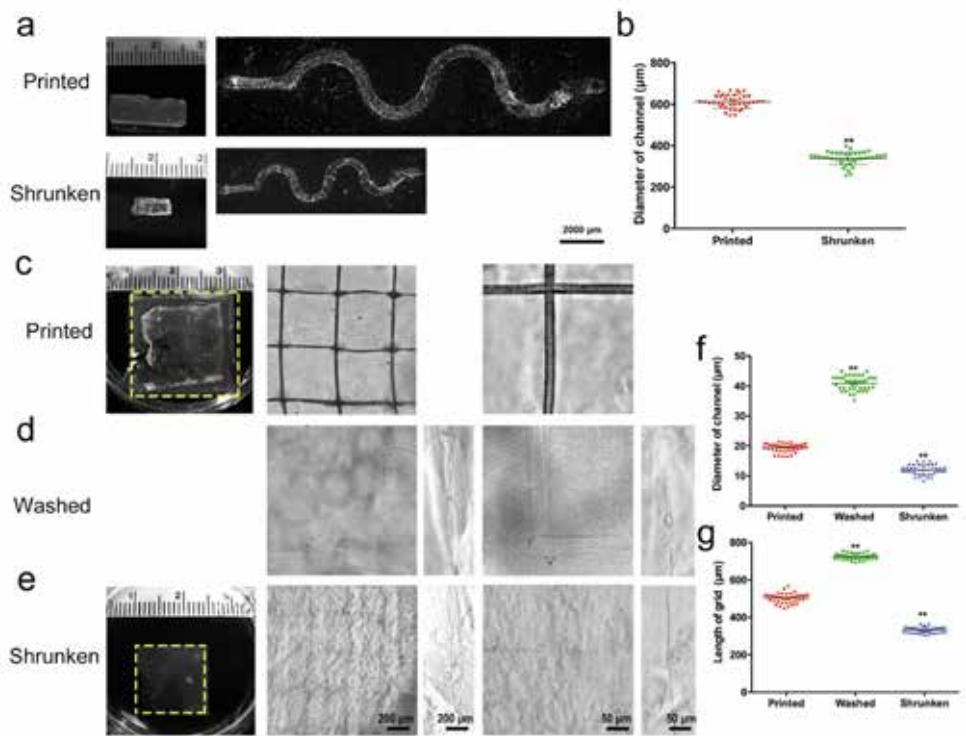
Supplementary Figure 27. Coaxial printing of small size cannular constructs and their shrinking behavior. **a**, Micrographs showing the coaxial printing of cannular HAMA-based constructs before (left) and after (right) 24 h of shrinkage in 2.0 w/v% HM_w chitosan dissolved in 1.0 v/v% acetic acid aqueous solution. **b**, Corresponding quantitative analyses of diameter (inner diameter, outer diameter, wall thickness) changes before and after shrinkage of HAMA-based constructs. **c**, Micrographs showing the coaxial printing of cannular GelMA-based constructs before (left) and after (right) 24 h of shrinkage in 2.0 w/v% HM_w chitosan dissolved in 1.0 v/v% acetic acid aqueous solution. **d**, Corresponding quantitative analyses of diameter (inner diameter, outer diameter, wall thickness) changes before and after shrinkage of GelMA-based constructs. **b, d**, * $P < 0.05$, ** $P < 0.01$; two-tailed Student's *t*-test (**b, d**, compared with the corresponding as-printed structures); mean \pm s.d. ($n = 40$).



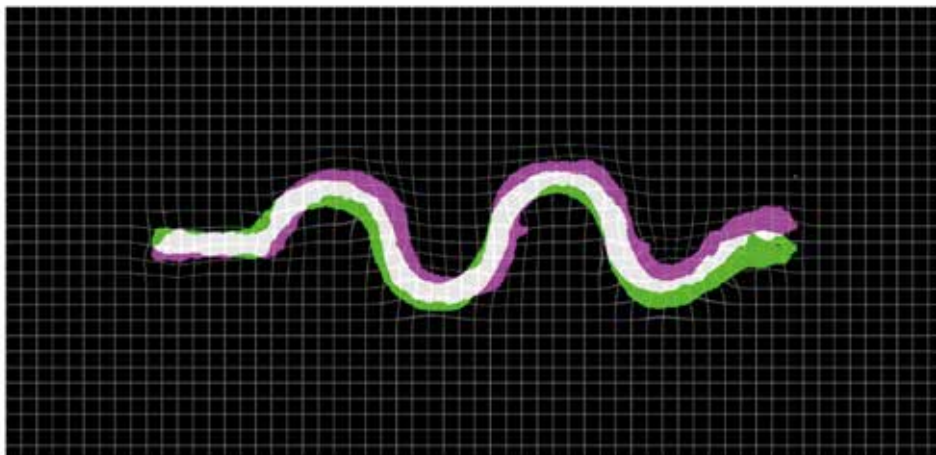
Supplementary Figure 28. Changes in Young's modulus and volume of HAMA/alginate hydrogel constructs. **a**, Change in Young's modulus of HAMA hydrogels containing 0.5 w/v% alginate made with different concentrations of HAMA before and after shrinking in 2.0 w/v% HM_w chitosan. **b**, Change in volume of HAMA hydrogels containing 0.5 w/v% alginate made with different concentrations of HAMA before and after shrinking in 2.0 w/v% HM_w chitosan. ** $P < 0.01$; one-way ANOVA (compared with the values of corresponding as-prepared samples); mean \pm s.d. ($n = 3$ or 4).



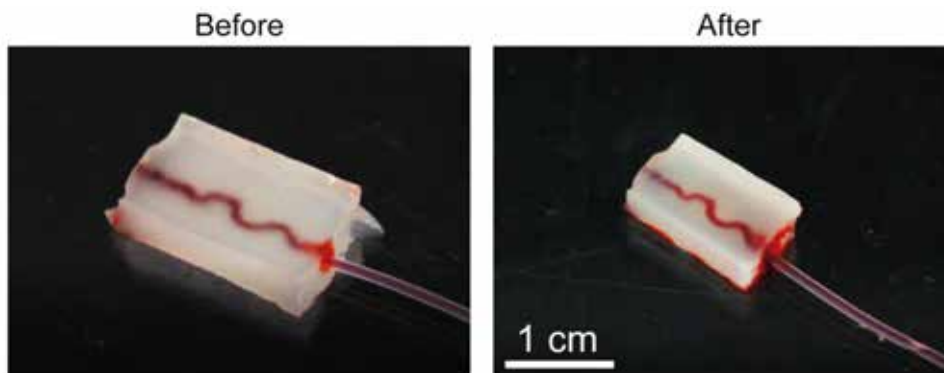
Supplementary Figure 29. Changes in volume and Young's modulus of HAMA/alginate hydrogel constructs. **a**, Change in volume of 1.0 w/v% HAMA/0.5 w/v% alginate hydrogels before and after shrinkage in HM_w chitosan, Q. chitosan (both dissolved at 2.0 w/v % in 1.0 v/v % acetic acid aqueous solution), and an aqueous solution of perchloric acid at pH 1.0. **b**, Change in Young's modulus of 2.0 w/v% HAMA/0.5 w/v% alginate hydrogels before and after shrinkage in HM_w chitosan, Q. chitosan (both dissolved at 2.0 w/v % in 1.0 v/v % acetic acid aqueous solution), and an aqueous solution of perchloric acid at pH 1.0. **P < 0.01; one-way ANOVA (compared with the group shrunken in the chitosan solution); mean ± s.d. % (n = 3 or 4).



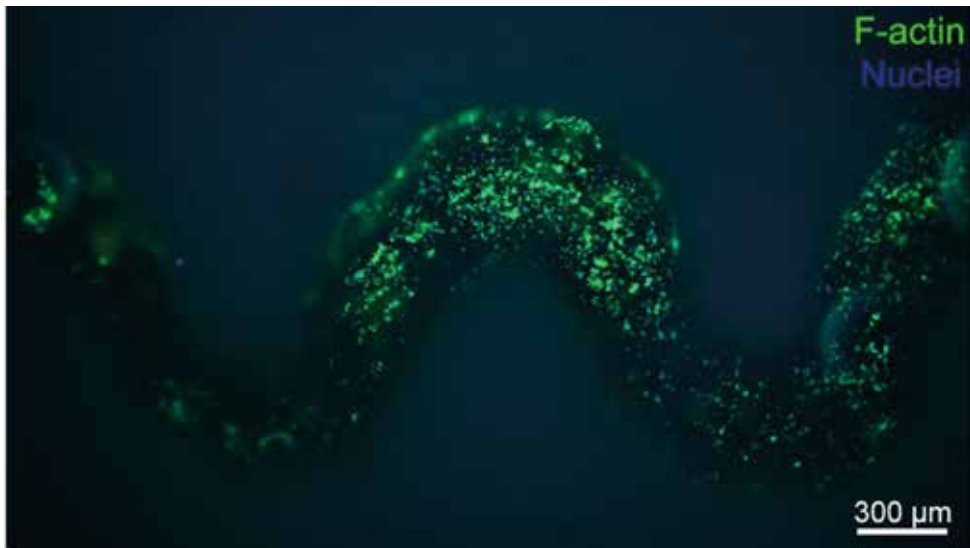
Supplementary Figure 30. Sacrificial printing of microchannel-embedded GelMA constructs and their shrinking behavior. **a**, Photographs showing the size change of the GelMA construct (5.0 w/v%) along with the embedded microchannel before (upper) and after (lower) 24 h of shrinkage in 2.0 w/v% HM_w chitosan dissolved in 1.0 v/v% acetic acid aqueous solution. **b**, Corresponding quantitative analysis of diameter change of the microchannel before and after shrinking. **c, d, e**, Photographs (left) and micrographs (right) showing the size change of the GelMA construct (5.0 w/v%) along with the embedded microchannel printed (**c**), washed (**d**) and shrunken (**e**) in 2.0 w/v% HM_w chitosan dissolved in 1.0 v/v% acetic acid aqueous solution (24 h). **f, b**, Corresponding quantitative analyses of changes in (**f**) diameter of the microchannel and (**g**) length of the grid before and after shrinking. ****** $P < 0.01$; two-tailed Student's t-test (**b**), one-way ANOVA (**f, g**, compared with the corresponding as-printed structures); mean \pm s.d. (n = 40).



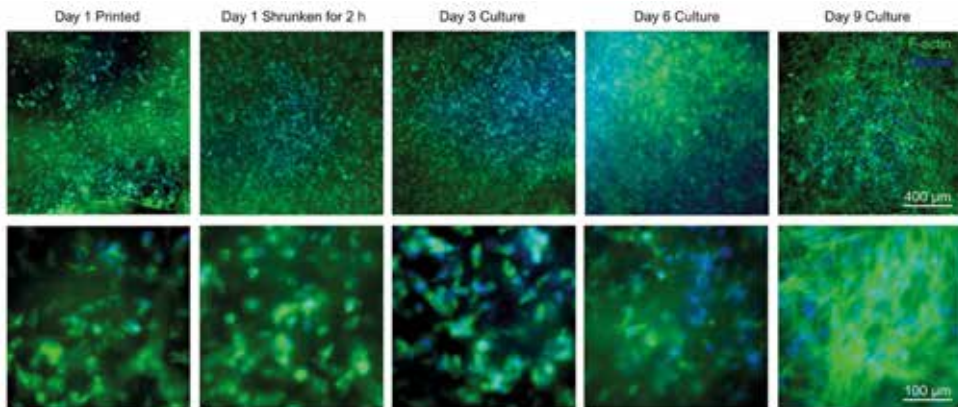
Supplementary Figure 31. Vector-field map of the sacrificially printed microchannel-embedded GelMA hydrogel (relating to Supplementary Figure 30a). Comparing the post-shrinking image (magenta) to the corresponding pre-shrinking image (green) by a B-spline-based non-rigid registration algorithm, where the overlaps appear in white and the grids show local distortions. Note that the pre-shrinking images have been rescaled to match the sizes of the post-shrinking images to enable comparisons.



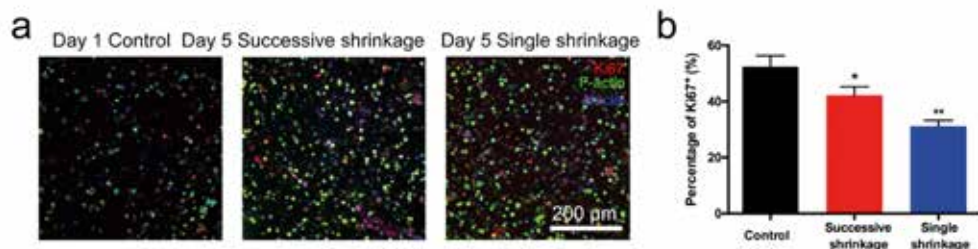
Supplementary Figure 32. Photographs showing perfusion of the same embed sacrificially printed microchannel-embedded GelMA/HAMA hydrogel construct. (a) Before and (b) after shrinking in 2.0 w/v% HM_w chitosan dissolved in 1.0 v/v% acetic acid aqueous solution. After perfusion before shrinking, the construct was immersed in a large volume of water to wash out all the dyes to facilitate subsequent shrinking and re-perfusion.



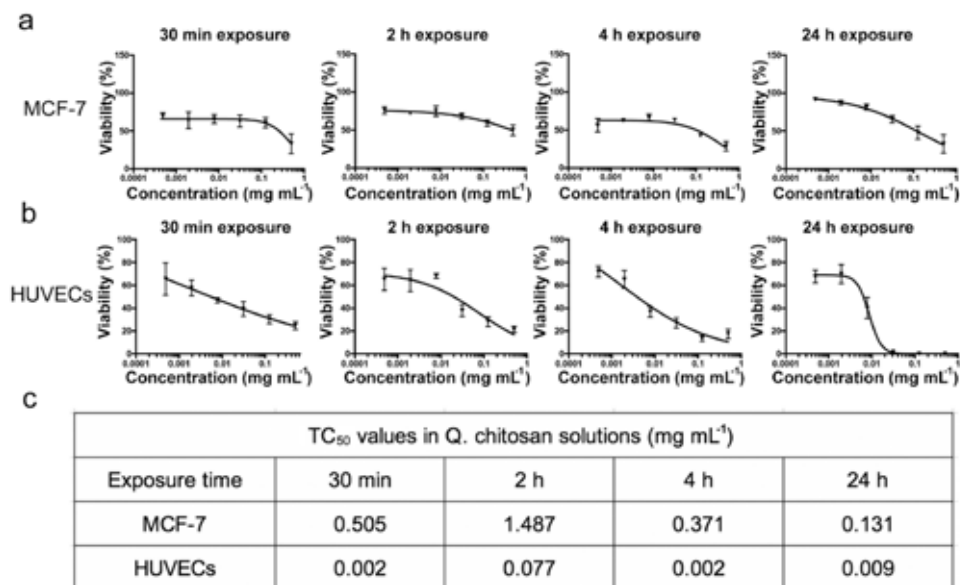
Supplementary Figure 33. Immunofluorescent imaging of HUVECs in printed hydrogel. Presence of HUVECs on the internal surfaces of a shrunken microchannel in an embedded sacrificially printed GelMA/HAMA hydrogel construct, at day 5, stained for F-actin (green) and nuclei (blue).



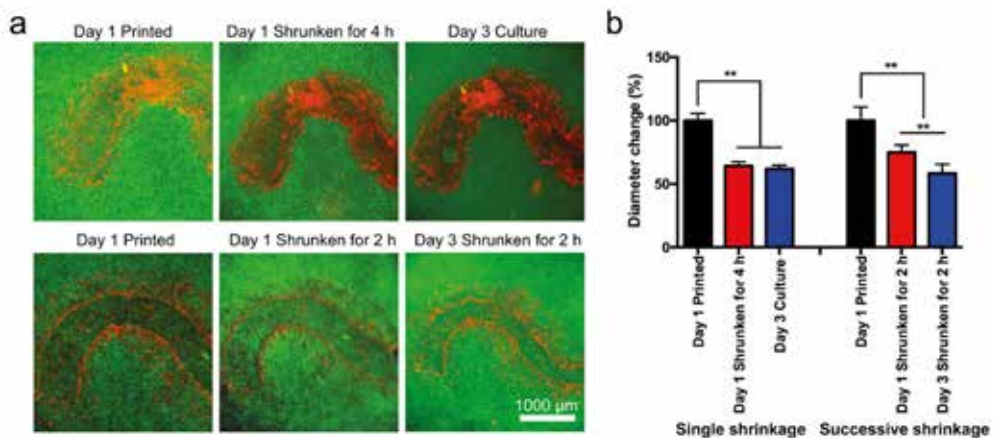
Supplementary Figure 34. The spreading of C2C12 embedded in the GelMA/HAMA constructs before and after shrinking. Morphological observation of C2C12 embedded in mixed hydrogel before and after shrinkage for 1, 3, 6, and 9 days, stained for F-actin (green) and nuclei (blue).



Supplementary Figure 35. HUVECs proliferation after shrinking. **a**, Fluorescence micrographs of HUVECs in GelMA/HAMA constructs without any treatment (control) as well as after successive shrinkage and single shrinkage, stained for Ki67 (red), F-actin (green), and nuclei (blue). **b**, Corresponding quantitative analyses of the percentages of Ki67+ stained nuclei in the three groups. * $P < 0.05$, ** $P < 0.01$; one-way ANOVA (compared with the control group on Day 1), mean \pm s.d. ($n = 3$)



Supplementary Figure 36. TC₅₀ values of Q. chitosan for MCF-7 cells and HUVECs **a**, The viability of MCF-7 cells exposed to different concentrations of Q. chitosan solutions in culture medium for 30 min, 2 h, 4 h, and 24 h. **b**, The viability of HUVECs exposed to different concentrations of Q. chitosan solutions in culture medium for 30 min, 2 h, 4 h, and 24 h. **c**, The calculated TC₅₀ values of Q. chitosan for MCF-7 cells and HUVECs. mean \pm s.d. ($n = 2$ for MCF-7, $n = 4$ for HUVECs).



Supplementary Figure 37. Changes in microchannel diameter after shrinkage. **a**, Micrographs showing the changes of the microchannel diameters (red) and the GFP-HUVECs densities (green) in sacrificially bioprinted GelMA/HAMA constructs using Pluronic F-127 as the fugitive bioink, following single shrinkage (upper) and successive shrinkage (lower). Pluronic F-127 was stained in red prior to removal to aid visualization of the microchannels. **b**, Corresponding quantitative analyses of microchannel diameter changes. $**P < 0.01$; one-way ANOVA; mean \pm s.d. (n = 10).

Supplementary Table 1. Characteristic of different types of chitosan and the shrinkage ratio of HAMA hydrogel.

Shrinking agent	Deacetylation degree ¹ (%)	Quaternization degree ¹ (%)	Polymer Mw ¹ (kDa)	Theoretical average charge per monomer	Average positive charge density ² (+1 per x Da)	Hydrogel ³ volume after shrinking (%)
Chitosan	85	0	~15	0.62	271.8	28.9 ± 1.1
	85		50-190			21.6 ± 0.9
	85		700-800			11.0 ± 0.7
	72.5		100-250	0.53	328.8	23.6 ± 1.0
	77.8			0.56	298.7	18.5 ± 0.8
	94.6			0.69	238.3	12.6 ± 0.7
Q chitosan	90	95	50-100	1.6	163.4	9.7 ± 0.4

¹per suppliers' information

²at pH 4.7 (1.0 v/v% acetic acid aqueous solution), with a pKa of 6.5 for chitosan amine.

³HAMA hydrogels (1.0 w/v%) incubated in 2.0 w/v% of the chitosan dissolved in 1.0 v/v% acetic acid aqueous solution for 24 h.

References

1. Murphy, S. V. & Atala, A. 3D bioprinting of tissues and organs. *Nat. Biotechnol.* 32, 773–785 (2014).
2. Lorenzo, M. et al. Biofabrication strategies for 3D in vitro models and regenerative medicine. *Nat. Rev. Mater.* 3, 21–37 (2018).
3. Malda, J. et al. 25th anniversary article: engineering hydrogels for biofabrication. *Adv. Mater.* 25, 5011–5028 (2013).
4. Miri, A. K. et al. Effective bioprinting resolution in tissue model fabrication. *Lab a Chip* 19, 2019–2037 (2019).
5. Zhang, Y., Yu, Y., Chen, H. & Ozbolat, I. T. Characterization of printable cellular micro-fluidic channels for tissue engineering. *Biofabrication* 5, 025004 (2013).
6. Tromayer, M. et al. Wavelength-optimized two-photon polymerization using initiators based on multipolar aminostyryl-1,3,5-triazines. *Sci. Rep.* 8, 17273 (2018).
7. Oran, D. et al. 3D nanofabrication by volumetric deposition and controlled shrinkage of patterned scaffolds. *Science* 362, 1281–1285 (2018).
8. Highley, C. B., Rodell, C. B. & Burdick, J. A. Direct 3D printing of shear-thinning hydrogels into self-healing hydrogels. *Adv. Mater.* 27, 5075–5079 (2015).
9. Ying, G., Jiang, N., Yu, C. & Zhang, Y. S. Three-dimensional bioprinting of gelatin methacryloyl (GelMA). *Bio-Des. Manuf.* 1, 215–224 (2018).
10. Lee, K. Y. & Mooney, D. J. Alginate: properties and biomedical applications. *Prog. Polym. Sci.* 37, 106–126 (2012).
11. Rodrigues, S., Dionisio, M., Lopez, C. R. & Grenha, A. Biocompatibility of chitosan carriers with application in drug delivery. *J. Funct. Biomater.* 3, 615–641 (2012).
12. Li, Y. et al. Lysozyme uptake by oxidized starch polymer microgels. *Biomacromolecules* 11, 1754–1762 (2010).
13. Schuurmans, C. C. L. et al. Complex coacervation-based loading and tunable release of a cationic protein from monodisperse glycosaminoglycan microgels. *Soft Mater.* 14, 6327–6341 (2018).
14. van der Gucht, J., Spruijt, E., Lemmers, M. & Cohen Stuart, M. A. Polyelectrolyte complexes: bulk phases and colloidal systems. *J. Colloid Interface Sci.* 361, 407–422 (2011).
15. de Kruif, C. G., Weinbreck, F. & de Vries, R. Complex coacervation of proteins and anionic polysaccharides. *Curr. Opin. Colloid Interface Sci.* 9, 340–349 (2004).
16. Tang, S. C., Huang, L., Shi, Z. Q. & He, W. Water-based synthesis of cationic hydrogel particles: effect of the reaction parameters and in vitro cytotoxicity study. *J. Mater. Chem. B* 3, 2842–2852 (2015).
17. Rodell, C. B., Dusaj, N. N., Highley, C. B. & Burdick, J. A. Injectable and cytocompatible tough double-network hydrogels through tandem supramolecular and covalent crosslinking. *Adv. Mater.* 28, 8419–8424 (2016).
18. Chen, F., Tillberg, P. W. & Boyden, E. S. Expansion microscopy. *Science* 347, 543–548 (2015).
19. Sahariah, P. & Masson, M. Antimicrobial chitosan and chitosan derivatives: a review of the structure-activity relationship. *Biomacromolecules* 18, 3846–3868 (2017).
20. Zhang, Y. S. et al. Bioprinted thrombosis-on-a-chip. *Lab a Chip* 16, 4097–4105 (2016).
21. Lin, N. Y. C. et al. Renal reabsorption in 3D vascularized proximal tubule models. *Proc. Natl Acad. Sci. USA* 116, 5399–5404 (2019).
22. Kolesky, D. B., Homan, K. A., Skylar-Scott, M. A. & Lewis, J. A. Three-dimensional bioprinting of thick vascularized tissues. *Proc. Natl Acad. Sci. USA* 113, 3179–3184 (2016).
23. Visser, J. et al. Reinforcement of hydrogels using three-dimensionally printed microfibrils. *Nat. Commun.* 6, 6933 (2015).
24. Hochleitner, G. et al. Additive manufacturing of scaffolds with sub-micron filaments via melt electrospinning writing. *Biofabrication* 7, 035002 (2015).

25. Haigh, J. N. *Melt electrospinning writing as a method to form novel hydrogel architectures and constructs*. (Science and Engineering Faculty, Queensland University of Technology, 2017)
26. Carmeliet, P. & Jain, R. K. Molecular mechanisms and clinical applications of angiogenesis. *Nature* 473, 298–307 (2011).
27. Alitalo, K., Tammela, T. & Petrova, T. V. Lymphangiogenesis in development and human disease. *Nature* 438, 946–953 (2005).
28. Rosines, E. et al. Constructing kidney-like tissues from cells based on programs for organ development: toward a method of in vitro tissue engineering of the kidney. *Tissue Eng. Part A* 16, 2441–2455 (2010).
29. Datta, P., Ayan, B. & Ozbolat, I. T. Bioprinting for vascular and vascularized tissue biofabrication. *Acta Biomaterialia* 51, 1–20 (2017).
30. Jia, W. et al. Direct 3D bioprinting of perfusable vascular constructs using a blend bioink. *Biomaterials* 106, 58–68 (2016).
31. Pi, Q. et al. Digitally tunable microfluidic bioprinting of multilayered cannular tissues. *Adv. Mater.* 30, e1706913 (2018).
32. Morizane, R. et al. Nephron organoids derived from human pluripotent stem cells model kidney development and injury. *Nat. Biotechnol.* 33, 1193–1200 (2015).
33. Loessner, D. et al. Functionalization, preparation and use of cell-laden gelatin methacryloyl-based hydrogels as modular tissue culture platforms. *Nat. Protoc.* 11, 727–746 (2016).
34. Shirahama, H., Lee, B. H., Tan, L. P. & Cho, N. J. Precise tuning of facile one-pot gelatin methacryloyl (GelMA) synthesis. *Sci. Rep.* 6, 31–36 (2016).
35. Burdick, J. A. & Prestwich, G. D. Hyaluronic acid hydrogels for biomedical applications. *Adv. Mater.* 23, H41–H56 (2011).
36. Van Den Bulcke, A. I. et al. Structural and rheological properties of methacrylamide modified gelatin hydrogels. *Biomacromolecules* 1, 31–38 (2000).
37. Stenekes, R. J. H. & Hennink, W. E. Polymerization kinetics of dextran-bound methacrylate in an aqueous two phase system. *Polymer* 15, 5563–5569 (2000).
38. Eva Hoch et al. Chemical tailoring of gelatin to adjust its chemical and physical properties for functional bioprinting. *J. Mater. Chem. B* 1, 5675–5685 (2013).

A. M. van Genderen^{1,^}, K. Jansen^{1,^}, M. Kristen^{1,2}, J. van Duijn^{2,3}, Y. Li^{2,3}, C. C. L. Schuurmans^{1,4}, J. Malda^{2,3,5}, T. Vermonden^{3,4}, J. Jansen⁶, R. Masereeuw^{1,3,*}, and M. Castilho^{2,3,7*}

1 Division of Pharmacology, Utrecht Institute for Pharmaceutical Sciences, Utrecht University, 3584 CG Utrecht, The Netherlands

2 Department of Orthopaedics, University Medical Center Utrecht, Utrecht University, 3508 GA Utrecht, The Netherlands

3 Regenerative Medicine Center Utrecht, University Medical Center Utrecht, 3584 CT Utrecht, The Netherlands

4 Division of Pharmaceutics, Utrecht Institute for Pharmaceutical Sciences, Utrecht University, Universiteitsweg 99, 3584 CG Utrecht, The Netherlands

5 Department of Clinical Sciences, Faculty of Veterinary Medicine, Utrecht University, Yalelaan 112, 3584 CM Utrecht, The Netherlands

6 Department of Pathology and Pediatric Nephrology, Radboud University Medical Center, Radboud Institute for Molecular Life Sciences, 6525 GA Nijmegen, The Netherlands

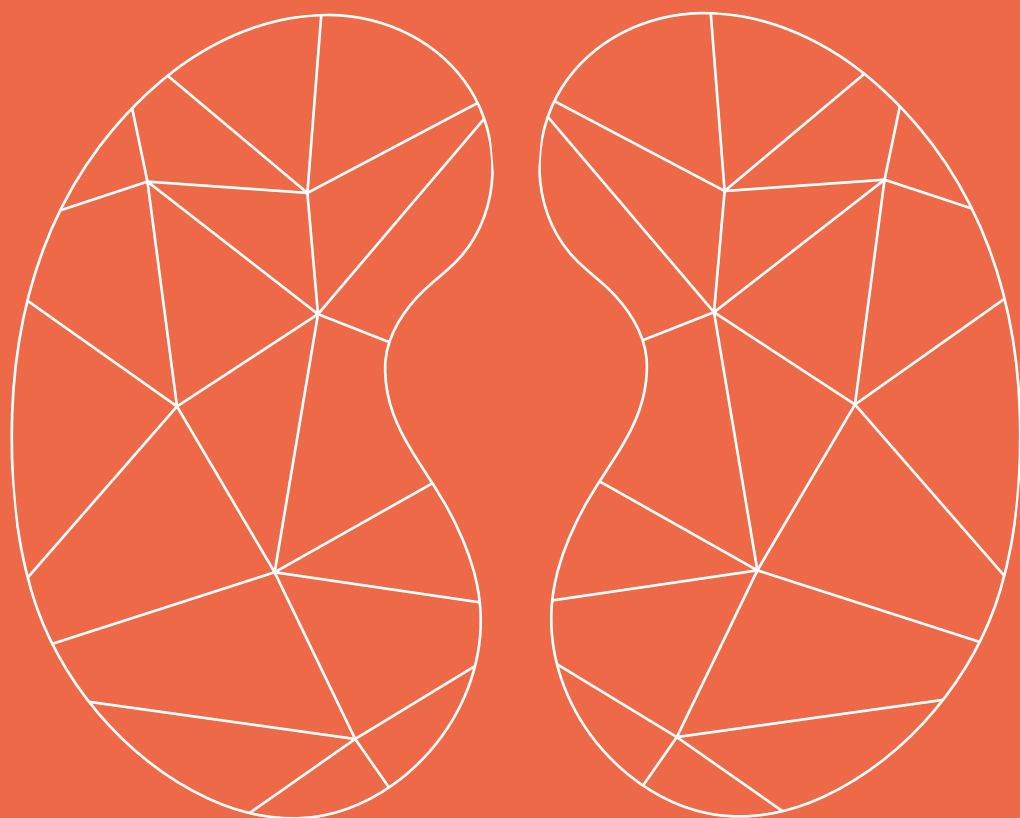
7 Department of Biomedical Engineering, Eindhoven University of Technology, 5600 MB Eindhoven, The Netherlands

[^] These authors contributed equally to this work

^{*} Corresponding authors

CHAPTER 5

TOPOGRAPHIC GUIDANCE IN MELT- ELECTROWRITTEN TUBULAR SCAFFOLDS ENHANCES ENGINEERED KIDNEY TUBULE PERFORMANCE



Abstract

Introduction: To date, tubular tissue engineering relies on large, non-porous tubular scaffolds ($\varnothing > 2$ mm) for mechanical self-support, or smaller ($\varnothing 150\text{--}500$ μm) tubes within bulk hydrogels for studying renal transport phenomena. To advance the engineering of kidney tubules for future implantation, constructs should be both self-supportive and yet small-sized and highly porous. Here, we hypothesize that the fabrication of small-sized porous tubular scaffolds with a highly organized fibrous microstructure by means of melt-electrowriting (MEW) allows the development of self-supported kidney proximal tubules with enhanced properties.

Materials and Methods: A custom-built melt-electrowriting (MEW) device was used to fabricate tubular fibrous scaffolds with small diameter sizes ($\varnothing = 0.5, 1, 3$ mm) and well-defined, porous microarchitectures (rhombus, square, and random). Human umbilical vein endothelial cells (HUVEC) and human conditionally immortalized proximal tubular epithelial cells (ciPTEC) were seeded into the tubular scaffolds and tested for monolayer formation, integrity, and organization, as well as for extracellular matrix (ECM) production and renal transport functionality.

Results: Tubular fibrous scaffolds were successfully manufactured by fine control of MEW instrument parameters. A minimum inner diameter of 1 mm and pore sizes of 0.2 mm were achieved and used for subsequent cell experiments. While HUVEC were unable to bridge the pores, ciPTEC formed tight monolayers in all scaffold microarchitectures tested. Well-defined rhombus-shaped pores outperformed and facilitated unidirectional cell orientation, increased collagen type IV deposition, and expression of the renal transporters and differentiation markers organic cation transporter 2 (OCT2) and P-glycoprotein (P-gp).

Discussion and Conclusion: Here, we present smaller diameter engineered kidney tubules with microgeometry-directed cell functionality. Due to the well-organized tubular fiber scaffold microstructure, the tubes are mechanically self-supported, and the self-produced ECM constitutes the only barrier between the inner and outer compartment, facilitating rapid and active solute transport.

1. Introduction

In vivo, cells are surrounded by an extracellular matrix (ECM), a three-dimensional network composed of collagen, glycoproteins, polysaccharides, and other macromolecules [1]. Underneath epithelial and endothelial cells, including renal proximal tubules and peritubular vasculature, the ECM is formed as a thin, highly specialized basement membrane (BM), which acts both as supporting scaffold for the cells, and as barrier between an inner and outer compartment [1]. For kidney tubule engineering, a big challenge is the creation of renal proximal tubules in close proximity to peritubular vasculature. To allow for rapid exchange of solutes between blood and urine, the epithelial and endothelial BM should be virtually the only barriers between both cell types. To date, tubular tissue engineering mostly relies on non-porous, large diameter tubular scaffolds ($\text{\O} > 2 \text{ mm}$) for sufficient self-support, or smaller tubular lumens ($\text{\O} < 1 \text{ mm}$) surrounded by hydrogels to account for physiological functions, including vectorial transport [2-6]. The latter has been addressed recently in valuable *in vitro* tools for drug screening and disease modeling, with proven apical-basal cell polarity, and active reabsorption and transepithelial secretion function. These models provided evidence for the fact that tubular 3D curvature and biomimetic ECM properties enhance kidney cell functionality [2,3,5-8]. However, for the engineering of potentially implantable and durable kidney tubules, scaffolds must meet at least three criteria: they must be (1) small-sized and highly porous to increase the surface area, (2) freely accessible from the basolateral and luminal sides for rapid solute exchange and removal, and (3) flexible and yet strong enough to withstand intracorporeal forces such as pressure, tear and wear. Ideally, scaffolds for tubular tissue should also be resorbable and initially provide biophysical instructions to promote cell growth, differentiation, and BM production.

Fibrous scaffold meshes, alone or as reinforcement of hydrogels, can greatly improve the mechanical properties of engineered tissue. At the same time, they can influence cellular functionality and ECM deposition through proper scaffold design. Fibrous scaffolds have shown to facilitate cell migration and functionality by providing physiologically relevant mechanical stimulation [9-11]. For instance, cell growth and growth directionality can be positively affected by microfibers when ordered along a preferential direction [10,12].

Previously, we provided proof-of-concept for stand-alone $\text{\O} < 1 \text{ mm}$ kidney tubule grafts fabricated by solution electrospinning (SES), in which human kidney cells were able to bridge considerable fiber-to-fiber distances without the need of embedding hydrogels, which ensured rapid solute uptake [11]. Although SES was successful on manufacturing porous tubular fiber scaffolds, this process was rather limited by poor patterning control

and hence fabrication reproducibility. Here, we fabricated tubular scaffolds using a superior electrohydrodynamic fiber printing technique called melt electrowriting (MEW) [13,14]. MEW is a solvent-free technique that involves extrusion of a molten polymer fiber onto a computer-controlled collector. Organized 3D tubular constructs are obtained by precise fiber deposition on a rotating cylinder and successive layer-by-layer stacking, which require fine control over instrument parameters, in particular mandrel rotation and translation velocity [14-16]. Using MEW, we report the successful fabrication of $\varnothing < 1$ mm proximal tubule units that meet all above-mentioned criteria (**Figure 1**). The first aim was to determine optimal fabrication parameters for $\varnothing = 0.5$ mm and 1 mm tubular scaffolds and to assess their mechanical characteristics. The second aim was to apply these scaffolds to renal epithelial and vascular tubule engineering using conditionally immortalized proximal tubule epithelial cells (ciPTEC) and human umbilical vein endothelial cells (HUVEC); however, only renal epithelial cells were able to form monolayers within the scaffold pores and were used for subsequent experiments. Positive effects of tube structure and biomimetic materials on renal function have already been proven in literature; here, we hypothesized that by engineering tubular scaffolds with defined pore microarchitecture (i.e., rhombus, square and random), we can provide adequate topographic cues to promote cell directionality, autologous BM production, and renal transport function.

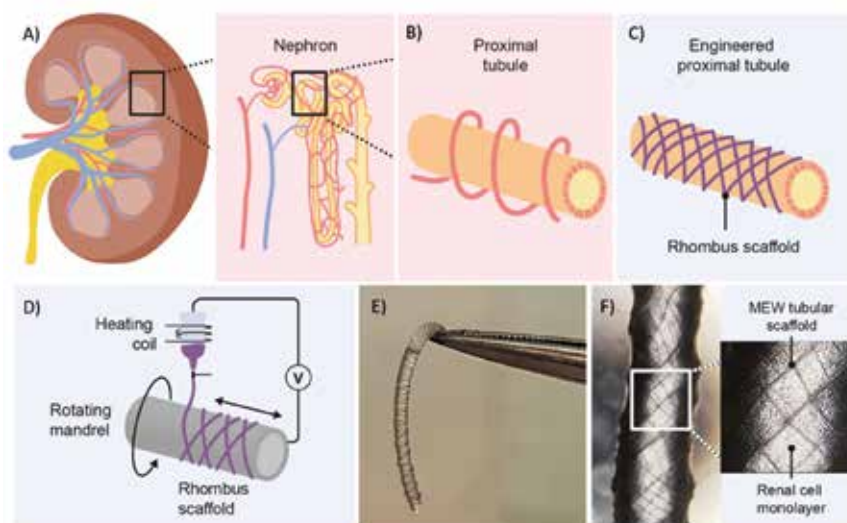


Figure 1. Graphical overview of design and fabrication of MEW medical grade polycaprolactone (PCL) tubular scaffolds. (A) The kidney consists of roughly 1 million functional units, called nephrons. (B) Active secretion takes mostly place in the proximal tubule, which is surrounded by peritubular capillaries. (C,D) Melt-electrowriting was used to fabricate tubular scaffolds with defined pore geometries. (E,F) Engineered kidney tubules contained confluent monolayers of proximal tubule epithelial cells.

2. Materials and Methods

2.1 Melt Electrowriting

We used a custom-built MEW device consisting of a rotating aluminum mandrel ($\varnothing = 3, 1, 0.5$ mm) mounted on a x-y axis and a custom print head mounted of a movable z-axis. The x-y-z axes were computer-controlled using an advanced motion controller MC403 (Trio Motion Technology Ltd.). Granular medical grade polycaprolactone (PCL, Purasorb PC 12, Corbion) was loaded into a 3 ml electrically heated glass syringe with a 27G size metallic nozzle and molten for 30 min prior printing. The molten polymer was electrified using a high voltage source (Heinzinger, LNC 30000-5 POS, 0–30 kV), and extrusion was assisted by a high-resolution air pressure regulator (VPPE-3-1-1/8-2-010-E1, Festo). In order to control scaffold microarchitectures, the effect of tangential rotation velocity (V_{tang}) and translation velocity (V_{trans}) on the laydown fiber winding angle (α) was investigated (**Supplementary Figure 1**). The theoretical winding angle was determined according to,

$$\alpha = \text{ArcTang} (V_{\text{tang}} / V_{\text{trans}}) \quad (1)$$

for $0 < \alpha < 90^\circ$. The V_{tang} expressed in mm/s was assessed by,

$$V_{\text{tang}} = \pi d V_r \quad (2)$$

where d is the diameter of the collecting mandrel in mm and V_r is the rotational velocity of the mandrel in rad/s. Both V_{tang} and V_{trans} were varied according to specified in **Table 1** in order to obtain scaffolds with winding angles of 30° and 45° , corresponding to a square and rhombus microarchitecture, respectively; and a densely distributed crossed fibremat (alternating winding angles between 30° , 45° , and 60°) here named random. The x-y position of the mandrel and respective translational velocity were programmed using a commercially available software package (Motion Perfect V4.2, Trio Motion Technology Ltd.) while the rotational velocity was controlled by Arduino IDE software. The combination of parameters used to obtain the three different scaffold microgeometries and tubular diameters is summarized in **Table 1**. After fabrication, the mandrel with the printed tubular scaffold was soaked in ethanol for 5 min to facilitate scaffold removal. As the 0.5 mm mandrels showed some variation of working distance between the mandrel and the nozzle, 1 mm tubes were used for the biological experiments.

Table 1. Summary of printing parameters used to fabricate melt-electrowritten tubular scaffolds.

Winding angle (°)	Tube diameter (mm)	Effective speed (mm/s)	Tangential speed, Vtang (mm/s)	Translational speed, Vtrans (mm/s)	High voltage (kV)	Melting temperature (°C)	Dispensing pressure	Collecting distance (mm)
30	0.5	3	1.5	2.6	6.5	90	0.65	4
	1	3	1.5	2.6	5.5	85	1	4
	3	3	1.5	2.6	5.0	80	1	4
45	0.5	3	2.1	2.1	6.5	90	0.65	4
	1	3	2.1	2.1	5.5	85	1	4
	3	3	2.1	2.1	5.0	80	1	4
60	0.5	3	2.6	1.5	6.5	90	0.65	4
	1	3	2.6	1.5	5.5	85	1	4
	3	3	2.6	1.5	5.0	80	1	4

2.2 Imaging and Structural Characterization

Tubular scaffolds microstructure and fiber size were analyzed by stereomicroscopy (Olympus SZ61) and by scanning electron microscopy (SEM, Phenom Pro, Phenom-World). SEM was performed at an acceleration speed of 5–10 kV. Prior imaging, SEM scaffolds were gold sputtered coated (1 nm) using a Q150R rotary-pumped sputter (Quorum Technologies). Images from both stereomicroscope and SEM were analyzed with Image J (National Instruments). Scaffold porosity was determined gravimetrically.

2.3 Cell Culture

Human conditionally immortalized proximal tubule epithelial cells (ciPTEC), isolated from human kidney tissue, were developed by Jansen et al. [17]. The tissue used for cell line development was obtained from non-transplanted donors with given informed consent. Briefly, proximal tubule cells obtained from healthy volunteers were infected with a temperature sensitive mutant U19tsA58 of SV40 large T antigen (SV40T) and the essential catalytic subunit of human telomerase (hTERT). ciPTEC were cultured at 33°C and 5% (v/v) CO₂ up to 90% confluency to maintain a cell proliferation state. For maturation, ciPTEC were transferred to 37°C for at least 7 days prior to experimental readout. ciPTEC were cultured in T175 cultures flasks (Greiner Bio-One), using Dulbecco's modified eagle medium/HAM's F12 without phenol red (Thermofisher Scientific), supplemented with 5 µg mL⁻¹ insulin, 5 µg mL⁻¹ transferrin, 5 µg mL⁻¹ selenium, 35 ng mL⁻¹ hydrocortisone, 10 ng mL⁻¹ epidermal growth factor, 40 pg mL⁻¹ tri-iodothyronine (Sigma-Aldrich), 10% fetal bovine serum (FBS) (Greiner Bio-One), and 1% penicillin/streptomycin (Thermofisher Scientific). For 2D cultures, ciPTEC were cultured and matured in 6 well plates. Primary human umbilical vein endothelial cells (HUVEC) [American Type Culture Collection (ATCC)] were cultured using vascular cell basal medium and endothelial cell growth kit-VEGF (ATCC). HUVEC were cultured in T175 culture flasks (Greiner Bio-One) at 37°C and 5% (v/v) CO₂, and confluency was maintained at a maximum of 90% throughout the culture period.

2.4 Scaffold Coating and Cell Seeding Onto Scaffolds

Before cell seeding, PCL tubular scaffolds were sterilized using 70% ethanol evaporation and UV exposure (365 nm for 15 min). 2 mg/mL L-3,4- dihydroxyphenylalanine (L-DOPA, Sigma-Aldrich) was dissolved in 10 mM tris(hydroxyethyl)aminomethane (Tris) pH 8.5 buffer at 37°C for 45 min [17-19]. After sterile filtration (0.2 µm pore size), scaffolds were coated through submersion for 4 h at 37°C and thoroughly washed with phosphate buffered saline (PBS without calcium and magnesium, Lonza). Next, 10 × 10⁶ cells/ml were added in small culture medium drops onto flat scaffolds or injected into tubular scaffolds. Cells were incubated for

4 h at 33°C (ciPTEC) or 37°C (HUVEC); tubular scaffolds were turned 180° after 2 h. Afterwards, culture medium was added, and the constructs were cultured until confluency at 33°C and then at 37°C (ciPTEC), or directly at 37°C (HUVEC). Scaffolds were cultured for 1–4 weeks at 37°C. Culture medium was refreshed 3x per week. Changes on polymer surface wettability before and after L-DOPA coating were evaluated by static contact angle measurements using sessile drop technique (Data Physics, OCA 15EC). Measurements were performed according to a procedure described elsewhere [10].

2.5 Immunofluorescence

Scaffolds were fixed for 5 min with 4% (v/v) paraformaldehyde in PBS and permeabilized with 0.3% (v/v) triton X-100 in PBS for 10 min at RT. Subsequently, cells were exposed to blocking buffer consisting of 2% (v/v) FCS, 0.5% (w/v) bovine serum albumin (BSA), and 0.1% (v/v) Tween20 in PBS for 30 min at RT. Antibodies were diluted in blocking buffer. Primary antibodies were incubated O/N at 4°C and secondary antibodies for 1 h at RT. We used the following primary and secondary antibodies and dilutions: mouse monoclonal anti- α -tubulin 1:150 (T6793, Sigma-Aldrich), goat monoclonal anti-collagen IV 1:50 (1340-01, Southern Biotech), and mouse monoclonal anti CD31 1:250 (ab119339, Abcam), AlexaFluor 488 donkey-anti-rabbit 1:200 (Invitrogen), AlexaFluor 488 goat-anti-mouse 1:200 (Invitrogen), and AlexaFluor 647 donkey-anti-goat 1:200 (Invitrogen). Moreover, we used AlexaFluor 546 phalloidin 1:1000 (A22283, Thermo Fisher Scientific) to stain actin filaments, and nuclei were stained using DAPI 1:1000 (Sigma-Aldrich). Immunofluorescence was examined using confocal microscopy (Leica TCS SP8 X) and software Leica Application Suite X. Images were analyzed using ImageJ. Images were converted to 8-bit, Z-projections were made, and the same threshold was applied for every image. Actin filament directionality was quantified using the directionality functionality and Fourier components analysis.

2.6 Gene Expression

Gene expression analysis was performed by RT-qPCR on ciPTEC after growing at 33°C until confluency and 7 days at 37°C. RNA was isolated from ciPTEC grown in tubular scaffolds or in L-Dopa coated well plates (control) using a PureLink RNA mini kit (Invitrogen), and cDNA was prepared using 500 ng sample RNA templates using iScript¹ cDNA Synthesis Kit (BioRad). RT-qPCR analysis was performed on a CFX96 real-time PCR detection system (BioRad) using TaqMan Universal PCR Master Mix and TaqMan Gene Expression Assay (Thermo Fisher Scientific) for *COL4A1* (TaqMan Assay ID: Hs00266237_m1), *ABCG2* (Hs01053790_m1), *ABCC4* (Hs00988721_m1), *ABCB1* (Hs00184500_m1)

and SLC22A2 (Hs00533912_m1), RPS18 (Hs01375212_g1). All reactions were carried out with equivalent dilutions of each cDNA sample.

2.7 Mechanical Testing

The mechanical properties of cell free and cell cultured tubular constructs (day 14 of culture at 37°C) were studied under uniaxial tensile test using a Dynamic Mechanical Analyzer (DMA Q800, TA Instruments). Before testing, cell cultured constructs were washed with HBSS, fixated for 10 min with 4% (v/v) paraformaldehyde and then washed again with HBSS. Tensile tests were performed at a rate of 0.1 N/min. Prior testing, nominal diameter and length of each construct was measured using stereomicroscopic and SEM images. The tangent modulus, yield strain and elastic strain energy were determined from engineered stress-strain curves. Tangent moduli were determined using a least square fit of the initial slope of the stress-strain elastic region (E_t , as presented in **Supplementary Figure 3**), yield point (ϵ_{el}) was defined as point where nonlinear deformation begins and elastic strain energy (U_0) was obtained,

$$U_0 = \int_0^{\epsilon_{el}} \sigma \, d\epsilon \quad (3)$$

where σ and ϵ represent engineered stress and strain, respectively.

2.8 Functional Assays

To test the functionality of various transporters (BCRP, MRP4, P-gp and OCT2), tubular scaffolds with rhombus-shaped pores and ciPTEC were matured for 3 weeks, rinsed in HBSS, and incubated with fluorescent substrates. Cells were incubated with 1 μ M non-fluorescent calcein-AM for 15 min at 37°C to confirm cellular metabolism through enzymatic conversion of calcein-AM to fluorescent calcein. Incubation was performed in presence or absence of 5 μ M MK-571 and KO173 (inhibitors of MRP4 and BCRP) to validate functional excretion of calcein. Moreover, tubular scaffolds were incubated with 10 μ M rhodamine123 (RH123), substrate for uptake transporter OCT2 and excretion transporter P-gp, in presence or absence of 5 μ M tetrapentylammonium (TPA⁺, OCT2 inhibitor) or 5 μ M PSC-833 (P-gp inhibitor) for 40 min at 37°C. After incubation, the scaffolds were rinsed with HBSS and images were captured with green filters using the Keyence BZ-9000 fluorescence microscope (Keyence). ImageJ (National Instruments) was used to measure fluorescence intensity in 16-bit images after background subtraction. In addition, a leakage assay was performed with rhombus-shaped scaffolds to assess engineered proximal tubule function. First, a customized perfusion chamber was designed and printed with polylactic acid (PLA) using a fused

filament fabrication method (Ultimaker). The printed chamber was mounted on a glass slide using epoxy glue (Loctite), and tubular scaffolds were fixed inside with dental glue (GI-MASK Automix, Coltene) (**Supplementary Figure 4**). Scaffolds were perfused with 0.1 mg/ml fluorescein isothiocyanate-inulin for 5 min (inulin-FITC, Sigma-Aldrich), and real-time imaged using a fluorescence microscope with a green filter (Keyence BZ-9000).

2.9 Statistical Analysis

Unless otherwise stated, 3 scaffolds per condition were used in 3 independent experiments respectively. Statistical analysis was carried out in Graphpad Prism 8.1.0 (GraphPad Software Inc.) using a student *t*-test when two groups were compared, and a one-way ANOVA and Tukey's multiple comparisons *post-hoc* test when 3 or more groups were compared. A two-way ANOVA and multiple comparisons were used for comparison of multiple groups with 2 independent variables. Differences were considered significant with a *p*-value of $p < 0.05$. * indicates $p < 0.05$, ** $p < 0.01$, *** $p < 0.001$ and **** $p < 0.0001$. Data are represented as mean \pm standard error of the mean (SEM) or as mean \pm standard deviation (SD).

3. Results

3.1 Design and Fabrication of Microfibrous Tubular Scaffolds

Fully resorbable medical grade polycaprolactone (PCL) tubular scaffolds were manufactured with a reproducible quality using an in-house built MEW set-up (**Figures 1, 2, Supplementary Movie 1**). Scaffolds were fabricated with a range of winding angles, from 30° to 60°, by controlling the ratio between the tangential rotation velocity (V_{tang}) and the translation velocity (V_{trans}) (**Supplementary Figure 1**). No significant differences in fiber diameter were observed when varying the winding angle (constant fiber diameter of approximately 20 μm , **Figure 2A**), and the measured winding angle was in accordance with the theoretical design (**Figure 2B**). Additionally, the effect of fiber stacking on printed winding angle was evaluated (**Figure 2C, Supplementary Figure 2**). In general, an increase in the deviation between designed and printed winding angle was observed when increasing the number of staked fibers from 1 to 10 layers. This difference was in average 33 ± 8 for 0.5 mm mandrels (**Supplementary Figure 2A**) and $7 \pm 3\%$ for 3 mm (**Supplementary Figure 2B**) and 1 mm mandrels (**Figure 2C**). Importantly, our results demonstrate that the fiber diameter did not change significantly when increasing the number of staked layers, as well as when varying the winding angle. Furthermore, while 3 and 1 mm diameter tubes could be easily removed from the mandrels, harder removal of 0.5 mm tubes from the mandrel was observed, which compromised their structural integrity. Based on these post-processing handling characteristics and printing

fidelity results, tubes with 1 mm diameter and 10 layers (final thickness of $\sim 100\ \mu\text{m}$) were selected for further experiments. Tubular scaffold with three different microarchitectures were fabricated, i.e., rhombus (winding angle 30°), square (winding angle 45°) and random (densely distributed crossed fiber mat, with winding angles varying between 30° , 45° , and 60°). Notably, interconnected porosities above 90% and controlled pore sizes of $200\ \mu\text{m}$ were obtained for rhombus (Figures 2D-F) and square pore shaped scaffolds, while only 40% porosity were observed for random scaffolds and no controlled pore size (Figure 2D).

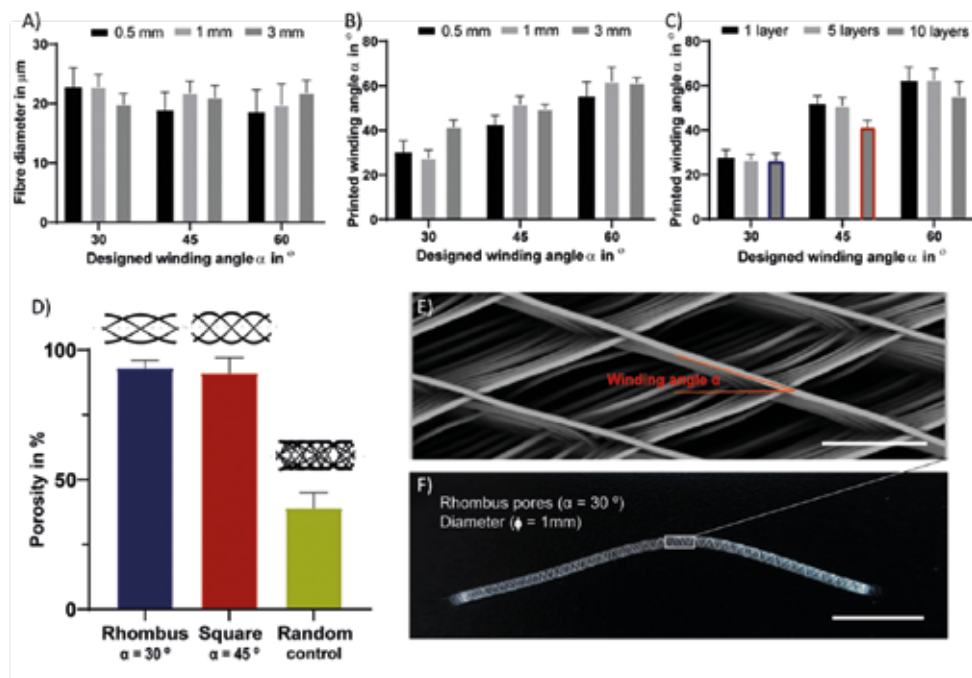


Figure 2. Tubular scaffold design and fabrication. (A) variation of printed fiber diameters according to designed winding angles. (B) Comparison between designed and printed winding angle used to assess printing accuracy. (A,B) were investigated for constructs with a single layer and for mandrels with three different diameters, 3, 1- and 0.5-mm. (C) Comparison between designed and printed winding angle for constructs with 1, 5 and 10 stacked layers and mandrel with 1 mm in diameter. Blue and red identify rhombus and square constructs used for further mechanical and biological experiments. (D) Porosity of fabricated tubes with 1 mm diameter. Representative (E) stereoscopic and (F) SEM image of printed tubular scaffolds with a rhombus (30°) microstructure for 1 mm mandrel. Scale bars = $100\ \mu\text{m}$ (E) and 1 cm (F).

3.2 Cell Growth and Directionality

The first requirement of functional bioengineered kidney tubules is cell adherence and growth into a barrier-forming monolayer. Confirming our previous data, ciPTEC were able to form tight monolayers in L-DOPA biofunctionalized tubular scaffolds by stretching across the pores between the PCL microfibers [11]. L-DOPA coating increased scaffold hydrophilicity compared to non-coated tubular scaffolds (**Supplementary Table 1**). Cells grew on the PCL-fibers, then they started bridging the pores from the corners and moved further inward; ultimately, the pores were entirely filled by ciPTEC monolayers. Only at a pore size of 400 μm and higher, ciPTEC were not able to bridge the gap.

Cell growth and filamentous actin (F-actin) orientation were studied in scaffolds with rhombus, square and random pore geometries (**Figures 3A-I**). For HUVEC, no microgeometry allowed monolayer formation; the cells only surrounded the PCL fibers (**Figures 3A-C**). When stained for platelet endothelial cell adhesion molecule 1 (PECAM-1 or CD31), a marker for endothelial cell junctional integrity, we observed irregular expression (**Figures 3A-C**). PECAM-1 is only expressed at the cell borders of confluent monolayers, whereas little or no expression is observed in sparse or migrating endothelial cells [20, 21]. In contrast to HUVEC, ciPTEC were able to fill the pores with all geometries investigated. For ciPTEC, rhombus-shaped pores caused preferential cell alignment along the scaffold fiber direction. The angle of deviation for ciPTEC grown in rhombus-shaped pores was approximately 25° , which is in accordance with the 30° winding angle of the pores, indicating that ciPTEC are aligned as instructed by the geometry. The cell alignment order parameter S was calculated for ciPTEC, where a value of $S = 1$ would indicate that the long axis of the cells perfectly aligned with the scaffold fiber direction and $S = 0$ indicated no particular cell alignment. CiPTEC grown on rhombus-shaped pores exhibited cell alignment with an S of 0.51 ± 0.06 , whereas both square and random microgeometries resulted in an isotropic distribution of cells with order parameters of 0 (**Figure 3D-I**) [22,23].

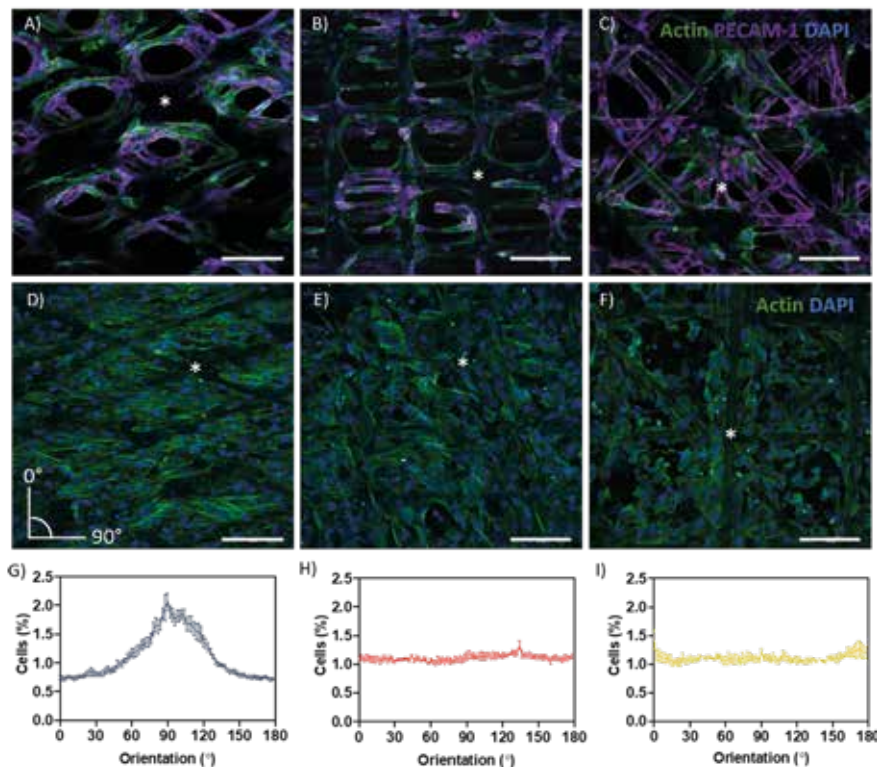


Figure 3. Cell growth and directionality. (A–C) Actin filament (green), PECAM-1 (purple), and DAPI (blue) in (A) rhombus-, (B) square-, and (C) random-shaped scaffolds for HUVEC. (D–F) Actin filament (green) and DAPI (blue) in (D) rhombus-, (E) square- and (F) random-shaped scaffolds for ciPTEC. Asterisks identify fiber scaffold position. (G–I) Quantification of cell directionality in (G) rhombus-, (H) square- and (I) random-shaped scaffolds for ciPTEC. Scale bars = 250 μ m. Mean \pm SEM, $n = 3$.

3.3 Renal Transporter Expression and Function

The proximal tubule has a major role in waste secretion from the blood into the urine, and, therefore, expresses a broad range of functional transporters to facilitate this transport. We tested the effect of pore microgeometries on the gene expression of four relevant transporters: the efflux pumps breast cancer resistance protein (BCRP), multidrug resistance-associated protein 4 (MRP4), and P-glycoprotein (P-g), and the uptake transporter organic cation transporter 2 (OCT2). For all microgeometries, mRNA levels were compared to 2D culture (**Figures 4A–D**). For BCRP (**Figure 4A**, CT value 2D: 33.47 ± 0.12) and MRP4 (**Figure 4B**, CT value 2D: 29.60 ± 0.03), no differences were found. Remarkably, mRNA expression for P-gp increased 2.4-fold (**Figure 4C**, $p < 0.05$, CT value 2D: 29.43 ± 0.03) for tubular scaffolds with rhombus-shaped pores compared to 2D culture. Also, OCT2 expression was 3.4-fold

higher (**Figure 4D**, $p < 0.01$, CT value 2D: 37.85 ± 0.30). In tubular scaffolds with isotropic pore microgeometries, transporter expression showed no significant increase compared to traditional 2D culture. Two functional assays were performed to validate transporter function in rhombus-shaped pores (**Figures 4E-J**). Calcein-AM diffuses into the cell, where it is hydrolyzed by esterases into fluorescent calcein, which is then secreted by BCRP and MRP4 (**Figure 4E**) [24]. When incubating the engineered kidney tubules with calcein-AM in presence of BCRP and MRP4 inhibitors KO143 and MK571, calcein accumulated in the cells (**Figures 4G,I**) ($p < 0.05$). Rhodamine-123 (RH123) is a chemical fluorescent compound that is actively transported into the cell via OCT2 and actively excreted into the urinary compartment by P-gp and BCRP (**Figure 4F**). When the OCT2 inhibitor TPA was added, RH123 intracellular fluorescence intensity tended to be lower, although not significantly. When the P-gp inhibitor PSC-833 was added, intracellular fluorescence intensity increased ($p < 0.05$) (**Figures 4I-J**).

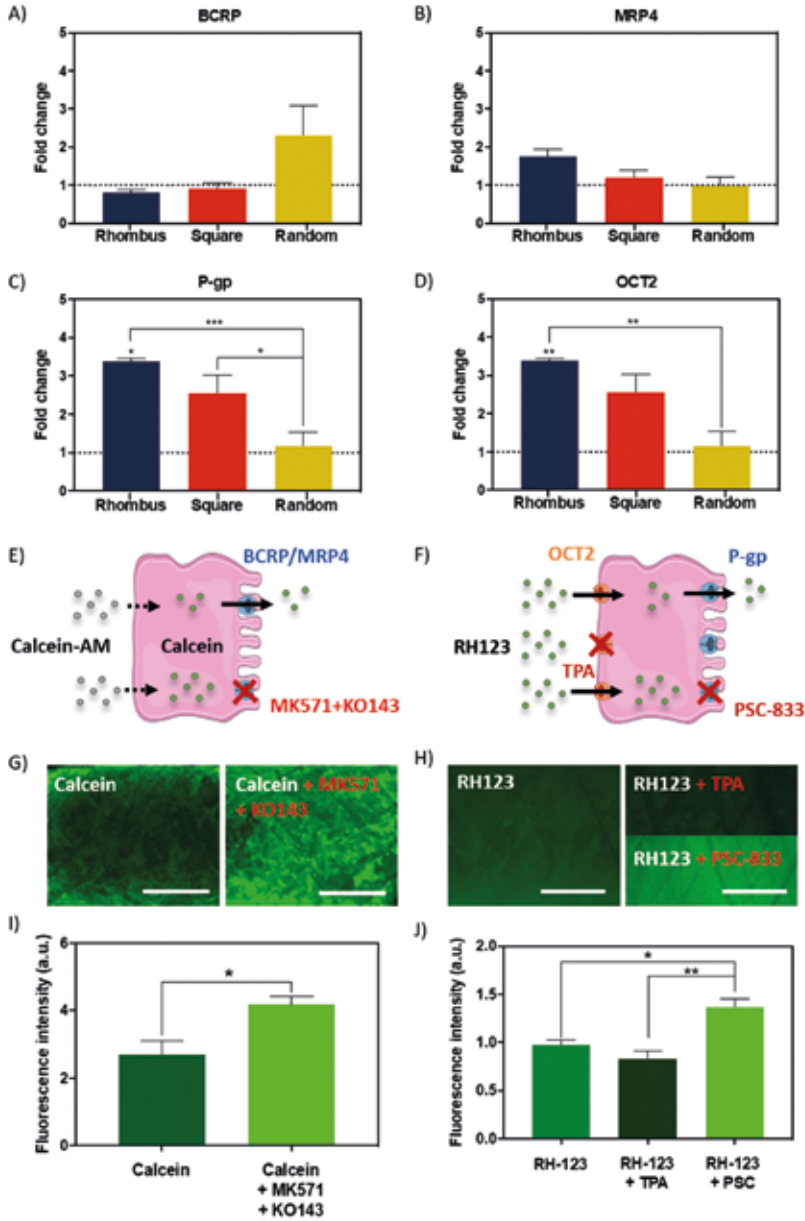


Figure 4. Renal transporter expression and function. (A–D) Relative mRNA gene expression of ciPTEC cultured in tubular scaffolds with rhombus-shaped pores compared to ciPTEC cultured in 2D (dotted line). (E,F) Graphical overview of (E) calcein-AM assay and (F) rhodamine123 assay. (G,H) Immunofluorescent images of (G) calcein-AM assay and (H) rhodamine123 assay in presence or absence of inhibitors. (I,J) Quantification of immunofluorescent images measured as fluorescence intensity for (I) calcein and (J) rhodamine123. Scale bars = 500 μ m. Mean \pm SEM, n = 3. *P < 0.05; **P < 0.01; ***P < 0.001.

3.4 Collagen IV Deposition

Collagen type IV is the most abundant component of the renal BM, making up 50% or more of the total [1]. To investigate how pore microgeometries affected ECM deposition, collagen type IV expression was measured over time, i.e., at day 7, 14, and 28, after starting maturation at 37°C (**Figures 5A,B**). In all pore microgeometries tested, ciPTEC deposited collagen type IV and filled all pores at the earliest timepoint measured (day 7). While collagen type IV deposition remained equal over time in random and square microgeometries, it significantly increased ($p < 0.05$) in rhombus scaffolds, with a maximum collagen type IV expression on day 28 (**Figure 5B**). On mRNA level, collagen type IV expression increased 5.5-fold in rhombus-shaped pores compared to traditional 2D culture at day 7 ($p < 0.001$, CT value 2D: 32.46 ± 0.33) (**Figure 5C**). Square-shaped pores also increased collagen IV mRNA levels in ciPTEC (4.4-fold, $p < 0.01$), whereas random-shaped pores did not have any beneficial effect compared to 2D cell culture (**Figure 5C**). Finally, we assessed how cells and their BM affected the mechanical properties of the MEW tubular scaffolds. Engineered kidney tubules were matured for 14 days before they were evaluated under uniaxial tensile loading to determine tangent modulus, yield strain, and elastic strain energy (**Figures 5D-F, Supplementary Figure 3**). A non-linear stress-strain behavior was observed for the different tested microarchitectures (**Supplementary Figure 3**). Interestingly, without cells scaffolds with a rhombus geometry were able to reach higher elastic deformations (2-fold higher, approximately 10% deformation) and lower tangent modulus (1.7-fold lower, 4 MPa) than scaffolds with random microstructure (**Figures 5D, E, Supplementary Figure 3**). No significant differences were observed on tangent modulus and elastic strain between scaffolds with a squared and random microarchitecture. In tubular scaffolds with ciPTEC monolayers, we observed a trend for an increase in yield strain ($p = 0.0515$) and an increase in elastic strain energy ($p < 0.0002$) in tubules with rhombus-shaped pores compared to scaffolds without cells (2- to 3-fold higher). It should be noted that a promising elastic behavior (shape recovery without visual permeant deformation) was observed for rhombus scaffolds after repetitive manual stretching, not observed for square and random tubular scaffolds (data not shown).

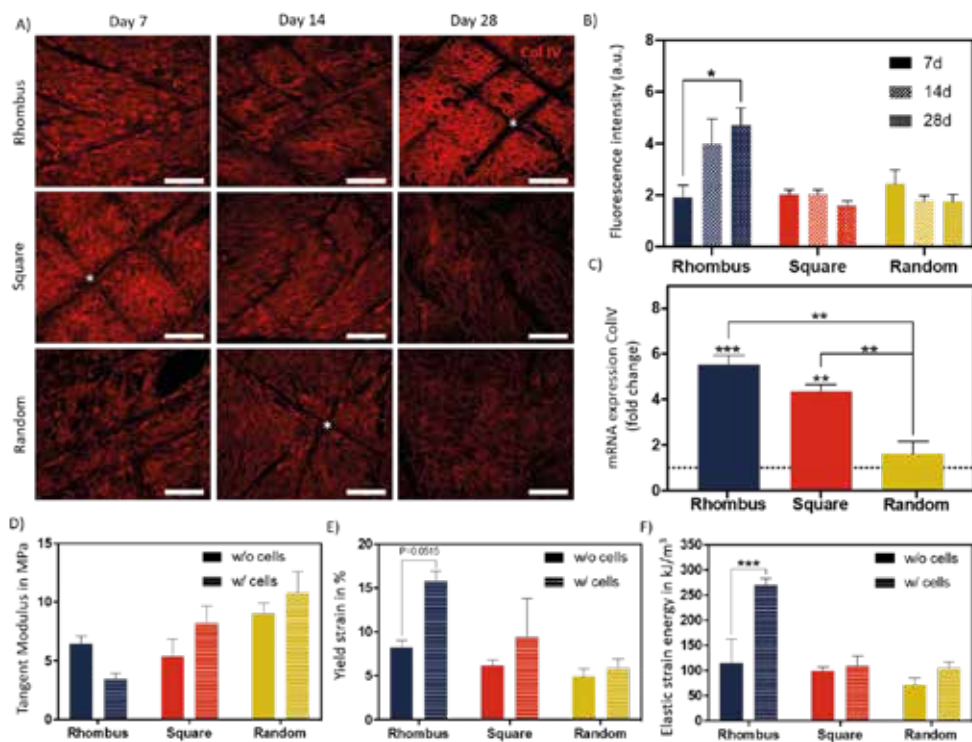


Figure 5. Collagen IV deposition and mechanical behavior of fiber constructs under tensile loading. (A) Immunofluorescent images of collagen type IV (red) in rhombus-, square-, and random-shaped scaffolds captured at day 7, 14, and 28. Asterisks identify fiber scaffold position. Scale bars = 100 μm . (B) Quantification of fluorescence intensity of the immunofluorescent images. (C) Relative mRNA collagen type IV gene expression of ciPTEC cultured in tubular scaffolds compared to ciPTEC cultured in 2D (dotted line). (D–F) Mechanical properties measured in tubular scaffolds with and without cells. Mean \pm SEM, $n = 3$. * $P < 0.05$; ** $P < 0.01$; *** $P < 0.001$.

3.5 Barrier Function

In our engineered kidney tubules, cells and their self-made BM deposited within the scaffold pores formed the only barrier between the basolateral and luminal side of the tubes. A thin but tight barrier is crucial for vectorial solute transport. To functionally assess barrier formation, inulin-FITC leakage was measured using a custom-made perfusion system. When mounting cell-free scaffolds in a dry chamber, inulin-FITC remained inside the scaffold due to surface tension (**Figure 6A**), but when PBS was added to the chamber, inulin-FITC directly leaked out (**Figure 6B**). In contrast, ciPTEC-laden scaffolds kept the inulin-FITC inside the lumen, indicating that the cells and their BM functioned as a leak-tight barrier between the luminal and basolateral sides of the engineered kidney tubule (**Figure 6C**). Engineered kidney

tubules were also stained for collagen type IV and DAPI, and cross-sections were randomly made to confirm monolayer formation throughout the tubular construct (**Figures 6D, E**). For rapid solute exchange and future implantation purposes, engineered kidney tubules must be flexible, wear-resistant, small in diameter, highly porous, and freely accessible from both the basolateral and luminal side. Using MEW, we fabricated self-supported, highly ordered tubular scaffolds with controlled pore microarchitectures (i.e., rhombus and square). We were able to produce scaffolds with an inner diameter of 0.5 mm, which is around 7 times the diameter of native kidney tubules and only 2 times the diameter of common dialysis fibers. While smaller diameters might be possible in future, the constructs also needed to remain easy to handle for experimental testing. The ability to control tubular scaffold microarchitecture is a unique characteristic of MEW that distinguishes the process from other conventional fiber formation technologies like SES. For kidney tubule engineering, we identified rhombus-shaped pores as a superior microgeometry over square- and random-shaped pores: topographic guidance resulted in directed cell growth, enhanced collagen type IV deposition, remarkably improved yield strain and elastic strain energy, and increased functional OCT2 and P-gp expression.

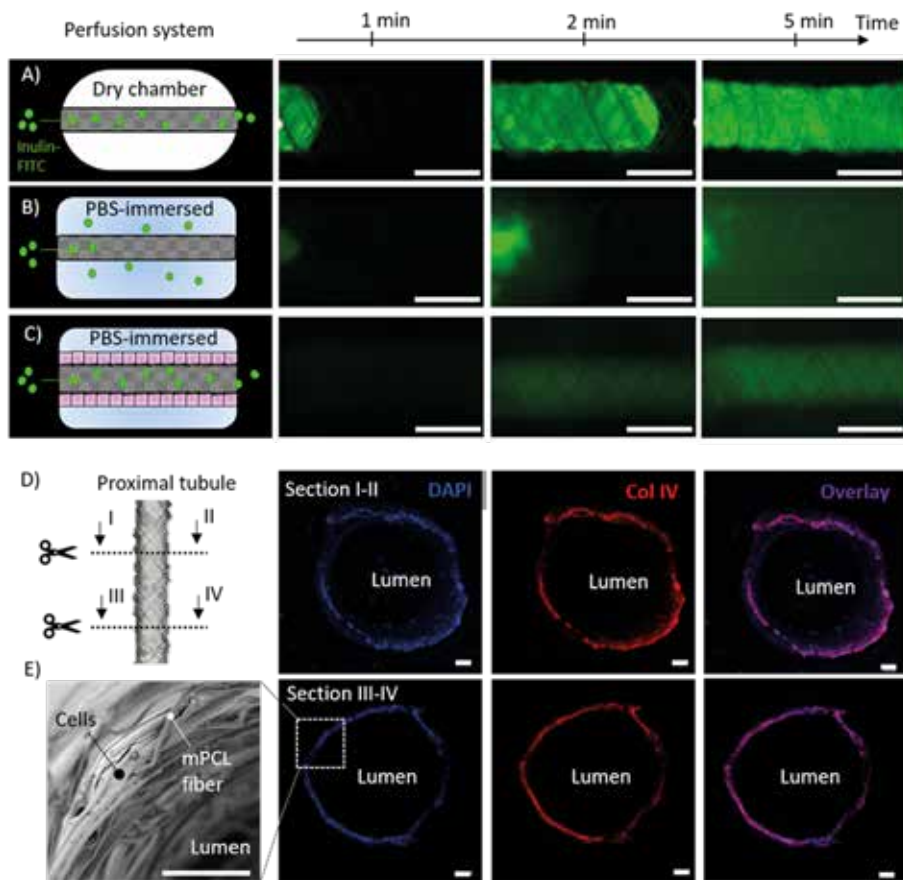


Figure 6. Renal barrier function. (A–C) Inulin-FITC leakage assay in rhombus-shaped tubular scaffolds (A,B) without and (C) with cells. Perfusion chamber (A) dry and (B,C) immersed in PBS. Immunofluorescent images are captured after 1, 2 and 5 min of Inulin-FITC perfusion. (D) Cross-sectional immunofluorescent images indicating a monolayer of ciPTEC throughout the construct. Immunofluorescent staining for DAPI (blue) and collagen type IV (red). (E) Representative SEM image of cell laden rhombus-shaped tubular scaffolds demonstrating a renal monolayer. Scale bars = 100 μm .

4. Discussion

4.1 Rhombus-Shaped Pores Mimic *in vivo* Renal Tubular Basement Membrane Anisotropy Through Topographic Guidance

In vivo, the renal tubular BM exhibits an anisotropic structure, i.e., a directional preference in form of a polygonal meshwork of corrugated appearance [25]. In contrast to square- and random-shaped pores, rhombus-shaped pores guided cell growth along the scaffold fibers into a preferred cell direction with an angle of deviation that was even smaller than

the winding angle of the scaffold. This phenomenon is called contact or topographic guidance [26, 27]. The effects of various topographic features on ciPTEC have been evaluated previously; already small features ($<5 \mu\text{m}$) could induce cell organization and alignment, which made the cells more susceptible to mechanical cues such as fluid shear stress (FSS) [28-30]. The alignment of the actin cytoskeleton might have contributed to the increased BM and transporter gene expression. Importantly, the cytoskeleton reorganization is known to alter force-activated pathways, as well as nuclear actin structures that can regulate gene expression and cell differentiation [31, 32]. Although more research is needed to confirm such underlying mechanisms in renal cells, our data do confirm beneficial effects of anisotropic cues on cell growth behavior and differentiation. The effects of different pore sizes and shapes of MEW scaffolds on cell alignment and gene expression have been shown to vary per cell type, including macrophages, bone marrow, smooth muscle cells, cardiomyocytes, and skeletal stem cells [33-37]. This indicates that the choice of pore size and shape need to be carefully considered depending on cell type of interest. For HUVEC, it has been shown that topographic cues of ridges and grooves can stabilize the endothelial phenotype. Based on the physiological BM microarchitecture *in vivo*, alignment in circumferential direction would be preferred [27, 38]. In our study, HUVEC failed in filling the MEW-fabricated pores of any microgeometry tested. Most likely, HUVEC have a smaller spreading length compared to ciPTEC, which is the only parameter besides initial pore size needed for predictions of void filling [39].

4.2 Renal Monolayers in MEW Pores Are Freely Accessible for Solute Uptake and Separate Compartments

Inhibitor-sensitive cellular uptake and excretion of fluorescent compounds demonstrated functional transport activity of our engineered kidney tubules. Vectorial solute transport requires an intact and polarized epithelial monolayer that forms a barrier between the luminal and the outer compartment. Microscopic images revealed consistent monolayer formation throughout the construct, which was confirmed by retainment of inulin-FITC during luminal perfusion. For uptake and subsequent drainage of metabolic waste products, an outside-oriented basolateral side, and an apical membrane facing the lumen are crucial. Usually, the interaction between cells and ECM are a determinant factor in the orientation and stabilization of cell polarity [40]. However, freshly seeded cells are not provided with a pre-existent ECM in our scaffolds, thus polarization likely depends on factors other than ECM cues. It is known that fluid shear stress (FSS) can facilitate cell polarization and has moreover been shown to enhance transporter expression in epithelial cells [2, 41-43]. Possibly, FSS could induce polarization and further enhance cellular functionality in our scaffolds,

therefore future steps will include the establishment of a long-term flow-compatible cell culture system.

4.3 Rhombus-Shaped Pores Increase Yield and Elastic Strain Energy of Engineered Kidney Tubules

When handled or potentially implanted, engineered kidney tubules should be able to withstand external influences like pressure, tear and friction. When subjected to axial forces, controlled pore microgeometries themselves had a significant effect on tangent modulus, yield strain and elastic energy of tubular scaffolds when compared with non-controlled pore microgeometries. This evidence was even more pronounced when cells formed monolayers within the pores. Kidney tubules with rhombus-shaped pores could sustain higher strain (~15%) before yielding compared to random and square (<10%), probably due to the contact guided cell alignment with the fiber direction. Compared to tangent moduli of kidney tissue reported in literature (3–10 MPa), the tangent modulus of 4 MPa for the kidney tubules with rhombus-shaped pores (evaluated 14 days after monolayer formation) was close to the lower limit of this range [1]. It should be noted that mechanical properties were tested after fixation which tends to increase the tangent modulus [44,45]. However, considering the increase in ECM deposition over the course of 28 days in culture, an overall improvement in mechanical properties can be expected over time. Notably, the control over scaffold microarchitecture on tubular constructs with 1 mm allowed for aligned ECM deposition and consequent impressive compliance using PCL, a rather stiff thermoplastic material, as scaffolding material. It is important to mention, that future improvement of the MEW process is required to generate tubular scaffolds with tunable mechanical properties and internal diameters below 1 mm diameter. Recent works have reported the design and melt-electrowriting of auxetic tubular microfibers with unprecedented control of elastic deformations that could be applied in engineered kidney tubules. However, internal diameters obtained were one order of magnitude higher, 10 mm, than the ones reported here [46].

4.4 Next Steps Toward Perfusable and Vascularized Engineered Kidney Tubules

As mentioned above, the establishment of long-term perfusion systems will further advance kidney tubule performance and readouts. Moreover, the flexible nature of MEW tubular scaffolds allows the intertwinement of multiple scaffolds, which would create direct contact between epithelium and endothelium, mimicking the physiological situation [1,25]. Twisting scaffolds would additionally protect and stabilize the constructs. To engineer peritubular blood vessels, the initial pore size could be reduced by combination of MEW with electrospinning, as shown by Jungst et al. (2019) and Pennings et al. (2019) [47, 48].

Furthermore, the use of supportive cell types like pericytes or fibroblasts could help in the formation of endothelial monolayers [49]. In fact, direct contact between different cell types on PCL scaffolds, as opposed to indirect contact, can improve cell functionality [50]. Also, co-cultures of endothelial cells with renal epithelial cells have been shown to stimulate the balanced expression of various endothelial factors, which in turn improved the performance of renal cells [51].

In conclusion, we report the fabrication of self-supportive and yet small-sized porous MEW tubular scaffolds for kidney tubule engineering. MEW scaffolds enable direct access to the basolateral and luminal cell sides to facilitate solute exchange with vasculature in immediate proximity, which is critical for functional proximal tubule constructs. We showed that rhombus-shaped pores can enhance kidney tubule performance through topographic guidance, highlighting the fact that proper scaffold design offers opportunities to improve cell function.

Data Availability Statement

The datasets presented in this study can be found in online repositories. The names of the repository/repositories and accession number(s) can be found below:

<https://doi.org/10.1101/2020.09.16.300004>

Author Contributions

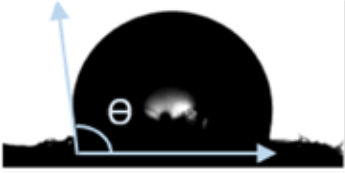

AG, KJ, JJ, RM, and MC contributed to the conception of this research. AG, KJ, TV, JJ, RM, and MC contributed to the experimental setup. AG, KJ, MK, JD, YL, CS, and MC performed the experimental work and data analysis. AG, KJ, MK, RM, and MC wrote the content of the manuscript. All authors contributed to drafting and critically revising it and have read and approved the final submitted manuscript.

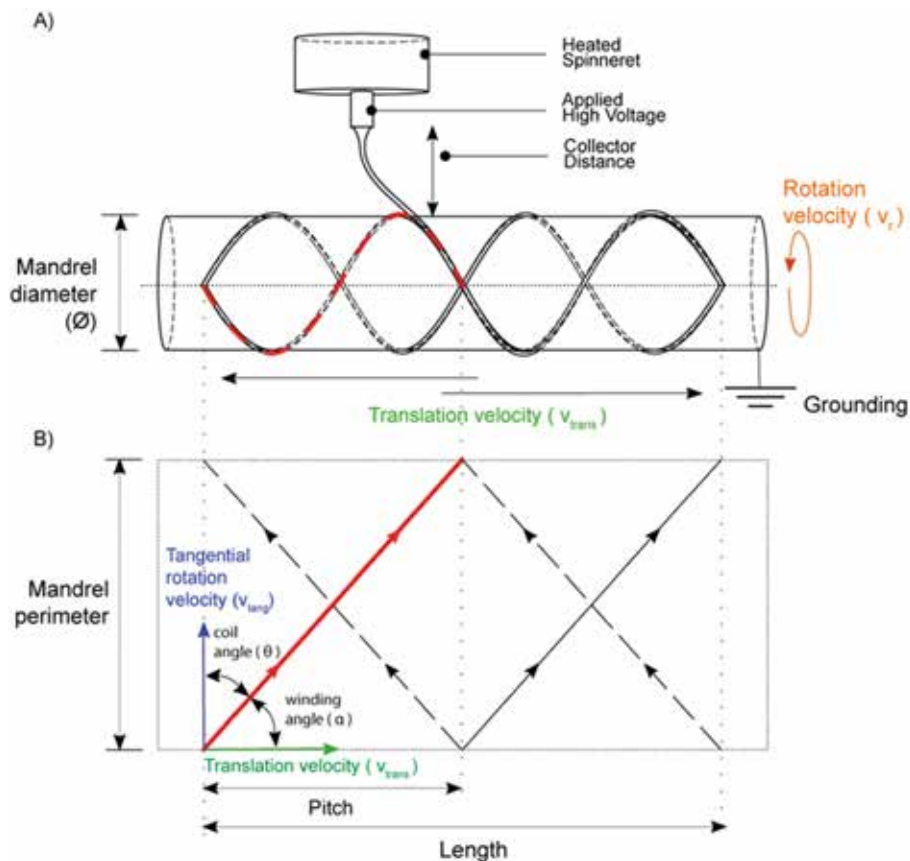
Funding

The Dutch Kidney Foundation (17PHD16) supported the work of AG. The Netherlands Organization for Scientific Research (NWO) as part of the Future Medicines Program (022.006.003) supported the work of KJ and CS. The authors are also grateful for the support of the Gravitation Program Materials Driven Regeneration by the Netherlands Organization for Scientific research (024.003.013).

Supplementary Materials

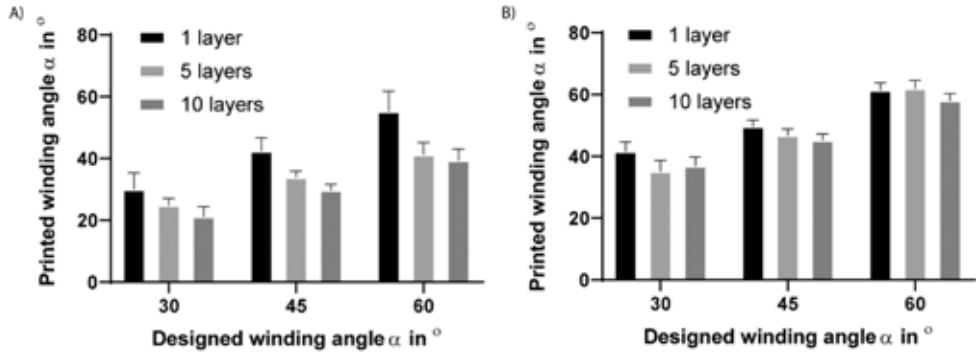
Supplementary Table 1: Water contact angles on uncoated PCL and L-DOPA coated PCL surfaces. Mean \pm SEM, n=3.

Composition	Water contact angle
PCL (close to hydrophobic)	$93.07 \pm 3.87^\circ$  A photograph showing a large, dark, spherical water droplet on a light-colored surface. A blue arrow points upwards from the center of the droplet, and another blue arrow points horizontally to the right from the contact point. The angle between these two arrows is labeled with the Greek letter theta (θ).
L-DOPA coated PCL (close to absolute wetting)	$0.5 \pm 1.87^\circ$  A photograph showing a very thin, dark, horizontal layer of water spread across the surface, indicating near-complete wetting.

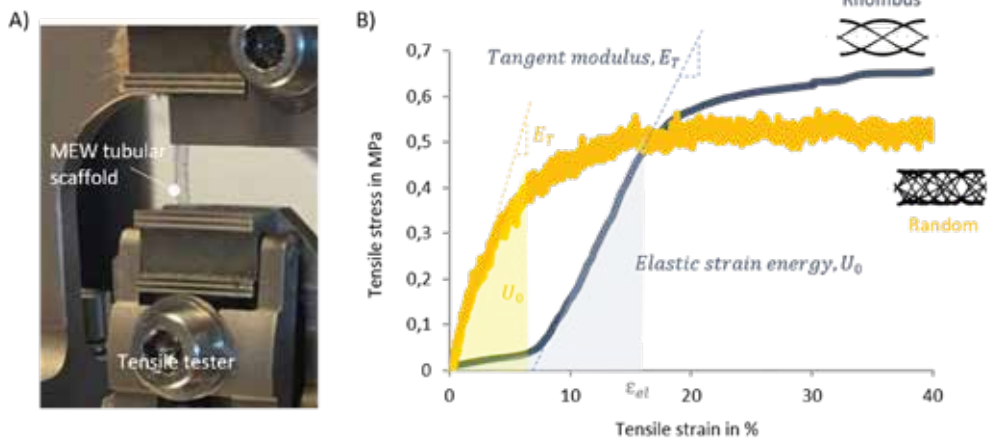


Supplementary Figure 1. Schematic of the melt electrowriting set-up, explaining the different parameters.

A) Schematic of the melt electrowriting set-up, showing the collection of thin electrified polymer jets onto a computer controlled, rotating and translating mandrel. B) Representation of the mandrel velocities, translational (V_{trans}), tangential (V_{tang}), rotational (V_{rot}), as well as winding angle (α), coil angle (θ), tube length, pitch and mandrel perimeter (r) in the mandrel surface during fiber collection. Winding angle was engineered by the ratio between V_{tang} and V_{trans} at constant fiber length.



Supplementary Figure 2. Winding angle design versus printed. Comparison between designed and printed winding angle for constructs with 1, 5 and 10 stacked layers and mandrel with A) 0.5 mm and B) 3mm in diameter.



Supplementary Figure 3. Mechanical tests. A) Tensile tester set up and B) representative engineered stress-strain curves with determined mechanical parameters for tubular scaffolds with rhombus and random microarchitecture with cells.



Supplementary Figure 4. Custom made perfusion system used for renal barrier function studies. MEW tubular scaffolds were mounted in a 3D printed PLA customized chamber and then perfused.

Supplementary Movie 1. Video for melt-electrowriting of tubular constructs with rhombus microstructure

<https://www.frontiersin.org/articles/10.3389/fbioe.2020.617364/full>

Supplementary Movie 2. Perfusion of engineered tubules for renal barrier function testing.

<https://www.frontiersin.org/articles/10.3389/fbioe.2020.617364/full>

References

1. van Genderen, A. M., Jansen, J., Cheng, C., Vermonden, T. & Masereeuw, R. Renal Tubular- and Vascular Basement Membranes and their Mimicry in Engineering Vascularized Kidney Tubules. *Adv Healthc Mater* vol. 7 1800529
2. Homan, K. A. *et al.* Bioprinting of 3D Convoluted Renal Proximal Tubules on Perfusable Chips. *Sci Rep* **6**, 1–13 (2016).
3. Lin, N. Y. C. *et al.* Renal reabsorption in 3D vascularized proximal tubule models. *Proc Natl Acad Sci U S A* **116**, 5399–5404 (2019).
4. Jansen, K., Schuurmans, C. C. L., Jansen, J., Masereeuw, R. & Vermonden, T. Hydrogel-Based Cell Therapies for Kidney Regeneration: Current Trends in Biofabrication and In Vivo Repair. *Curr Pharm Des* **23**, 3845–3857 (2017).
5. Rayner, S. G. *et al.* Reconstructing the Human Renal Vascular–Tubular Unit In Vitro. *Adv Healthc Mater* **7**, 1801120 (2018).
6. Singh, N. K. *et al.* Three-dimensional cell-printing of advanced renal tubular tissue analogue. *Biomaterials* **232**, (2020).
7. Jansen, J. *et al.* Human proximal tubule epithelial cells cultured on hollow fibers: living membranes that actively transport organic cations. *Sci Rep* **5**, 16702 (2015).
8. Jansen, J. *et al.* Bioengineered kidney tubules efficiently excrete uremic toxins. *Sci Rep* **6**, 26715 (2016).
9. Castilho, M., Mouser, V., Chen, M., Malda, J. & Ito, K. Bi-layered micro-fibre reinforced hydrogels for articular cartilage regeneration. *Acta Biomater* **95**, 297–306 (2019).
10. Castilho, M. *et al.* Melt Electrospinning Writing of Poly-Hydroxymethylglycolide- ϵ -Caprolactone-Based Scaffolds for Cardiac Tissue Engineering. *Adv Healthc Mater* **6**, 1700311 (2017).
11. Jansen, K. *et al.* Fabrication of Kidney Proximal Tubule Grafts Using Biofunctionalized Electrospun Polymer Scaffolds. *Macromol Biosci* **19**, 1800412 (2019).
12. Kennedy, K. M., Bhaw-Luximon, A. & Jhurry, D. Cell-matrix mechanical interaction in electrospun polymeric scaffolds for tissue engineering: Implications for scaffold design and performance. *Acta Biomater* **50**, 41–55 (2017).
13. Brown, T. D. *et al.* Melt electrospinning of poly(ϵ -caprolactone) scaffolds: Phenomenological observations associated with collection and direct writing. *Mater Sci Eng: C* **45**, 698–708 (2014).
14. Brown, T. D., Dalton, P. D. & Hutmacher, D. W. Direct Writing By Way of Melt Electrospinning. *Adv Mater* **23**, 5651–5657 (2011).
15. Robinson, T. M., Hutmacher, D. W. & Dalton, P. D. The Next Frontier in Melt Electrospinning: Taming the Jet. *Adv Funct Mater* **29**, 1904664 (2019).
16. McColl, E., Groll, J., Jungst, T. & Dalton, P. D. Design and fabrication of melt electrowritten tubes using intuitive software. *Mater Des* **155**, 46–58 (2018).
17. Jansen, J. *et al.* A morphological and functional comparison of proximal tubule cell lines established from human urine and kidney tissue. *Exp Cell Res* **323**, 87–99 (2014).
18. Oo, Z. Y. *et al.* The performance of primary human renal cells in hollow fiber bioreactors for bioartificial kidneys. *Biomaterials* **32**, 8806–8815 (2011).
19. Ni, M. *et al.* Characterization of membrane materials and membrane coatings for bioreactor units of bioartificial kidneys. *Biomaterials* **32**, 1465–1476 (2011).
20. RayChaudhury, A., Elkins, M., Kozien, D. & Nakada, M. T. Regulation of PECAM-1 in Endothelial Cells during Cell Growth and Migration. *Exp Biol Med* **226**, 686–691 (2001).
21. Privratsky, J. R. & Newman, P. J. PECAM-1: regulator of endothelial junctional integrity. *Cell Tissue Res* **355**, 607–619 (2014).

22. Duclos, G., Garcia, S., Yevick, H. G. & Silberzan, P. Perfect nematic order in confined monolayers of spindle-shaped cells. *Soft Matter* **10**, 2346–2353 (2014).
23. Li, X. *et al.* On the mechanism of long-range orientational order of fibroblasts. *PNAS* **114**, 8974–8979 (2017).
24. Caetano-Pinto, P. *et al.* Fluorescence-Based Transport Assays Revisited in a Human Renal Proximal Tubule Cell Line. *Mol Pharm* **13**, (2016).
25. Hironaka, K., Makino, H., Yamasaki, Y. & Ota, Z. Renal basement membranes by ultrahigh resolution scanning electron microscopy. *Kidney Int* **43**, 334–345 (1993).
26. Andalib, M. N., Dzenis, Y., Donahue, H. J. & Lim, J. Y. Biomimetic substrate control of cellular mechanotransduction. *Biomater Res* **20**, 11 (2016).
27. Bourget, J.-M., A., F., Germain, L., Guillemette, M. & Veres, T. Alignment of Cells and Extracellular Matrix Within Tissue-Engineered Substitutes. in *Advances in Biomaterials Science and Biomedical Applications* (InTech, 2013).
28. Frohlich, E. M., Zhang, X. & Charest, J. L. The use of controlled surface topography and flow-induced shear stress to influence renal epithelial cell function. *Integr. Biol.* **4**, 75–83 (2012).
29. Frohlich, E. M. *et al.* Topographically-patterned porous membranes in a microfluidic device as an in vitro model of renal reabsorptive barriers. *Lab Chip* **13**, 2311 (2013).
30. Hulshof, F. *et al.* New insights into the effects of biomaterial chemistry and topography on the morphology of kidney epithelial cells. *J Tissue Eng Regen Med* **12**, (2018).
31. Sankaran, J., Uzer, G., van Wijnen, A. J. & Rubin, J. Gene regulation through dynamic actin control of nuclear structure. *Exp Biol Med* **244**, 1345–1353 (2019).
32. Tremblay, D., Andrzejewski, L., Leclerc, A. & Pelling, A. E. Actin and microtubules play distinct roles in governing the anisotropic deformation of cell nuclei in response to substrate strain. *Cytoskeleton* **70**, 837–848 (2013).
33. Tylek, T. *et al.* Precisely defined fiber scaffolds with 40 μm porosity induce elongation driven M2-like polarization of human macrophages. *Biofabrication* **12**, 025007 (2020).
34. Brennan, C. M., Eichholz, K. F. & Hoey, D. A. The effect of pore size within fibrous scaffolds fabricated using melt electrowriting on human bone marrow stem cell osteogenesis. *Biomed Mater* **14**, 065016 (2019).
35. Saidu, N. T. *et al.* Biologically Inspired Scaffolds for Heart Valve Tissue Engineering via Melt Electrowriting. *Small* **15**, 1900873 (2019).
36. Eichholz, K. F. & Hoey, D. A. Mediating human stem cell behaviour via defined fibrous architectures by melt electrospinning writing. *Acta Biomater* **75**, 140–151 (2018).
37. Castilho, M. *et al.* Melt Electrowriting Allows Tailored Microstructural and Mechanical Design of Scaffolds to Advance Functional Human Myocardial Tissue Formation. *Adv Funct Mater* **28**, 1803151 (2018).
38. Gasiorowski, J. Z. *et al.* Alterations in gene expression of human vascular endothelial cells associated with nanotopographic cues. *Biomaterials* **31**, 8882–8888 (2010).
39. Joly, P. *et al.* Geometry-Driven Cell Organization Determines Tissue Growths in Scaffold Pores: Consequences for Fibronectin Organization. *PLoS One* **8**, e73545 (2013).
40. Chambard, M., Gabrion, J. & Mauchamp, J. Influence of collagen gel on the orientation of epithelial cell polarity: follicle formation from isolated thyroid cells and from preformed monolayers. *JCB* **91**, 157–166 (1981).
41. Jang, K.-J. *et al.* Human kidney proximal tubule-on-a-chip for drug transport and nephrotoxicity assessment. *Integr Biol* **5**, 1119–1129 (2013).
42. Weber, E. J. *et al.* Development of a microphysiological model of human kidney proximal tubule function. *Kidney Int* **90**, 627–637 (2016).
43. Vriend, J. *et al.* Flow stimulates drug transport in a human kidney proximal tubule-on-a-chip independent of primary cilia. *Biochimica et Biophysica Acta (BBA) - General Subjects* **1864**, 129433 (2020).
44. Ling, Y. *et al.* Effects of fixation and preservation on tissue elastic properties measured by quantitative optical coherence elastography (OCE). *J Biomech* **49**, 1009–1015 (2016).

45. Kim, S.-O., Kim, J., Okajima, T. & Cho, N.-J. Mechanical properties of paraformaldehyde-treated individual cells investigated by atomic force microscopy and scanning ion conductance microscopy. *Nano Converg* **4**, 5 (2017).
46. Paxton, N. C., Daley, R., Forrestal, D. P., Allenby, M. C. & Woodruff, M. A. Auxetic tubular scaffolds via melt electrowriting. *Mater Des* **193**, 108787 (2020).
47. Jungst, T. *et al.* Heterotypic Scaffold Design Orchestrates Primary Cell Organization and Phenotypes in Cocultured Small Diameter Vascular Grafts. *Adv Funct Mater* **29**, 1905987 (2019).
48. Pennings, I. *et al.* Layer-specific cell differentiation in bi-layered vascular grafts under flow perfusion. *Biofabrication* **12**, 015009 (2019).
49. Bertlein, S. *et al.* Development of Endothelial Cell Networks in 3D Tissues by Combination of Melt Electrospinning Writing with Cell-Accumulation Technology. *Small* **14**, 1701521 (2018).
50. Wang, Z. *et al.* Dual-Microstructured Porous, Anisotropic Film for Biomimicking of Endothelial Basement Membrane. *ACS Appl Mater Interfaces* **7**, 13445–13456 (2015).
51. Tasnim, F. & Zink, D. Cross talk between primary human renal tubular cells and endothelial cells in cocultures. *Am J Physiol Renal Physiol* **302**, F1055–F1062 (2012).

CHAPTER 6

ORGANIZED MELT-ELECTROWRITTEN TUBULAR SCAFFOLDS TO BUILD VASCULARIZED KIDNEY PROXIMAL TUBULES



Abstract

Introduction: Kidney tubular engineering requires tubular structures of small sizes (≤ 1 mm) to mimic curvature of native kidney proximal tubule, which is key for cellular functionality and maturation. Here, we created highly porous rhombus tubules to achieve both a vascular and an epithelial tubular scaffold for the formation of a vascularized proximal tubule.

Materials and methods: A custom-built MEW device was used to fabricate small polycaprolactone tubular scaffolds (inner $\varnothing=1$ mm) with defined rhombus microarchitectures (winding angles of 30° , 50° and 70°). Human conditionally immortalized proximal tubule epithelial cells (ciPTEC) and glomerular endothelial cells (ciGEnC) were seeded in the scaffolds and evaluated for monolayer formation and tightness, cell directionality, polarization, and collagen IV deposition.

Results and discussion: Engineered tubular scaffolds with different rhombus microarchitectures were successfully manufactured by controlling key instrument parameters. Both CiPTEC and ciGEnC formed tight, homogenous monolayers within the tubular scaffolds and generated a collagen IV-enriched ECM. The 30° winding angles induced preferential cell alignment along the scaffold fiber direction for ciPTEC. Preliminary results indicated that ciGEnC prefer both 30° and 50° winding angles. By decreasing the pore size of the tubular scaffolds, the ciGEnC could form a tight monolayer.

Conclusions: MEW tubes with highly controlled fibrous microarchitectures advance both ciPTEC and ciGEnC cell organization and ECM deposition. Our preliminary results show the first prototype of a vascularized scaffold, where the basement membrane formed by ciPTEC supports ciGEnC adhesion and growth.

1. Introduction

The kidney, comprised of about a million functional units called nephrons, is responsible for clearing the blood from toxins and other waste products. Nephrons consist of multiple segments, including the proximal tubule (PT) that contributes to body homeostasis by reabsorbing 60-70% of water and salts and most nutrients in the ultrafiltrate [1]. The PT is surrounded by peritubular capillaries to facilitate continuous transport between proximal tubule and its surrounding vasculature. The cells of these capillaries are fenestrated, similar to the glomerular endothelial cells surrounding the glomerulus, which allow for solutes to easily enter and leave the circulation [2,3]. Various PT models have been developed for better understanding of PT function, as well as to study drug transport, interactions and/or nephrotoxicity. Most of these models were developed using either thick, slow-diffusive hydrogels or on-chip strategies that contain drug-absorptive, low porous materials [4-7]. To allow for the intimate interaction between the vascular bed and the highly specialized proximal tubule, we propose the use of melt-electrowriting (MEW) to generate tubular-structure in which tissue-specific cells retain key functionalities. MEW is a solvent-free, additive manufacturing technology that can precisely deposit thin ((sub) micrometer scale) polymer fibers on a computer-controlled collector [8,9]. A high voltage pulls a molten polymer out of a syringe, into thin fibers with a diameter in the low- and even sub-micron range [10]. To match the pulling force of the established electrical field between the syringe and the collector plate, only a relatively low pressure is needed for a constant polymer feed. The distance between the syringe and collector plate is generally a few millimeters and the thin fiber solidifies while being collected on the moving collector plate. The precise deposition of the biopolymer allows the generation of intricate self-standing structures with user-controlled features.

Polycaprolactone (PCL) is a commonly used polymer for MEW as it can be easily processed, it is biodegradable, and shows high reproducibility as of the purity of the material [11]. By changing MEW parameters, constructs can be easily optimized and fine-tuned for cell-specific scaffolds [12-15]. Using a tubular collector plate for MEW, tubular scaffolds with large pore size (here: 0.05-0.53mm²) can be created. The deposited frame will provide the anchorage-points for cells to attach, form a monolayer and deposit their own matrix, resulting in a cell-made barrier. The tubular configuration allows for the seeding of cells on both apical (outer lumen) and basal (inner lumen) side. In our previous work, we show that the topographic guidance generated via MEW, namely pore geometry and area in tubular scaffolds, can enhance monolayer formation, directionality and functionality of proximal tubule epithelial cells, but not of macrovascular endothelial cells [12]. Fabrication of vessels

of $\varnothing = 3\text{mm}$ using bi-layered grafts has been reported, however, smaller ($\varnothing \leq 1\text{mm}$) vessel tissue engineering via MEW remains a challenge [16,17]. Here, we aimed to develop a tubular vascular unit using MEW-generated tubular scaffolds loaded with proximal tubular cells and kidney-specific endothelial cells, the building blocks of the renal capillary system. However, fenestrated peritubular capillary cells are not widely available [18]. Glomerular endothelial cells, although they differ from peritubular capillaries, also have fenestrations, which facilitate exchange of *e.g.*, nutrients and waste. Thus, conditionally immortalized glomerular endothelial cells (ciGEnC) were used [19,20]. Since, we showed that rhombus-shaped pores in MEW-tubular scaffolds allow for barrier formation, all the MEW-tubes generated within this study have rhombus-shaped pores of different winding angles (30° , 50° , or 70°) [12].

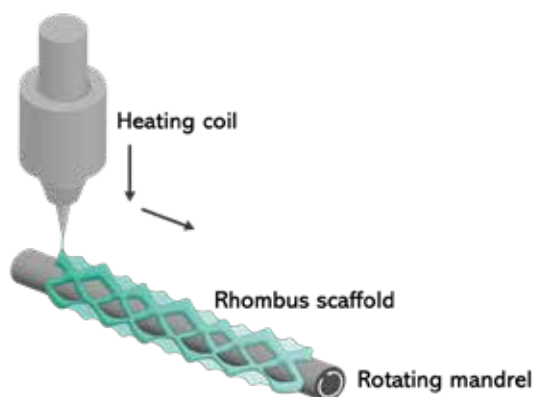


Figure 1. Principle of tubular MEW. Thin heated PCL fibers are spun around a rotating mandrel. By controlled movement of the mandrel tubular scaffold are formed with defined geometries.

2. Materials and Methods

2.1 Melt electrowriting

Tubular scaffolds were printed using a custom-built MEW device consisting of a rotating aluminum mandrel ($\varnothing = 1\text{mm}$) mounted on a x-y axis and a custom print head mounted on a movable z-axis. The x-y-z axes were computer-controlled using G-code and commercially available software (Motion Perfect V4.2, Trio Motion Technology Ltd., Gloucestershire, UK). Mandrel rotation was controlled by Arduino IDE software, and all movement was executed using an advanced MC403 motion controller (Trio Motion Technology Ltd.). Medical grade polycaprolactone granules (PCL, Purasorb PC12, Corbion, Gorinchem, The Netherlands) were loaded into a glass syringe with a 27G size metallic nozzle and heated to 88°C for 30

minutes. A high-resolution air pressure regulator (VPPE-3-1-1/8-2-010-E1, Festo, Delft, The Netherlands), and a high voltage source (Heinzinger, LNC 30000-5 POS, 0-30 kV, Rosenheim, Germany), kept constant at 2.5 bar and 6.2 kV, respectively, extruded and electrified the PCL into thin fibers. The distance between the nozzle and the mandrel was maintained at 4 mm. Printed PCL MEW tubules were designed using an open source software (MewTubes, [21]). had 8 pivot points (smaller pore size: 28) and 20 layers stacked on top of each other, with winding angles varying from 30°, 50°, to 70°. This range encompassed three distinctly different pore morphologies and sizes. The effective printing speed (V_{eff}), a vector obtained by combing translational and rotational velocity, was 3 mm/s for 30°, 5 mm/s for 50°, and 7 mm/s for 70° tubules (Table 1). Before removal from the mandrel, printed MEW tubules were imaged with a stereoscope (Olympus SZ61, Tokyo, Japan) and winding angles were analyzed with ImageJ (National Institutes of Health, Bethesda, MD, USA). 70% ethanol was used for easy removal of tubules from the mandrel.

Table 1: Printing parameters

Winding angle (°)	Tube inner diameter (mm)	Length	Pivot points*	Pore area	Layers	V_{eff}
30°	1	22.45 mm	8	0.53 mm ²	20	3 mm/s
50°	1	24.05 mm	8	0.26 mm ²	20	5 mm/s
70°	1	21.87 mm	8	0.11 mm ²	20	7 mm/s
30° (small pore size)	1	21.97 mm	26	0.05 mm ²	20	6 mm/s

*Pivot Points are locations where one length iteration ends and the next one begins.

2.2 Imaging and Structural Characterization

The micro-architecture of the scaffold and the fiber diameter were evaluated using stereomicroscopy (Olympus SZ61) and scanning electron microscopy (SEM, Phenom Pro, Phenom-World). SEM scaffolds were gold sputtered coated (1nm) using a Q150R rotary-pumped sputter (Quorum Technologies). ImageJ was used to analyze the images of stereomicroscopy.

2.3 Cell culture

CIPTeC 21.2 (MTA number A16-0147) were obtained from Cell4Pharma (Nijmegen, The Netherlands) and developed as described [22]. Conditionally immortalized glomerular

endothelial cells (ciGenC) were kindly provided by the group of Prof. J. van der Vlag (RadboudUMC, Nijmegen, The Netherlands) via an MTA with Prof. S. Satchell (Bristol Medical School (THS), Bristol, UK) [19]. Both cell lines proliferate at the permissive temperature of 33°C and mature at 37°C. CiPTEC 21.2 were cultured in T75 flasks (Greiner Bio-One, Alphen aan den Rijn, The Netherlands) in Dulbecco's modified eagle medium/HAM's F12 without phenol red (ThermoFisher Scientific, Paisley, UK), with added insulin, transferrin, selenium (all 5 µg/ml), hydrocortisone (35 ng/ml), epidermal growth factor (10 ng/ml), tri-iodothyronine (40 pg/ml) (Sigma-Aldrich, Saint Louis, MO, USA), 10% fetal bovine serum (v/v, FBS, Greiner Bio-One, Alphen aan den Rijn, The Netherlands), and 1% penicillin/streptomycin (v/v, Gibco, Thermo Fisher Scientific, Paisley, UK) to prevent infections. CiGenC were cultured in T75 flasks (Greiner Bio-One, Alphen aan den Rijn, The Netherlands) in Endothelial Cell Basal Medium-2 (Lonza, Basel, Switzerland) containing Microvascular Endothelial Cell Growth Medium-2 SingleQuots Kit (EGM-2 MV, Lonza, Basel, Switzerland).

2.4 Tubular scaffold coating and cell seeding in scaffolds

PCL tubular scaffolds were sterilized in a laminar flow cabinet using 70% ethanol for 30 minutes, followed by UV exposure in a laminar flow cabinet (365 nm for 30 min). Thereafter, tubular scaffolds were biofunctionalized using 2 mg/ml L-3,4-dihydroxyphenylalanine (L-DOPA, Sigma-Aldrich Saint Louis, MO, USA) dissolved in 10 mM tris(hydroxyethyl) aminomethane (Tris) pH 8.5 buffer (Sigma Aldrich, Saint Louis, MO, USA). L-DOPA was first dissolved and put at 37°C for 45 minutes, whereafter it was filter-sterilized and used for biofunctionalization. Coating was performed for minimal 4 hours at 37°C, and MEW scaffolds were thoroughly washed with phosphate buffered saline (PBS without calcium and magnesium, Lonza, Basel, Switzerland) before cell seeding. CiPTEC 21.2 were seeded at a concentration of 10×10^6 cells/ml, ciGenC at a concentration of 20×10^6 cells/ml. Cells were injected in the tubular scaffolds using gel loading pipette tips. Scaffolds were turned 180° after 2 hours, after 4 hours culture medium was added. The scaffolds were cultured until confluency at 33°C, followed by 7 days at 37°C. Culture medium was refreshed 3x per week.

2.5 Double seeding

PCL tubular scaffolds were coated using L-DOPA (Sigma-Aldrich, Saint Louis, MO, USA), ciPTEC were seeded inside (inner lumen, $\varnothing = 1$ mm) and grown until confluency, as described above. Upon confluency of ciPTEC, usually within 7 days of culture, ciGenC were seeded on the outside of the tubular scaffold. The tubular scaffold with a confluent layer of ciPTEC 21.2 was added to 1.5 mL cell suspension (ciGenC at a concentration of 4×10^6 cells/ml) in Eppendorf tubes (Eppendorf, Nijmegen, The Netherlands) and incubated at 33°C for 4 hours.

The Eppendorf tubes were turned 90° every 15 min. After incubation, the tubular scaffolds were added to a 6-well plate containing 40 % of ciGEnC culture medium and 60% of ciPTEC culture medium. After that cells were cultured at 33°C for 1 or 2 weeks.

2.6 Immunocytochemistry

Scaffolds were fixed for 10 min using 4% (v/v) paraformaldehyde in PBS (Pierce™, Thermo Fisher Scientific, Carlsbad, CA, USA). 0.3% (v/v) triton X-100 (Sigma Aldrich, Saint Louis, Mo, USA) in PBS was used to permeabilize the cells for 10 min at room temperature. Blocking buffer was prepared (2% (v/v) FBS, 0.1% (v/v) Tween20 (Sigma Aldrich, Saint Louis, MO, USA), 0.5% (w/v) bovine serum albumin (Sigma Aldrich, Saint Louis, MO, USA) in PBS) and added for 30 minutes at room temperature. Antibodies were diluted in blocking buffer. Primary and secondary antibodies were incubated at room temperature for 90 and 60 minutes, respectively. A list of primary and secondary antibodies and their dilutions can be found in

Supplementary Table 1.

A Leica TCS SP8 X confocal microscope (Leica, Wetzlar, Germany) and Leica Application Suite X software were used to image immunofluorescent PCL MEW tubules. ImageJ ((National Institutes of Health, Bethesda, MD, USA) free software was used to make Z-projections and to quantify cell alignment via actin filament direction with the directionality function and Fourier components analysis.

3. Results

3.1 Optimized parameters lead to highly accurate geometry design

PCL tubular scaffolds with defined winding angles (30°, 50°, and 70°), 8 or 26 pivot points and 20 fiber layers were successfully fabricated with a custom-built MEW device. Using stereoscope imaging and ImageJ analysis, printing accuracy was assessed (**Figure 2A-F**). All winding angles were obtained with high accuracy, as no differences were found between the theoretical and measured winding angles (**Figure 2G**).

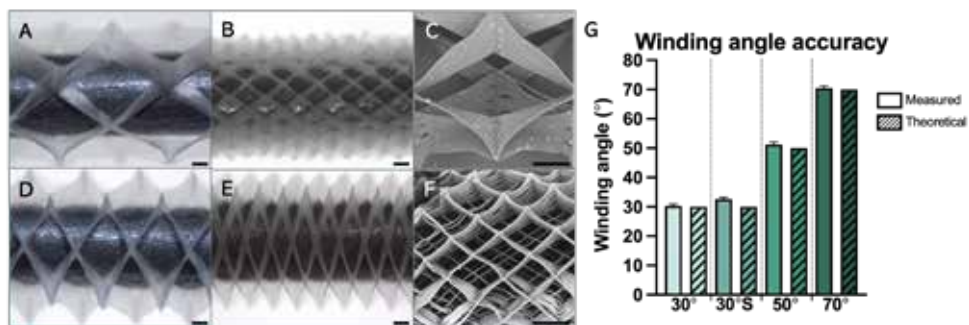


Figure 2. Winding angle accuracy. Stereoscopic images of PCL tubular scaffolds printed on 1 mm \varnothing mandrel with winding angles of 30°(A), 30° small pore size (B), 50°(D), and 70°(E), scale bars: 200 μ m. Scanning electron microscope images of PCL tubular scaffolds with winding angles 30° (C) and 30° small pore size (F), scale bars: 300 μ m. (G) Winding angle accuracy displayed as average \pm SEM, n = 3.

3.2 ciPTEC and ciGenC form monolayers in all scaffolds

ciPTEC and ciGenC were seeded in tubular MEW scaffolds with winding angles of 30°, 50°, or 70°. Both cell-lines were able to form monolayers in all tested winding angles (**Figure 3**). However, based on actin filament staining, it was observed that ciPTEC (**Figure 3A-F**) show preferential cell alignment in the 30° winding angle tubular scaffolds (**Figure 3A, D**). For ciGenC (**Figure 3G-L**) the difference between the 3 winding angles was less pronounced, ciGenC show preferential cell alignment in both 30° and 50° (**Figure 3G, H, J, K**).

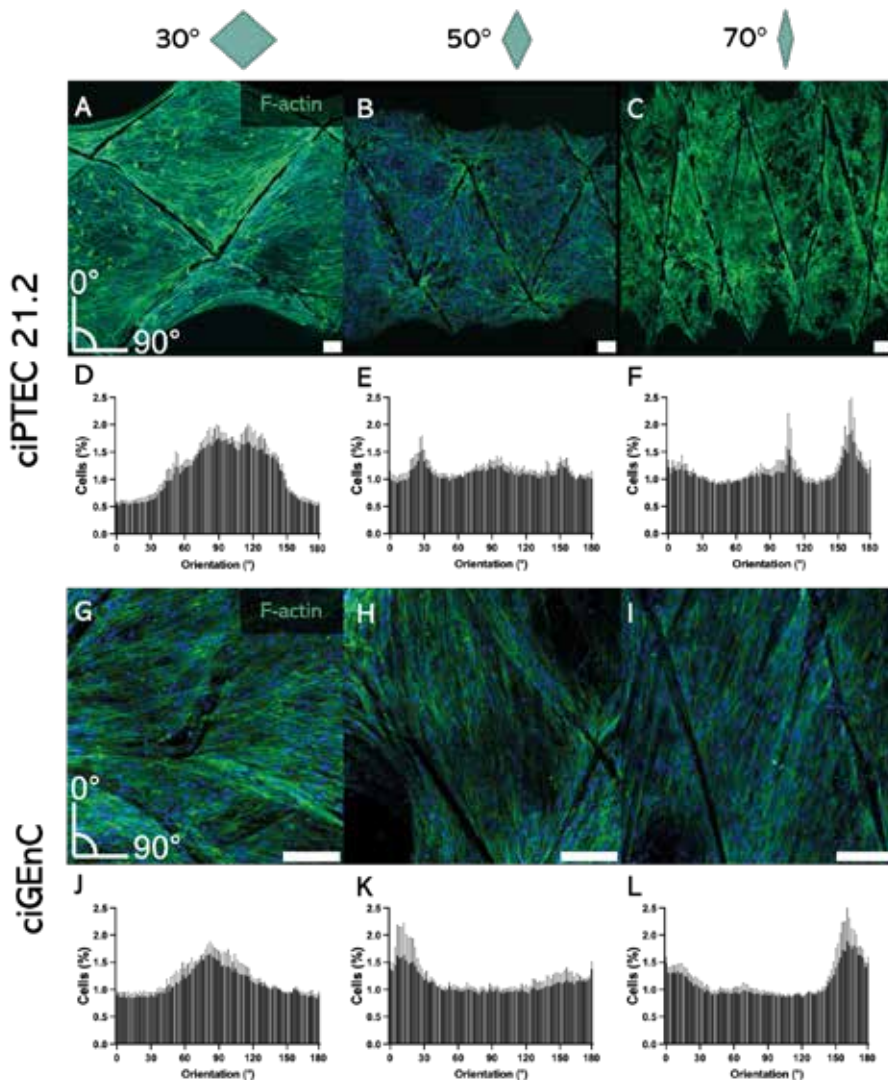


Figure 3. Cell growth and directionality. (A-C) Actin filament (green), DAPI (blue) for ciPTEC grown in tubular scaffolds with rhombus geometry and winding angles of 30°, 50°, and 70°. (D-F) Quantification of cell directionality for ciPTEC. (G-I) Actin filament (green), DAPI (blue) for ciGenC grown in tubular scaffolds with rhombus geometry and winding angles of 30°, 50°, and 70°. (J-L) Quantification of cell directionality for ciGenC. Scale bars: 100 mm. Mean + SEM, $n = 3$.

3.3 Tight/adherent junction markers and polarization

Zonula occludens-1 (ZO-1), a tight junction associated protein, is an important indicator for monolayer tightness. It plays a major role in the formation of the intercellular barrier between epithelial cells, whereby it regulates selective movement of solutes across the epithelial layer

[23]. CiPTEC expressed ZO-1 when grown in 30° (**Figure 4A**), but not in the 50° (**Figure 4B**) and 70° (**Figure 4C**) PCL tubular scaffolds. Endothelial marker cluster of differentiation 31 (CD31, also known as platelet endothelial cell adhesion molecule 1, PECAM-1) is a cell-cell adhesion protein that is often used as an endothelial cell marker. CD31 was expressed in ciGenC in all winding angles (**Figure 4D-F**). Finally, to assess cell polarization, ciPTEC were stained for the sodium-potassium pump (Na^+/K^+ -ATPase), expressed at the basolateral side of the cells, and for apically expressed α -tubulin. Immunostainings show presence of both polarization markers (**Figure 4 G-I**). In the 30° and 50° scaffolds, ciPTEC formed a polarized layer (**Figure 5A, B**), as indicated by apical presence of α -tubulin and basolateral presence of Na^+/K^+ -ATPase. However, in the 70° scaffolds cells did not form a polarized layer, as α -tubulin was located on both apical and basolateral side (**Figure 5C**).

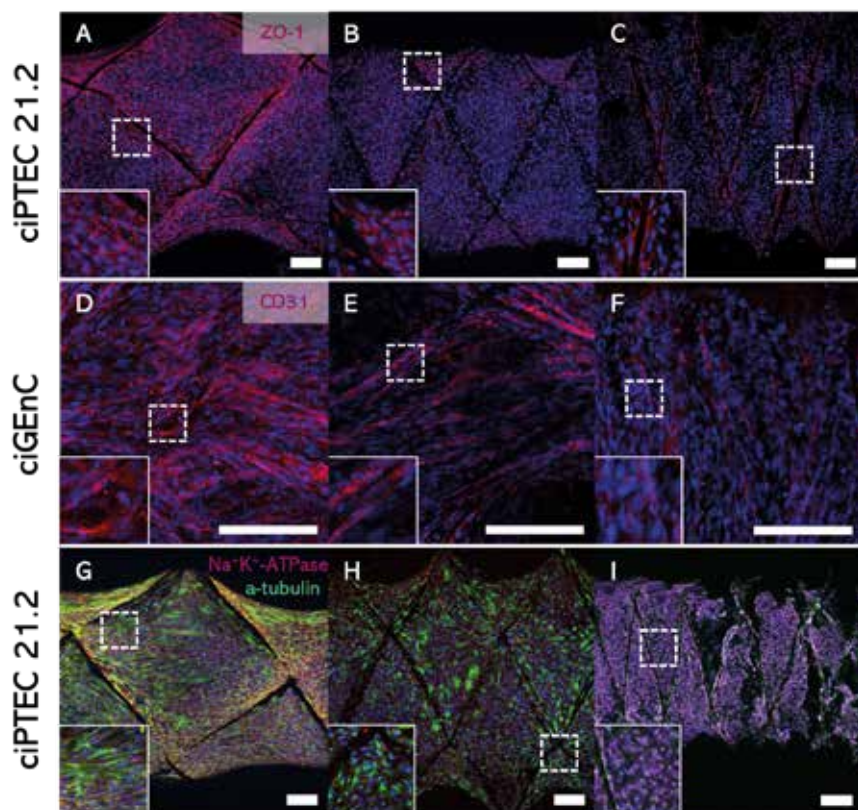


Figure 4. Cell-specific markers. (A-C) Tight-junction marker zonula occludens-1 (red) in ciPTEC and (D-F) cell-adhesion marker CD31 (red) in ciGenC grown in tubular scaffolds with rhombus geometry and winding angles of 30° (A, D), 50° (B, E) and 70° (C, F). (G-I) Na^+/K^+ -ATPase (magenta), α -tubulin (green), DAPI (blue) in ciPTEC grown in tubular scaffolds with rhombus geometry and winding angles of 30°, 50°, and 70°. Scale bars: 100 μm . $n = 3$.

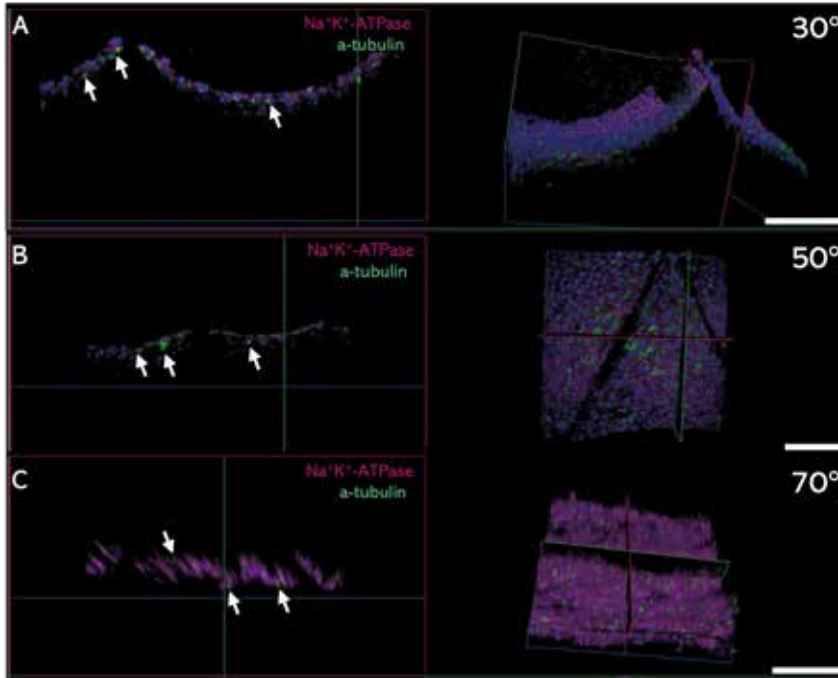


Figure 5. CiPTEC polarization. 3D images of immunostaining for Na⁺/K⁺-ATPase (magenta), α-tubulin (green), DAPI (blue) in ciPTEC grown in tubular scaffolds with rhombus geometry and winding angles of 30°, 50°, and 70°. White arrows indicate location of α-tubulin. Scale bars: 200 μm. n = 3.

3.4 Collagen IV deposition by ciPTEC and ciGenC

Since the PCL tubular scaffolds are highly porous, the formation of a cellular barrier on the luminal sides of the tubes depends on the cells attachment to the printed frame and deposition of a basement membrane (BM) that spans over the open pores. It is reported that the BM of both the proximal tubule and its surrounding peritubular capillaries consists for over 50% of collagen IV [24]. Staining for collagen IV after 7 days of maturation at 37°C indicated that both ciPTEC (**Figure 6A-C**) and ciGenC (**Figure 6G-I**) deposited collagen IV and thereby formed their own BM as support. Collagen I is an indicator for fibrosis and within a healthy BM, only modest collagen I is expected to be present [25]. Immunostaining for collagen I revealed that ciPTEC only very limitedly deposited collagen I (**Figure 6D-F**).

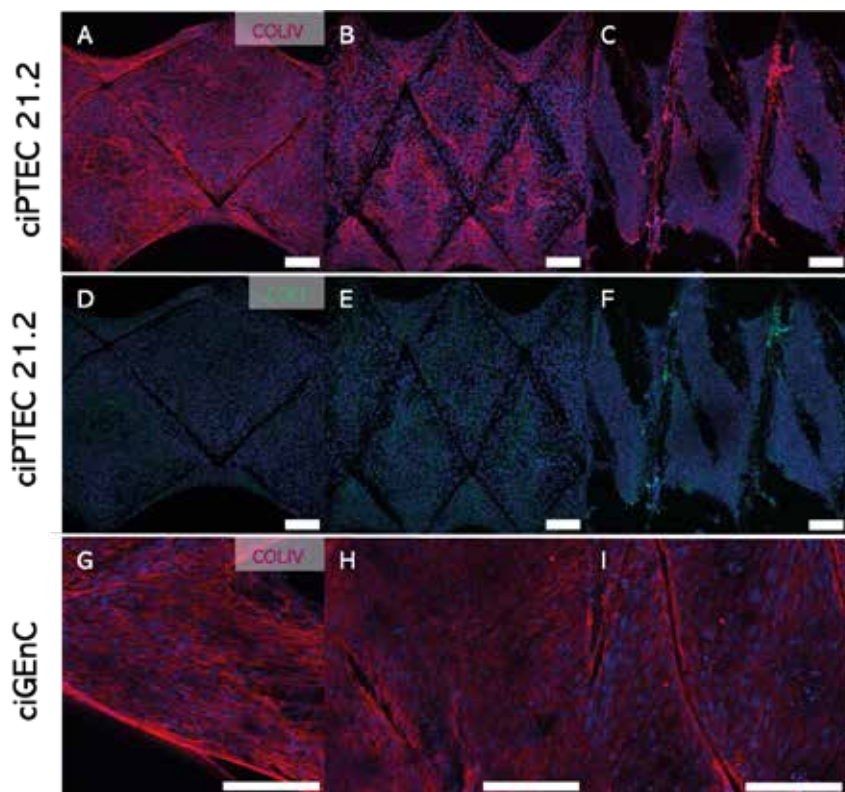


Figure 6. ECM deposition by ciPTEC and ciGENC. Collagen I and IV deposition (A-F) collagen IV (red), collagen I (green) and DAPI (blue) in ciPTEC grown in tubular scaffolds with rhombus geometry and winding angles of 30° (A, D), 50° (B,E), and 70° (C,F). (G-I) collagen IV (red), DAPI (blue) in ciGENC grown in tubular scaffolds with rhombus geometry and winding angles of 30° (G), 50° (H), and 70° (I). Scale bars: 100 μ m. n = 3.

3.5 Smaller pore sizes to advance ciGENC monolayer formation

While ciGENC were able to bridge the large pores of the PCL tubular scaffolds, growth was rather slow as it could take 4 weeks up to several months to cover the full tubes. Pore size optimization was performed to define which pore sizes promote ciGENC monolayer formation. For this, the winding angle was kept at 30°, while the areas of the pores were reduced from 0.53 mm² to 0.11 mm², 0.055 mm², and 0.027 mm² (**Figure 7**). CiGENC could fill up pores with an area of 0.055 mm² and 0.027 mm² (**Supplementary Figure 1**), but not larger. Next, a new tube design was generated (using MewTubes) to print PCL tubular scaffolds with a 30° winding angle and a pore area of 0.05 mm² (**Figures 7E-H**), which resulted in ciGENC monolayers within 7 days of culture at 33°C (**Figure 7G-H**). CiGENC monolayers were further studied after 7 days of maturation at 37°C. Staining for collagen IV and collagen I (**Figure 8A-B**)

indicated the formation of a healthy BM, with low collagen I and high collagen IV content. F-actin directionality measurements indicated alignment of ciGenC within the tubular scaffolds (**Figure 8C,F**). Finally, endothelial marker CD31 was expressed (**Figure 8D**), as well as endothelial markers vascular endothelial (VE) -cadherin (endothelial specific adhesion molecule, which controls cellular junctions and blood vessel formation) (**Figure 8E**), and Von Willebrand Factor (VWF, a procoagulant protein expressed by endothelial cells) (**Figure 8E**).

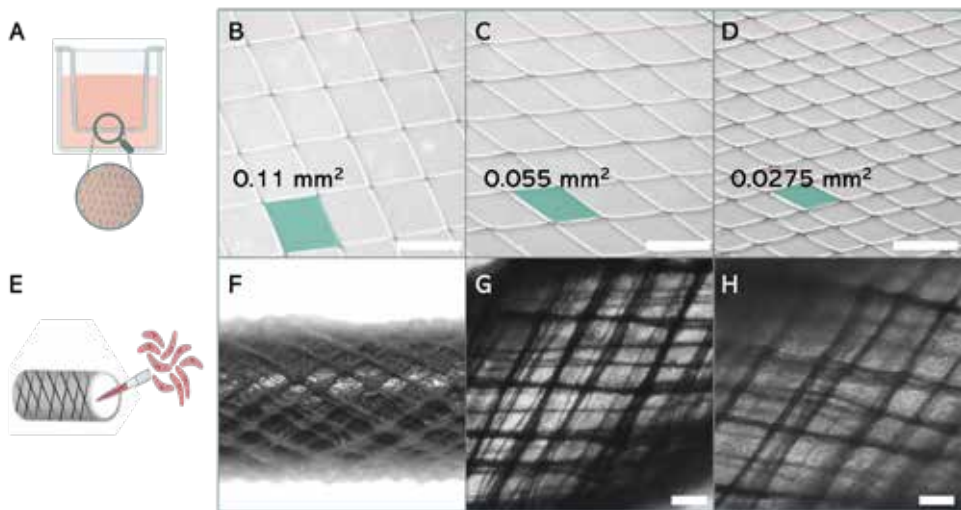


Figure 7. Pore size optimization for ciGenC. A) Flat membranes are mounted in a Transwell set-up. B) 0.11 mm² C) 0.055 mm² D) 0.027 mm². E) Graphical overview of seeding of endothelial cells in PCL tubular scaffolds. F) PCL tubular scaffold with pore size 0.05 mm² printed on 1mm Ø tubular mandrel. G, H) Brightfield photo of ciGenC grown in tubular scaffolds 1 day (G) and 7 days (H) after seeding. Scale bars: 100 µm, n = 3

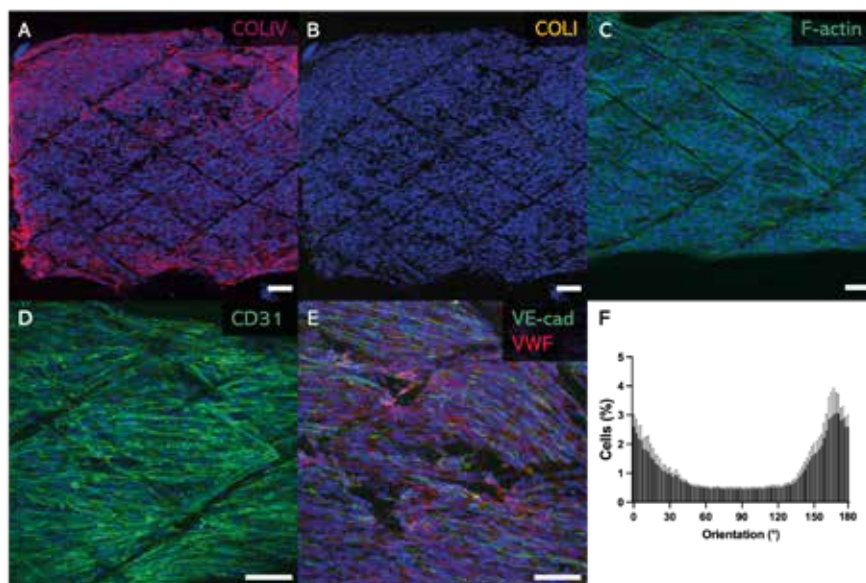


Figure 8. ciGENC grown in tubular scaffolds with small pore size (30° winding angle). Extracellular matrix markers: A-C Collagen IV (red), Collagen I (yellow), F-actin (green) and DAPI (blue). Endothelial markers: D) CD31 (green) and DAPI (blue). E) VE-cadherin (green), Von Willebrand Factor (red), DAPI (Blue). F) Quantification of F-actin directionality for ciGENC, Mean \pm SEM. Scale bars: 100 μ m. n = 3.

3.6 First steps towards vascularized proximal tubule within one MEW tubular scaffold

Finally, we hypothesized that the BM formed by the PTEC supports the endothelial cells to adhere and grow on the scaffolds. ciGENC were seeded on the outside of PCL tubular scaffolds with already a monolayer of ciPTEC grown on the inside (**Figure 9A-D**). The endothelial marker CD31 was used to confirm the phenotype of ciGENC and to verify that no ciPTEC infiltrated in the outer lumen. After 1 week, ciGENC were clearly visible on the ciPTEC-covered scaffolds (**Figure 9E**), while after 2 weeks ciGENC were close to forming a monolayer (**Figure 9F**). Staining for ZO-1 and occludin, 1 week after seeding ciGENC, (**Figure 9G**) indicated presence of tight monolayers. However, since ZO-1 and occludin are expressed by both ciPTEC and ciGENC no differentiation between both cell types can be made at this stage.

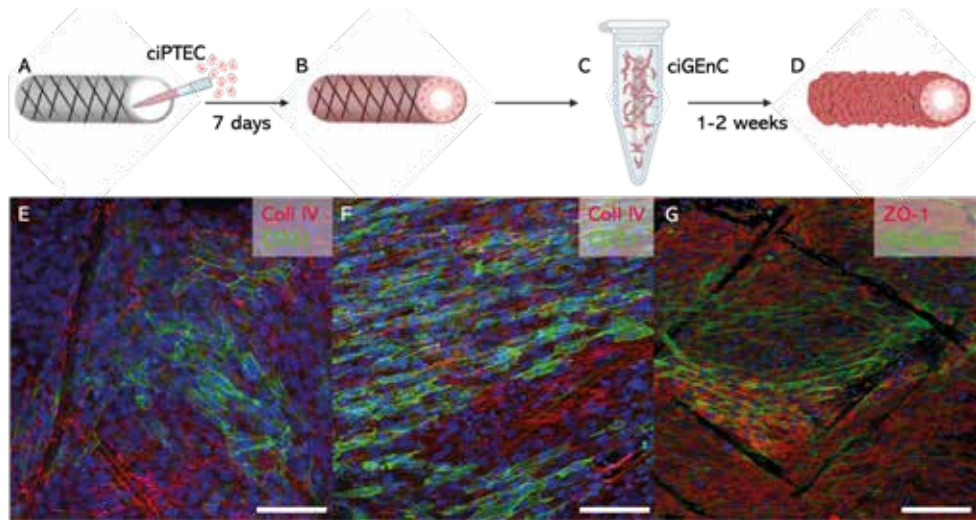


Figure 9. Graphical overview of seeding process. A) ciPTEC seeded inside tubular MEW scaffolds B) ciPTEC monolayer within tubular scaffold, cultured at 33°C until confluency. C) ciGenC seeded on the outside of tubular MEW scaffolds with a monolayer of ciPTEC on the inside. D) ciGenC form a monolayer on the outside of the scaffolds. E-F) Immunofluorescent staining for CD31 (green), collagen IV (red) and DAPI (blue) at E) 1 week after seeding and F) 2 weeks after seeding. G) Staining for ZO-1 (red) and occludin (green), 1 week after seeding ciGenC. Scale bars: 100 μ m. n=2

4. Discussion

4.1 Proximal tubule

The PT is a highly specialized part of the nephron with an important role in waste management. Here, we aimed to mimic the vascularized PT for *in vitro* modeling, which could eventually be used to produce biocompatible scaffolds for implantation. MEW was used to create the scaffolds because of the ability to design the winding angles of the printed scaffolds [14,15]. Previously, we have shown the effect of scaffold geometry on ciPTEC proliferation and maturation [12]. In this chapter, rhombus geometry was further studied by including three different winding angles: 30°, 50° and 70°. CiPTEC formed monolayers in scaffolds of all three winding angles, but only showed preferential directionality in the 30° scaffolds, confirming our previous study results, further highlighting the effect of topographic guidance by the scaffold [26,27].

In native kidneys, PTEC are attached to the BM, a complex and specialized network that gives the cells support by acting as a scaffold and a barrier [24]. The cells deposit BM components like collagens and laminins, with collagen IV being the main component of the tubular BM

(TBM), while collagen I is associated with tubular fibrosis [24,25,28,29]. Hence, abundant presence of collagen IV, but not collagen I, is indicative of a healthy BM formed by ciPTEC, which was found for all winding angles.

Tight junction associated protein ZO-1 forms a barrier complex that separates the apical and basolateral sides of cells, its presence indicates both cell maturation as well as the degree of tightness of the monolayer [30]. Although a scattered signal of ZO-1 was found to be present in the 50° and 70° tubes, solely cells in 30° tubes showed a defined immunostaining for the protein. Reduced ZO-1 has been associated with increased proliferation of epithelial cells, while increased ZO-1 expression is linked to confluent dense layers of differentiated cells [31,32]. Our findings suggest that the cells within the 30° tubes are in a more differentiated state compared to the cells in the 50° and 70° tubes.

Also, cell polarity is critical for proper cell function and architecture, especially for epithelial cells like PTEC that utilize apical-basal polarity to create a barrier function [33]. Loss of PTEC polarity is a hallmark of kidney injury, emphasizing its important role [34]. Polarity is guided by proteins and lipid regulators that respond to extracellular cues to initiate polarization; it is hypothesized that junctions also play an important role in this [35-37]. A polarized layer of ciPTEC was found in both 30° and 50° tubes, indicating that even limited extracellular cues, as the cells grow on highly porous scaffolds, can lead to polarized monolayers. Additionally, collagen IV might play a role by anchoring the cells in a polarized manner [25].

Finally, the PT has an irregular lumen that is often star-like shaped, opposed to the round distal lumen [38]. This PT stellate lumen is partially mimicked by the vertices of the MEW scaffolds and the pendant cell layer (**Supplementary Figure 2**), which might be another explanation why ciPTEC can deposit BM that covers the entire pores of these scaffolds.

4.2 Vascularized proximal tubule

Previously, we showed that HUVEC cannot form monolayers within the highly porous MEW scaffolds [12]. We therefore chose ciGenC, cells with a kidney origin that more closely mimic the peritubular capillaries by forming fenestrated endothelial monolayers [19]. GenC monolayers are, however, different from native peritubular capillaries as the fenestrations are covered by a thick glycocalyx, whereas those of peritubular capillaries are covered by a very thin diaphragm composed of glycoproteins organized in fibrils [3,39-41]. But, since primary peritubular capillary cells are rarely studied and poorly available, we chose to use GenC for model optimization. The cells formed monolayers in all scaffolds within 7 days, after

pore size optimization, with the formation of a collagen IV-rich BM, F-actin directionality, and expression of endothelial markers CD31, VE-cadherin and VWF. Larger pores were more difficult to bridge by GEnC, which can be explained by the fact that in native tissue, endothelial cells are surrounded by various supportive cells like pericytes. These cells are embedded in the BM and involved in homeostatic functions related to angiogenesis, vessel maturation and respond to injury [42,43]. In the future, incorporation of pericytes and renal interstitial fibroblasts might further boost GEnC proliferation and maturation [42].

Co-culturing epithelial and endothelial cells have previously been reported to lead to increased proliferation, enhanced enzyme activity and, amongst others, increased hepatocyte growth factor and vascular endothelial growth factor expression [44-46]. Preliminary results using our double-seeded model showed that ciGEnC can benefit from the tubular BM deposited by ciPTEC. They formed a monolayer on the deposited BM in about 2 weeks when seeding at a relatively low density, compared to seeding ciGEnC in monoculture, where it took >2 months to form monolayers. Further studies are needed to elucidate the exact effects of the co-culture on endothelial cell functionality and *e.g.*, growth factor release.

5. Conclusions

Our PCL tubular scaffolds are self-supportive, small-sized ($\varnothing = 1$ mm), and highly porous, yet they provide enough support to the cells to form monolayers within the tubular scaffolds. ciPTEC and ciGEnC form organized monolayers within mainly the 30° tubes and exhibit mature markers, such as ZO-1 and CD31, while forming polarized monolayers. Moreover, by seeding both cell types consecutively, ciPTEC can provide an extra support layer in forming a BM for ciGEnC. Nevertheless, cell functionality of both ciPTEC and ciGEnC in co-culture needs to be studied further. Additionally, with the future aim to incorporate the double seeded tube within a perfusable chip (**Supplementary Figure 3**), we will study the effect of fluid shear stress, as well as study cell functionality and polarized transport between the two cell types. After extensive validation, this model can be widely used for PT transport assessment and drug safety testing.

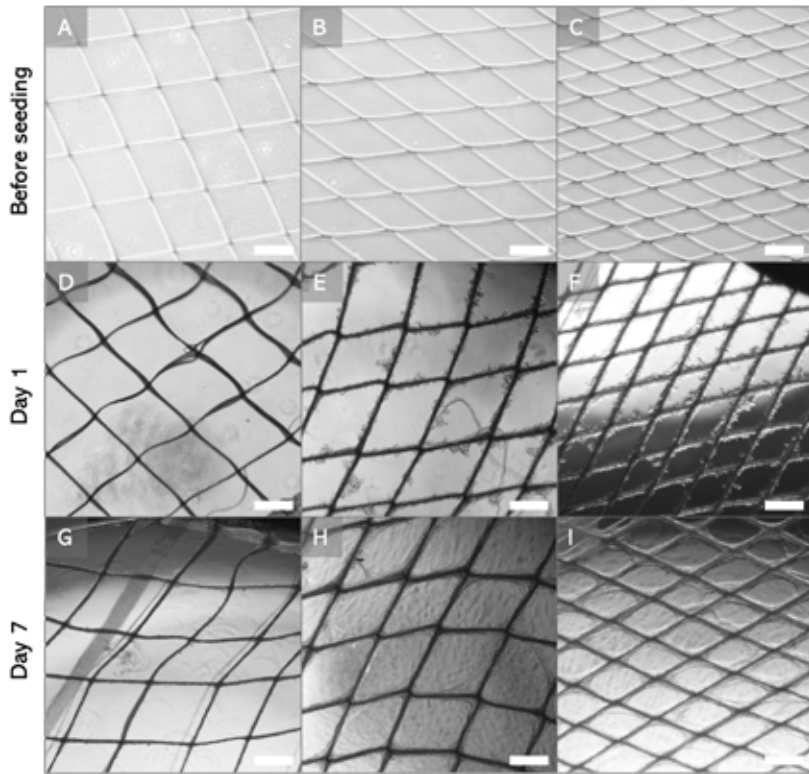
Acknowledgements

The authors would like to gratefully thank Prof. J. van der Vlag and Prof. S. Satchell for providing us with ciGEnC, Dr. A. Hrynevich for assistance with melt-electrowriting, and Dr. Y. Li for helping with the chip design.

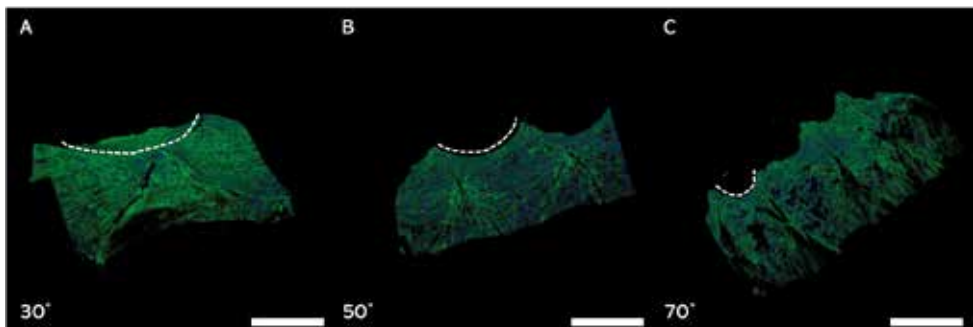
Supplementary Materials

Supplementary Table 1. Antibodies for immunocytochemistry

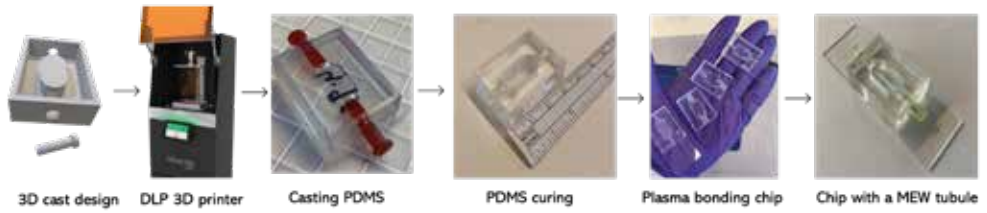
Primary antibody	Secondary antibody
Mouse monoclonal anti- α -tubulin 1:200 T6793, Sigma-Aldrich	AlexaFluor 488 donkey-anti-mouse 1:200 Invitrogen
Rabbit anti human Na-K-ATPase 1:250 Generously provided by Prof. Jan Koenderink, RadboudUMC, The Netherlands	AlexaFluor 568 donkey-anti-rabbit 1:200 Invitrogen
Goat monoclonal anti-collagen IV 1:50 1340-01, Southern Biotech	AlexaFluor 647 donkey-anti-goat 1:200 Invitrogen
Rabbit polyclonal anti collagen I 1:100 Ab34710, Abcam	AlexaFluor 568 donkey-anti-rabbit 1:200 Invitrogen
Rabbit anti- ZO-1 1:100 Ab216880, Abcam	AlexaFluor 568 donkey-anti-rabbit 1:200 Invitrogen
Mouse anti CD31/PECAM-1 1:150 BBA7, R&D Systems	AlexaFluor 488 donkey-anti-mouse 1:200 Invitrogen
Mouse anti occludin 1:100 Ab242202, Abcam	AlexaFluor 488 donkey-anti-mouse 1:200 Invitrogen
Rabbit anti VWF 1:100 Ab143193, Abcam	AlexaFluor 568 donkey-anti-rabbit 1:200 Invitrogen
Mouse anti VE-cadherin 1:200 Sc-9989, Santa Cruz	AlexaFluor 488 donkey-anti-mouse 1:200 Invitrogen
AlexaFluor 488 phalloidin 1:1000 A22283, Thermo Fisher Scientific	N.a.
DAPI 1:1000 D9542, Sigma-Aldrich	N.a.



Supplementary Figure 1. Pore size optimization for ciGenC. Membranes with different pore sizes are mounted in a Transwell Set-up: A) 0.11 mm² B) 0.055 mm² C) 0.027 mm². D-F) ciGenC on 0.11, 0.055 and 0.027 mm² membranes, respectively, directly after seeding. G-I) ciGenC on 0.11, 0.055 and 0.027 mm² membranes, respectively, 7 days after seeding.



Supplementary Figure 2. 3D images of F-actin staining in PCL tubular scaffolds with 30° (A), 50° (B), and 70° (C) winding angles. White dotted lines indicate the curvature of the cell monolayer formed between the PCL fibers. Scale bars: 500 μ m.



Supplementary Figure 3. First steps towards a perfusable chip for PCL tubular scaffolds. Cast is printed with DLP 3D printer after design. PDMS is casted into the printed mold. After curing, PDMS is plasma bonded to a glass slide, after which is incubated at 115 °C overnight. PCL tubular scaffold is mounted in the chip using 19G blunt needles and tygon tubing which tightly fit the PDMS chip.

References

1. Zhuo, J. L. & Li, X. C. Proximal Nephron. in *Compr Physiol* 1079–1123 (Wiley, 2013).
2. Pallone, T. L. & Cao, C. Renal Cortical and Medullary Microcirculations. in *Seldin and Giebisch's The Kidney* 627–670 (Elsevier, 2008).
3. Stolz, D. B. & Sims-Lucas, S. Unwrapping the origins and roles of the renal endothelium. *Pediatric Nephrology* **30**, 865–872 (2015).
4. Homan, K. A. *et al.* Bioprinting of 3D Convoluted Renal Proximal Tubules on Perfusable Chips. *Sci Rep* **6**, 1–13 (2016).
5. Jansen, K., Schuurmans, C. C. L., Jansen, J., Masereeuw, R. & Vermonden, T. Hydrogel-Based Cell Therapies for Kidney Regeneration: Current Trends in Biofabrication and In Vivo Repair. *Curr Pharm Des* **23**, 3845–3857 (2017).
6. Singh, N. K. *et al.* Three-dimensional cell-printing of advanced renal tubular tissue analogue. *Biomaterials* **232**, (2020).
7. Lin, N. Y. C. *et al.* Renal reabsorption in 3D vascularized proximal tubule models. *Proc Natl Acad Sci U S A* **116**, 5399–5404 (2019).
8. Dalton, P. D., Joergensen, N. T., Groll, J. & Moeller, M. Patterned melt electrospun substrates for tissue engineering. *Biomed Mater* **3**, 034109 (2008).
9. Brown, T. D., Dalton, P. D. & Hutmacher, D. W. Direct Writing By Way of Melt Electrospinning. *Adv Mater* **23**, 5651–5657 (2011).
10. Hochleitner, G. *et al.* Additive manufacturing of scaffolds with sub-micron filaments via melt electrospinning writing. *Biofabrication* **7**, 035002 (2015).
11. Youssef, A., Hollister, S. J. & Dalton, P. D. Additive manufacturing of polymer melts for implantable medical devices and scaffolds. *Biofabrication* **9**, 012002 (2017).
12. van Genderen, A. M. *et al.* Topographic Guidance in Melt-Electrowritten Tubular Scaffolds Enhances Engineered Kidney Tubule Performance. *Front Bioeng Biotechnol* **8**, 1542 (2021).
13. King, W. & Bowlin, G. Near-Field Electrospinning and Melt Electrowriting of Biomedical Polymers—Progress and Limitations. *Polymers (Basel)* **13**, 1097 (2021).
14. Kade, J. C. & Dalton, P. D. Polymers for Melt Electrowriting. *Adv Healthc Mater* **10**, 2001232 (2021).
15. McCosker, A. B., Snowdon, M. E., Lamont, R., Woodruff, M. A. & Paxton, N. C. Exploiting Nonlinear Fiber Patterning to Control Tubular Scaffold Mechanical Behavior. *Adv Mater Technol* 2200259 (2022)
16. Jungst, T. *et al.* Heterotypic Scaffold Design Orchestrates Primary Cell Organization and Phenotypes in Cocultured Small Diameter Vascular Grafts. *Adv Funct Mater* **29**, 1905987 (2019).
17. Pennings, I. *et al.* Layer-specific cell differentiation in bi-layered vascular grafts under flow perfusion. *Biofabrication* **12**, 015009 (2019).
18. Ligresti, G. *et al.* A Novel Three-Dimensional Human Peritubular Microvascular System. *JASN*, 2370–2381 (2016).
19. Satchell, S. C. *et al.* Conditionally immortalized human glomerular endothelial cells expressing fenestrations In response to VEGF. *Kidney Int* **69**, 1633–1640 (2006).
20. Dumas, S. J. *et al.* Phenotypic diversity and metabolic specialization of renal endothelial cells. *Nat Rev Nephrol* **17**, 441–464 (2021).
21. McColl, E., Groll, J., Jungst, T. & Dalton, P. D. Design and fabrication of melt electrowritten tubes using intuitive software. *Mater Des* **155**, 46–58 (2018).
22. Jansen, J. *et al.* A morphological and functional comparison of proximal tubule cell lines established from human urine and kidney tissue. *Exp Cell Res* **323**, 87–99 (2014).

23. Fromm, M., Piontek, J., Rosenthal, R., Günzel, D. & Krug, S. M. Tight junctions of the proximal tubule and their channel proteins. *Pflugers Arch* **469**, 877–887 (2017).
24. van Genderen, A. M., Jansen, J., Cheng, C., Vermonden, T. & Masereeuw, R. Renal Tubular- and Vascular Basement Membranes and their Mimicry in Engineering Vascularized Kidney Tubules. *Adv. Healthc. Mater.* vol. 7 1800529 (2018).
25. Karsdal, M. A. *et al.* The good and the bad collagens of fibrosis—Their role in signaling and organ function. *Adv Drug Deliv Rev* **121**, 43–56 (2017).
26. Bourget, J.-M., A., F., Germain, L., Guillemette, M. & Veres, T. Alignment of Cells and Extracellular Matrix Within Tissue-Engineered Substitutes. in *Advances in Biomaterials Science and Biomedical Applications* (InTech, 2013).
27. Andalib, M. N., Dzenis, Y., Donahue, H. J. & Lim, J. Y. Biomimetic substrate control of cellular mechanotransduction. *Biomater Res* **20**, 11 (2016).
28. Abrahamson, D. R. & Leardkamolkarn, V. Development of kidney tubular basement membranes. *Kidney Int* **39**, 382–393 (1991).
29. Martin, C. R., Timpl, R. & Kühn, K. Basement Membrane Proteins: Molecular Structure and Function. in 1–50 (1988).
30. Pozzi, A. & Zent, R. ZO-1 and ZONAB Interact to Regulate Proximal Tubular Cell Differentiation. *JASN* **21**, 388–390 (2010).
31. Balda, M. S. & Matter, K. Tight junctions and the regulation of gene expression. *Biochimica et Biophysica Acta (BBA) - Biomembranes* **1788**, 761–767 (2009).
32. Balda, M. S., Garrett, M. D. & Matter, K. The ZO-1-associated Y-box factor ZONAB regulates epithelial cell proliferation and cell density. *JCB* **160**, 423–432 (2003).
33. Jabbarzadeh, E. Polarity as a physiological modulator of cell function. *Front Biosci* **24**, 4728 (2019).
34. Stoops, E. H. & Caplan, M. J. Trafficking to the Apical and Basolateral Membranes in Polarized Epithelial Cells. *JASN* **25**, 1375–1386 (2014).
35. Riga, A., Castiglioni, V. G. & Boxem, M. New insights into apical-basal polarization in epithelia. *Curr Opin Cell Biol* **62**, 1–8 (2020).
36. Rodriguez-Boulán, E. & Macara, I. G. Organization and execution of the epithelial polarity programme. *Nat Rev Mol Cell Biol* **15**, 225–242 (2014).
37. Drubin, D. G. & Nelson, W. J. Origins of Cell Polarity. *Cell* **84**, 335–344 (1996).
38. Ross, M. H. & Pawlina, W. *Histology: A Text and Atlas: with Correlated Cell and Molecular Biology*. (Wolters Kluwer Health, 2016).
39. Jourde-Chiche, N. *et al.* Endothelium structure and function in kidney health and disease. *Nat Rev Nephrol* **15**, 87–108 (2019).
40. Singh, A. *et al.* Glomerular Endothelial Glycocalyx Constitutes a Barrier to Protein Permeability. *JASN* **18**, 2885–2893 (2007).
41. Haraldsson, B. & Nyström, J. The glomerular endothelium. *Curr Opin Nephrol Hypertens* **21**, 258–263 (2012).
42. Kramann, R. & Humphreys, B. D. Kidney Pericytes: Roles in Regeneration and Fibrosis. *Semin Nephrol* **34**, 374–383 (2014).
43. Shaw, I., Rider, S., Mullins, J., Hughes, J. & Péault, B. Pericytes in the renal vasculature: roles in health and disease. *Nat Rev Nephrol* **14**, 521–534 (2018).
44. Bertocchi, C. *et al.* Differential Effects of NO Inhibition in Renal Epithelial and Endothelial Cells in Mono-Culture vs. Co-Culture Conditions. *Cell. Physiol. Biochem.* **26**, 669–678 (2010).
45. Tasnim, F. & Zink, D. Cross talk between primary human renal tubular cells and endothelial cells in cocultures. *Am. J. Physiol. Renal Physiol.* **302**, F1055–F1062 (2012).
46. Aydin, S. *et al.* Influence of microvascular endothelial cells on transcriptional regulation of proximal tubular epithelial cells. *Am. J. Physiol. Cell Physiol.* **294**, C543–C554 (2008).

CHAPTER 7

SUMMARY AND GENERAL DISCUSSION



Chronic kidney disease (CKD) affects more than 10% of the population, being one of the leading causes of mortality worldwide [1]. Studies report that the incidence of CKD continues to rise. Hence, effective prevention and treatment for kidney diseases are needed. Despite the growing incidence, in the past 70 years only few major advances were made in the treatment of end stage kidney disease (ESKD) [2]. Novel promising replacement platforms to advance secretion of uremic toxins encompasses cell-based therapies, such as a bioartificial kidney [3-12]. While results are encouraging, devices are limited to an extracorporeal application, sequential to hemodialysis. I hypothesize that an implantable kidney tubule system is more preferred as it will facilitate a continuous clearance of waste products. Moreover, it may also improve the socio-economic status of the patient. Since an implantable kidney tubule system is highly complex, it requires a step-by-step approach. Thus, the aim of this thesis was: “*Develop 3D bioprinted vascularized kidney tubules in a microfluidic system and study the effect of scaffold design on the clearance of protein bound uremic toxins.*” With this, fundamental knowledge will be gained that can be used for development of implantable kidney tubules in the future. To achieve this, we started by optimizing extracellular matrix (ECM) mimicking scaffolds and selecting functional cells that can closely mimic the complex environment of the proximal tubule and its surrounding peritubular capillaries.

1. Potential of regenerative medicine for the kidney

Regenerative medicine strives to focus on repair or replacement of damaged tissue rather than directly treating the symptoms associated with the disease. Regenerative nephrology includes repair of injured structures, replacement of (certain) kidney functions and *de novo* generation of the whole kidney [13,14]. The relatively recent developments, such as differentiation of induced pluripotent stem cells (iPSC) towards kidney organoids, single-cell transcriptional profiling, and Clustered Regularly Interspaced Short Palindromic Repeats (CRISPR)-associated system 9 (Cas9) gene editing have enforced the field of regenerative medicine [14]. These techniques led to three distinct approaches for the development of kidney disease therapies: i) organ repair by manipulating processes to reverse injury and reduce fibrosis, ii) *ex vivo* models including stem cell derived models for modeling human kidney disease and/or improving drug development, iii) *de novo* creation of human kidney tissue to replace kidney function [14]. For the first approach, organ repair, recent advances using stem cells or therapeutics have been shown to enhance tissue regeneration [15-17]. Although interesting and with potential for regenerative nephrology, this thesis is focused on the development of *ex vivo* models of healthy and diseased human kidney and work towards *de novo* kidney tissue rather than kidney repair.

2. Modeling the proximal tubule, starting with the extracellular matrix

Kidney replacement strategies vary from whole organ engineering to (bio)fabrication of kidney assist devices, or cell therapy for kidney regeneration. For biofabrication of kidney devices or whole organ engineering, often biomimetic micro-environments are being developed for culturing cells. These microenvironments mimic parts of the ECM, e.g. by replicating mechanical properties or ECM alignment. **Chapter 2** gives an elaborative overview of the composition of both the tubular and vascular basement membranes (BM) [18]. The BM is a thin sheet-like and highly specialized form of the ECM that underlies all epithelia and endothelia. BMs give cells support and act as barriers, while they can also topographically guide the cells via their collagen networks. Cells continuously form and degrade the BM and their macromolecular composition and stiffness can affect the interactions between the cell and the BMs. Defects of the BM have been associated with adverse kidney outcome [19]. Hence, it is important to mimic the BM in such a way that cells have the support they need to form functional and healthy tissue and deposit/renew their own ECM macromolecules. Hydrogels are commonly utilized as ECM mimicking materials, because of their wide applicability and tunable properties [20]. Hydrogels can be prepared from hydrophilic biological and/or synthetic polymers that are stably connected via physical or chemical crosslinks. Previously, researchers showed that a gelatin-fibrin hydrogel, within a sacrificial bioprinting set-up, supported the growth of human immortalized proximal tubule epithelial cells and glomerular microvascular endothelial cells [21-23]. Another approach is the use of decellularized organs to create organ-specific ECM, which still includes the native ECM components. Decellularized ECM can be used to create hydrogels, which enhances vascularization and maturation of hPSC-derived kidney organoids [24].

In **Chapter 3**, we used a gelatin-alginate hydrogel to enable co-axial printing of kidney tubules. Co-axial printing using alginate and CaCl_2 allows the formation of hollow coiled microfibers that mimic the convoluted proximal tubule. This approach was based on the results by Xu. et al (2017) who reported a fabrication method of microfibers with helical channels, which was ascribed to the instant interaction of calcium with alginate (Ca-Alg) that causes the hydrogel to acquire a higher viscosity while printing [25]. By incorporating gelatin into the hydrogel, we used the favorable properties of alginate to cross-link with calcium, while also adding the advantageous properties of gelatin to boost cell growth. Additionally, while the hydrogel served as a cell-substrate, the coiling of the channels replicated the convoluted architecture of the proximal tubule.

Though distinctive 3D-printing strategies offer opportunities to mimic the structure of the convoluted proximal tubule, printing resolution remains restricted for soft hydrogel materials [21,26,27]. In **Chapter 4**, we reported a unique method whereby post-printing treatment induced resolution enhancement of our methacrylated hyaluronic acid / gelatin methacryloyl (HAMA/GelMA) based hydrogels. 3D-printed hydrogels, consisting of hydrophilic polyanionic polymer networks, were immersed in a solution of polycations, resulting in rapid shrinking of the hydrogels while maintaining the same shape. Additionally, for proof of concept polycationic chitosan-based hydrogel constructs were successfully shrunken using polyanionic alginate. This shrinking technique opens a wide application to create higher resolutions for 3D printing. However, we also found that the polycationic shrinking reagents used were relatively toxic for our cells of interest, namely conditionally immortalized proximal tubule epithelial cells (ciPTEC) and human umbilical vein endothelial cells (HUVEC). Therefore, more research is needed to prevent the direct exposure of cells to the shrinking reagents, e.g. by reducing the concentration of polycations, embedding the cells within gels for a protective effect by the gel, or via the use of protective ECM-like nano-coatings [28].

3. Patterning scaffolds to guide tubular cell differentiation

Besides hydrogels, there are numerous other materials that can be used as ECM mimicking substrates [9,29-32]. Hollow fiber membranes (HFM) are often used for BAK development, nonetheless, HFM might not be suitable for implantation [33] and the fibers are not easily tunable when it comes to topography or mechanical properties. Electrospun polycaprolactone (PCL) nanofiber scaffolds are suitable for the formation of proximal tubule grafts using ciPTEC [30]. PCL is a commonly used biomaterial that generally shows good biocompatibility, making it a good candidate material for developing implantable grafts. However, electrospinning is rather limited in terms of tunability, especially regarding topography design [30,34]. In contrast, melt-electrowriting (MEW), a solvent-free printing technique, can be used to create 3D (tubular) scaffolds with defined geometries, thereby precisely controlling the mechanical properties and design of the scaffolds. By defining the printed geometry, MEW scaffolds can closely imitate the ECM framework. Hence, we used MEW in **Chapters 5** and **6** to design small diameter ($\varnothing = 1\text{mm}$) tubular PCL scaffolds. PCL tubular scaffolds are highly porous (pore sizes: 0.11-0.53 mm²) and thereby only give limited support to the cells. Cells can form monolayers within the scaffolds, while also depositing their own BM, indicated by presence of collagen IV and laminin, major components of the BM. Additionally, MEW enables the use of patterned scaffolds to guide tubular cell

differentiation. When cells are provided with optimal structural cues, the cytoskeleton undergoes re-orientation followed by cell attachment, migration, and proliferation [35]. In **Chapter 5**, we showed that topographical guidance of rhombus pores enhanced kidney tubule performance, whereas this effect was not seen in tubes with square shaped pores or a random geometry. In **Chapter 6**, this was studied further to define the optimal angle, which revealed that ciPTEC perform best at a winding angle of 30°, as measured by BM formation, monolayer tightness, directionality of F-actin fibers and cell polarization.

4. Working towards implantable kidney grafts using iPSC

In **Chapters 3, 5**, and **6**, ciPTEC were used as a source for proximal tubular cells. These cells have been well characterized over the past decade and appeared a suitable cell line for disease modeling, drug screening or nephrotoxicity testing [26,36-38]. Yet, our final aim was to work towards the development of implantable proximal tubule grafts. As for any implantable scaffold, biosafety is a major concern for an implantable proximal tubule. ciPTEC are conditionally immortalized cells and, although previous research showed no signs of immunogenicity *in vitro* or tumorigenicity *in vivo*, the chances of these cells being accepted for cell therapy by regulatory authorities are limited [39,40]. Additionally, implantation of allogenic cells will most probably lead to immunogenicity. Hence, one of our aims was to study the use of iPSC derived proximal tubular cells to develop our implantable scaffolds. Human iPSC, since first described in 2007, have been used widely [41]. In 2015, the first iPSC derived kidney protocols were published, which have since been adapted by many researchers and advanced knowledge on kidney development [42-51]. This has been applied in studying kidney diseases, nephrotoxicity screening and regenerative medicine. Organoids, with their complex structures harboring multiple cell types, are believed to better mimic the complex physiology of the organ of interest than commonly used cell cultures which are limited to one cell type. Organoids originate from (i)PSC or adult stem or progenitor cells (ASC). Kidney biopsy- and urine-derived ASC, so called tubuloids, contain the tubular structures of the nephron, but not the glomerulus [52-54]. While iPSC derived organoids mimic nephrogenesis, explaining the often immature state, ASC tubuloids reiterate renewal and repair of the adult kidney. Both types of organoids have their own advantages and limitations. A major advantage of ASC tubuloids is the relatively mature state of the cells, as differentiation markers are comparable to adult kidney tissue. At the same time, tubuloids are missing interstitial cells as well as endothelial cells and some vital transporters are limitedly expressed [53]. One of the downsides of using iPSC-derived organoids is their limited maturity, although transplantation of these organoids under the

kidney capsule or onto the membrane of fertilized eggs advances their vascularization and maturation [49,55]. Furthermore, preliminary results showed that *in vitro* incorporation of endothelial cells or fluid shear stress can also improve vascularization and maturation of the organoids [56-58]. Additionally, researchers were able to perform pharmacodynamic studies by transplanting kidney organoids under the kidney capsule of athymic rats, indicating the relevance of kidney organoids for assessment of novel therapeutics before continuing in clinical trials [59]. Organoids are usually grown on animal derived matrices called Matrigel. However, these Matrigels have large batch-to-batch variations, raise ethical issues and are usually poorly defined. The use of synthetic hydrogels might in the future provide a solution for that, as first results using synthetic peptide-based hydrogels for iPSC differentiation are promising [60]. Moreover, synthetic hydrogels are easily tunable in stiffness, which could also advance cell fate specification [60-62]. We showed that topographic guidance can enhance cell phenotype and functionality (**Chapters 5 and 6**). This exposes an opportunity for iPSC differentiation. In a pilot study, we aimed to enhance iPSC differentiation of proximal tubule cells via topographic guidance in PCL tubular scaffolds. We cultured iPSC-derived organoids according to the protocol by Jansen et al. [44] until considered 'mature' on day 7+18. Organoids were then seeded at high density in our PCL-tubular scaffolds (**Figure 1A-B**). Dissociated kidney organoids formed monolayers in the PCL scaffolds within a few days (**Figure 1C-D**). To study the effect of fluid shear stress (FSS), we compared scaffolds that were cultured on a rocker for 3 days to scaffolds that were grown under static conditions (**Figure 1C-E**), which indicated that cells grown under FSS conditions form a tight monolayer (presence of tight junction protein zonula occludens-1 (ZO-1)) whereas cells that grow under static conditions did not show any expression for ZO-1. FSS also enhanced cell alignment as measured by filamentous actin directionality (**Figure 1D-E**). Nevertheless, staining for different nephron markers did not yield conclusive results about the cell phenotypes present in our PCL tubular scaffolds. More research is needed to study what happens after seeding kidney organoids, to elucidate how topography guides the cells towards different phenotypes. Additionally, studies on how tube diameter, pore size and different materials can guide differentiation of iPSC are recommended.

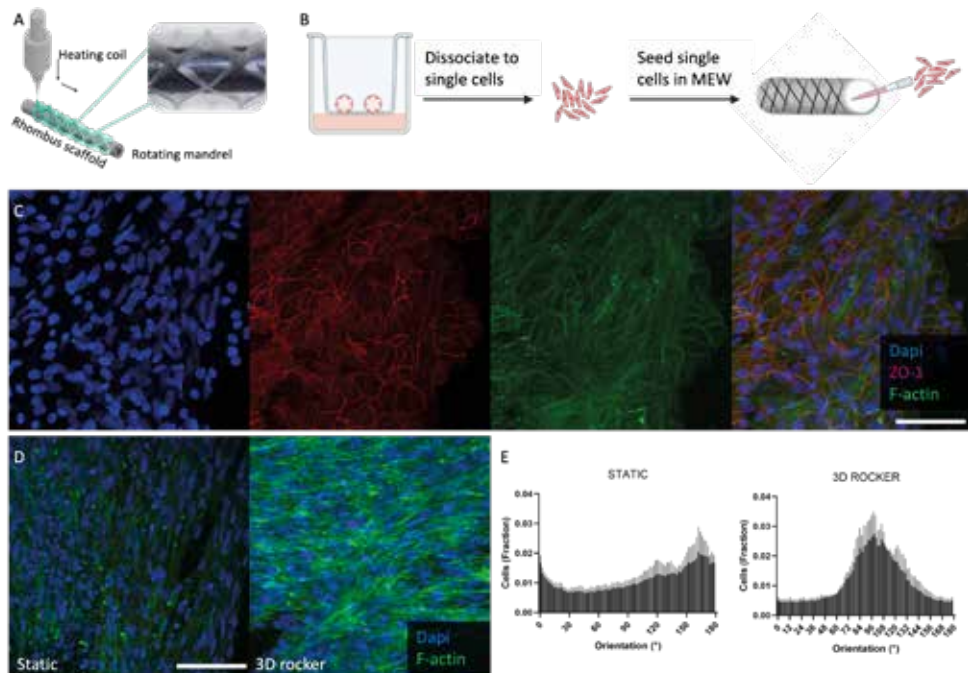


Figure 1. iPSC-derived kidney organoids grown in PCL tubular scaffolds A) Graphical overview of melt-electrowriting and photo of the printed PCL tubular scaffold with 30° rhombus geometry. B) Graphical overview of iPSC-derived organoid seeding, iPSC-derived organoids are cultured according to the protocol by Jansen et al. [44], on day 7+18 organoids are dissociated and seeded (106 cells/ml) in PCL tubular scaffolds. C) Immunofluorescent staining of dissociated iPSC derived organoids grown in PCL tubular scaffolds put on a rocker for 3 days after confluency. DAPI (blue), ZO-1 (red), F-actin (green). n = 2. D) Filamentous actin (green) and DAPI (blue) for dissociated iPSC derived organoids grown in PCL tubular scaffolds with and without 3D rocker exposure. E) Quantification of cell directionality. Scale bars = 100 mm. Mean ± SEM, n = 3

5. Advantages and challenges of iPSC in regenerative medicine

Because of their ability to serve as autologous stem cell therapies, iPSCs have been named a promising cell source for regenerative medicine. Pluripotent stem cells are favorable as they can proliferate infinitely and are able to differentiate into the three germ layers [63]. The generation of human iPSC has recently led to the start of the first Phase I/IIa clinical trials for the treatment of e.g. heart failure, Covid19-infections, cancer and neurodegenerative diseases [41,64]. Moreover, patients that received autologous iPSC-derived cells did not suffer from severe adverse events, despite not taking immunosuppression [65,66]. Most of the research and development regarding iPSCs, however, has been performed using allogenic iPSCs [64,65]. Yet, the main challenges for using PSCs in regenerative medicine or cell therapy are to proof that the cells do not form a risk in terms of tumorigenicity, immunogenicity and

heterogeneity. Another challenge using iPSC derived kidney organoids is upscalability of organoid cultures. Recent advances using optimized protocols, bioreactors, or bioprinters for upscaling of iPSC cultures may provide a solution for this [67,68].

6. Importance of vascularization

The kidneys filter and reabsorb solutes from approximately 180 liter blood every day, which make them susceptible to damage from drugs and toxins [69]. The proximal tubule is responsible for the reabsorption of nearly all glucose, albumin, amino acids, and phosphate, as well as for around 65-80% of sodium and water. For studying kidney reabsorption, incorporation of vasculature is key [22]. Additionally, to increase physiological relevance, and recapitulate the complexity of engineered tissues, vascularization should be incorporated. While vascularization is needed for oxygen supply in thicker tissues, it is also known to enhance maturation and differentiation [23,70]. Recently, the culture of HUVEC with iPSC derived kidney organoids was demonstrated in an on-chip system, where co-culture induced enhanced vascularization of the organoids compared to single culture [58]. In **Chapter 6**, we aimed to mimic this crosstalk between colocalized epithelium and endothelium using a co-seeding of ciPTEC and conditionally immortalized glomerular endothelial cells (ciGenC) in our PCL tubular scaffolds. For mimicking the tubular-vascular exchange, tubular and vascular cells need to be grown in close proximity, enabling crosstalk. Preferably, the scaffold separating the cells is highly permeable to not prevent any transport between both cell types. For our PCL tubular scaffolds we hypothesized that the cells are the only barrier between inside and outside of the tubular scaffolds, because the tubes have a large pore size. In our co-seeding model, there was no membrane or thick hydrogel hampering the transport as endothelial cells were directly seeded on top of the basement membrane formed by the epithelial cells. Our preliminary results indicated that ciGenC benefit from the basement membrane deposited by ciPTEC, as they form a monolayer on this deposited basement membrane within 2 weeks after seeding them at a relatively low density. However, further studies on functionality of both cell types are needed to study the exact effects of the co-culture model. In **Chapter 3**, we showed preliminary results where co-axial printing was used to create a vascularized proximal tubule by printing dual helical channels within one microfiber. Here, having a vascular compartment would further mimic the vascularized proximal tubule, and allow for studying transport between both channels.

Vascularization or endothelial cell proliferation can also be stimulated in other ways than co-cultures alone. Growth factors like vascular endothelial growth factor (VEGF), platelet

derived growth factor, fibroblast growth factor, stromal derived factor 1 β , and angiopoietins play an important role in angiogenesis in vivo and are therefore often incorporated to enhance vascularization in vitro [71]. VEGF-A is known to induce proliferation, sprouting and tube formation of endothelial cells. To further boost vascularization of iPSC derived organoids or proliferation of endothelial cells in our PCL tubular scaffolds, VEGF could be coupled to the polycaprolactone fibers of our PCL tubular scaffolds via covalent protein immobilization [72]. Similarly, extracellular vesicles (EVs), nanoparticles released by cells consisting of lipid bilayer structures that can mediate transfer of e.g. proteins, nucleic acids, and lipids, play an important role in communication between cells. EVs have been found to mediate communication between endothelial and vascular smooth muscle cells via transfer of microRNAs miR-539 and miR-582 [73]. Furthermore, it has been shown that EVs can trigger biological pathways involved in mesenchymal-to-epithelial transition, crucial for maturation of tubular epithelial cells [74]. Therefore, EVs could provide a promising tool for vascularization or maturation. Finally, nephrons consist of complex microenvironments with different cell types, including different endothelial cell populations [75]. In our studies, we used either HUVEC, non-kidney endothelial, or ciGEnC, which both are not similar to cells forming the peritubular capillaries surrounding the proximal tubule. Peritubular capillaries and ciGEnC express different proteins and require special growth factors, which needs to be taken into account when developing vascularized proximal tubule models.

7. Conclusions

In this thesis, I demonstrated the fabrication of two kidney proximal tubule models. Our coaxial printing system allowed the robust and straightforward fabrication of coiled perfusable microfibers, replicating the kidney proximal convoluted tubules. The alginate-gelatin microfibers offer a complex tubular shape in which the cells exhibit mature markers, such as functional transporters and polarized monolayers. Moreover, this model has proven to support both healthy and cystinotic proximal tubule cell lines and allows for mechanistically studying tubulopathies. Using MEW, scaffolds were fabricated that are self-supportive, yet small-sized and highly porous. These scaffolds enable direct access to the basolateral and luminal cell sides to facilitate solute exchange with vasculature in immediate proximity, which is critical for functional proximal tubule constructs. The polymer applied, PCL, is used to prepare biomaterials that generally show good biocompatibility and is compatible with implantation in the future. Kidney proximal tubule cells and glomerular endothelial cells form polarized monolayers in our tubules, form their own ECM, and show functionality for important kidney transporters. In our preliminary results we showed initial work with

iPSC-derived kidney organoids, which is very promising for the development of implantable proximal tubule grafts. The aim was to develop vascularized kidney tubules for studying the clearance of protein bound uremic toxins, while gaining knowledge for the development of implantable kidney tubules. The developed models allow for studying transepithelial secretion of uremic toxins, an overarching application for these constructs. This will further advance our understanding of the kidney secretion processes and aid in studying interventions to main proximal tubule function in CKD conditions *in vitro*. Furthermore, while fundamental by nature, our research deliverables enhance mechanistic insight in additive manufacturing and kidney development processes. Altogether, our findings will further advance the field of kidney engineering, while working towards kidney replacement therapies.

References

1. Kovesdy C P 2022 Epidemiology of chronic kidney disease: an update 2022 *Kidney Int Suppl* (2011) **12** 7–11
2. Barker C F and Markmann J F 2013 Historical Overview of Transplantation *Cold Spring Harb Perspect Med* **3** a014977–a014977
3. MACKAY S M, FUNKE A J, BUFFINGTON D A and HUMES H D 1998 Tissue Engineering of a Bioartificial Renal Tubule *ASAIO Journal* **44** 179–83
4. Humes H D, Weitzel W F, Bartlett R H, Swaniker F C, Paganini E P, Luderer J R and Sobota J 2004 Initial clinical results of the bioartificial kidney containing human cells in ICU patients with acute renal failure *Kidney Int* **66** 1578–88
5. Tumlin J, Wali R, Williams W, Murray P, Tolwani A J, Vinnikova A K, Szerlip H M, Ye J, Paganini E P, Dworkin L, Finkel K W, Kraus M A and Humes H D 2008 Efficacy and Safety of Renal Tubule Cell Therapy for Acute Renal Failure *JASN* **19** 1034–40
6. Pino C J, Westover A J, Buffington D A and Humes H D 2017 Bioengineered Renal Cell Therapy Device for Clinical Translation *ASAIO Journal* **63** 305–15
7. Buffington D A, Pino C J, Chen L, Westover A J, Hageman G and Humes H D 2012 Bioartificial Renal Epithelial Cell System (BRECS): A Compact, Cryopreservable Extracorporeal Renal Replacement Device *Cell Med* **4** 33–44
8. Westover A J, Buffington D A, Johnston K A, Smith P L, Pino C J and Humes H D 2017 A bio artificial renal epithelial cell system conveys survival advantage in a porcine model of septic shock *J Tissue Eng Regen Med* **11** 649–57
9. Jansen J, Fedecostante M, Wilmer M J, Peters J G, Kreuser U M, van den Broek P H, Mensink R A, Boltje T J, Stamatialis D, Wetzels J F, van den Heuvel L P, Hoenderop J G and Masereeuw R 2016 Bioengineered kidney tubules efficiently excrete uremic toxins *Sci Rep* **6** 26715
10. Fissell W H and Roy S 2009 The Implantable Artificial Kidney *Semin Dial* **22** 665–70
11. Chevtchik N V, Fedecostante M, Jansen J, Mihajlovic M, Wilmer M, R uth M, Masereeuw R and Stamatialis D 2016 Upscaling of a living membrane for bioartificial kidney device *Eur J Pharmacol* **790** 28–35
12. Chevtchik N v., Mihajlovic M, Fedecostante M, Bolhuis-Versteeg L, Sastre Tor a o J, Masereeuw R and Stamatialis D 2018 A bioartificial kidney device with polarized secretion of immune modulators *J Tissue Eng Regen Med* **12** 1670–8
13. Little M H 2006 Regrow or Repair: Potential Regenerative Therapies for the Kidney *JASN* **17** 2390–401
14. Little M H and Humphreys B D 2022 Regrow or Repair: An Update on Potential Regenerative Therapies for the Kidney *JASN* **33** 15–32
15. Huang W, Hickson L J, Eirin A, Kirkland J L and Lerman L O 2022 Cellular senescence: the good, the bad and the unknown *Nat Rev Nephrol* **18** 611–27
16. Wong P-F, Devi M D and Ramasamy T S 2022 Senotherapeutics for mesenchymal stem cell senescence and rejuvenation *Drug Discov Today* 103424
17. Tsuji K, Kitamura S and Wada J 2022 Potential Strategies for Kidney Regeneration With Stem Cells: An Overview *Front Cell Dev Biol* **10**
18. van Genderen A M, Jansen J, Cheng C, Vermonden T and Masereeuw R 2018 Renal Tubular- and Vascular Basement Membranes and their Mimicry in Engineering Vascularized Kidney Tubules *Adv Healthc Mater* **7** 1800529
19. Chew C and Lennon R 2018 Basement Membrane Defects in Genetic Kidney Diseases *Front Pediatr* **6**
20. Jansen K, Schuurmans C C L, Jansen J, Masereeuw R and Vermonden T 2017 Hydrogel-Based Cell Therapies for Kidney Regeneration: Current Trends in Biofabrication and In Vivo Repair *Curr Pharm Des* **23** 3845–57

21. Homan KA, Kolesky D B, Skylar-Scott MA, Herrmann J, Obuobi H, Moisan A and Lewis J A 2016 Bioprinting of 3D Convulated Renal Proximal Tubules on Perfusable Chips *Sci Rep* **6** 1–13
22. Lin N Y C, Homan K A, Robinson S S, Kolesky D B, Duarte N, Moisan A and Lewis J A 2019 Renal reabsorption in 3D vascularized proximal tubule models *Proc Natl Acad Sci U S A* **116** 5399–404
23. Kolesky D B, Homan K A, Skylar-Scott M A and Lewis J A 2016 Three-dimensional bioprinting of thick vascularized tissues *PNAS* **113** 3179–84
24. Kim J W, Nam S A, Yi J, Kim J Y, Lee J Y, Park S, Sen T, Choi Y, Lee J Y, Kim H L, Kim H W, Park J, Cho D and Kim Y K 2022 Kidney Decellularized Extracellular Matrix Enhanced the Vascularization and Maturation of Human Kidney Organoids *Adv. Sci.* **9** 210326
25. Xu P, Xie R, Liu Y, Luo G, Ding M and Liang Q 2017 Bioinspired Microfibers with Embedded Perfusable Helical Channels *Adv. Mater.* **29**
26. van Genderen A M, Valverde M G, Capendale P E, Kersten M v, Garvı E S, Schuurmans C C L, Ruelas M, Soeiro J T, Tang G, Janssen M J, Jansen J, Mihaila S M, Vermonden T, Zhang Y S and Masereeuw R 2022 Co-axial printing of convoluted proximal tubule for kidney disease modeling *Biofabrication* **14** 044102
27. Bernal P N, Bouwmeester M, Madrid Wolff J, Falandt M, Florczak S, Rodriguez N G, Li Y, Grosbacher G, Samsom R, van Wolferen M, van der Laan L J W, Delrot P, Loterie D, Malda J, Moser C, Spee B and Levato R 2022 Volumetric Bioprinting of Organoids and Optically Tuned Hydrogels to Build Liver Like Metabolic Biofactories *Advanced Materials* **34** 2110054
28. Liu C-Y, Matsusaki M and Akashi M 2016 Control of vascular network location in millimeter-sized 3D-tissues by micrometer-sized collagen coated cells *Biochem Biophys Res Commun* **472** 131–6
29. Jansen K, Evangelopoulou M, Pou Casellas C, Abrishamcar S, Jansen J, Vermonden T and Masereeuw R 2021 Spinach and Chive for Kidney Tubule Engineering: the Limitations of Decellularized Plant Scaffolds and Vasculature *AAPS J* **23** 1–7
30. Jansen K, Castilho M, Aarts S, Kaminski M M, Lienkamp S S, Pichler R, Malda J, Vermonden T, Jansen J and Masereeuw R 2019 Fabrication of Kidney Proximal Tubule Grafts Using Biofunctionalized Electrospun Polymer Scaffolds *Macromol Biosci* **19** 1800412
31. Schophuizen C M S, de Napoli I E, Jansen J, Teixeira S, Wilmer M J, Hoenderop J G J, van den Heuvel L P W, Masereeuw R and Stamatialis D 2015 Development of a living membrane comprising a functional human renal proximal tubule cell monolayer on polyethersulfone polymeric membrane *Acta Biomater* **14** 22–32
32. Jansen J, Fedecostante M, Wilmer M J, Peters J G, Kreuser U M, van den Broek P H, Mensink R A, Boltje T J, Stamatialis D, Wetzels J F, van den Heuvel L P, Hoenderop J G and Masereeuw R 2016 Bioengineered kidney tubules efficiently excrete uremic toxins *Sci Rep* **6** 1–12
33. Irfan M and Idris A 2015 Overview of PES biocompatible/hemodialysis membranes: PES–blood interactions and modification techniques *Mater. Sci. Eng.: C* **56** 574–92
34. Miranda C C, Gomes M R, Moo M, Cabral J M S, Ferreira F C and Sanjuan-Alberte P 2022 A Concise Review on Electrospun Scaffolds for Kidney Tissue Engineering *Bioengineering* **9** 554
35. Lai H, Gong B, Yin J and Qian J 2022 3D printing topographic cues for cell contact guidance: A review *Mater Des* **218** 110663
36. Jansen J, Schophuizen C M S, Wilmer M J, Lahham S H M, Mutsaers H A M, Wetzels J F M, Bank R A, van den Heuvel L P, Hoenderop J G and Masereeuw R 2014 A morphological and functional comparison of proximal tubule cell lines established from human urine and kidney tissue *Exp Cell Res* **323** 87–99
37. Wilmer M J, Saleem M A, Masereeuw R, Ni L, van der Velden T J, Russel F G, Mathieson P W, Monnens L A, van den Heuvel L P and Levchenko E N 2010 Novel conditionally immortalized human proximal tubule cell line expressing functional influx and efflux transporters *Cell Tissue Res* **339**

38. Jamalpoor A, Gelder C A, Yousef Yengej F A, Zaal E A, Berlingerio S P, Veys K R, Pou Casellas C, Voskuil K, Essa K, Ammerlaan C M, Rega L R, Welle R E, Lilien M R, Rookmaaker M B, Clevers H, Klumperman J, Levtschenko E, Berkers C R, Verhaar M C, Altelaar M, Masereeuw R and Janssen M J 2021 Cysteamine–bicalutamide combination therapy corrects proximal tubule phenotype in cystinosis *EMBO Mol Med* **13**
39. Mihajlovic M, Hariri S, Westphal K C G, Janssen M J, Oost M J, Bongiovanni L, van den Heuvel L P, Bruin A de, Hilbrands L B and Masereeuw R 2019 Safety evaluation of conditionally immortalized cells for renal replacement therapy *Oncotarget* **10** 5332–48
40. Mihajlovic M, van den Heuvel L P, Hoenderop J G, Jansen J, Wilmer M J, Westheim A J F, Allebes W A, Stamatialis D, Hilbrands L B and Masereeuw R 2017 Allostimulatory capacity of conditionally immortalized proximal tubule cell lines for bioartificial kidney application *Sci Rep* **7** 7103
41. Takahashi K, Tanabe K, Ohnuki M, Narita M, Ichisaka T, Tomoda K and Yamanaka S 2007 Induction of Pluripotent Stem Cells from Adult Human Fibroblasts by Defined Factors *Cell* **131** 861–72
42. Takasato M, Er P X, Chiu H S, Maier B, Baillie G J, Ferguson C, Parton R G, Wolvetang E J, Roost M S, Chuva de Sousa Lopes S M and Little M H 2015 Kidney organoids from human iPS cells contain multiple lineages and model human nephrogenesis *Nature* **526** 564–8
43. Takasato M, Er P X, Chiu H S and Little M H 2016 Generation of kidney organoids from human pluripotent stem cells *Nat Protoc* **11** 1681–92
44. Jansen J, van den Berge B T, van den Broek M, Maas R J, Daviran D, Willemsen B, Roverts R, van der Kruit M, Kuppe C, Reimer K C, di Giovanni G, Mooren F, Nlandu Q, Mudde H, Wetzels R, den Braanker D, Parr N, Nagai J S, Drenic V, Costa I G, Steenbergen E, Nijenhuis T, Dijkman H, Endlich N, van de Kar N C A J, Schneider R K, Wetzels J F M, Akiva A, van der Vlag J, Kramann R, Schreuder M F and Smeets B 2022 Human pluripotent stem cell-derived kidney organoids for personalized congenital and idiopathic nephrotic syndrome modeling *Development* **149**
45. Jansen J, Reimer K C, Nagai J S, Varghese F S, Overheul G J, de Beer M, Roverts R, Daviran D, Fermin L A S, Willemsen B, Beukenboom M, Djudjaj S, von Stillfried S, van Eijk L E, Mastik M, Bulthuis M, Dunnen W den, van Goor H, Hillebrands J-L, Triana S H, Alexandrov T, Timm M-C, van den Berge B T, van den Broek M, Nlandu Q, Heijntjens J, Bindels E M J, Hoogenboezem R M, Mooren F, Kuppe C, Miesen P, Grünberg K, Ijzermans T, Steenbergen E J, Czogalla J, Schreuder M F, Sommerdijk N, Akiva A, Boor P, Puellas V G, Floege J, Huber T B, van Rij R P, Costa I G, Schneider R K, Smeets B, Kramann R, Achdout H, Aimon A, Bar-David E, Barr H, Ben-Shmuel A, Bennett J, Boby M L, Borden B, Bowman G R, Brun J, BVNBS S, Calmiano M, Carbery A, Cattermole E, Chernychenko E, Choder J D, Clyde A, Coffland J E, Cohen G, Cole J, Contini A, Cox L, Cvitkovic M, Dias A, Donckers K, Dotson D L, Douangamath A, Duberstein S, Dudgeon T, Dunnett L, Eastman P K, Erez N, Eyermann C J, Fairhead M, Fate G, Fearon D, Federov O, Ferla M, Fernandes R S, Ferrins L, Foster R, Foster H, Gabizon R, Garcia-Sastre A, Gawriljuk V O, Gehrtz P, Gileadi C, Giroud C, Glass W G, Glen R, Itai Glinert, et al 2022 SARS-CoV-2 infects the human kidney and drives fibrosis in kidney organoids *Cell Stem Cell* **29** 217–231.e8
46. Kalejaiye T D, Barreto A D and Musah S 2022 Translating Organoids into Artificial Kidneys *Curr Transplant Rep*
47. Karp S, Pollak M and Subramanian B 2022 Disease Modeling with Kidney Organoids *Micromachines (Basel)* **13** 1384
48. Treacy N J, Clerkin S, Davis J L, Kennedy C, Miller A F, Saiani A, Wychowanec J K, Brougham D F and Crean J 2023 Growth and differentiation of human induced pluripotent stem cell (hiPSC)-derived kidney organoids using fully synthetic peptide hydrogels *Bioact Mater* **21** 142–56
49. Koning M, Dumas S J, Avramut M C, Koning R I, Meta E, Lievers E, Wiersma L E, Borri M, Liang X, Xie L, Liu P, Chen F, Lin L, Luo Y, Mulder J, Spijker H S, Jaffredo T, van den Berg B M, Carmeliet P, van den Berg C W and Rabelink T J 2022 Vasculogenesis in kidney organoids upon transplantation *NPJ Regen Med* **7** 40

50. Montalbetti N, Przepiorski A J, Shi S, Sheng S, Baty C J, Maggiore J C, Carattino M D, Vanichapol T, Davidson A J, Hukriede N A and Kleyman T R 2022 Functional characterization of ion channels expressed in kidney organoids derived from human induced pluripotent stem cells *Am. J. Physiol. Renal Physiol.* **323** F479–91
51. Lawrence M L, Elhendawi M, Morlock M, Liu W, Liu S, Palakkan A, Seidl L F, Hohenstein P, Sjögren A K and Davies J A 2022 Human iPSC-derived renal organoids engineered to report oxidative stress can predict drug-induced toxicity *iScience* **25** 103884
52. Schutgens F, Rookmaaker M B, Margaritis T, Rios A, Ammerlaan C, Jansen J, Gijzen L, Vormann M, Vonk A, Viveen M, Yengej F Y, Derakhshan S, de Winter-de Groot K M, Artegiani B, van Boxtel R, Cuppen E, Hendrickx A P A, van den Heuvel-Eibrink M M, Heitzer E, Lanz H, Beekman J, Murk J-L, Masereeuw R, Holstege F, Drost J, Verhaar M C and Clevers H 2019 Tubuloids derived from human adult kidney and urine for personalized disease modeling *Nat Biotechnol* **37** 303–13
53. Yousef Yengej F A, Jansen J, Rookmaaker M B, Verhaar M C and Clevers H 2020 Kidney Organoids and Tubuloids *Cells* **9** 1326
54. Xu Y, Kuppe C, Perales-Patón J, Hayat S, Kranz J, Abdallah A T, Nagai J, Li Z, Peisker F, Saritas T, Halder M, Menzel S, Hoefl K, Kenter A, Kim H, van Roeyen C R C, Lehrke M, Moellmann J, Speer T, Buhl E M, Hoogenboezem R, Boor P, Jansen J, Knopp C, Kurth I, Smeets B, Bindels E, Reinders M E J, Baan C, Gribnau J, Hoorn E J, Steffens J, Huber T B, Costa I, Floege J, Schneider R K, Saez-Rodriguez J, Freedman B S and Kramann R 2022 Adult human kidney organoids originate from CD24+ cells and represent an advanced model for adult polycystic kidney disease *Nat Genet* **54** 1690–701
55. van den Berg C W, Ritsma L, Avramut M C, Wiersma L E, van den Berg B M, Leuning D G, Lievers E, Koning M, Vanslambrouck J M, Koster A J, Howden S E, Takasato M, Little M H and Rabelink T J 2018 Renal Subcapsular Transplantation of PSC-Derived Kidney Organoids Induces Neo-vasculogenesis and Significant Glomerular and Tubular Maturation In Vivo *Stem Cell Reports* **10** 751–65
56. Homan K A, Gupta N, Kroll K T, Kolesky D B, Skylar-Scott M, Miyoshi T, Mau D, Valerius M T, Ferrante T, Bonventre J v., Lewis J A and Morizane R 2019 Flow-enhanced vascularization and maturation of kidney organoids in vitro *Nat Methods* **16** 255–62
57. Khoshdel-Rad N, Zahmatkesh E, Moeinvaziri F, Haghparast N, Baharvand H, Aghdami N and Moghadasali R 2021 Promoting Maturation of Human Pluripotent Stem Cell-Derived Renal Microtissue by Incorporation of Endothelial and Mesenchymal Cells *Stem Cells Dev* **30** 428–40
58. Menéndez A B-C, Du Z, van den Bosch T P P, Othman A, Gaio N, Silvestri C, Quirós W, Lin H, Korevaar S, Merino A, Mulder J and Hoogduijn M J 2022 Creating a kidney organoid-vasculature interaction model using a novel organ-on-chip system *Sci Rep* **12** 20699
59. Westerling-Bui A D, Fast E M, Soare T W, Venkatachalan S, DeRan M, Fanelli A B, Kyrychenko S, Hoang H, Corriea G M, Zhang W, Yu M, Daniels M, Malojcic G, Pan-Zhou X-R, Ledebor M W, Harmange J-C, Emani M, Tibbitts T T, Reilly J F and Mundel P 2022 Transplanted organoids empower human preclinical assessment of drug candidate for the clinic *Sci Adv* **8**
60. Treacy N J, Clerkin S, Davis J L, Kennedy C, Miller A F, Saiani A, Wychowanec J K, Brougham D F and Crean J 2023 Growth and differentiation of human induced pluripotent stem cell (hiPSC)-derived kidney organoids using fully synthetic peptide hydrogels *Bioact Mater* **21** 142–56
61. Hagelaars M J, Rijns L, Dankers P Y W, Loerakker S and Bouten C V C 2022 Engineering Strategies to Move from Understanding to Steering Renal Tubulogenesis *Tissue Eng Part B Rev*
62. van Sprang J F, de Jong S M J and Dankers P Y W 2022 Biomaterial-driven kidney organoid maturation *Curr Opin Biomed Eng* **21** 100355
63. Yamanaka S 2020 Pluripotent Stem Cell-Based Cell Therapy—Promise and Challenges *Cell Stem Cell* **27** 523–31

64. Kim J Y, Nam Y, Rim Y A and Ju J H 2022 Review of the Current Trends in Clinical Trials Involving Induced Pluripotent Stem Cells *Stem Cell Rev Rep* **18** 142–54
65. Madrid M, Sumen C, Aivio S and Saklayen N 2021 Autologous Induced Pluripotent Stem Cell–Based Cell Therapies: Promise, Progress, and Challenges *Curr Protoc* **1**
66. Mandai M, Watanabe A, Kurimoto Y, Hirami Y, Morinaga C, Daimon T, Fujihara M, Akimaru H, Sakai N, Shibata Y, Terada M, Nomiya Y, Tanishima S, Nakamura M, Kamao H, Sugita S, Onishi A, Ito T, Fujita K, Kawamata S, Go M J, Shinohara C, Hata K, Sawada M, Yamamoto M, Ohta S, Ohara Y, Yoshida K, Kuwahara J, Kitano Y, Amano N, Umekage M, Kitaoka F, Tanaka A, Okada C, Takasu N, Ogawa S, Yamanaka S and Takahashi M 2017 Autologous Induced Stem-Cell–Derived Retinal Cells for Macular Degeneration *NEJM* **376** 1038–46
67. Wiersma L E, Avramut M C, Liewers E, Rabelink T J and van den Berg C W 2022 Large-scale engineering of hiPSC-derived nephron sheets and cryopreservation of their progenitors *Stem Cell Res Ther* **13** 208
68. Lawlor K T, Vanslambrouck J M, Higgins J W, Chambon A, Bishard K, Arndt D, Er P X, Wilson S B, Howden S E, Tan K S, Li F, Hale L J, Shepherd B, Pentoney S, Presnell S C, Chen A E and Little M H 2021 Cellular extrusion bioprinting improves kidney organoid reproducibility and conformation *Nat Mater* **20** 260–71
69. Wilmer M J, Ng C P, Lanz H L, Vulto P, Suter-Dick L and Masereeuw R 2016 Kidney-on-a-Chip Technology for Drug-Induced Nephrotoxicity Screening *Trends Biotechnol* **34** 156–70
70. Agarwal T, Kazemi S, Costantini M, Perfeito F, Correia C R, Gaspar V, Montazeri L, de Maria C, Mano J F, Vosough M, Makvandi P and Maiti T K 2021 Oxygen releasing materials: Towards addressing the hypoxia-related issues in tissue engineering *Mater. Sci. Eng. C* **122** 111896
71. Omorphos N P, Gao C, Tan S S and Sangha M S 2021 Understanding angiogenesis and the role of angiogenic growth factors in the vascularisation of engineered tissues *Mol Biol Rep* **48** 941–50
72. Ainsworth M J, Lotz O, Gilmour A, Zhang A, Chen M J, McKenzie D R, Bilek M M M, Malda J, Akhavan B and Castilho M 2022 Covalent Protein Immobilization on 3D Printed Microfiber Meshes for Guided Cartilage Regeneration *Adv Funct Mater* 2206583
73. Fontaine M, Herkenne S, Ek O, Paquot A, Boeckx A, Paques C, Nivelles O, Thiry M and Struman I 2021 Extracellular Vesicles Mediate Communication between Endothelial and Vascular Smooth Muscle Cells *Int J Mol Sci* **23** 331
74. Lindoso R S, Yousef Yengej F A, Voellmy F, Altelaar M, Mancheño Juncosa E, Tsikari T, Ammerlaan C M E, van Balkom B W M, Rookmaaker M B, Verhaar M C and Masereeuw R 2022 Differentiated kidney tubular cell-derived extracellular vesicles enhance maturation of tubuloids *J Nanobiotechnology* **20** 326
75. Dumas S J, Meta E, Borri M, Luo Y, Li X, Rabelink T J and Carmeliet P 2021 Phenotypic diversity and metabolic specialization of renal endothelial cells *Nat Rev Nephrol* **17** 441–64

CHAPTER 8

NEDERLANDSE SAMENVATTING

ABOUT THE AUTHOR

LIST OF PUBLICATIONS

**DANKWOORD -
ACKNOWLEDGEMENTS**

Het Ontwikkelen van een (gevasculariseerd) Nierbuisje, een Leidraad voor Toepasbaarheid

Chronische nierziekte (CKD) treft meer dan 10% van de bevolking en is één van de belangrijkste doodsoorzaken wereldwijd. Studies rapporteren dat de incidentie van CKD blijft stijgen. Effectieve preventie en behandeling van nierziekten zijn daarom hard nodig. Ondanks de toenemende incidentie zijn er in de afgelopen 70 jaar, sinds de introductie van dialyse door W.J. Kolff, weinig grote vorderingen gemaakt in de behandeling van nierziekten. De nieren zijn opgebouwd uit ongeveer 2 miljoen nefronen, ook wel de filtreerbuisjes van de nieren. De functie van deze nefronen is het reguleren van allerlei processen in het lichaam, waaronder de bloeddruk, hormoonproductie, afvaluitscheiding en urineproductie. De nefronen zelf bestaan uit de glomerulus en de nierbuis. De nierbuis kan weer opgedeeld worden in de proximale tubulus, de lus van Henle, de distale tubulus en de verzamelbuis. De proximale tubulus, waar in dit proefschrift op gefocust is, is verantwoordelijk voor het reabsorberen van voedingsstoffen, water en ionen uit het glomerulaire ultrafiltraat en het actief uitscheiden van afvalstoffen.

De regeneratieve geneeskunde streeft naar het repareren of vervangen van beschadigd weefsel. Regeneratieve nefrologie richt zich op het herstellen van de beschadigde nierstructuren, het vervangen van de nierfunctie, maar ook het *de novo* maken van een compleet nieuwe nier. Het doel van dit proefschrift was het construeren van nierbuisjes door middel van drie-dimensionaal (3D) printen, om vervolgens het gemaakte buisje te bestuderen op de mogelijkheid om afvalstoffen, *zgn.* eiwitgebonden toxines, uit te scheiden.

In **hoofdstuk 2** wordt een uitgebreide samenvatting gegeven van de compositie van het basale membraan van zowel de proximale nierbuis als de omliggende peritubulaire capillairen. Het basale membraan is een dun laagje wat zich onder endotheel- en epitheelcellen bevindt. Het bestaat voornamelijk uit collageen type IV, laminine, fibronectine en glycoproteïnen zoals heparaansulfaat-proteoglycanen, maar de exacte samenstelling verschilt per weefseltype. Tevens is in dit hoofdstuk gekeken naar hoe het basale membraan door andere onderzoekers wordt nagebootst voor *tissue engineering*: het creëren van nieuw weefsel in een laboratorium. Dit hoofdstuk vormt daarmee de basis voor dit proefschrift door een overzicht van zowel de structurele als de mechanische eigenschappen van het basale membraan te presenteren. Deze eigenschappen proberen we in de andere hoofdstukken na te bootsen met behulp van verschillende 3D-printtechnieken.

Hoofdstuk 3 beschrijft een nieuwe techniek voor het printen van een hol, gedraaid kanaaltje in een hydrogel, gemaakt van een mengsel van alginaat en gelatine. Dit zogenaamde

coaxiaal-printsysteem zorgt voor een robuuste en eenvoudige fabricage van perfuseerbare kanaaltjes waarin humane proximale tubuluscellen (PTEC) een functioneel nierbuisje kunnen vormen. Door de draaiing in de kanaaltjes bootst dit functionele nierbuisje de fysiologische structuur van het nefronsegment nog beter na. De buisjes bieden verder een complexe micro-omgeving waarin de cellen eigenschappen van een volwassen nierbuis vertonen, zoals functionele transporteiwitten en gepolariseerde monolagen. Bovendien kan het model ook worden gebruikt voor mechanistische studies van nierziekten.

Printresolutie is tot op heden een beperkende factor voor het 3D-printen op micron schaal. In **Hoofdstuk 4** is gekeken naar een innovatieve manier om hydrogels te laten krimpen, om zo dicht bij de dimensies van de proximale nierbuis (50 μm) te komen en daarmee de fysiologische dimensies na te bootsen. Door het toevoegen van een vloeistof met positief geladen polymeren worden de negatief geladen polymeerketens gebonden en verdwijnt er water uit de hydrogel. Het resultaat is dat het materiaal kleiner wordt en de printresolutie dus groter. In dit hoofdstuk is aangetoond dat met het krimpen de hydrogels een factor 10 kleiner worden, terwijl ze hun vorm behouden. Deze krimptechniek is breed toepasbaar, maar helaas bleek wel dat de reagentia met hun positieve lading schadelijk zijn voor de PTEC en navelstrengendotheelcellen (HUVEC). Daarom is er meer onderzoek nodig om een oplossing te zoeken waardoor een directe blootstelling van cellen aan de krimpreegentia kan worden voorkomen.

Zoals beschreven zijn **hoofdstuk 3** en **hoofdstuk 4** vooral gericht op het gebruik van hydrogels om de extracellulaire matrix na te bootsen. De dikte van de hydrogel kan de zuurstoftoevoer naar de cellen echter belemmeren, vooral bij weefsels die niet worden geperfuseerd. Daarnaast kan ook het transport van voedingsstoffen worden belemmerd, wat juist van levensbelang is voor de nierbuisjes. Dus hebben we gezocht naar andere manieren om de buisjes vorm te geven. Melt electrowriting (MEW, een techniek waarmee met gesmolten plastic een structuur kan worden geprint) kan worden gebruikt om holle buisjes te maken met goed gedefinieerde geometrieën. Daarnaast zijn deze buisjes stevig, klein van formaat en zeer poreus. Deze buisjes kunnen met cellen worden bekleed die de uitwisseling van stoffen vanuit bloedvaten vergemakkelijken. Het gebruikte materiaal, polycaprolactone, is biocompatibel en zou in de toekomst ook voor implantatie kunnen worden gebruikt.

Hoofdstuk 5 beschrijft hoe met behulp van MEW buisjes zijn geprint met drie verschillende geometrieën (vierkant, ruit en willekeurig) met een diameter van 1 mm. Door het gebruik van verschillende geometrieën kan het effect van topografische begeleiding op celfunctie worden

gemeten. De resultaten laten zien dat humane proximale tubuluscellen in ruitvormige poriën beter presteren. Ze maken meer collageen IV aan, vertonen een gestuurde celgroei en ze hebben een verhoogde aanwezigheid van transporteiwitten. Dit toont opnieuw aan dat het ontwerp van het membraan belangrijk is voor de functie van de cellen. HUVEC (een veelgebruikt celtype voor het nabootsen van endotheel) slaagden er niet in om een monolaag te vormen in de gemaakte buisjes. Dit betekent dus dat de geometrie van een buisjes celtype-specifiek is.

In **hoofdstuk 6** zijn de ruitvormige buisjes, gemaakt via MEW, verder bestudeerd en is er eerst gekeken naar de optimale wikkelhoek voor de ruitvormige buisjes. De resultaten laten zien dat PTEC het best presteren bij een wikkelhoek van 30° . Verder is er onderzocht hoe het buisje geoptimaliseerd kon worden voor het ontwikkelen van een vasculaire buis en daarmee ook voor de uiteindelijke constructie van een gevasculariseerd proximaal nierbuisje. Door een reeks van poriegroottes, wikkelhoeken en celtypes te bestuderen, hebben we de buisjes kunnen optimaliseren voor endotheelcellen. Humane glomerulaire endotheelcellen (GEnC), die tevens meer gelijkenis vertonen met peritubulaire capillairen, vormen monolagen in de buisjes met een kleinere poriegrootte (0.05 mm^2 in plaats van 0.53 mm^2) en een wikkelhoek van 30° . Tot slot hebben we de PTEC en GEnC gecombineerd in een enkel buisje voor een directe co-kweek van beide cellen. Alhoewel dit nog gaat om pilot-experimenten, zijn de eerste resultaten positief en lijken de endotheelcellen een monolaag te vormen op het basale membraan wat opgebouwd is door de PTEC. Hiermee is een eerste stap in de richting van een gevasculariseerd-nierbuisje gezet.

Tot slot presenteert **hoofdstuk 7** een samenvatting en discussie van het proefschrift, waarbij vooruitgekeken wordt naar een systeem waarin holle buisjes, gemaakt met de MEW-techniek, gecombineerd worden met van stamcel- (iPSC-) afgeleide nierorganoïden. Hoewel dit nog in de kinderschoenen staat, is deze benadering veelbelovend voor de ontwikkeling van gepersonaliseerde nierkanaalsystemen. Het doel van dit proefschrift was om gevasculariseerde proximale nierbuisjes te ontwikkelen voor het bestuderen van de uitscheiding van lichaamseigen afvalstoffen, terwijl tegelijkertijd kennis kan worden opgedaan voor de ontwikkeling van implanteerbare nierbuisjes. De in dit proefschrift gepresenteerde modellen maken het mogelijk om actieve uitscheiding van afvalstoffen te bestuderen. Dit helpt ons bij het beter begrijpen van de processen die plaatsvinden in de nierbuisjes. Al met al zullen onze bevindingen het veld van de regeneratieve nefrologie en *tissue engineering* vooruithelpen, terwijl we blijven zoeken naar nieuwe oplossingen voor niervervangende therapieën.

About the author

Anne Metje van Genderen was born on the 6th of July 1992 in Gorinchem, The Netherlands. After graduating from high school (Gymnasium Camphusianum, Gorinchem) in 2010, she moved to Rotterdam to study Medicine. After 1.5 years she switched studies and continued with the 6-month 'EH-Traject' at the Evangelische Hogeschool, Amersfoort. In 2012 she was admitted to the bachelor programme College of Pharmaceutical Sciences (Utrecht University) which led to a B.Sc. degree in Pharmaceutical Sciences in August 2015. Two years later she finished her M.Sc. degree (Drug Innovation, Utrecht University) for which she performed her graduation project at Harvard Medical school in the laboratory of Prof. Ali Khademhosseini, under the supervision of Dr. Y. Shrike Zhang. During her masters she co-wrote a PhD proposal with Dr. Jitske Jansen which was granted by the Dutch Kidney Foundation (17PHD16) and enabled her to start her PhD trajectory in October 2017 under the supervision of Dr. Jitske Jansen, Prof. Roos Masereeuw and Prof. Tina Vermonden at the Division of Pharmacology within the Utrecht Institute for Pharmaceutical Sciences at Utrecht University, where she also enrolled in the Drug Innovation PhD Program. In 2019, she received the Young Talent Incentives Grant (Materials Driven Regeneration) together with Carl Schuurmans, MSc. to perform part of her PhD at Harvard Medical School and continue the collaboration with Dr. Y. Shrike Zhang. The results of her PhD research are described and discussed in this thesis. Anne Metje presented her research at various (inter)national conferences, was awarded travel grants (Ohio, USA and Cambridge, MA, USA), received several awards for the *best poster* (UIPS 30th Anniversary, MDR annual meeting, NBTE annual meeting) and *best presentation* (UIPS PhD Competition), and recently received the ISBF New Investigator Award (2022). Besides her research activities, Anne Metje was actively involved in education via the supervision of numerous master and bachelor students and as a member of the Future Medicine Fellows (UIPS) she organized a Summerschool (2020) on Future Medicines: Gene and Cell therapies. Since February 2022, Anne Metje is appointed as a postdoc within the Virtual Human Platform for Safety Consortium (VHP4Safety), under the supervision Prof. Roos Masereeuw and Prof. Marianne Verhaar.



List of Publications

van Genderen, A.M.*, Valverde, M.G.*, Capendale, P.E., Kersten, M.V., Sendino Garv, E., Schuurmans, C.C.L., Ruelas, M., Soeiro, J.T., Tang, G., Janssen, M.J., Jansen, J., Mihil, S.M., Vermonden, T., Zhang, Y.S., Masereeuw, M. (2022) Co-axial Printing of Convolut ed Proximal Tubule for Kidney Disease Modeling. *Biofabrication*, 14(4), 044102.

van Genderen, A. M.*, Jansen, K.*, Kristen, M., van Duijn, J. H., Li, Y., Schuurmans, C. C. L., Malda, J., Vermonden, T., Jansen, J., Masereeuw, R., & Castilho, M. (2021). Topographic Guidance in Melt-Electrowritten Tubular Scaffolds Enhances Engineered Kidney Tubule Performance. *Frontiers in Bioengineering and Biotechnology*, 8, [617364].

Gong, J.*, Schuurmans, C. C. L.*, **van Genderen, A. M.**, Cao, X., Li, W., Cheng, F., He, J. J., Lpez, A., Huerta, V., Manrquez, J., Li, R., Li, H., Delavaux, C., Sebastian, S., Capendale, P.E., Wang, H., Xie, J., Yu, M., Masereeuw, R., Vermonden, T., Zhang, Y. S. (2020). Complexation-induced resolution enhancement of 3D-printed hydrogel constructs. *Nature Communications*, 11(1), [1267].

Duchamp, M., Liu, T., **van Genderen, A. M.**, Kappings, V., Oklu, R., Ellisen, L. W., Zhang, Y. S. (2019). Sacrificial Bioprinting of Mammary Ductal Carcinoma Model. *Biotechnology Journal*, 1700703

Jochems, P., van Bergenhenegouwen, J., **van Genderen, A.M.**, Eis, S., Wilod Versprille, L., Wichers, H. J., Jeurink, P., Garssen, J., Masereeuw, R. (2019). Development and validation of bioengineered intestinal tubules for translational research aimed at safety and efficacy testing of drugs and nutrients. *Toxicology in Vitro*, 60, 1-11.

van Genderen, A. M., Jansen, J., Cheng, C., Vermonden, T., & Masereeuw, R. (2018). Renal Tubular-and Vascular Basement Membranes and their Mimicry in Engineering Vascularized Kidney Tubules. *Advanced healthcare materials*, 7(19), 1800529.

Pi, Q., Maharjan, S., Yan, X., Liu, X., Singh, B., **van Genderen, A. M.**, Robledo-Padilla, F., Parra-Saldivar, R., Hu, N., Jia, W., Xu, C., Kang, J., Hassan, S., Cheng, H., Hou, X., Khademhosseini, A., & Zhang, Y. S. (2018). Digitally tunable microfluidic bioprinting of multilayered cannular tissues. *Advanced Materials*, 30(43), 1706913.

Zhang, Y. S., Pi, Q., & **van Genderen, A. M.** (2017). Microfluidic Bioprinting for Engineering Vascularized Tissues and Organoids. *J Vis Exp*, 126.

*These authors contributed equally

